The tectonic structure and seismicity of West Antarctica from a regional seismic deployment

Charles Kingsley Dunham

Submitted in accordance with the requirements for the degree of
Doctor of Philosophy

The University of Leeds
School of Earth and Environment

October 2020

Declaration

The candidate confirms that the work submitted is his own, except where work which has formed part of jointly authored publications has been included. The contribution of the candidate and the other authors to this work has been explicitly indicated below. The candidate confirms that appropriate credit has been given within the thesis where reference has been made to the work of others.

The work in Chapter 3 of the thesis has appeared in publication as follows:
Dunham,, C.K., O'Donnell, J.P., Stuart, G., Brisbourne, A., Rost, S., Jordan, T., Nyblade, A., Wiens, D., and Aster, R., 2020. A Joint Inversion of Receiver Function and Rayleigh Wave Phase Velocity Dispersion Data to Estimate Crustal Structure in West Antarctica. Geophysical Journal International, 223(3), pp.1644-1657. https://doi.org/10.1093/gji/ggaa398.

I performed all receiver function processing, modelling and analysis. Rayleigh Wave phase velocity dispersion data was produced by J.P. O'Donnell. I wrote the manuscript, which was improved by suggestions and comments from the co-authors.

Acknowledgements

The work in this PhD was supported by the School of Earth and Environment at The University of Leeds. Having now spent a combined 9 years with the School of Earth and Environment through both my undergraduate and postgraduate studies, I owe a great deal of gratitude to both the School and to all the people who have made it such a fantastic place to be during my time here. A special thanks to my supervisors Graham Stuart and Sebastian Rost, who have provided me with guidance throughout all of my studies in Leeds. Their support has really helped to push me over the line, particularly over the past few months, with all the complications that writing a thesis during a global pandemic entails. I also have to give a massive thanks to JP O'Donnell, who gave up huge amounts of his time to help me with much of the nitty-gritty that went into this thesis and my publication. JP was also kind enough to take me under his wing during our time in the field in Antarctica, and I'm sure that legend of his ice digging ability is still well known within the Antarctic community. Being able to go to Antarctica as part of this project truly was a dream come true, and the memories I have of my time there will stay with me for the rest of my life. I would also like to thank Alex Brisbourne, and all the people at the British Antarctic Survey who made the deployment of the UKANET a success. UKANET was supported by the Natural Environment Research Council [grant NE/L006065/1]. I also thank all of our collaborators from the POLENET project for allowing data access.

Throughout the five years of my PhD there have been some tremendous highs, but also some very difficult times as well. I know for a fact that I would not have made it to this point were it not for the phenomenal people that I have been lucky enough to surround myself with. I'm sure that I would have thrown in the towel a long time ago if it were not for the support of the magnificent Eleanor Hopkinson. Through your endless kindness, compassion and hilarity, you have managed to keep me sane, and give me the drive I needed to get to this far. I'm sure that living with a PhD student during thesis writing is testing at the best of times, let alone through a national lockdown, so the fact that you have managed to come to the end of this process without cancelling the wedding is a true testament to your patience and resilience. I am so excited for our future together, and I could not imagine my life without you by my side.

I would like to thank all of my wonderful family, who have loved and supported me in every aspect of life. My parents have given, and continue to give so much encouragement, guidance and love, without which I would be lost. Thank you to Honor and Perrie, who constantly inspire me, and to all of my Grandparents, who have brought so much joy to my life and supported me since before I put on the cape. A special thanks to Joe Cann, who has provided me with so much wisdom and opportunity throughout my studies, your help in getting me to the end of my PhD has been invaluable. I would also like to thank the Hopkinson clan for taking me in as one of their own despite my lack of Yorkshire heritage, getting to know you all has been a highlight of the past four years. A final thank you to all of my brilliant friends near and far, who are always on hand to provide help and laughter at the drop of a hat. Dave, Oran, Jack, Becky, Matt, Dan, Alex, Fletch, Dav, Josh, Rowly, Maurits, thank you all.

Abstract

In this thesis I investigate the tectonic structure and seismicity of West Antarctica using recently deployed seismic networks. To study the crustal thickness of West Antarctica's constituent tectonic blocks, I model crustal shear-wave velocity structure using a joint inversion of receiver functions and Rayleigh wave phase velocity dispersion. I model crustal thickness from 30-38 km in the Antarctic Peninsula, and 38-40 km in the Haag-Ellsworth Whitmore block. Within the West Antarctic Rift System (WARS), I model a crustal thickness range of 18-28 km, and show that the thinnest crust is in the vicinity of the Byrd Subglacial Basin and Bentley Subglacial Trench. I find that the thin WARS crust extends towards the Pine Island Rift, suggesting that the northern boundary of the WARS lies in this region, ∼200 km north of its previously accepted position. I additionally forward model high frequency receiver functions to assess if any thick, low velocity subglacial sediment accumulations are present, finding a 0.1-0.8 km thick layer at 10 stations. Such subglacial sediment could provide a source region for the soft basal till that acts to accelerate ice flow.

To investigate the active processes occurring in West Antarctica I study local seismicity recorded from 2015-2018. I locate 86 events during this period, of which I categorise 32 as 'likely tectonic', 17 as 'likely ice-quakes' and 37 as 'possible ice-quakes'. The distribution of events correlates well with modelled regions of high uplift resulting from Glacial Isostatic Adjustment. I also investigate styles and patterns of cryoseismicity produced by Pine Island Glacier, recorded at nearby stations from 2016-2018. High frequency (1-5 Hz) tremor produced by iceberg calving was detected at stations >250 km away from the glacier's calving front, whilst smaller repetitive seismicity produced by the destruction of the glacier's ice melánge is also located.

Contents

List of Figures

List of Tables

Nomenclature

List of acronyms

ANET	Antarctic Network
AP	Antarctic Peninsula
ASE	Amundsen Sea Embayment
BEDMAP2	Ice thickness and subglacial topographic model of Antarctica
BSB	Byrd Subglacial Basin
BSE	Bellingshausen Sea Embayment
BST	Bentley Subglacial Trench
EA	East Antarctica
EIS	Evans Ice Stream
EM	Ellsworth Mountains
ERH	Horizonal event location error
ERZ	Vertical event location error
ETMTRF	Extended Time Multi-Taper Frequency Domain Cross Correlation Receiver Function
EWM	Ellsworth Whitmore Mountains
GAMSEIS	Gamburtsev Antarctic Mountains Seismic Experiment
GPS	Global Positioning System
GSM	Gamburtsev Subglacial Mountains
HEW	Haag-Ellsworth Whitmore Mountains
HMSV	Hudson Mountains Subglacial Volcano

HN	Haag Nunataks
IRIS	Incorporated Research Institution for Seismology
ITDD	Iterative Time Domain Deconvolution
LPO	Lattice preferred orientation
LTA	Long time average
MBL	Marie Byrd Land
MTRF	Multi-Taper Frequency Domain Cross Correlation Receiver Function
NEIC	National Earthquake Information Center
NERC	National Environment Research Council
P arrival	Arrival of the primary/pressure wave
P wave	Primary/pressure/compressional wave
PASSCAL	Program for Array Seismic Studies of the Continental Lithosphere
PIG	Pine Island Glacier
PIR	Pine Island Rift
Pms	Primary to shear wave converted phase produced at the Moho
POLENET	Polar Earth Observing Network
PpPms, PpSms, PsPms	Multiply reflected phases with phase conversions occuring at the surface and Moho
Ps_{ice}	Pressure to shear wave converted phase produced at the ice/bedrock interface
RIS	Rutford Ice Stream
RMS	Root Mean Square
RSE	Ross Sea Embayment
S arrival	Arrival of the secondary/shear
S wave	Secondary/shear wave
SPO	Shape preferred orientation

STA	Short time average
TAM	Transantarctic Mountains
TAMSEIS	Transantarctic Mountains Seismic Experiment
TG	Thwaites Glacier
TI	Thurston Island
UKANET	UK Antarctic Network
WA	West Antarctica
WARS	West Antarctic Rift System
WM	Whitmore Mountains
WSRS	Weddell Sea Rift System

List of symbols

κ	V_P/V_S ratio	[-]
ρ	Density	[kg/m^3]
A_0	Distance correction term	[-]
A_{WA}	Wood Anderson amplitude	[-]
M_b	Body-wave magnitude	[-]
M_W	Moment magnitude	[-]
H	Crustal thickness	[km]
M	Earthquake magnitude (generic)	[-]
M_L	Local magnitude	[-]
R	Hypocentral distance	[km]
S	Station correction	[-]
V_P	Velocity of primary/pressure wave	[km/s]
V_S	Velocity of secondary/shear wave	[km/s]

Chapter 1

Introduction

1.1 Overview

Antarctica is a tectonically diverse and enigmatic continent. The continent hosts two distinct tectonic provinces, East and West Antarctica, which are roughly separated by the 3500 km long Transantarctic Mountains (Fig. 1.1). East Antarctica features ∼40 km thick cratonic crust (e.g. *Ritzwoller et al.*, 2001) with anomalously high deglaciated elevations (*Cogley*, 1984), whilst West Antarctica is considered an assemblage of discrete geological terranes (*Dalziel and Elliot*, 1982) featuring thinner crust at ∼27 km (*Ritzwoller et al.*, 2001) (Fig. 1.2). The crustal blocks that comprise West Antarctica are separated by the diffuse West Antarctic Rift System (WARS), which features thin crust (20-25 km (e.g. *Chaput et al.*, 2014)) and deglaciated bedrock elevations well below sea level (*Cogley*, 1984). Given the extensive ice coverage provided by the vast West Antarctic Ice Sheet, the exact bounds of the rift system are poorly constrained. Antarctica's inherent dichotomy in both its geology and hypsometry stem from its complex tectonic evolution since the break-up of Gondwana (e.g. *Jordan et al.*, 2020), yet our understanding of the continent's tectonic framework remains limited. Only ∼2% of Antarctica's bedrock is exposed (*Fretwell et al.*, 2013), therefore probing the continent's geology is heavily reliant on geophysical techniques. Additionally, the hostile environment presented by Antarctica has historically restricted field studies of the continent's tectonics.

Over the past 20 years there has been an increase in the availability and quality of satellite and airborne potential field data, along with the deployment of major seismic networks in the interior of the continent for the first time. The GAMSEIS (2007-2014) and TAMSEIS (2000-2004) seismic networks have probed East Antarctica, whilst

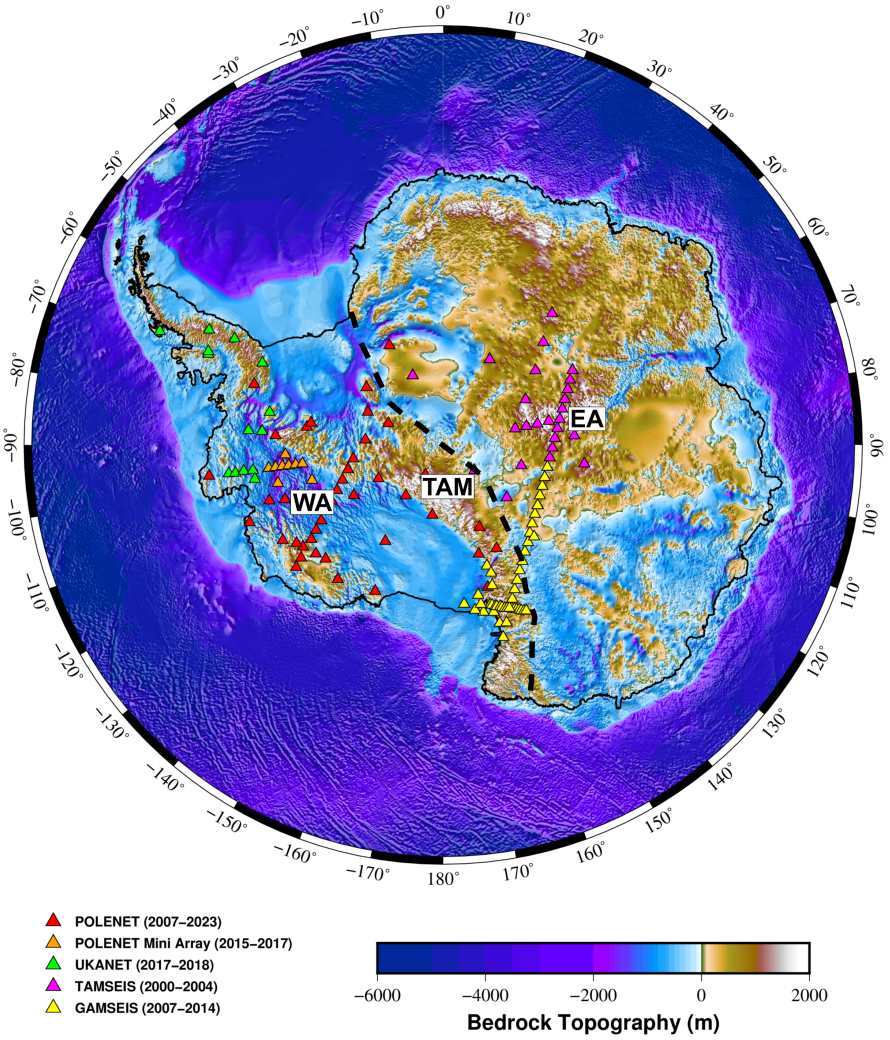

Figure 1.1: A map of Antarctica with West Antarctica (WA), East Antarctica (EA) and the Transantarctic Mountains (TAM) labelled over BEDMAP2 bedrock topography (*Fretwell et al.*, 2013). The TAM roughly deliniate the boundary between East and West Antarctica, and the boundary is shown in black dashed. The major seismic networks distributed across the interior of Antarctica are also displayed. The POLENET/ANET and POLENET Mini Array are displayed in red and orange triangles respectively (*Wilson et al.*, 2006) (DOI: https://doi.org/10.7914/SN/YT_2007), UKANET in green (DOI: https://doi.org/10.7914/SN/1D_2016), TAMSEIS in pink (*Hansen et al.*, 2015) (DOI: https://doi.org/10.7914/SN /ZJ_2012), and GAMSEIS in yellow (DOI: https://doi.org/10.7914/SN /ZM_2007).

in West Antarctica the POLENET/ANET network was installed in 2007, with some backbone stations still active (Fig. 1.1). These networks have been hugely beneficial for the study of Antarctica's tectonics, yet given the scale of the continent there are still large areas which lack seismic coverage. One such area is the Ellsworth Land region to the south of the Antarctic Peninsula and further inland towards the WARS (Fig. 1.2). Studying this area is crucial for constraining the progression of the WARS towards the Amundsen and Bellingshausen Sea embayments, and if there is any linkage between the WARS and the neighbouring Jurassic Weddell Sea Rift System (Fig. 1.2). To this end, the UKANET seismic and GPS network was deployed (2016-2018), featuring stations in Ellsworth Land, along the spine of the Antarctic Peninsula and around the Pine Island Rift for the first time (Fig. 1.1). Another motivating factor for the deployment of the UKANET seismic network was to probe the viscosity of the upper mantle (*O'Donnell et al.*, 2017), and improve models of the Glacial Isostatic Adjustment processes occurring in West Antarctica (*Nield et al.*, 2018). Improving the accuracy of Glacial Isostatic Adjustment models can in turn improve the ability to model ice mass change using satellite data, as any surface uplift relating to Glacial Isostatic Adjustment can be isolated.

Improving our understanding of West Antarctic Rift System's structure and extent will help to enhance the accuracy in modelling West Antarctica's tectonic evolution and active processes. The ambiguity in the size of the WARS and how much extension it has accommodated is important for accurate modelling of plate circuit closure (e.g. *Granot et al.*, 2013). Additionally, knowledge of the crustal and upper mantle structure across this region will allow for a more accurate estimation of geothermal heat flux (e.g. *Shapiro and Ritzwoller*, 2004, *An et al.*, 2015). Constraining geothermal heat flux is of particular importance in West Antarctica, given that the basal heat flow into the overlying West Antarctic Ice Sheet is a key control for modelling ice dynamics. Given the ∼58 m of potential sea level rise held in grounded ice in the West Antarctic Ice Sheet (*Fretwell et al.*, 2013), and its rapidly accelerating outlet glaciers (*Rignot et al.*, 2011), having a more complete understanding of its basal processes is critical. Another factor which influences the basal environment of an ice sheet is the presence of soft subglacial sediment, which reduces basal friction and promote ice flow (e.g. *King et al.*, 2016). Given the large subglacial basins present within the WARS (Fig. 1.2), there is a significant potential for substantial sediment accumulation.

This thesis aims to use the UKANET and POLENET/ANET seismic networks (Fig. 1.1) to improve our understanding of the structure, seismicity and tectonics of West Antarctica. A particular focus of this study is constraining the progression of the WARS

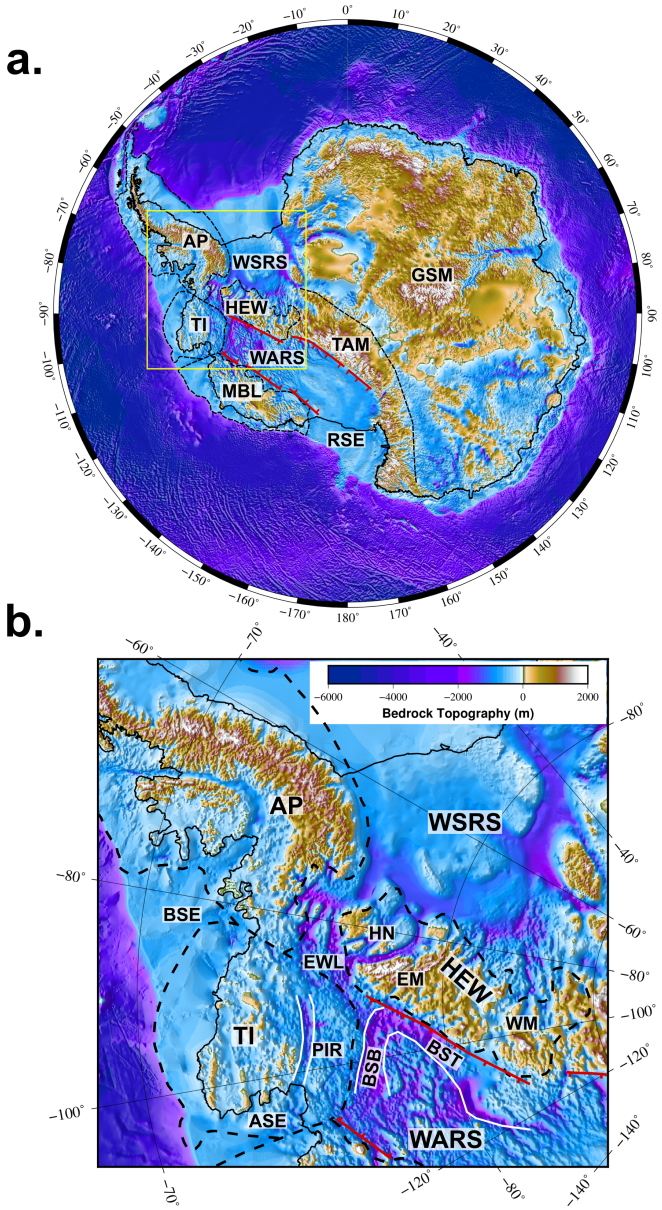

Figure 1.2: a) A bedrock topography map of Antarctica (*Fretwell et al.*, 2013) with major tectonic structures labelled and the West Antarctic block boundaries of *Dalziel and Elliot* (1982) added in black dashed. Additionally the margins of the WARS are shown in red. The tectonic features labelled are the Antarctic Peninsula (AP), Weddell Sea Rift System (WSRS), Haag-Ellsworth Whitmore block (HEW), Thurston Island (TI), Marie Byrd Land (MBL), Transantarctic Mountains (TAM), Gamburtsev Subglacial Mountains (GSM) as well as the Ross Sea Embayment (RSE). b) The area of West Antarctica that forms the focus of this study with additional structures/regions added. These are Ellsworth Land (EWL), Haag Nunataks (HN), Ellsworth Mountains (EM), Whitmore Mountains (WM) Bellingshausen Sea Embayment (BSE), Amundsen Sea Embayment (ASE), Pine Island Rift (PIR), Byrd Subglacial Basin (BSB), and Bentley Subglacial Trench (BST). The bounds of b) are shown by the yellow box in a).

into Ellsworth Land and towards the Amundsen and Bellingshausen Sea embayments; regions in which the tectonic framework is poorly understood (Fig. 1.2). To do this, I aim to use a joint inversion of receiver functions and Rayleigh wave dispersion curves to probe the West Antarctica's crustal structure, further demonstrating how seismology can be used to model features of the solid earth in the presence of thick ice cover. I also aim to model if there is any subglacial sediment present beneath each seismic station, and if the sediment distribution is likely to have influenced the regional ice flow. Thick subglacial sediment accumulations can provide a source region for basal till, which in turn can reduce a glacier's basal friction. By modelling the presence of subglacial sediment using receiver functions I therefore aim to demonstrate how passive seismicity can be used to infer more about the basal environment of an ice sheet, which could be applied in other glaciated regions. An additional aim of this thesis is to investigate the styles and patterns of cryoseismicity produced by Pine Island Glacier, recorded at UKANET stations from 2016-2018. Pine Island Glacier is one of the largest outlet glaciers from the West Antarctic Ice Sheet, as has experienced a rapid acceleration over recent decades (*Rignot et al.*, 2011). Temporal patterns in the rates of automatically detected seismicity surrounding Pine Island Glacier may provide additional detail on the glacier's ice dynamics. To probe Pine Island Glacier's ice dynamics using records of passive seismicity I aim to look at any possible correlation between the rate of automatically detected seismicity, and other observed/modelled features such as the glacier's flow speed and mean monthly temperature. Using long term records of passive seismicity to study glacial dynamics could provide valuable insight into glacial characteristics in other polar regions (e.g. Greenland, West/East Antarctica).

1.2 Thesis outline

This thesis is comprised of 7 chapters. Chapter 1 overviews the tectonic setting of Antarctica from its origins as part of Gondwana through to present. Chapter 2 introduces the seismic networks used in this study, including details of the deployment of the UKANET seismic network. Chapter 3 describes the generation and modelling of receiver functions from the UKANET and POLENET/ANET records. The chapter presents work from the *Dunham et al.* (2020) publication. In Chapter 3 I aim to infer the presence of any potential subglacial sediment beneath the West Antarctic Ice Sheet by forward modelling of high frequency receiver functions. In this chapter I additionally aim to model crustal thickness and structure across West Antarctica using a joint inversion of receiver functions and ambient noise derived Rayleigh wave phase dispersion curves. Chapter 4 aims to identify if any local tectonic seismicity is present in the UKANET record, and whether any located seismicity correlates with the regional

tectonic processes. In Chapter 5 rates of automatically detected seismicity at UKANET stations close to Pine Island Glacier are used to infer more detail on the glacier's ice dynamics, and seismicity associated with iceberg calving is investigated. In Chapter 6 the results from all previous chapters are brought together to build a comprehensive interpretation of the tectonic structure and seismicity of West Antarctica. The results are additionally considered in the context of previous studies of the region. The overall conclusions of the study are presented in Chapter 7.

1.3 Tectonic background

Antarctica originated as part of the Paleozoic super-continent of Gondwana (Fig. 1.3), during which time it was in contact with Australia, Africa, India and South America (e.g. *Boger*, 2011). The emplacement of the Karoo-Ferrar Large Igneous Province at ∼183 Ma in the Weddell Sea region preceded the Mesozoic breakup of Gondwana, initiating rifting between Africa and Antarctica (*Storey et al.*, 1996). In addition, the smaller crustal blocks that make up West Antarctica were separated from Gondwana along the paleo-Pacific margin (Fig. 1.3). East Antarctica remained in contact with Australia until the opening of the Tasman Gateway in the Cenozoic at ∼40-30 Ma, eventually leaving Antarctica isolated. The growth of the Tasman Gateway and Drake Passage in the late Oligocene then allowed for the establishment of the Antarctic Circumpolar Current, leading to the subsequent glaciation of Antarctica (*Kennett*, 1977).

1.3.1 East Antarctica and the Transantarctic Mountains

Following Antarctica's separation from Gondwana, the Cenozoic formation of the 3500 km long Transantarctic Mountains created a natural divide between East and West Antarctica. The Transantarctic Mountains feature elevations up to 4500 m, but the lack of compression between East and West Antarctica leaves their origin unclear (*Robinson and Splettstoesser*, 1986). In central regions of the Transantarctic Mountains the substantial topography has been attributed to flexural uplift (*Stern and ten Brink*, 1989, *Wannamaker et al.*, 2017), whilst other explanations include high plateau collapse (*Bialas et al.*, 2007). The Transantarctic Mountains link with the Haag-Ellsworth Whitmore block to form the eastern edge of the extensional WARS, and as such is a rift bounding mountain range (*Behrendt and Cooper*, 1991) (Fig. 1.2).

To the east of the Transantarctic Mountains lies East Antarctica, a remnant of Gondwanan lithosphere. It has been suggested that East Antarctica is a Precambrian shield,

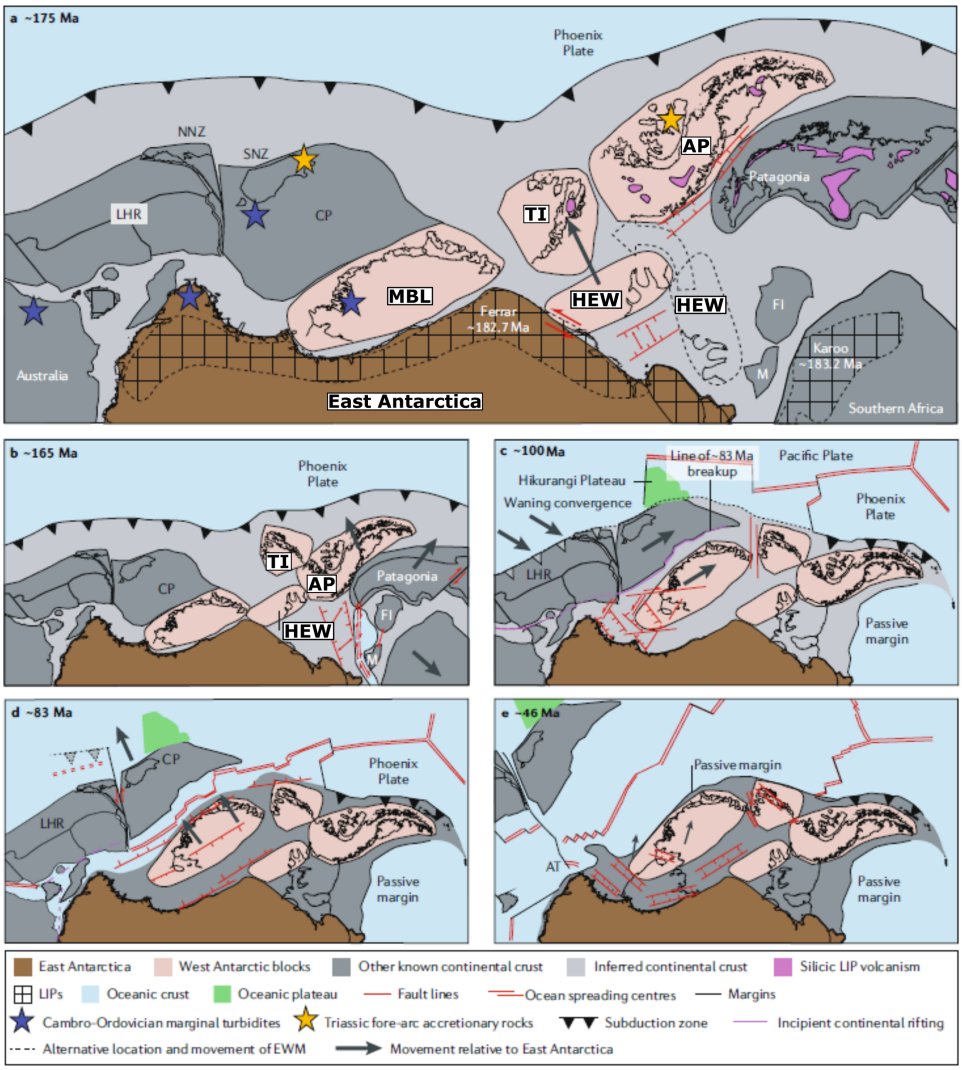

Figure 1.3: A West Antarctic plate reconstruction from 175 to 45 Ma modified from *Jordan et al.* (2020) with East Antarctica as a fixed reference. West Antarctica's crustal blocks are shown in pink, along with other present day continental regions in dark grey and intervening areas in light grey. a) The initiation of Gondwanan break up in the mid Jurassic. Mafic large igneous provinces (LIP) are shown in hashed regions with silicic LIPs in dark pink. Rotation of the HEW block has already occurred, with its previous position in dashed line. b) South Africa moving away from Antarctica in the mid Jurassic. c) Initiation of extension between Marie Byrd Land and the Transantarctic Mountains leading to the development of the WARS. d) Separation of Zealandia from Marie Byrd Land. e) Further development and extension of the WARS in the Cenozoic. Key annotated features: Antarctic Peninsula (AP), Haag-Ellsworth Whitmore block (HEW), Thurston Island (TI), Marie Byrd Land (MBL), Falkland Islands (FI), South New Zealand (SNZ), North New Zealand (NNZ)

formed from an Archean nuclei in the Proterozoic (*Boger*, 2011). The correlation between the marginal cratons along East Antarctica's coastline and those of Australia, Africa and India led to the interpretation that the region was a key part of Gondwana prior to its break-up (*Dalziel*, 1992). East Antarctic crust is on average ∼40 km thick (*Ritzwoller et al.*, 2001), hosting substantial subglacial features such as the Gamburtsev Subglacial Mountains and the Aurora and Wilkes Subglacial Basins. The Gamburtsev Subglacial Mountains are of a similar scale to the European Alps, maintaining an elevation of >2000 m. A lack of geologic samples due to the total ice cover in the region has resulted in the origin and timing of uplift in the Gamburtsev Subglacial Mountains being debated (*Ferraccioli et al.*, 2011).

1.3.2 West Antarctica

West Antarctica is a younger and more tectonically complex counterpart to East Antarctica. Its varied geological terranes and complicated tectonic history means that a simple tectonic classification for the region is not suitable. The extensive ice cover provided by the West Antarctic Ice Sheet makes delineating the exact bounds of the region's crustal blocks difficult. West Antarctica features three blocks originally defined in *Dalziel and Elliot* (1982), which formed along the convergent paleo-Pacific margin of Gondwana: the Antarctic Peninsula, Thurston Island and the volcanic Marie Byrd Land dome (e.g. *Lawver et al.*, 1992) (Fig. 1.3). Separated from the convergent tectonics of the ancient Pacific Gondwanan margin is the Haag-Ellsworth Whitmore (HEW) block. The HEW block is a displaced fragment of the East Antarctic craton margin (*Dalziel and Elliot*, 1982, *Dalziel*, 1992), with the rifted domains of the WARS and Weddell Sea Rift System on either side (Fig. 1.2). The WARS grew as a result of broad Cretaceous to Cenozoic rifting, whilst rifting in the Weddell Sea Rift System was initiated by the Jurassic break-up of Gondwana (*Jordan et al.*, 2020; and references therein).

Haag-Ellsworth Whitmore block

The HEW is a composite block consisting of the Haag-Nunataks, Ellsworth Mountains and Whitmore Mountains (Fig. 1.2). The block features atypical stratigraphy and crustal structure with respect to its surroundings, and is proposed to be a remnant of Gondwanan lithosphere. The northwest-southeast structural trend within the HEW is perpendicular to the neighbouring Thiel Mountains, which are part of the Transantarctic Mountains (*Storey and Dalziel*, 1987), suggesting that it has undergone significant rotation (*Dalziel and Elliot*, 1982). Models of how the HEW arrived at its current position are contentious. Paleomagnetic and geological interpretations

(*Schopf*, 1969, *Randall and Mac Niocaill*, 2004) include a 90° rotation and ∼1500 km of translation from a pre-rift position in between South Africa and East Antarctica. A recent geophysical study of the Weddell Sea by *Jordan et al.* (2017) proposes a 'less travelled' model, whereby the HEW was originally located in the Weddell Sea region before Jurassic extension. The model of *Jordan et al.* (2017) only accounts for a ∼30° rotation, but they suggest that deformation associated with the Permian Gondwanide Orogen may have provided the additional rotation required to reconcile with previous studies.

The Haag Nunatak sector of the HEW block features a ∼2 km^2 outcrop of Mesoproterozoic age magmatic arc rocks, which are roughly twice as old as any other rocks found in West Anatarctica (*Millar and Pankhurst*, 1987). Despite the small outcrop, aeromagnetic data indicates that the Mesoproterozoic basement extends ∼120,000 km^2 across this region (*Golynsky et al.*, 2018, *Jordan et al.*, 2020). The petrology and age of the Mesoproterozoic basement is similar to the Natal Embayment of South Africa, and the basement of East Antarctica. This suggests that the basement rocks of the Haag Nunataks may have developed at ∼1200 Ma along the margin of the proto-Kalahari Craton (e.g. *Jacobs et al.*, 2008). The exposed geology of the neighbouring Ellsworth-Whitmore Mountain section of the HEW block features Cambrian to Permian sedimentary rock with isolated igneous intrusions. The basement rock within the Ellsworth Mountain section is not exposed, however, a Hf isotope study of detrital zircons (*Flowerdew et al.*, 2007) suggests that it is a similar age to the exposure in the Haag Nunataks. It has been suggested that the Ellsworth-Whitmore Mountains were thrust over the Haag Nunataks in the Permo-Triassic (*Maslanyj and Storey*, 1990), forming the HEW block.

Antarctic Peninsula and Thurston Island

To the northwest of the HEW lies the Antarctic Peninsula, which along with Thurston Island has experienced a range of magmatism relating to the evolution of the convergent Paleo-Pacific Gondwanan margin. The oldest basement exposure in the Antarctic Peninsula relates to early Ordovician arc magmatism (*Riley et al.*, 2012). Ordovician magmatism of the same type has similarly been identified further along the Paleo-Pacific Gondwanan margin, in the North Patagonian Massif (e.g. *Pankhurst et al.*, 2006). The peak of arc magmatism in the Antarctic Peninsula and Thurston Island was in the Jurassic and Cretaceous (Fig. 1.4). In the Jurassic, the Chon Aike Large Igneous Province added felsic volcanism to the eastern Antarctic Peninsula, and was influenced by the early stages of the break-up of Gondwana (*Pankhurst et al.*, 1998a). At a similar time (188-180 Ma) there was also a separate episode of granitic

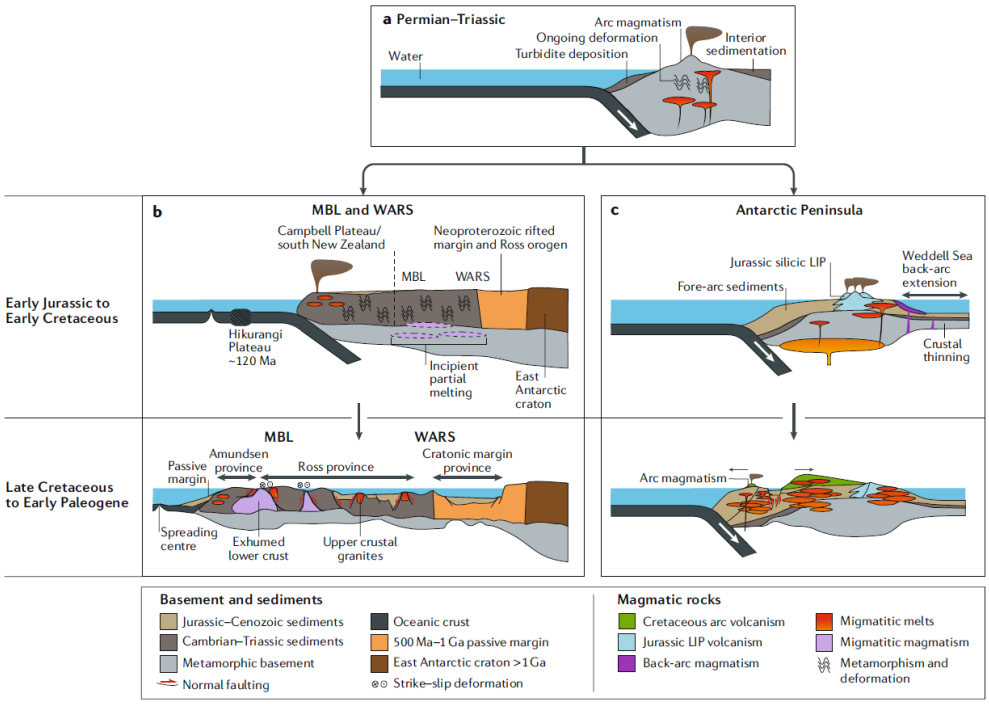

Figure 1.4: Cross sections through the Antarctic Peninsula, Marie Byrd Land (MBL) and the WARS from the Permian to Early Paleogene, taken from *Jordan et al.* (2020). a) The paleo-Pacific Antarctic margin with associated arc magmatism. b) The movement of Marie Byrd Land away from East Antarctica, leading to the development of the WARS. The extension in Marie Byrd Land led to the exhumation of lower crustal rocks and emplacement of upper crustal granites through associated melting. c) The subduction and magmatism experienced by the Antarctic Peninsula through the Jurassic.

magmatism attributed to subduction related melting (*Riley et al.*, 2017). By the Mid-Cretaceous, the proto-Pacific Gondwanan margin experienced widespread magmatism, impacting the Antarctic Peninsula as well as Thurston Island and Marie Byrd Land to a lesser degree (Fig. 1.4). Subduction and associated arc magmatism ceased on the Antarctic Peninsula at ∼20 Ma, however, subduction continued in the South Shetland trench to the north until ∼4 Ma (*Larter and Barker*, 1991). To restore the Antarctic Peninsula to its pre-Gondwanan break up position, it must be rotated anticlockwise with respect to East Antarctica, eventually aligning with the southern tip of South America (Fig. 1.3). Thurston Island underwent a similar rotation to the Antarctic Peninsula (*Grunow et al.*, 1991). Rotation of all West Antarctic blocks was likely complete prior to the opening of the Weddell Sea at *c.* 165 Ma (*Jordan et al.*, 2020) (Fig. 1.3).

Marie Byrd Land

Some of the Mesozoic magmatism experienced by the Antarctic Peninsula and Thurston Island also influenced the Marie Byrd Land dome, however, this region has had a more varied tectonic history. The ∼505 Ma gneissic basement identified near Mount Murphy (*Pankhurst et al.*, 1998b) indicates that this block originated near the geochemically similar Transantarctic Mountains Ross orogen. Arc magmatism occurred from the subduction of the Pheonix plate in pulses throughout Marie Byrd Land in the Ordovician-Silurian, Devonian-Carboniferous and Permian-Triassic (*Pankhurst et al.*, 1998b, *Siddoway and Fanning*, 2009, *Yakymchuk et al.*, 2015). Following the dominant convergent tectonics experienced by Marie Byrd Land, back arc extension starting at ∼105 Ma led to the block moving away from the Transantarctic Mountains, and the formation of the WARS (Fig. 1.3). Between ∼105 and ∼85 Ma the central WARS experienced ∼600 km of crustal extension (e.g. *Divenere et al.*, 1996) (Fig. 1.4). Mafic alkaline magmatism occurred in Marie Byrd Land since ∼34 Ma (*Rocchi et al.*, 2006). The alkali basalts and Cenozoic shield volcanoes of Marie Byrd Land suggest that a deep mantle source may be responsible for the volcanism in the region (*Wörner*, 1999). In addition, Marie Byrd Land features relatively thin crust, but high surface elevation, indicating that the region may be dynamically supported (*An et al.*, 2015). There are competing hypotheses regarding the driving mechanism for uplift in Marie Byrd Land, one being a plume source (e.g. *Behrendt*, 1999, *Spiegel et al.*, 2016) and the other a hydrous mantle wedge (*Finn et al.*, 2005). Despite the geochemical evidence for a plume-type source for the Marie Byrd Land volcanism, geophysical studies have not been able to clearly image a high temperature structure stretching into the deep mantle. Whether or not the source of Marie Byrd Land uplift and volcanism is linked to WARS extension has not been established.

West Antarctic Rift System

The WARS grew to be an asymmetric rift system 750-1000 km in width and 3000 km in length (*Behrendt et al.*, 1991). It has been proposed that extension in the WARS occurred in two pulses; the first being a well documented period of broad extension across the whole WARS in the Jurassic-Cretaceous (*Luyendyk*, 1995, *Siddoway et al.*, 2004) (Fig. 1.4). A second pulse of extension in the Neogene has been observed in the sedimentary basins of the Ross Sea (e.g. *Behrendt*, 1999, *Wilson and Luyendyk*, 2006), although whether the entire WARS was impacted is unclear. WARS extension seemingly slowed at *ca.* 17 Ma (*Cande et al.*, 2000). The lack of recent significant seismicity in the region (*Winberry and Anandakrishnan*, 2004) combined with the very low rates of intra-plate deformation (*Donnellan and Luyendyk*, 2004), may imply that the WARS is currently inactive.

Given the ambiguity over the exact timing of extension and the substantial ice cover, estimates of the total amount of extension encompassed by the WARS are poorly constrained. One-layer crustal stretching models assuming a ∼35 km initial thickness compared to the presently estimated 17-27 km thick crust suggesting ∼400-600 km of extension has occurred in the central WARS and up to 1000 km in the Ross Sea. Paleomagnetic modelling (*DiVenere et al.*, 1994) indicates a range from 440-1820 km. Paleomagnetic studies in this region are hampered by uncertainties in the amount of rotation between West Antarctica's crustal blocks, and a lack of Cretaceous correlative poles. As such improving estimates of contemporary crustal thickness within the WARS will allow for more accurate one-layer stretching modelling of the total extension.

1.4 Geophysical studies of West Antarctica's tectonics

1.4.1 Studies of crustal and upper mantle structure

Prior to the deployment of major seismic networks within the interior of Antarctica, studies of the continent's tectonic structure largely relied on isolated stations around the coastline. Despite the sparse station coverage, early surface wave dispersion studies were able to identify the disparity in gross crustal thickness between East and West Antarctica (*Evison et al.*, 1960, *Kovach and Press*, 1961). These pioneering studies estimated crustal thickness to be on the order of ∼25-30 km in West Antarctica and ∼35-40 km in East Antarctica. The findings of these early studies were later refined by surface wave tomography studies such as *Ritzwoller et al.* (2001), who modelled average crustal thickness at 27 km in the WARS and 40 km in East Antarctica. Studies of this type were able to give a first order approximation of crustal thickness variation across

the continent, but lacked the resolution to image shorter wavelength structure. Other studies used isolated stations within West Antarctica to obtain localised estimates of crustal thickness. *Winberry and Anandakrishnan* (2004) used receiver functions to estimate crustal structure at 7 stations distributed across West Antarctica, finding a minimum crustal thickness of 21 km within the Bentley Subglacial Trench. The crustal thickness modelled by these early studies indicated that the WARS had likely been subjected to crustal thinning, but to build a more complete understanding of West Antarctica's tectonics, a more substantial seismic network would be required.

Since the deployment of POLENET/A-NET (2008-) (Fig. 1.1), numerous studies have used the network to investigate crustal structure across West Antarctica. *Chaput et al.* (2014) produced P-wave receiver functions from the POLENET/A-NET deployment and inverted for crustal structure using a Markov Chain Monte Carlo inversion approach. They found 20-25 km thick crust in the central WARS, surrounded by thicker adjacent crustal blocks; ∼35 km in the HEW block, ∼30 km in Marie Byrd Land, and up to 45 km in the Transantarctic Mountains (Fig. 1.5(d)). Additionally, *Chaput et al.* (2014) infer a layer of low velocity subglacial sediment at many stations, with a thickness of up to ∼0.4 km within the Bentley Subglacial Trench. The presence of subglacial sediment in the region had previously been suggested by *Anandakrishnan and Winberry* (2004), who identified a ∼0.6 km thick layer in the vicinity of the Bentley Subglacial Trench.

An et al. (2015) modelled the 3-D lithospheric S-wave velocity structure across Antarctica using 122 stations distributed across the continent (Fig. 1.5(a)). They modelled the crust to be >50 km in the Gamburtsev Mountains of East Antarctica, and as low as ∼20 km within the WARS. *An et al.* (2015) also calculated a density ratio between the crust and lithospheric mantle, finding that either the average crustal density for Antarctica is much higher than average continental crust, or the lithospheric mantle density is at the low end of expected values for Archean lithosphere. The latter would suggest that much of the Antarctic lithosphere is of Archean age.

To avoid the complex near surface reverberation in P-wave receiver functions over ice, *Ramirez et al.* (2016) use S-to-P receiver functions at POLENET/A-NET stations across West Antarctica. They found crustal thickness to be in general agreement with *Chaput et al.* (2014), varying from 19-29 km across the WARS. *Ramirez et al.* (2017) built upon this study by using a joint inversion of Rayleigh wave phase velocities and P-wave receiver functions to image crustal structure at bedrock stations in West Antarctica. They reported average crustal thicknesses of ∼37 km in the HEW block, ∼30 km

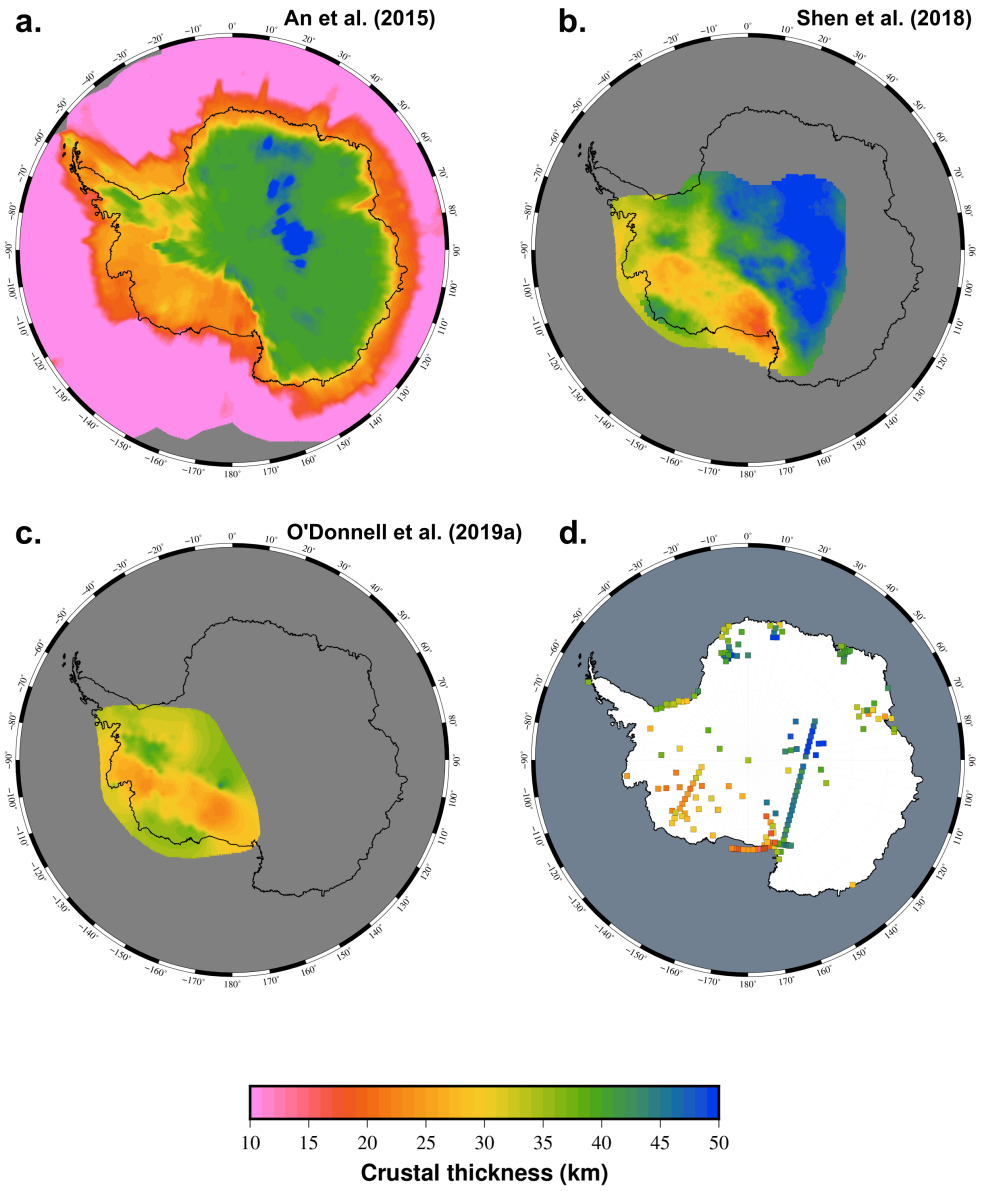

Figure 1.5: Seismicially derived crustal thickness models across Antarctica. a) Crustal thickness model derived from the 3D shear wave velocity model AN1-S of *An et al.* (2015). b) The crustal thickness model of *Shen et al.* (2018) produced using a Bayesian inversion of Rayleigh waves and receiver functions. The West Antarctic crustal thickness model of *O'Donnell et al.* (2019a), produced by modelling Rayleigh wave phase velocities from ambient noise. d) A compilation of crustal thickness estimates from a number of receiver function and wide angle refraction studies.

in Marie Byrd Land, 35 km at station MECK in the southern Antarctic Peninsula, and 38 km at THUR on Thurston Island. Crustal thickness from *Ramirez et al.* (2017) generally agree with *Chaput et al.* (2014), however they found the crust to be ∼10 km thicker at stations MECK and THUR, which they attribute to the presence of a 10-20 km thick mafic lower crust.

Shen et al. (2018) combine Rayleigh wave dispersion and receiver functions in a Bayesian Monte Carlo algorithm to construct a 3-D shear velocity model of the crust and uppermost mantle across Antarctica (Fig. 1.5(b)). In the WARS they find crustal thickness to range from 20-30 km, which is consistent with aforementioned studies. Additionally *Shen et al.* (2018) image thinner crust and upper mantle low velocity anomalies in the Amundsen Sea Embayment and Byrd Subglacial Basin, suggesting that these regions have experienced recent extension. *O'Donnell et al.* (2019a) and *O'Donnell et al.* (2019b) modelled fundamental mode Rayleigh wave phase velocities at periods 7-143 s across West Antarctica using seismic ambient noise and earthquake data recorded on the UKANET and POLENET/ANET stations. *O'Donnell et al.* (2019a) find ∼22 km thick extended crust in the Ross and Amundsen Sea Embayments, and suggest that the Cenozoic evolution of the WARS shows along strike variability. In addition, *O'Donnell et al.* (2019a) model the crust to be ∼32-35 km thick in the southern Antarctic Peninsula and ∼30-40 km thick in the HEW (Fig. 1.5(c)). *O'Donnell et al.* (2019b) used the modelled fundamental mode Rayleigh wave phase velocities to study West Antarctica's upper mantle, suggesting that recent WARS tectonism is focussed on the rift margins, and confined to the uppermost 180 km of the mantle. *O'Donnell et al.* (2019b) also identified a low velocity anomaly in the upper mantle stretching from Marie Byrd Land to Pine Island Bay, which could correspond to a ∼150-200 °C temperature difference relative to the central WARS if of plume origin (Fig. 1.6). Given the similarity in strike between this anomaly and the paleo-Pacific Gondwanan margin, the low velocity anomaly may instead be a result of subduction related melt.

Owing to the gradual improvement in data coverage over the past 20 years, gravity studies have also provided valuable insight into Antarctica's tectonic structure (*von Frese et al.*, 1999, *Llubes et al.*, 2003, *Block et al.*, 2009, *O'Donnell and Nyblade*, 2014). By inverting GRACE satellite gravity data, *Block et al.* (2009) modelled crust up to 46 km thick in East Antarctica and in the region of ∼30 km in the centre of the WARS. *O'Donnell and Nyblade* (2014) followed up this study using an inversion of GOCO03S satellite gravity data, finding a mean crustal thickness of 40 km in East Antarctica, and 24 km in West Antarctica. Aerogravity has also been used in more localised studies to image shorter wavelength structure. *Jordan et al.* (2010) focus on the Pine Island

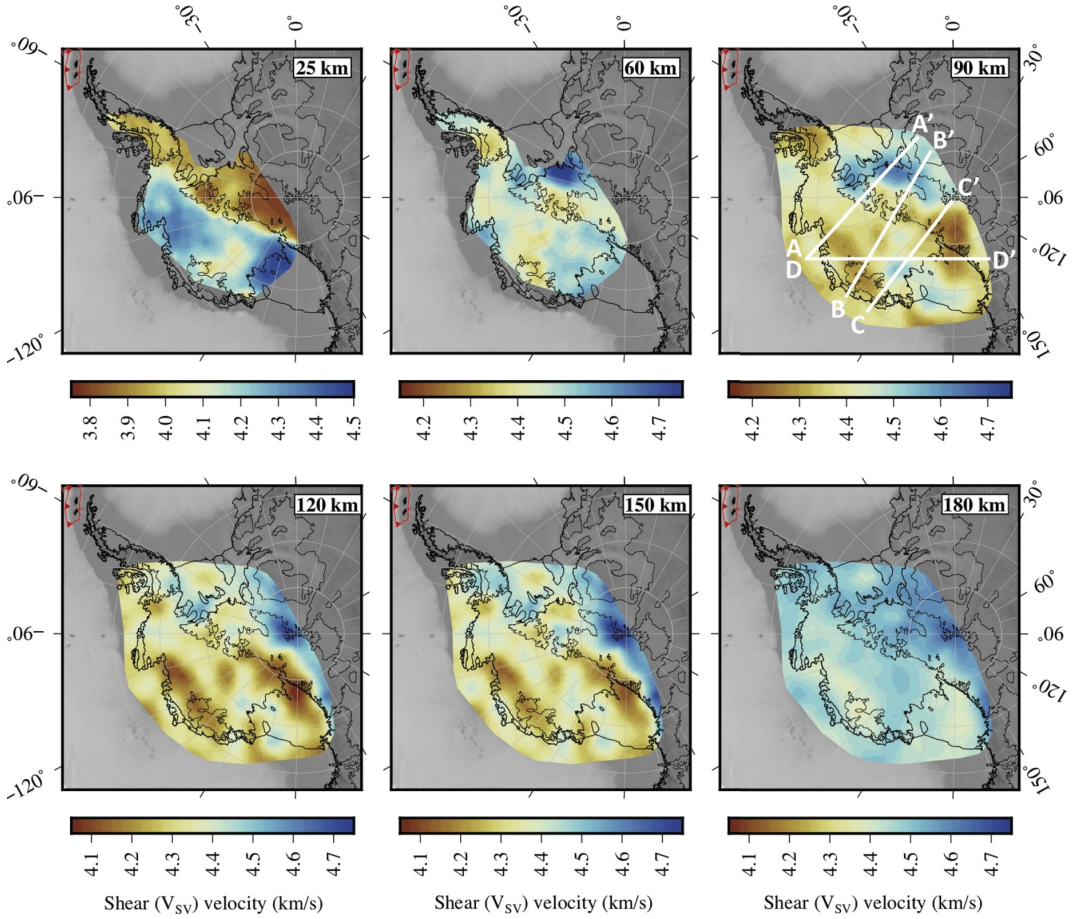

Figure 1.6: Shear wave velocity maps of the crust and upper mantle at various depths from *O'Donnell et al.* (2019a). A low velocity anomaly stretching from Marie Byrd Land to the Amundsen Sea Embayment is present from the 90 km panel to 150 km. Figure is taken from *O'Donnell et al.* (2019a).

Glacier region and model crust as thin as 19 km, suggesting that the region has been subject to enhanced crustal thinning.

1.4.2 Studies of intracontinental seismicity

The deployment of major seismic networks across Antarctica has also allowed for the study of intracontinental seismicity on a local and regional scale. Prior to these networks being deployed, seismic instrumentation was largely limited to the continent's coastline, with large interstation distances meaning that small magnitude events produced in the continental interior could not be reliably detected or located. Few large magnitude events originating from Antarctica had been detected teleseismically (*Adams et al.*, 1985, *Adams and Akoto*, 1986), which combined with the sparse instrumentation across the continent and consequent lack of sensitivity to small magnitude events, suggested

that very little intracontinental seismicity was produced by Antarctica.

The reason for the apparent low level of tectonic seismicity originating from Antarctica is unclear. *Sykes* (1978) suggested that the low levels of tectonic stress within the Antarctic plate has led to a reduced level of seismicity. The low levels of tectonic stress are likely a result of the continent being surrounded by spreading ridges, with a low level of intra-continental stress. An alternate interpretation for the low levels of seismicity is that the weight of the substantial continental ice cover is acting to increase the normal stress on faults (*Johnston*, 1987). Whilst both interpretations can potentially explain the lack of teleseismic seismicity originating from Antarctica, an additional consideration is the historic lack of instrumentation within the continental interior. This is particularly pertinent in West Antarctica, where the lack of instrumentation has meant that any regional scale seismicity potentially originating from the WARS has not been detected. Were there to be significant local seismicity originating from the WARS then that may lead to a reappraisal of the rift system's current level of activity.

Since the deployment of major seismic networks across both East and West Antarctica, low magnitude local events have been successfully detected and located. In East Antarctica *Lough et al.* (2018) identified 27 tectonic events which they interpret as being produced by a reactivated ancient rift system. In West Antarctica clusters of $M_L >$ 2 events on the flank of Marie Byrd Land and in the centre of the WARS were located by *Winberry* (2003) and interpreted to be of tectonic origin, whilst seismicity attributed to Marie Byrd Land volcanism has also been identified (*Lough et al.*, 2013, *O'Donnell et al.*, 2017). The POLENET/ANET network has also allowed for the study of West Antarctica's cryoseismicity, with seismic sources being identified within the firn layer (*Lough et al.*, 2015), and seismicty produced by large scale calving events also detected (*Winberry et al.*, 2020).

1.5 Specific aims and objectives of the thesis

The growing wealth of geophysical and geological studies over the past 20 years in West Antarctica has drastically improved our understanding of the region's tectonic structure and evolution. Despite this, there are still many questions which remain unclear, so by using new seismic data primarily from the UKANET and POLENET/ANET seismic networks, in this thesis I aim to address the following issues:

- The progression of the WARS towards the Bellingshausen and Amundsen Sea embayments (Fig. 1.2) and the tectonic structure of the southern Antarctic Penin-

sula and Ellsworth Land to the south is loosely constrained due to a historically poor seismic coverage in the region. Improving our understanding of the tectonic structure of the Ellsworth Land region is significant as it will reveal if there is any linkage between the WARS and neighbouring Weddell Sea Rift System. By studying the crustal structure of Ellsworth Land and the region surrounding the Pine Island Rift I aim to enhance our knowledge of the bounds and extent of the WARS. To study crustal structure I will use a joint inversion of receiver functions and Rayleigh wave phase velocity dispersion data. The resultant shear wave velocity-depth models from the joint inversion will allow for the interpretation of crustal thickness and internal structure. This technique will also provide valuable insight into the style of the crust-mantle boundary throughout West Antarctica's various crustal blocks.

- An important issue in Antarctica is the interaction between the Earth and cryosphere. The Antarctic ice sheet has a volume of 27 million km^3, holding a potential 58 m contribution to sea-level rise if melted (*Fretwell et al.*, 2013). The study area featured in this thesis also hosts some of the fastest accelerating outlet glaciers on the planet, such as Pine Island Glacier. Conditions at the base of the West Antarctic Ice Sheet play a key role for its future stability; from the amount of geothermal heat provided by the underlying crust, to the basal friction between the ice and bed. To investigate the basal environment I aim to model the presence and abundance of subglacial sediment beneath each seismic station using high frequency receiver functions. Soft, likely saturated sediment layers of this type reduce basal friction and promote faster ice flow. I will also discuss the implications of my findings of crustal structure for the potential geothermal heat production in the region.

- Given the previous lack of instrumentation in much of the study region and its apparent seismic quiescence, I aim to investigate whether any local seismicity is present. Identifying, locating and characterising any tectonic seismicity in this region will reveal if there is any fault movement associated with the activity of the WARS. In addition the substantial ice loss and associated glacial isostatic rebound that has recently occurred in the region may influence the style of observed seismicity.

- The cryoseismicity of Pine Island Glacier has been subject to limited study relative to other major West Antarctic ice streams such as the Rutford Glacier (e.g. *Adalgeirsdóttir et al.*, 2008), Thwaites Glacier (e.g. *Winberry et al.*, 2020), and Whillans Ice Stream (e.g. *Winberry et al.*, 2009). Given that Pine Island Glacier is one of the continent's fastest accelerating ice streams, investigating the patterns and styles of its associated seismicity will be important for building a comprehensive understanding of its ice dynamics. To do this I aim to locate and

characterise the local seismicity detected at the Pine Island Glacier UKANET stations recorded from 2016-2018.

Chapter 2

Seismic networks and data

In this thesis I investigate the tectonic structure and seismicity of West Antarctica using seismic data from 33 stations in both the UKANET and POLENET/ANET seismic networks (Fig. 2.1, Table 2.1). The 33 stations are distributed from the Antarctic Peninsula down to Ellsworth Land and the WARS, and crossing from Thurston Island to the HEW block (Fig. 2.1). For studying local seismicity I use a more complex combination of stations given the lack of temporal overlap/ distance between certain POLENET and UKANET stations. The main focus for the local seismicity search are the UKANET PIG stations from 2016-18. These five stations traverse both Pine Island Glacier and potentially the boundary between the Thurston Island and the WARS, and are distributed densely enough for the detection of local events. The following sub-sections will provide an overview into the deployment and instrumentation of the seismic networks used in this thesis.

2.1 POLENET/ANET

POLENET/ANET features a total of 59 seismic stations spread across West Antarctica and the Transantarctic Mountains (Fig. 1.1). The POLENET/ANET network comprises two temporary station transects along with 35 'backbone' stations with a longer (5+ year) deployment length. The first temporary transect of 14 stations traversed from Marie Byrd Land to the Transantarctic Mountains and was deployed from 2010-2013, and the second named the 'Mini Array' was contemporaneous with UKANET and featured 10 stations in the eastern WARS from 2015-2017. Most of the 'backbone' stations featured Nanometrics Trillium 240 s instruments sampled at 1 Hz and 40 Hz digitised with a Quanterra 330 Linear Phase Composite, although some were replaced with Nanometrics Trillium 120 s instruments sampled at 1 Hz and 100 Hz in

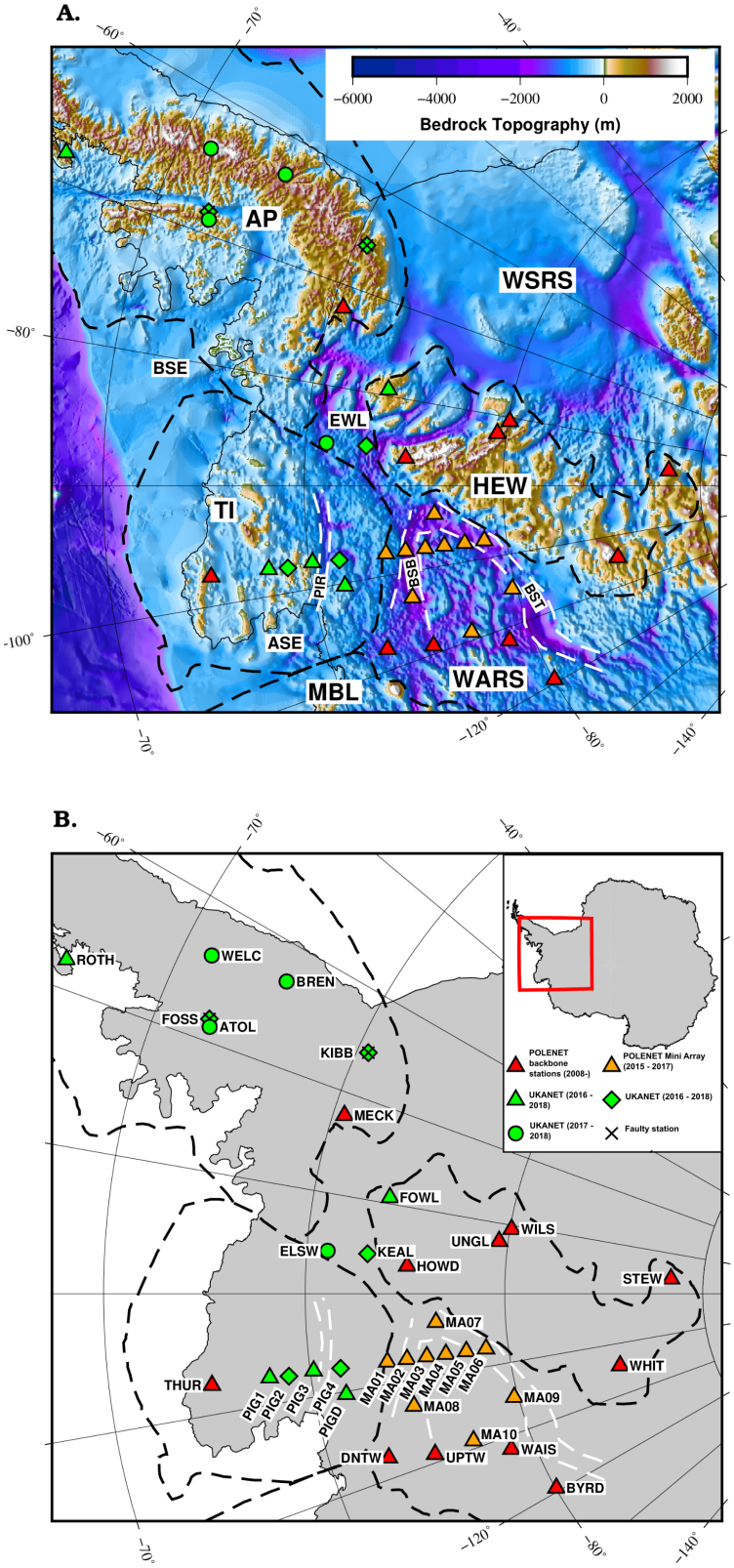

Figure 2.1: Maps of the study area in West Antarctica. Stations are coloured by network, with UKANET stations in green, POLENET/ANET backbone stations in red triangles, and POLENET Mini Array stations in orange triangles. UKANET station symbols correspond to the deployment period, with 2016-17 stations in diamonds, 2017-18 stations in circles and 2016-18 stations in triangles. The faulty stations KIBB and FOSS are also highlighted with a cross symbol. a) Seismic stations over bedrock topography (*Fretwell et al.*, 2013) with the block boundaries of *Dalziel and Elliot* (1982) in black dashed. b) Seismic stations with station names added next to each station symbol.

later field seasons (Table 2.1). The Marie Byrd Land temporary station traverse featured the same set up as the early 'backbone' stations, whilst the Mini Array consisted of Nanometrics Trillium 120 s instruments sampled at 1 Hz and 100 Hz (Table 2.1).

2.2 UKANET seismic network

The UKANET seismic network was deployed from 2016-2018 and aimed to fill some of the gaps left by the POLENET/ANET deployment. UKANET was comprised of 10 stations deployed in two network configurations, one from 2016-2017 and the second from 2017-2018 (Fig. 2.1). Moving some stations from the 2016-2017 to the 2017-2018 setup acted to maximise station coverage across Ellsworth Land and the southern Antarctic Peninsula. In addition to stations distributed across Ellsworth Land and the southern Antarctic Peninsula, UKANET featured five stations deployed in line with the POLENET Mini Array in the vicinity of Pine Island Glacier (PIG). These PIG and Mini Array stations created a station traverse spanning from Thurston Island to the WARS-HEW flank. The UKANET project also featured 10 Global Navigation Satellite System stations distributed across the southern Antarctic Peninsula, with the goal of modelling Glacial Isostatic Adjustment in the region.

2.2.1 Instrumentation and station set up

The seismic equipment used by UKANET follows the setup used by POLENET/ANET, and that advocated by IRIS PASSCAL (Incorporated Research Institutions for Seismology Program for Array Seismic Studies of the Continental Lithosphere) for seismic investigation in a polar environment (*Parker et al.*, 2011). UKANET used 10 cold rated 3-component Güralp CMG-3T Polar broadband sensors loaned from GEF SeisUK (Table 2.1). The CMG-3T Polar instruments are highly sensitive to ground velocity between 120 s and 100 Hz (Fig. A.1), and were sampled at 1 Hz and 100 Hz. A Quanterra Q330 and B44 baler combination were used at each station to digitise and log the data (Fig. 2.2). UKANET station deployment and maintenance was carried out with the assistance of the British Antarctic Survey.

Station	Network	Lat	Lon	Elevation (km)	Ice (km)	Date active from	Date active to	Total days active	Instrument	Techniques used
ATOL	1D	-71.3897	-68.8701	0.7	0.86	10/01/2017	29/01/2018	384	CMG3T	RF,LS
BREN	1D	-72.6750	-63.0210	1.6	0.13	19/01/2017	17/01/2018	363	CMG3T	RF,LS
BYRD	YT	-80.0170	-119.4738	1.5	2.45	13/01/2010	31/12/2019	3639	T240s	RF
DNTW	YT	-76.4512	-107.7769	1.0	2.11	02/01/2010	31/12/2019	3650	T240s/T120s	RF
ELSW	1D	-75.5194	-85.7076	1.2	1.89	06/01/2017	21/01/2018	380	CMG3T	RF,LS
FOWL	1D	-76.8928	-79.3011	1.3	0.00	13/02/2016	14/01/2018	701	CMG3T	RF,LS
HOWD	YT	-77.5286	-86.7694	1.5	0.00	09/01/2008	31/12/2017	3644	T240s	RF,LS
KEAL	1D	-76.5204	-85.6996	1.0	2.10	07/02/2016	06/01/2017	334	CMG3T	RF,LS
MA01	YT	-76.9397	-97.5596	1.3	2.03	07/01/2015	31/01/2018	1120	T120s	RF,LS
MA02	YT	-77.4394	-97.5595	1.5	3.00	08/01/2015	31/12/2016	723	T120s	RF,LS
MA03	YT	-77.9401	-97.5585	1.6	3.40	08/01/2015	31/12/2016	723	T120s	RF,LS
MA04	YT	-78.4221	-97.5879	1.7	3.10	10/01/2015	31/12/2016	721	T120s	RF,LS
MA05	YT	-78.9395	-97.5573	1.9	3.25	11/01/2015	31/12/2016	720	T120s	RF,LS
MA06	YT	-79.4397	-97.5587	1.9	3.80	12/01/2015	31/12/2016	719	T120s	RF,LS
MA07	YT	-78.2496	-93.4991	1.6	3.54	10/01/2015	31/12/2016	721	T120s	RF,LS
MA08	YT	-77.4014	-103.0022	1.3	3.05	06/01/2015	31/12/2016	725	T120s	RF,LS
MA09	YT	-79.8993	-104.9977	2.0	2.92	13/01/2015	31/12/2016	718	T120s	RF,LS
MA10	YT	-78.5999	-109.0003	1.7	1.80	22/12/2014	31/12/2016	740	T120s	RF,LS
MECK	YT	-75.2808	-72.1850	1.1	0.00	08/01/2008	31/12/2017	3645	T240s	RF,LS
PIG1	1D	-73.9782	-97.5750	1.0	1.20	28/01/2016	23/01/2018	726	CMG3T	RF,LS
PIG2	1D	-74.4557	-97.6830	1.0	1.10	29/01/2016	25/12/2016	331	CMG3T	RF,LS
PIG3	1D	-75.0841	-97.4744	0.7	0.90	30/01/2016	23/01/2018	724	CMG3T	RF,LS
PIG4	1D	-75.7599	-97.5830	0.8	1.60	30/01/2016	21/12/2016	326	CMG3T	RF,LS
PIGD	1D	-75.8026	-100.2758	0.8	1.25	31/01/2016	25/01/2018	725	CMG3T	RF,LS
ROTH	1D	-67.5200	68.1488	0.3	0.17	12/01/2016	14/01/2017	368	CMG3T	RF,LS
STEW	YT	-84.1863	-86.2349	1.6	0.88	08/01/2014	31/12/2017	1453	T240s	RF
THUR	YT	-72.5301	-97.5606	0.2	0.00	19/01/2011	31/12/2019	3268	CMG3T	RF,LS
UNGL	YT	-79.7746	-82.5240	0.7	0.00	28/12/2010	31/12/2017	2560	T240s	RF,LS
UPTW	YT	-77.5781	-109.0374	1.3	2.39	26/01/2011	31/12/2019	3261	T240s	RF
WAIS	YT	-79.4181	-111.7779	1.8	3.37	05/02/2009	31/12/2019	3981	CMG3T	RF
WELC	1D	-70.7318	-63.8274	1.5	0.64	18/01/2017	06/01/2018	353	CMG3T	RF,LS
WHIT	YT	-82.6823	-104.3867	2.3	0.00	19/01/2010	31/12/2017	2903	T240s	RF
WILS	YT	-80.0396	-80.5587	0.7	0.00	08/01/2008	31/12/2010	1088	T240s	RF

Table 2.1: Information on the location, deployment length and instrumentation of all stations used in this study. Ice thickness is taken from BEDMAP2 (*Fretwell et al.*, 2013). Instruments used are the Güralp CMG-3T 120 s (CMG3T), Nanometrics Trillium 240 s (T240s) and Nanometrics Trillium 120 s (T120s) sensors. Network codes: POLENET/ANET (YT, DOI: https://doi.org/10.7914/SN/YT_2007), UKANET (1D, DOI: https://doi.org/10.7914/SN/1D_2016). Abbreviations for techniques used: Receiver function analysis (RF), Local seismicity (LS). Some POLENET/ANET backbone stations are still active, as such the date active to column is the final date used in this thesis.

Most stations deployed in the Antarctic Peninsula were on or very close to bedrock on the flank of nunataks, whilst PIG and Ellsworth Land stations were deployed on ice. The field setup at each ice station is shown in Fig. 2.2 and was as follows. The sensor was deployed, with levelling checked using an air bubble on the instrument, then covered by a plastic drum and buried ∼2 m. At this depth the snow is firmer than at the surface, and provides a more thermally stable environment. Roughly 8-10 m away from the sensor enclosure is the electronics enclosure and solar panels. The electronics enclosure hosts the data aquisition, logging and storage systems as well as a rechargeable lead-acid battery and 10 primary lithium metal batteries. An aluminium sensor cable conduit linked the sensor to the electronics enclosure, and was also buried to avoid any influence from the wind on the sensor. Situated next to the electronics enclosure was the solar panel assemblage, which was mounted on a stand ∼2 m above the surface. The solar panels would act to provide additional power to the system, and also had a GPS clock and Xeos Iridium antenna mounted on top. Providing that the Iridium antenna stayed above the ice surface, it can provide a remote state of health check throughout the Antarctic winter. Prior to station burial the data recording stream, instrument mass positions and synchronisation with the GPS system were all checked using a handheld computer. Glacier poles ∼5 m in length were also erected next to the solar panels to identify the station should all other equipment be completely buried upon servicing/ retrieval.

2.2.2 Station deployment and servicing

UKANET stations were deployed in the 2016-17 network configuration (Fig. 2.1) in January to February 2016. All stations were installed without problem other than KIBB located next to McKibben Nunatak in the southern Antarctic Peninsula, and FOSS on Alexander Island. Challenging weather conditions during installation at KIBB meant that one of the horizontal components was not responding correctly and was therefore unusable. FOSS was deployed on a small outcrop of bedrock near the British Antarctic Survey field station Fossil Bluff, but became unresponsive soon after the field crew had departed. Upon return in the following field season it was discovered that additional melt water had flooded the area, completely submerging the station and rendering it unrecoverable.

Station servicing and reorganisation into the 2017-18 configuration was carried out from December 2016-February 2017, which the author was able to participate in. The field site for the station FOSS on Alexander Island was moved to a small plateau on top of the island and named ATOL. Given the loss on one instrument at FOSS, it was not possible to replace the faulty sensor at KIBB, and another instrument fault meant

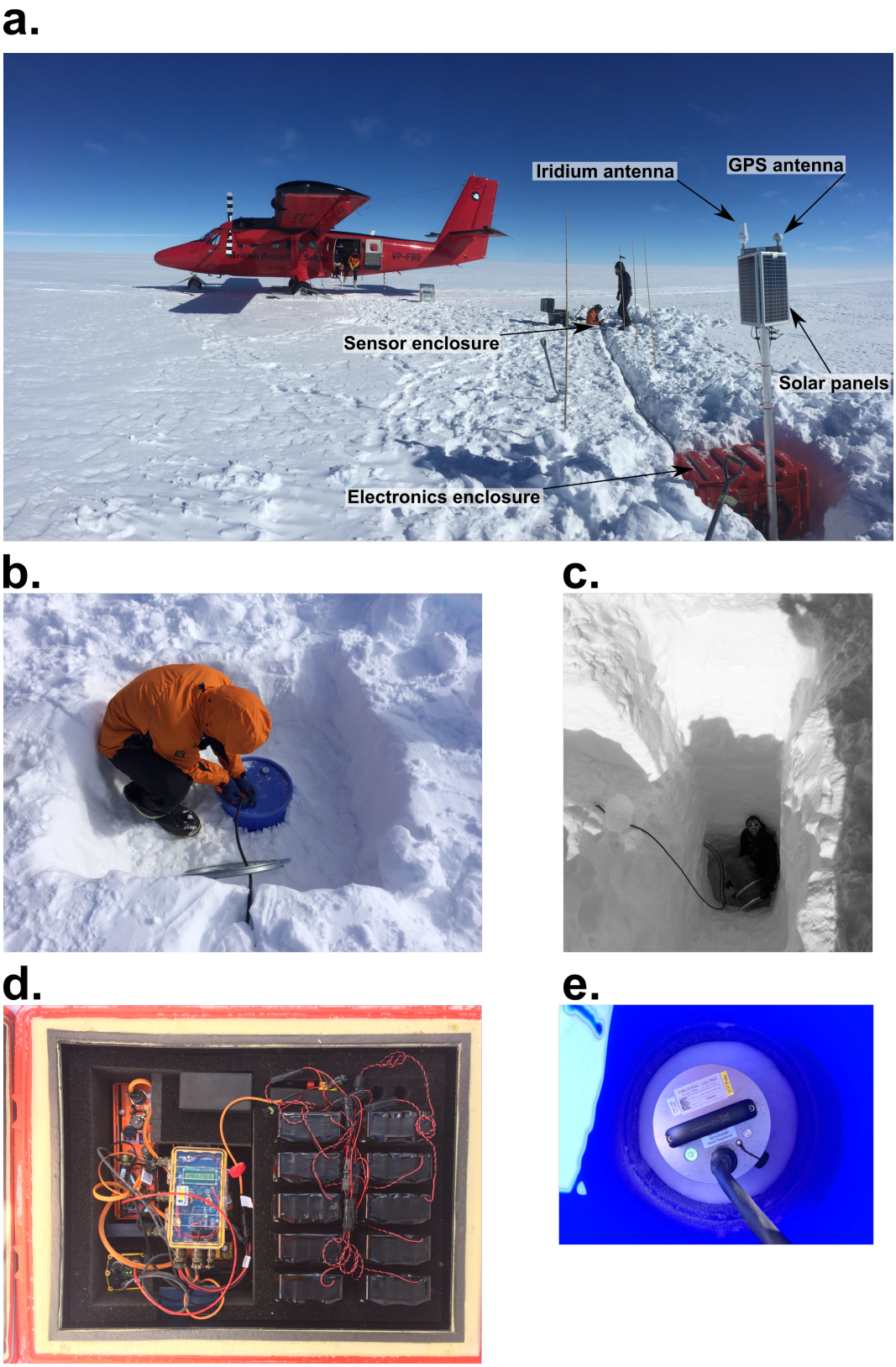

Figure 2.2: Field images from the 2016-2017 service run. a) The field setup of a seismic station during deployment. Once the station was installed and running all equipment/instrumentation is buried and bamboo canes removed. b) The sensor enclosure being sealed before burial during installation. c) A ∼5 m dig to recover a sensor after one year of burial. d) Inside of the electronics enclosure with the digitising, data logging, and power management systems on the left and batteries on the right. e) Inside of the sensor enclosure showing the installed Güralp CMG-3T Polar broadband instrument.

that PIGD only had a vertical component operational from 2017 to 2018. Stations were decommissioned in the 2017-18 field season.

2.3 Seismic noise in West Antarctica

The seismic noise conditions in West Antarctica differ somewhat relative to other continental environments, given the lack of any cultural noise from human activity. The dominant source of seismic noise at most stations in West Antarctica is produced by the strong katabatic winds, which are most influential at frequencies >1 Hz (e.g. *Frankinet et al.*, 2020). To counter this, all POLENET/ANET and UKANET instruments deployed on ice were buried 1-2 meters beneath the ice, however the solar panel enclosure and glacier pole (8-10 m from the instrument) both protrude above the ice surface, and will be impacted by the wind. Stations deployed on bedrock were often situated on the flanks of nunataks and as such were more susceptible to seismic noise introduced by the wind. POLENET/ANET stations buried 1-2 m beneath the ice surface were 5-7 dB quieter than bedrock stations in the short period band (*Anthony et al.*, 2015). As such many of the POLENET/ANET and UKANET 'bedrock' stations deployed on nunataks were in fact situated on the nunatak flank, where some ice cover was available.

Chapter 3

Joint inversion of receiver functions and Rayleigh wave phase velocity for crustal structure

3.1 Introduction

In this chapter I both forward model receiver functions to infer the presence of subglacial sediment at ice stations, and jointly invert receiver functions and Rayleigh wave phase velocity data for crustal structure at all stations within my region of interest (Fig 2.1). Modelling the crustal shear wave velocity structure allows for the interpretation of crustal thickness beneath each seismic station. The UKANET deployment includes stations in the southern Antarctic Peninsula and Ellsworth Land for the first time. Studying the crustal thickness at stations will provide valuable insight into the eastern termination of the WARS, and whether there is a connection between the WARS and the Weddell Sea Rift System. Additionally, I include stations from the UKANET - POLENET/ANET Mini Array traverse which straddle the Thurston Island-WARS boundary, which will allow for a better delineation of the northern edge of the WARS and its progression towards the Amundsen Sea Embayment. Interpreting the crustal shear wave velocity models at each station will also provide additional information on the relative proportions of likely felsic/intermediate to mafic crust (e.g. *Ramirez et al.*, 2017). This work has been published in Geophysical Journal International in August 2020 as *Dunham et al.* (2020).

Joint inversion of receiver function and surface wave dispersion data has become a standard technique for investigating lithospheric seismic velocity structure (e.g. *Julia et al.*, 2000, *Ramirez et al.*, 2017, *Shen et al.*, 2018). Receiver functions are sensitive to velocity discontinuities beneath the seismic station (e.g. the Moho), whilst surface wave dispersion data are more sensitive to the absolute velocity at a given depth. As such, the combination of these two data types in a joint inversion is complementary when attempting to model seismic velocity structure beneath a station (e.g. *Julia et al.*, 2000).

3.2 Receiver function method

The coda of a teleseismic P-wave arrival contains P-to-S-wave converted phases produced by major impedance contrasts in the local subsurface (e.g. the Moho - Fig. 3.1). Receiver function analysis is a technique which uses these converted phases to estimate the Earth structure that produced them (e.g. *Langston*, 1979, *Owens et al.*, 1984). P-wave receiver functions are generally calculated using teleseismic waves from 30° to 90° away, as these arrive at near vertical incidence, and minimise the influence of any source or path effects.

The recorded vertical component of a teleseismic event contains the convolution of the incident P-wave energy with the Earth structure beneath the instrument. By deconvolving the vertical component from the horizontal components after rotation to a radial-tangential sense, any source, path and instrument effects on the waveform are removed. The resulting horizontal components are named the radial and transverse receiver functions, and contain a series of spikes which represent phase conversions from the local Earth structure (Fig. 3.1). The relative timing and amplitude of these P-to-S-wave converted phases and associated multiples can be used to model the depth to the interface which produced them for a given velocity model. In an isotropic Earth where all interfaces are flat, all receiver function energy would be contained on the radial component. Any energy on the transverse component is therefore an indicator of heterogeneity in the Earth structure, be that anisotropy or dipping interfaces (e.g. *Kind et al.*, 1995).

In the case of a simple crust over mantle half-space model, the P-to-S-wave converted phases produced at the Moho are shown in Fig 3.1. Given that V_p is faster than V_s, the first arrival is the direct Pp phase, followed by the Pms Moho conversion. Phases denoted by lower case ‘p’ or ‘s’ indicate an up-going converted phase, whereas phases denoted by an upper case ‘P’ or ‘S’ indicate that they are travelling downwards

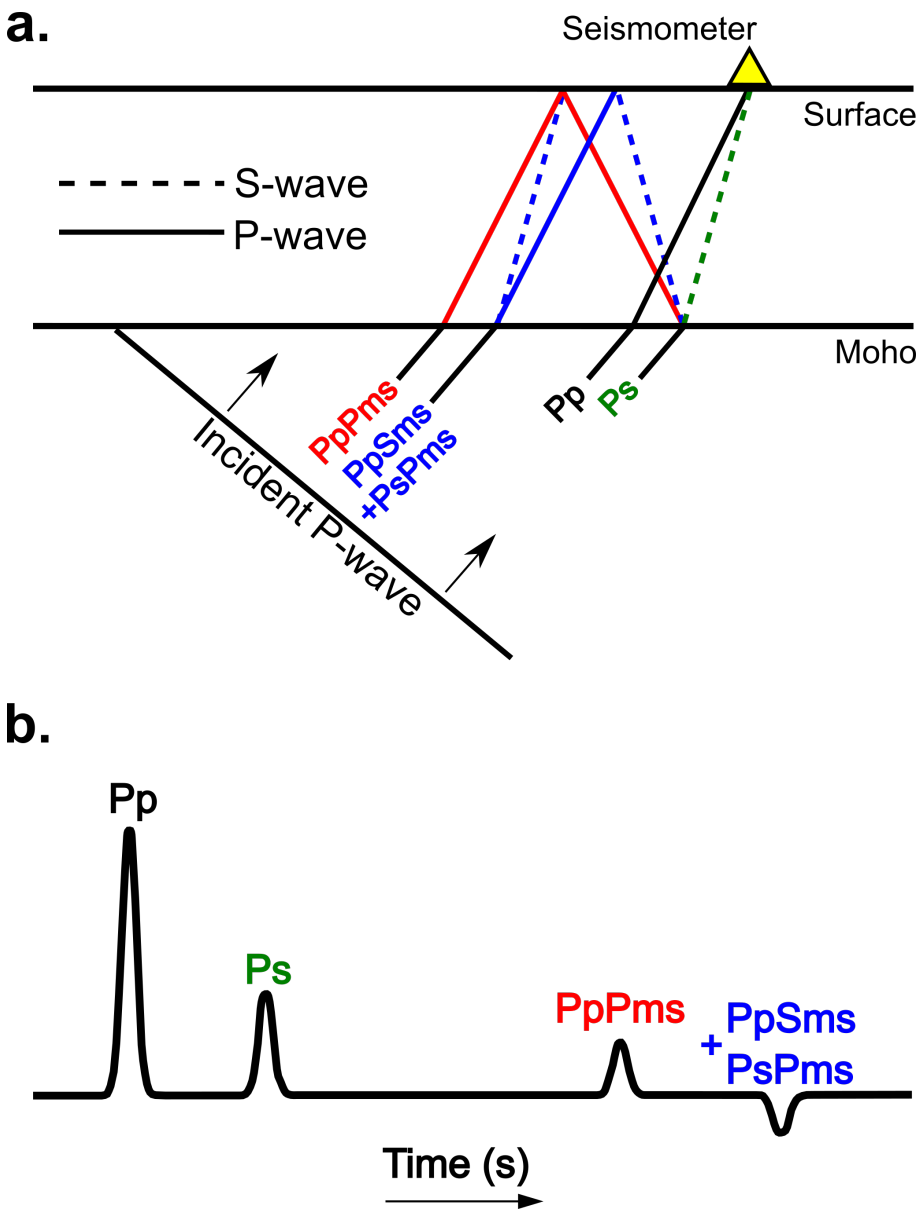

Figure 3.1: a) A schematic example of the key converted phases and associated multiples used in receiver function analysis for constraining crustal thickness. b) The resulting receiver function from the simple one layer crust over mantle half space earth model shown in panel a. This is a synthetic, noise free example, which shows easily distinguishable arrivals of the direct P-wave (Pp), P-to-s phase conversion from the Moho (Ps) and associated multiples (PpPms, PpSms + PsPms).

either from the source or a surface reflection/conversion (*Stein and Wysession*, 2009). Other converted phases which have subsequently been multiply reflected by the surface and Moho will also be recorded by the seismograph, and will appear in the receiver function. Notable phases of this type are the PpPms, PpSms and PsPms phases (Fig 3.1). The timing, amplitude and polarity of all converted and multiply reflected phases are controlled by the contrasts in acoustic impedance within the underlying crust and upper mantle.

In Antarctica, studying receiver functions is complex due to the pervasive ice cover across the continent. In addition to the converted phases from crustal interfaces in a receiver function, there will also be phase conversions and associated reverberation from the crust-ice boundary (Fig. 3.2). The high impedance contrasts at the bedrock-ice and ice-air interfaces mean that these arrivals are usually high amplitude and dominate the early portion of a receiver function, often interfering with the Moho Pms phase. These ice reverberations limit the viability of using traditional techniques such as H-κ stacking for modelling crustal thickness (H) and Vp/Vs (κ) ratio. H-κ stacking (*Zhu and Kanamori*, 2000) uses the relative timing of the Moho Pms, PpPms and PpSms/PsPms phases to estimate crustal thickness and Vp/Vs ratio for given crustal velocities and slowness. As such if the arrival of the Moho Pms phase is obscured by the ice reverberation then H-κ stacking will not work.

Strategies for accounting for the ice reverberation have been proposed if the ice thickness, P- and S- wave velocity are well constrained (e.g. *Cho*, 2011). The method of *Cho* (2011) involves creating a synthetic receiver function from an ice/crust model and deconvolving it with the receiver function to recover an ice-free receiver function. This method breaks down when the real structure is more complex than a simple ice over crust model, as is often the case in Antarctica with the presence of subglacial sediment. Another technique to address the ice reverberation in P-wave receiver function analysis has been developed, which uses downward continuation of the receiver function through the ice sheet (*Chai et al.*, 2017). To use this technique accurately however, one must have a firm understanding of the medium that the receiver functions are being downward continued through. The downward continuation technique is therefore also inappropriate in the presence of subglacial low velocity layers such as unconsolidated sediment, in which the velocity structure is often poorly constrained.

S-wave receiver functions have been used in ice covered regions in an attempt to avoid the ice reverberation issues faced by P-wave receiver functions (*Ramirez et al.*, 2016). In an S-wave receiver function S-to-P-wave phase conversions are used from the S-wave

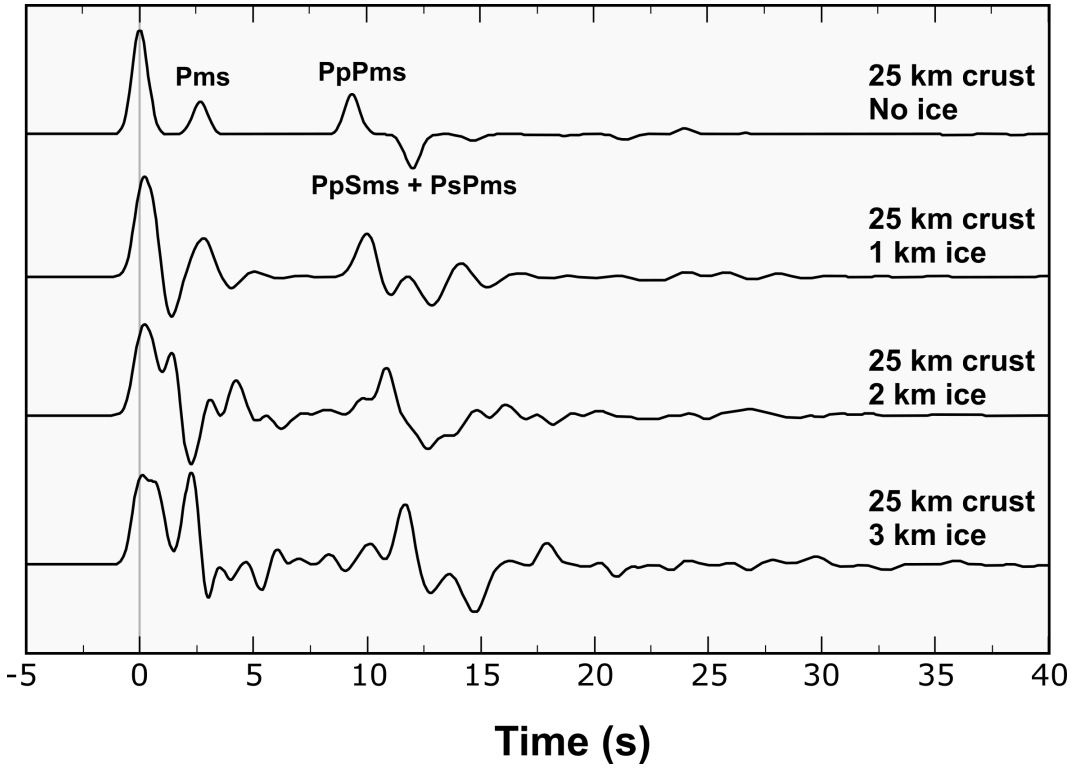

Figure 3.2: a) A synthetic example of the impact of a near surface ice layer on a receiver function. The uppermost trace features a simple 25 km thick, one layer crust over a mantle half space, with the key converted phases labelled. The following three traces feature the same earth model, but with an ice layer of increasing thickness on atop the crust. As the ice layer thickens, the more complex the receiver function becomes, due to the additional P-wave reverberation in the ice column.

coda. Given that the Moho Smp phase arrives before the direct Ss phase and there isn't as much reverberant P-wave energy present, S-wave receiver functions aren't as severely impacted by the presence of ice. The main issue for using S-wave receiver functions however is the more restrictive teleseismic event distribution required, typically from 60° to 80° versus 30° to 90° for P-wave receiver functions. The lower frequency content of the S-wave receiver function also limits the resolution to which thin crust can be detected. A typical S-wave receiver function has a maximum frequency of ~ 1 Hz, whereas P-wave receiver functions can be produced with much higher maximum frequencies. For a 25 km thick crust with P- and S- wave velocities of 5.8 km/s and 3.46 km/s respectively, the diameter of the first Fresnel zone (*Yilmaz*, 2001) from a S-wave receiver function with a maximum frequency of 1 Hz would be ~ 20 km, whilst the corresponding value from a P-wave receiver function with a maximum frequency of 2 Hz would be ~ 10 km.

3.2.1 Choice of receiver function technique

To account for the low velocity near surface structure present in the study area (ice/subglacial sediment) in the forward modelling and joint inversion processes, the use of high frequency receiver functions (>2 Hz) is necessary. Two of the most commonly used receiver function techniques for high frequency receiver function studies are the Iterative Time Domain Deconvolution (ITDD) method of *Ligorría and Ammon* (1999) and the Extended Time Multi-Taper Frequency Domain Cross Correlation Receiver Function (ETMTRF) method of *Helffrich* (2006). ITDD involves convolving the vertical component of a seismogram with an iteratively updated spike train (*Ligorría and Ammon*, 1999). Time domain deconvolution is often dominated by the highest amplitude Fourier components. The highest amplitude Fourier components are usually the lower frequencies, which can hinder the ability to resolve short wavelength structure.

In an attempt to generate receiver functions which better account for the lower amplitude parts of the signal *Park and Levin* (2000) developed the Multi-Taper Frequency Domain Cross Correlation (MTRF) technique, which was later extended by *Helffrich* (2006) to ETMTRF. MTRF uses multi-taper correlation as part of the deconvolution process in the frequency domain, allowing for the downweighting of the less correlated spectral noise, and reduced spectral leakage (*Park and Levin*, 2000). This makes the MTRF technique more suitable for stations with a high degree of ambient noise. As such it has been successfully applied in oceanic island studies (*Lodge and Helffrich*, 2006), where the noise conditions will be similar to stations on the Antarctic Peninsula (*Anthony et al.*, 2015). A limitation of the MTRF technique is that it is assumed that the signal is stationary within each taper, resulting in the receiver functions only containing usable energy over the first 10 s (*Helffrich*, 2006). To account for this, *Helffrich* (2006) developed ETMTRF to include an overlap-and-sum technique with sliding windows in which the stationary spectrum is estimated. To preserve phase information a series of short multiple tapers are used to window through the entire time series. The individual Fourier transformed signals for each taper are summed to build a frequency domain representation of the signal which preserves phase lag (*Helffrich*, 2006). ETMTRF's capacity to resolve arrivals from short wavelength near surface structure, in combination with the technique's ability to handle noise is why I decided to use the technique for all receiver function generation in this study.

Fig. 3.3 shows a comparison of the ITDD and ETMTRF techniques at station PIG1 which was deployed atop 1.2 km of ice. Receiver functions were calculated for each technique for all 134 suitable events recorded at PIG1 from 2016-2018, and then stacked using a phase weighted stacking scheme (*Schimmel and Paulssen*, 1997). Panel a)

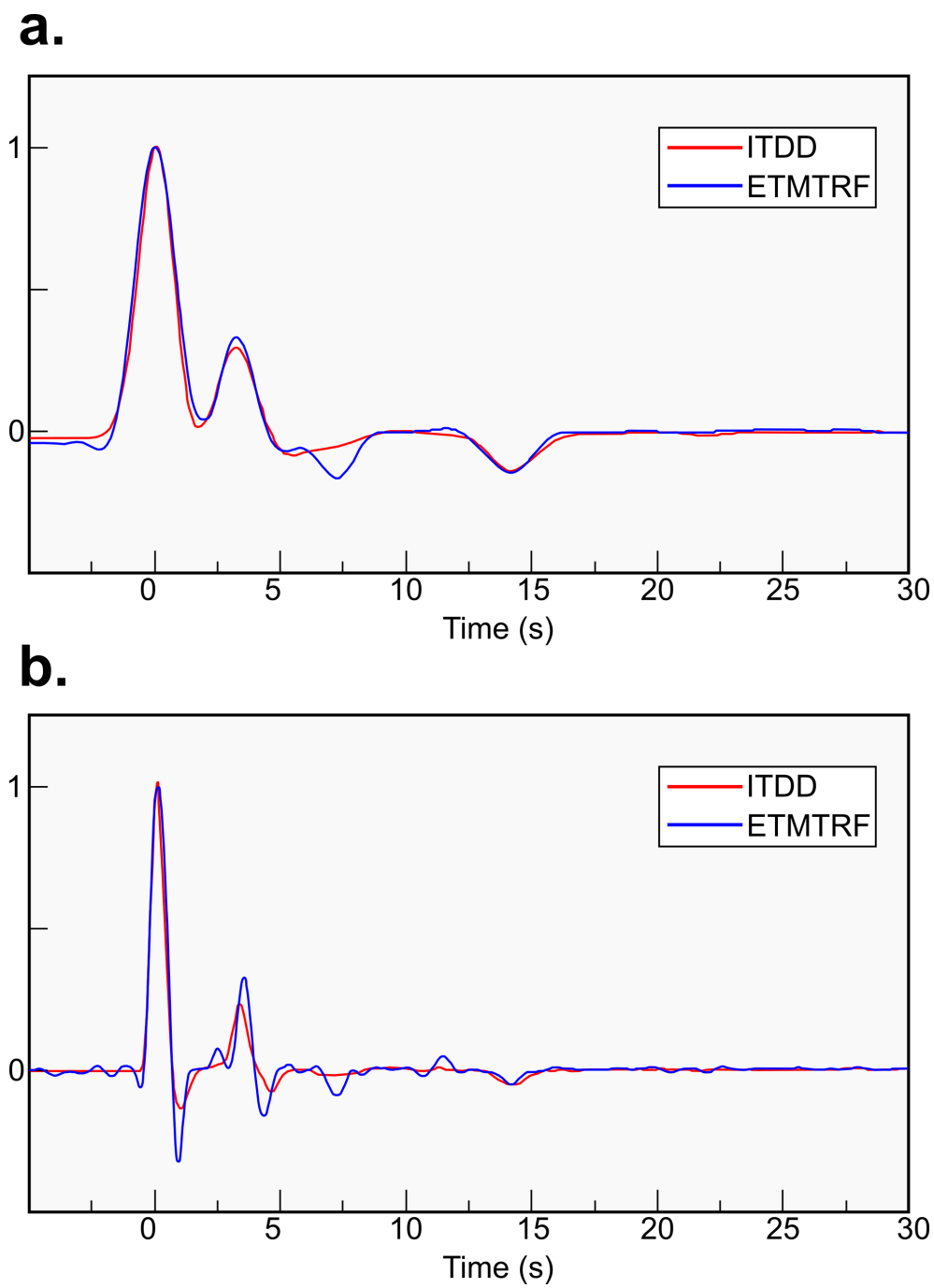

Figure 3.3: Comparison between the ITDD and ETMTRF techniques at station PIG1. a) 134 receiver functions stacked using a phase weighted scheme with a maximum frequency of ∼0.5 Hz, produced using ITDD (red) and ETMTRF (blue). b) The same as panel a. but with a maximum frequency of ∼2 Hz.

features a maximum frequency of 0.5 Hz, whilst panel b) features a maximum frequency of 2 Hz. At low frequency (0.5 Hz) both techniques perform similarly and are able to resolve the potential Pms phase at ∼4 s and the likely PpSms + PsPms crustal multiple at ∼14 s. At higher frequency (2 Hz) however the ability of the ETMTRF technique to resolve finer structure becomes more apparent. Given that PIG1 has 1.2 km of underlying ice the first 5 s will feature the Ps_{ice} phase and associated multiples. For a 30 km thick crust the Pms phase would be expected to arrive at 3-4 s, whilst the often-high amplitude reflected phases from the base of the ice sheet could arrive at roughly the same time depending on ice thickness. ETMTRF is better at resolving the arrivals from the near surface structure (Fig. 3.3), and as such is a more suitable technique for ice deployed stations used in this study.

3.2.2 Data and processing

The stations used for receiver function analysis and joint inversion are shown in Fig. 2.1 and Table 2.1. At each station I searched for all suitable events for the full duration of the station deployment or until 01/01/2018 if the station was still active. The longest running stations included in this study are the POLENET/ANET backbone stations, some of which are deployed from 2007 to present. The shortest term stations come from the UKANET deployment, and only have one year of activity (Table 2.1).

The search criteria for a suitable event was that it had $M_b > 5.8$ and an epicentral distance between 30° and 90° occurring between 2008 and 2018 in the NEIC catalogue. An initial quality check was carried out for each event to ensure that there was a visible P-wave arrival on the vertical component, ensuring it was not masked by noise. The horizontal components were then rotated into a radial-tangential sense according to the great circle path of the event, before being windowed from 10 seconds before the theoretical P-wave arrival according to the IASP91 global model (*Kennett and Engdahl*, 1991) to 120 seconds after (see A.2 - A.4). I then de-trend, taper and high pass filter at 0.05 Hz (see A.5) before calculating receiver functions using the ETMTRF technique at three maximum frequencies: 0.5 Hz, 2 Hz, and 4 Hz. The 0.5 Hz and 2 Hz maximum frequency receiver functions are used in the joint inversion, whilst the 4 Hz receiver functions are used in forward modelling for subglacial sediment. Calculating receiver functions at high frequencies allows for the interpretation of finer scale structure, whilst the lower frequency receiver functions are more sensitive to longer wavelength structure (e.g. *Piana Agostinetti and Malinverno*, 2018).

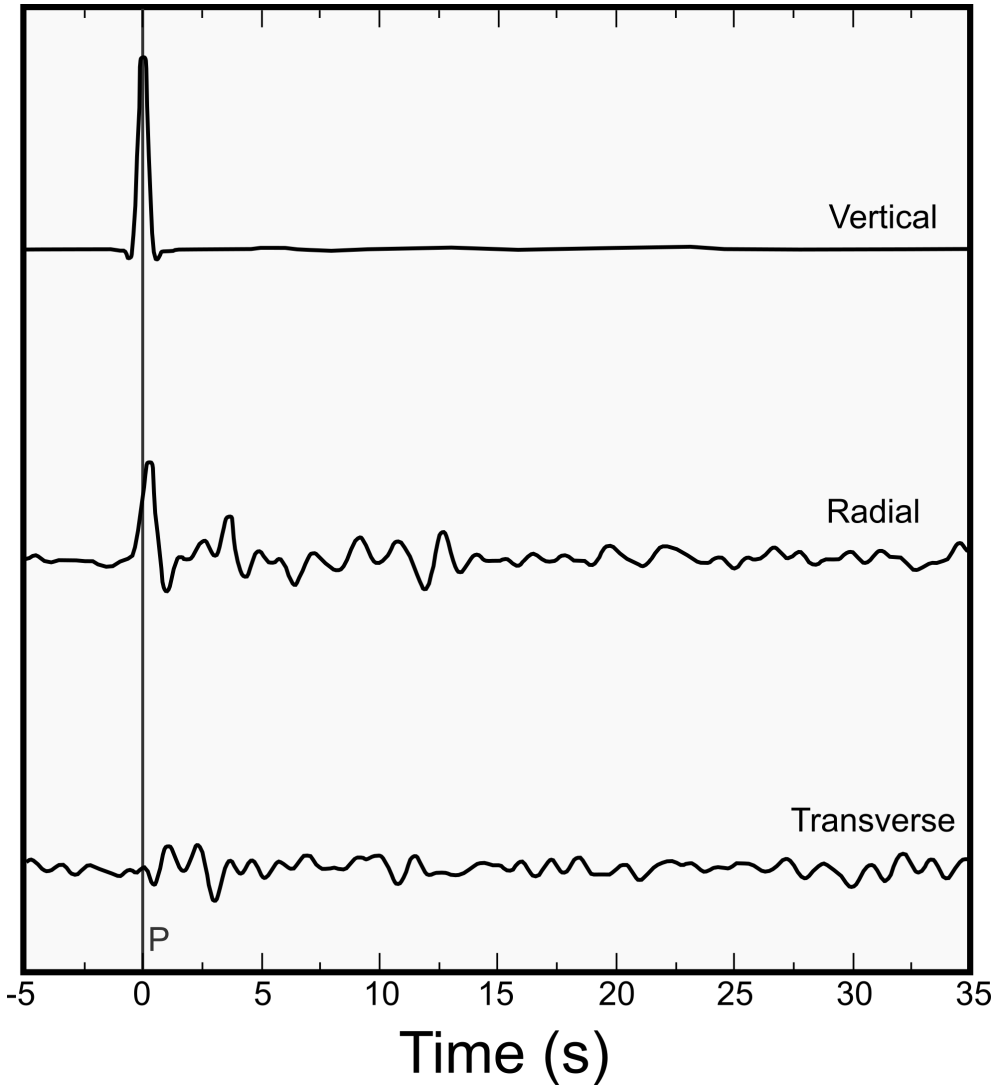

Figure 3.4: An example of the vertical, radial, and transverse components of a receiver function from a 'good' event recorded at PIG1.

After receiver functions were calculated, a subjective quality check was carried out to ensure that poor quality receiver functions, which arise due to a low signal to noise ratio or incorrectly predicted P-wave arrival time, were discarded. Each receiver function was observed to ensure that a clear impulsive direct P-wave arrival was visible on the deconvolved vertical component, and that the level of pre-signal noise on the radial component was low. An example of a 2 Hz maximum frequency 'good' event from station PIG1 is shown in Fig. 3.4, with a clear direct P-wave arrival on the vertical component, and little noise prior to the P-wave arrival on the radial component. Receiver function paramters were tested on all stations, but PIG1 is shown in Fig. 3.4 as an example. With a total period of study from 2007-2018 and 33 stations used this lead to a 11013 receiver functions being individually viewed and quality controlled. Fig. 3.5 shows an example of the event distribution of both accepted and rejected events at four stations, each with a different length of deployment. Given the tectonic framework of the Southern Hemisphere and the event search criteria, most events included in the study originate from the South American-Pacific margin or the fringes of the Australian plate. Fewer suitable events are included from the seismically quieter margins of the Antarctic and African/Somali plates, leading a large azimuthal gap at most stations. Fig. 3.6 shows a record section plotted by both slowness and back-azimuth for station PIG1, showing that whilst azimuthal coverage is patchy, event distrubution by slowness is more complete.

For stacking traces, I used the phase weighted stacking scheme of *Schimmel and Paulssen* (1997), which aims to down weight sections in which the instantaneous phase in the traces contributing to the final stack does not match. By doing this the coherent sections of the traces dominate the stack, which reduces the impact of incoherent noise. This gives a significant advantage over using a linear stacking technique, which can be dominated by large amplitude incoherent features produced by noise. One negative impact on the receiver function stacks sometimes introduced by phase weighted stacking scheme of *Schimmel and Paulssen* (1997) is that later arrivals can sometimes be misidentified as noise and downweighted (*Thurber et al.*, 2014). To help negate the impact of this on the receiver functions I stacked into narrow ray parameter bins, such that late arrivals with varying moveout appear as coherent features in the final stack.

To analyse the uncertainty of each stacked receiver function I used a bootstrap resampling scheme (e.g. *Efron and Tibshirani*, 1991). At each station and for each maximum frequency receiver function the bootstrapping process involved randomly selecting receiver functions with replacement before applying a phase weighted stacking (*Schimmel and Paulssen*, 1997). The RMS difference between each new stack and the original

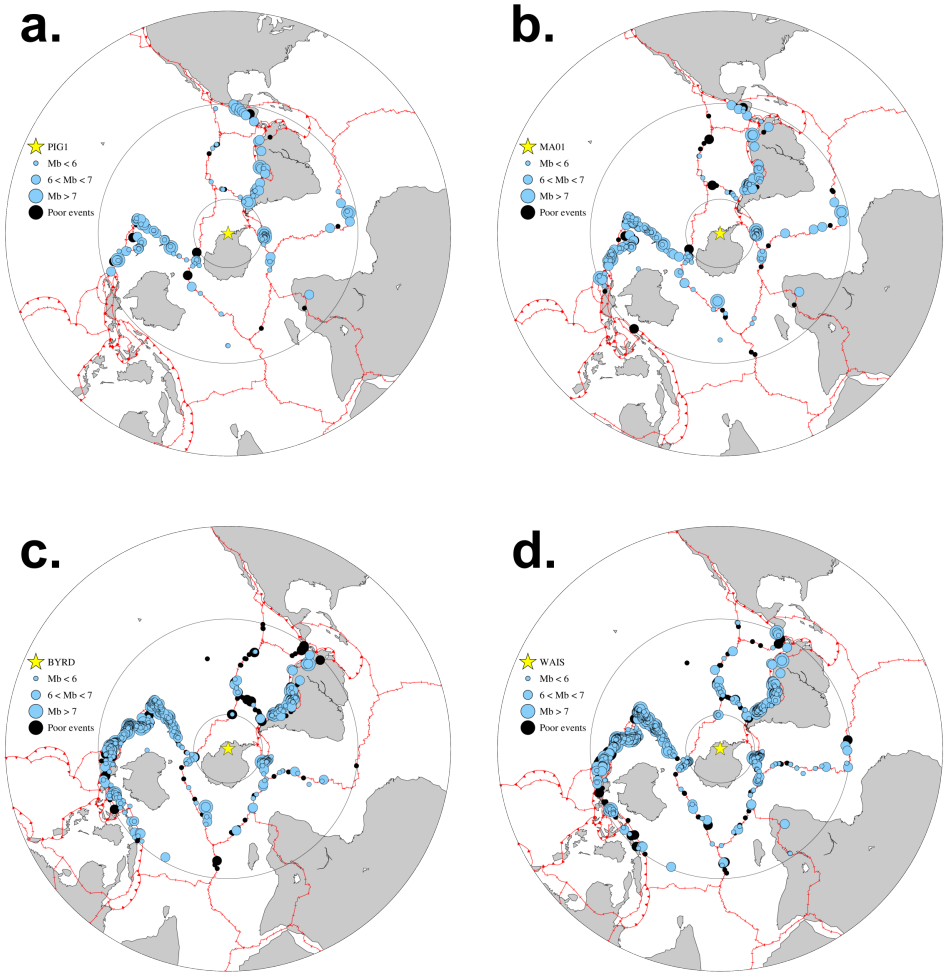

Figure 3.5: Example teleseismic event distribution for receiver function analysis at four stations with different deployment lengths. a.) PIGD (2016-2018) b.) MA01 (2015-2018) c.) BYRD (2010-2018) d.) WAIS (2009-2018). Accepted events are shown in blue circles, with the radius proportional to the event magnitude, rejected events are shown in black. The location of station in question for each panel is shown by a yellow star, with lines marked at 30°and 90°away.

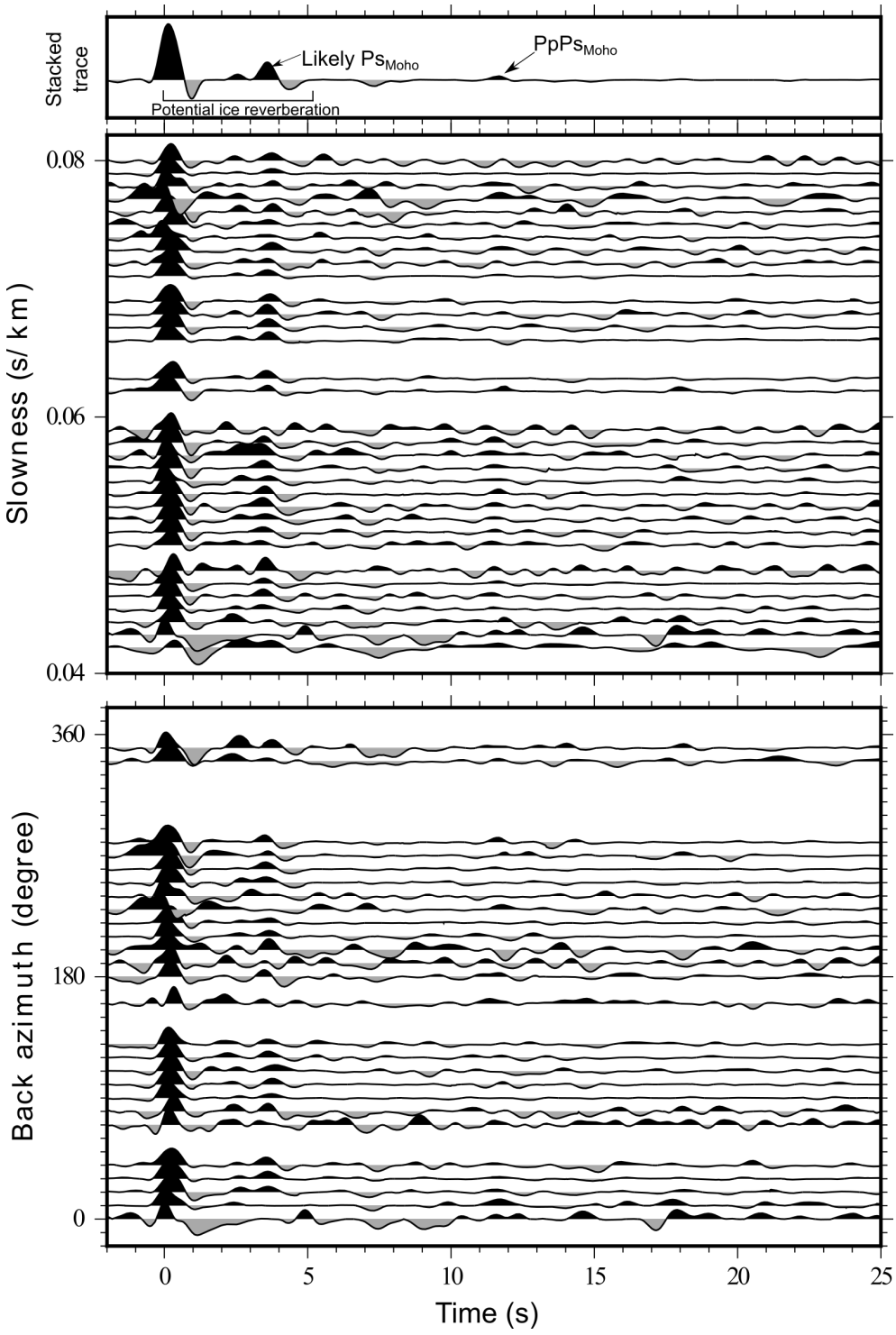

Figure 3.6: 2 Hz maximum frequency radial receiver functions recorded from 2016-2018 at station PIG1 binned by backazimuth every 10° and slowness every 0.001 s/km. A stacked trace containing 134 individual receiver functions after quality control is displayed above. PIG1 has 1.2 km of underlying ice (*Fretwell et al.*, 2013), as a result the relative signal contribution in the first 6 s from the crustal Ps_{Moho} phase and ice reverberation is difficult to constrain.

stacked trace was then computed and the process repeated 500 times. This allowed for the generation of 2σ uncertainty bounds for each stacked receiver function. Given that some stations had much shorter deployment periods than others, the receiver function uncertainty limits at these stations are larger.

3.3 Forward modelling receiver functions to detect subglacial sediment

Subglacial sediment accumulations can provide a source region for the generation of basal till, which in turn has been proposed to be necessary for the initiation of fast ice flow (*Blankenship et al.*, 2001). As such, the location of thick subglacial sediment accumulation can give an indication of likely areas of fast ice flow. Interpreting the location of inferred regions of subglacial sediment alongside West Antarctic ice velocity may help to explain the rapid acceleration of some of the continent's outlet glaciers (*Rignot et al.*, 2011). For example, within the Ross Sea Embayment a narrow rift basin filled with subglacial sediment was identified using airborne geophysics (*Bell et al.*, 1998). The sediment filled basin was located directly beneath the onset region for the fast flowing Ice Stream B, and likely influenced ice stream's flow dynamics. The presence of soft and potentially saturated subglacial sediment layers has previously been inferred across the WARS using receiver functions (*Anandakrishnan and Winberry*, 2004, *Chaput et al.*, 2014). The deep subglacial basins of the WARS provide ample accommodation space for large subglacial sediment accumulations, having been modelled at 0.6 km thick in the Bentley Subglacial Trench (*Anandakrishnan and Winberry*, 2004) and 0.3 km thick in the Byrd Subglacial Basin (*Chaput et al.*, 2014). It is additionally important to understand which stations have underlying subglacial sediment present for inclusion in the joint inversion initial model.

I forward model 4 Hz maximum frequency receiver functions to infer whether or not subglacial sediment is present at each station. I use the grid-search forward modelling approach of *Anandakrishnan and Winberry* (2004) to characterize any potential subglacial sediment at each station (Fig. 3.7). The modelling procedure involves computing a synthetic receiver function at each grid point in a search over subglacial sediment thickness and V_s, then calculating the misfit with respect to the real 4 Hz stacked receiver function. The L_2 norm residual between the synthetic and observed stacked 4 Hz receiver function was calculated over the first 4 s. By analysing misfit over the first 4 s I aim to exploit the shift in the relative timing of the P-to-S-wave ice phase conversion (Ps_{ice}) and reverberation ($PpPs_{ice}$) introduced by the addition of a subglacial sediment layer (Fig. 3.7). Fig. 3.7 displays the impact of adding a subglacial sediment

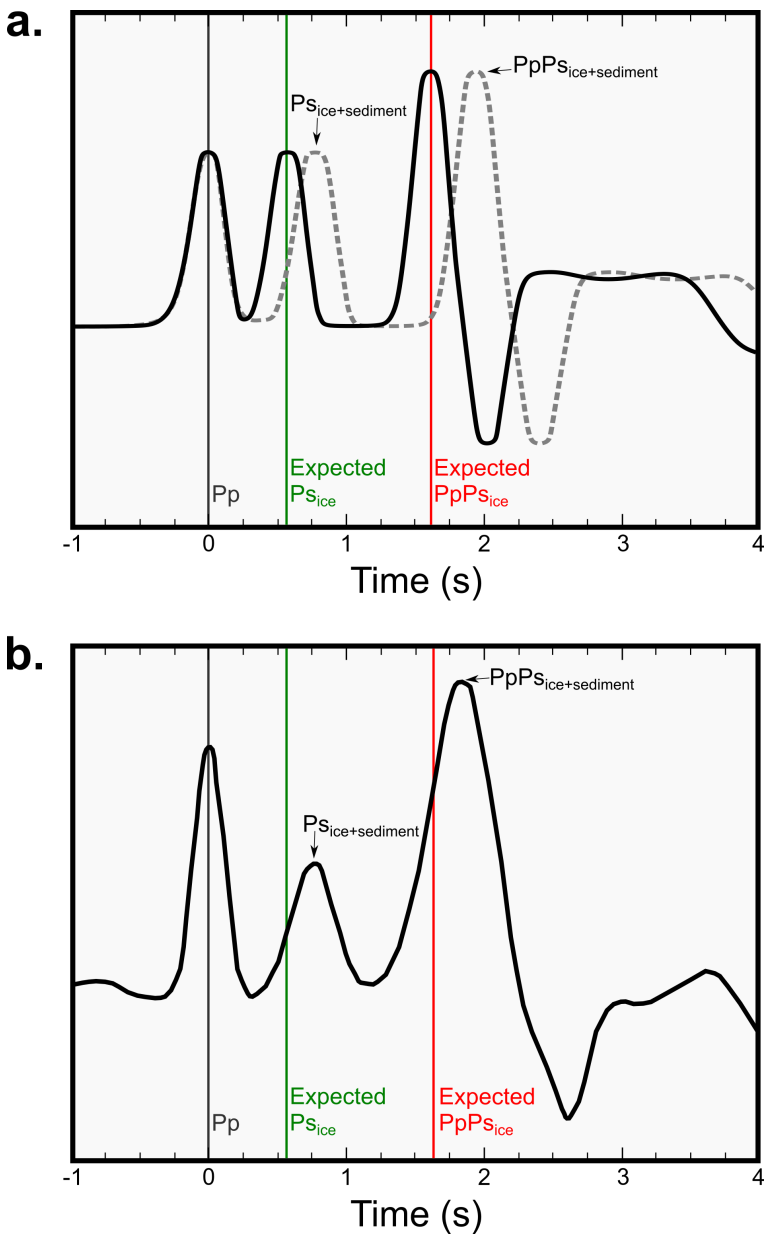

Figure 3.7: a.) A schematic demonstration of the impact introducing a low velocity subglacial sediment layer has on the early portion of a receiver function. In black is a synthetic receiver function, generated from an ice-over-crust model with a 2.1 km thick ice layer. The expected arrival times for the Ps_{ice} and $PpPs_{ice}$ phases are shown by a green and red line respectively. In dashed grey is a receiver function generated with the same ice thickness and physical properties as the model in black, but with a low velocity subglacial sediment layer introduced. The arrival time of the $Ps_{ice+sediment}$ and $PpPs_{ice+sediment}$ phases is shifted by the travel time within the sediment layer, as the impedance contrast between the ice and sediment layers is not significant enough to produce separate arrivals. b.) An example of the first 4 s of the stacked receiver function from KEAL, which has 2.1 km of underlying ice according to *Fretwell et al.* (2013). The expected arrival times for the Ps_{ice} and $PpPs_{ice}$ phases according to a 2.1 km thick ice sheet are again shown by a green and red line respectively. Both the Ps_{ice} and $PpPs_{ice}$ are later than their expected arrival times, suggesting that additional low velocity material is present in the near surface.

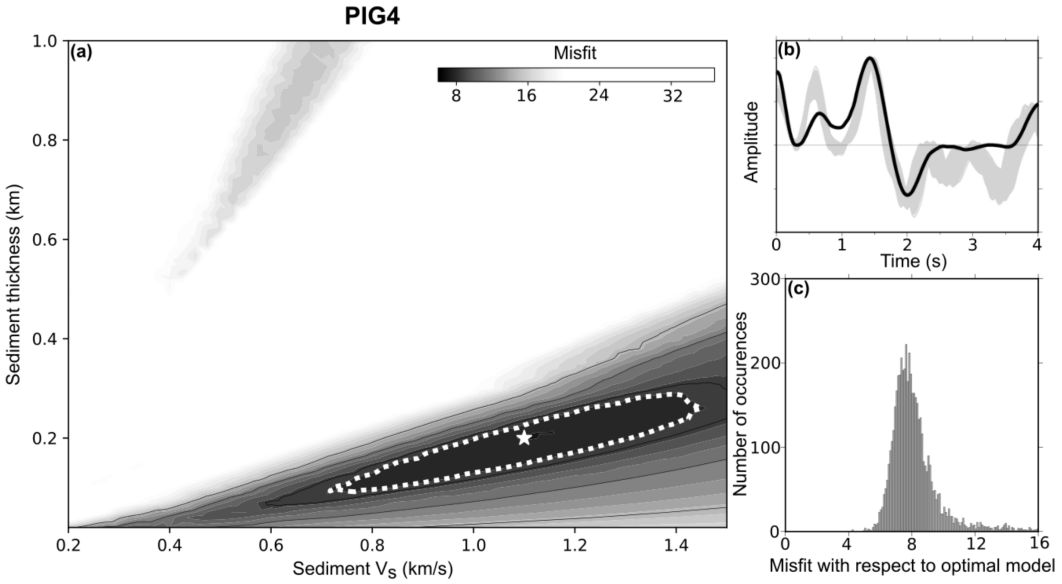

Figure 3.8: Forward modelling results from station PIG4. (a) The grid search over sediment thickness and shear wave velocity. The best fitting model is marked by a white star and the 95% confidence ellipse by a white dashed line. (b) The real stacked receiver function (black) and best fitting models (grey) taken from within the 95% confidence ellipse in panel (a). (c) Bootstrap analysis to estimate uncertainty of the forward modelling following the method of *Chaput et al.* (2014). I produced 5000 bootstrapped receiver functions from the data and computed misfit with respect to the best fitting models from panel (a). Assuming the misfit has a normal Gaussian distribution I could then estimate 95% confidence bounds.

layer to the Ps_{ice} and $PpPs_{ice}$ phases. The contrast in acoustic impedance between the ice layer and a low velocity subglacial sediment layer is small enough that the phase conversions produced at the boundary between the two layers is not resolvable in a receiver function. The timing of the Ps_{ice} and $PpPs_{ice}$ is shifted by the transit time through the sediment layer, relative to their expected arrival times for an ice-over-crust model.

Each model included an ice layer with the thickness taken from BEDMAP2 (*Fretwell et al.*, 2013), over the subglacial sediment layer, over a crustal halfspace. Ice thickness is constrained to less than ±100 m by BEDMAP2 (*Fretwell et al.*, 2013) at most stations, and is treated as a uniform layer in the forward modelling. Ice velocity is fixed at V_p = 3.87 km/s, V_s =1.9 km/s and density at $\rho = 0.9$ g/cm^3 based on seismic studies of polar ice (*Kohnen*, 1974). I allowed subglacial sediment thickness to vary from 0-1 km, and V_s from 0.2-2.0 km/s. V_p and ρ are calculated relative to V_s at each grid point using the empirical relations defined by *Brocher* (2005). A synthetic receiver function was generated, having been preprocessed and deconvolved with the same parameters as the data at a maximum frequency of 4 Hz.

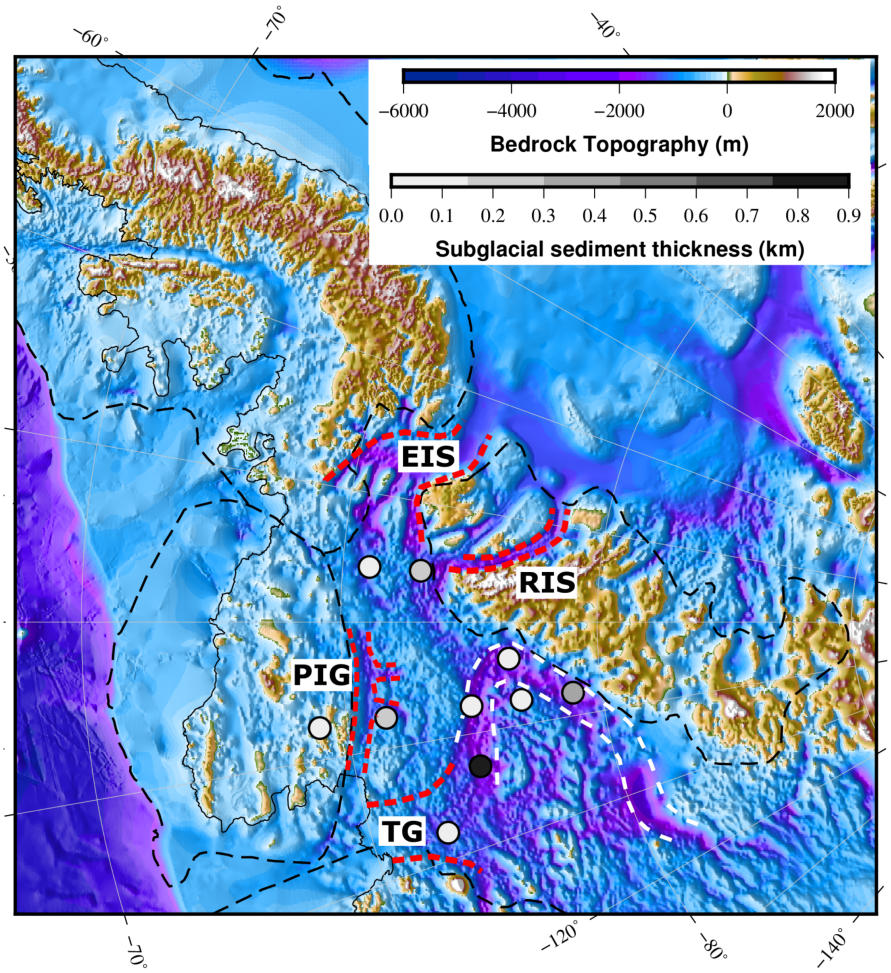

Figure 3.9: A map of stations at which I infer subglacial sediment from forward modelling, coloured by layer thickness over BEDMAP2 bedrock topography. All subglacial sediment that I identify in this study lies in the WARS, Thurston Island and Ellsworth Land, predominantly at stations in the vicinity of the Byrd Subglacial Basin and Bentley Subglacial Trench. Major ice streams roughly outlined in red dashed are the following: Evans Ice Stream (EIS), Rutford Ice Stream (RIS), Pine Island Glacier (PIG) and Thwaites Glacier (TG).

To obtain 95% confidence intervals for the grid search result I used a bootstrap re-sampling scheme (Fig. 3.8). I produced 5000 randomly sampled receiver function stacks from the data and then computed the misfit with respect to the best fitting synthetic receiver function produced by the forward modelling. Assuming a normal Gaussian distribution of misfit I could extract 95% confidence limits. Subglacial sediment thickness is generally reasonably well constrained to within ± 0.2 km, whilst sediment V_s is less so, varying from ± 0.2 km/s to ± 1.0 km/s at different stations (see Table 3.2).

Subglacial low velocity sediment is present at 10 stations within the WARS, Thurston Island and Ellsworth Land (Fig. 3.9) with a range of thicknesses from 0.1-0.8 km. Shear wave velocity in these layers varies from 0.4-1.6 km/s (see Table 3.2, Fig. A.45-A.47). At stations MA09 and MA10 my best fitting model features a 0.1-0.3 km thick subglacial layer with a V_s of ∼1.9 km/s which is close to that of ice (*Kohnen*, 1974), indicating that at these stations there may be thicker ice than indicated by BEDMAP2.

3.4 Joint inversion

Given that receiver functions are a time series, conversion of a time interval to depth requires knowledge of the corresponding velocity structure. Rayleigh wave phase velocity dispersion data are sensitive to average shear wave velocity structure, therefore it is often advantageous to use a joint inversion of Rayleigh wave dispersion data and receiver functions when aiming to constrain crustal structure. To estimate crustal thickness and obtain a crustal shear wave velocity model at each station, I used the method of *Julia et al.* (2000) for jointly inverting receiver functions and Rayleigh wave phase velocity dispersion data. The method produces a layered shear velocity-depth profile by solving a linearised damped least-squares joint inversion. This inversion technique also allows for the inclusion of *a priori* information on layer depths and velocities.

The joint inversion process involved first developing an initial model at each station, which included any potential ice and subglacial sediment layers. I then jointly inverted the Rayleigh wave phase velocity dispersion data from *O'Donnell et al.* (2019a) and *O'Donnell et al.* (2019b) with receiver functions at two maximum frequencies (0.5 Hz and 2 Hz) stacked into the following narrow ray parameter bins: 0.040-0.049, 0.050-0.059, 0.060-0.069 and >0.070 s km^{-1} (Fig. 3.10). Stacking into narrow ray parameter bins reduces the smearing of crustal phases due to the varying angles of incidence of each event, particularly the PpPms and PpSms + PsPms multiples. As described in *Julia et al.* (2000) the number of data points and physical units in both data sets are

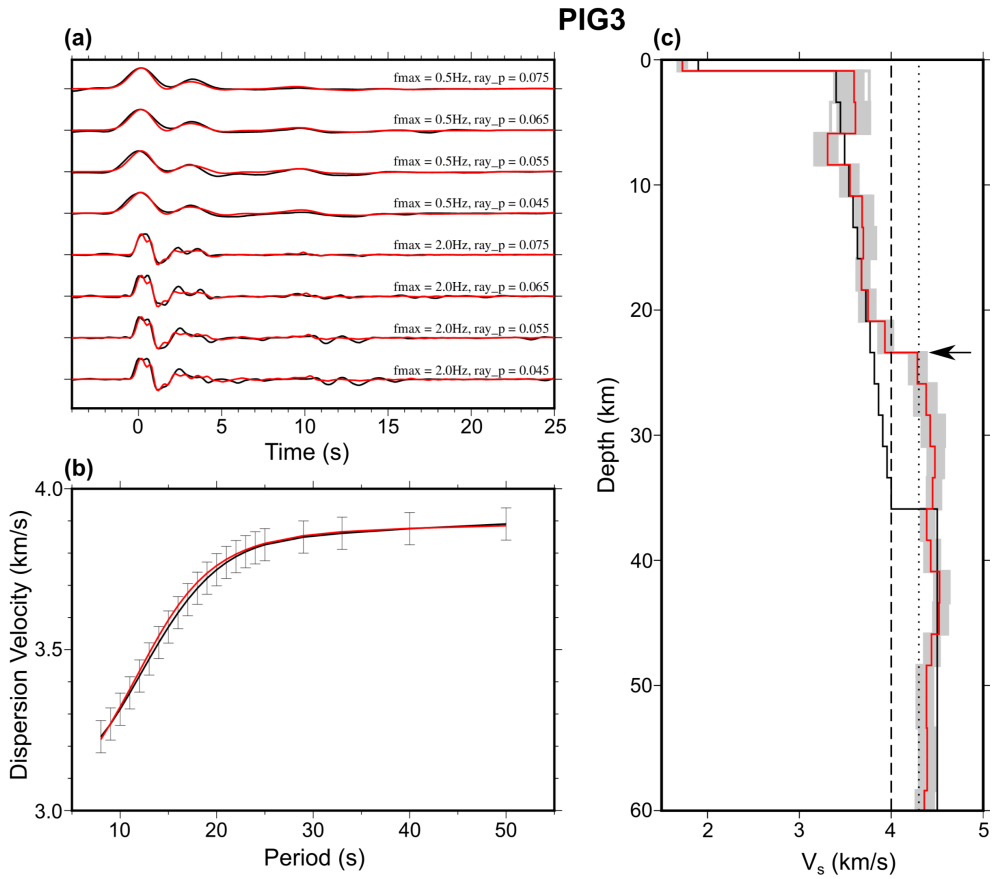

Figure 3.10: Joint inversion results from station PIG3. (a) Receiver functions with corresponding model results (red) stacked into narrow ray parameter bins at two maximum frequencies (0.5 Hz and 2 Hz). Stacked input receiver functions are in black and the resulting inverted receiver functions are in red.(b) Rayleigh wave phase velocity dispersion curve inversion results. The input Rayleigh wave phase velocity dispersion curve is in black and the inversion result in red, showing a good fit within the ± 0.05 km/s uncertainty limits. (c) The shear wave velocity-depth profile produced by the joint inversion. The initial model is in black and the final V_s-depth profile produced by the inversion is shown in red. Models produced by 500 bootstrap iterations are displayed in grey solid lines, indicating that V_s is generally constrained to within ± 0.15 km/s. Dashed and dotted lines are added at 4.0 and 4.3 km/s respectively to indicate the layers of likely mafic lower crust.

equalized, allowing me to give each equal weight in the joint inversion. Examples of testing the impact of the initial model on the joint inversion results are shown in Fig. A.48 - A.50.

I additionally tested running a joint inversion using receiver functions with a move-out correction applied, rather than using receiver functions stacked into narrow ray parameter bins. Receiver functions were corrected to a reference slowness of 0.06 s km^{-1} for the PpPms phase using the AK135 model prior to stacking. The PpPms

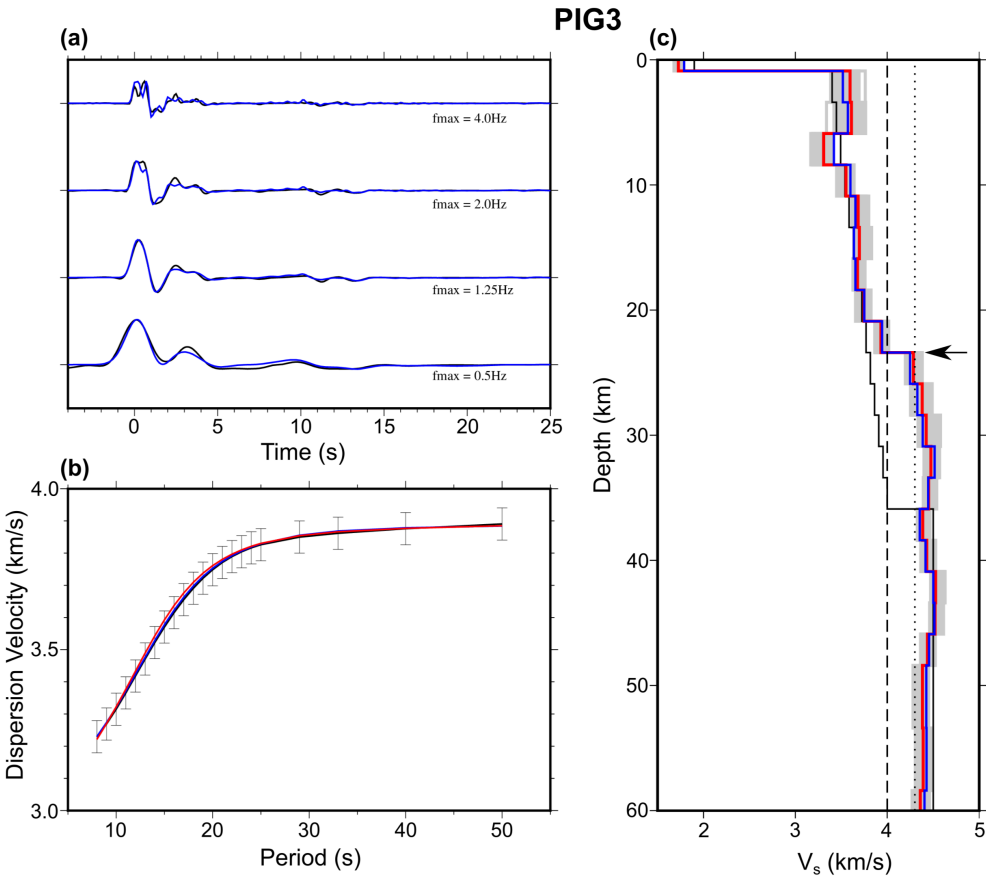

Figure 3.11: A comparison between running the joint inversion at PIG3 with receiver functions stacked into narrow ray parameter bins (red), or using receiver functions stacked after applying a moveout correction (blue). Whilst both shear wave velocity models agree within the bootstrap uncertainty bounds in panel (c), the ray parameter binning method produces a more pronounced velocity jump at the Moho.

phase is the focus for the moveout correction as its arrival time is usually later than most ice reverberation. Fig. 3.11 shows a comparison of a joint inversion using the moveout correction technique versus stacking into narrow ray parameter bins. Whilst the final shear wave velocity models produced from both techniques are similar, the ray parameter binning method produces a more pronounced jump in velocity at the interpreted Moho. Given that the one of the primary aims of this chapter is to model the crustal thickness at each station, the narrow ray parameter binning method is more appropriate. Whilst the moveout correction can act to enhance the PpPms phase, it may consequently smear other phases of interest earlier in the receiver function, chiefly the Pms phase. I therefore continued using receiver functions stacked into the aforementioned narrow ray parameter bins for all subsequent joint inversions. Results from running the joint inversion with moveout corrected stacked receiver functions are shown at all stations in Fig. A.56 - A.58. Generally the moveout correction and the narrow

ray parameter bin stacking joint inversion methods agree well, though the narrow ray parameter bin stacking method does provide a sharper modelled Moho at numerous stations.

3.4.1 Rayleigh Wave phase velocity dispersion curve generation

At each station I use a Rayleigh wave phase velocity dispersion curve in the 8-50 s period range modelled in *O'Donnell et al.* (2019a) and *O'Donnell et al.* (2019b). The dispersion curves are constrained to within ± 0.05 km/s at all periods. For a detailed description of how the Rayleigh wave phase velocity dispersion data and associated uncertainty was computed, please see *O'Donnell et al.* (2019a) and *O'Donnell et al.* (2019b). *O'Donnell et al.* (2019a) extracted Rayleigh wave phase velocities using ambient noise for 8-25 s periods, and *O'Donnell et al.* (2019a) used two-plane wave analysis of earthquake data for 20-143 s. Both studies used data from all POLENET/ANET and UKANET stations using from 2010-2018, along with additional stations from the Agentinean Italian Network, the Seismic Experiment in Patagonia and Antarctica Network, and Global Seismographic Network station PMSA. The two sets of curves were then merged to provide a composite 8-143 s phase velocity dispersion curve. Given that via the joint inversion I am only interested modelling in crustal thickness and structure, and that periods of 40 s and above predominantly reflect upper mantle structure (e.g. *O'Donnell et al.*, 2019b), I only used these curves in the 8-50 s period range.

3.4.2 Generation of the initial model

In the initial model at each station the crust is parameterised as 2.5 km thick layers with a linearly increasing shear wave velocity from 3.4-4.0 km/s and an overall crustal thickness of 35 km (Table 3.1). The layer thickness of 2.5 km was chosen to give a reasonable sensitivity to sharp changes in velocity structure, whilst not being too thin as to over-parameterise the final model. Layer thickness was fixed at 2.5 km from the base of the ice/sediment to 50 km, and at 5 km from 50 km to 80 km. The crust overlies a uniform upper mantle with a V_s of 4.5 km/s to follow the AK135 continental velocity model (*Kennett and Engdahl*, 1991). At each station I included the best fitting near surface subglacial sediment identified in the forward modelling, and ice thickness from BEDMAP2 (*Fretwell et al.*, 2013). Including the ice layer in the initial model allows the additional complexity in the receiver function to be accounted for in the joint inversion process. A similar approach was taken by *Shen et al.* (2018), who find the incorporation of receiver functions provides additional constraints on crustal structure than inverting surface wave data alone. The subglacial sediment layer thickness was fixed, but V_s was allowed to change in the inversion process, as the absolute shear wave velocity was

loosely constrained in the forward modelling step.

3.4.3 Interpreting shear wave velocity-depth models for crustal structure

The output from the joint inversion is a shear velocity-depth profile (Fig. 3.10), which requires interpretation to determine the crustal thickness at each station. I interpret the Moho in each final model to be the depth at which there is a >0.25 km/s shear wave velocity increase in the 4.0-4.3 km/s range, or when the shear wave velocity exceeds 4.3 km/s following *Ramirez et al.* (2017). As stated in *Ramirez et al.* (2017) lower crustal shear wave velocities derived from Vp/Vs ratios from experimental data (e.g. *Holbrook et al.*, 1992, *Christensen and Mooney*, 1995, *Christensen*, 1996) rarely exceed 4.3 km/s. Shear wave velocities at or above 4.3 km/s are therefore more likely to represent upper mantle than crustal lithologies. Whilst a shear wave velocity of 4.3 km/s is not globally characteristic of the upper mantle, the expectation of an instantaneous jump in V_s to values exceeding 4.5 km/s as indicated by global velocity models may not always be reasonable. *Lebedev et al.* (2009) suggest that upper mantle velocities increase with depth from the Moho to a maximum before decreasing again due to the spinel peridotite-garnet peridotite transition. When interpreting the Moho I therefore sought a rapid increase or jump in shear wave velocity from likely crustal values to values exceeding 4.3 km/s range, rather than when 4.5 km/s is reached.

My method for interpreting the Moho depth in the final shear wave velocity models follows other similar studies of crustal thickness in the same region (*Ramirez et al.*, 2017, *O'Donnell et al.*, 2019a). Despite this, a sharp jump from typical lower crustal to upper mantle shear wave velocities is not present at all stations. This is likely due to the Pms phase being masked by the near surface structure in the receiver function. My modelled crustal thickness at stations where this is the case are therefore predominantly controlled by the Rayleigh Wave dispersion data, and have a higher associated uncertainty.

To further characterise the composition and nature of the crust at each station, I divided the crust into likely sedimentary, felsic/intermediate upper crust, and mafic lower crustal layers based on the modelled shear wave velocity structure. Studies of crustal structure and composition (e.g. *Rudnick and Fountain*, 1995) have suggested that felsic-to-intermediate crust tends to have a shear wave velocity of <3.9 km/s, whilst common lower crustal mafic lithologies tend to have shear wave velocity of >3.9 km/s. I therefore interpreted that crustal layers with a V_s <3.2 km/s likely represent

Layer number	Vp (km/s)	Vs (km/s)	ρ (g/cm^3)	Layer thickness (km)
1	3.87	1.90	0.90	3.0
2	1.94	0.50	1.88	0.1
3	5.77	3.40	2.67	2.5
4	5.85	3.45	2.69	2.5
5	5.94	3.49	2.70	2.5
6	6.03	3.54	2.72	2.5
7	6.12	3.58	2.74	2.5
8	6.21	3.63	2.76	2.5
9	6.30	3.68	2.78	2.5
10	6.39	3.72	2.81	2.5
11	6.48	3.77	2.83	2.5
12	6.57	3.82	2.85	2.5
13	6.66	3.86	2.87	2.5
14	6.75	3.91	2.90	2.5
15	6.84	3.95	2.92	2.5
16	6.94	4.00	2.95	2.5
17	8.04	4.50	3.50	2.5
18	8.04	4.50	3.50	2.5
19	8.04	4.50	3.50	2.5
20	8.04	4.50	3.50	2.5
21	8.04	4.50	3.50	2.5
22	8.04	4.50	3.50	2.5
23	8.04	4.50	3.50	5.0
24	8.04	4.50	3.50	5.0
25	8.04	4.50	3.50	5.0
26	8.04	4.50	3.50	5.0
27	8.04	4.50	3.50	5.0
28	8.04	4.50	3.50	5.0
29	8.04	4.50	3.50	5.0
30	8.04	4.50	3.50	0.0

Table 3.1: An example of the initial model used for the joint inversion at station MA02, which contains 3.0 km of underlying ice (*Fretwell et al.*, 2013), and 0.1 km of subglacial sediment as identified in the forward modelling.

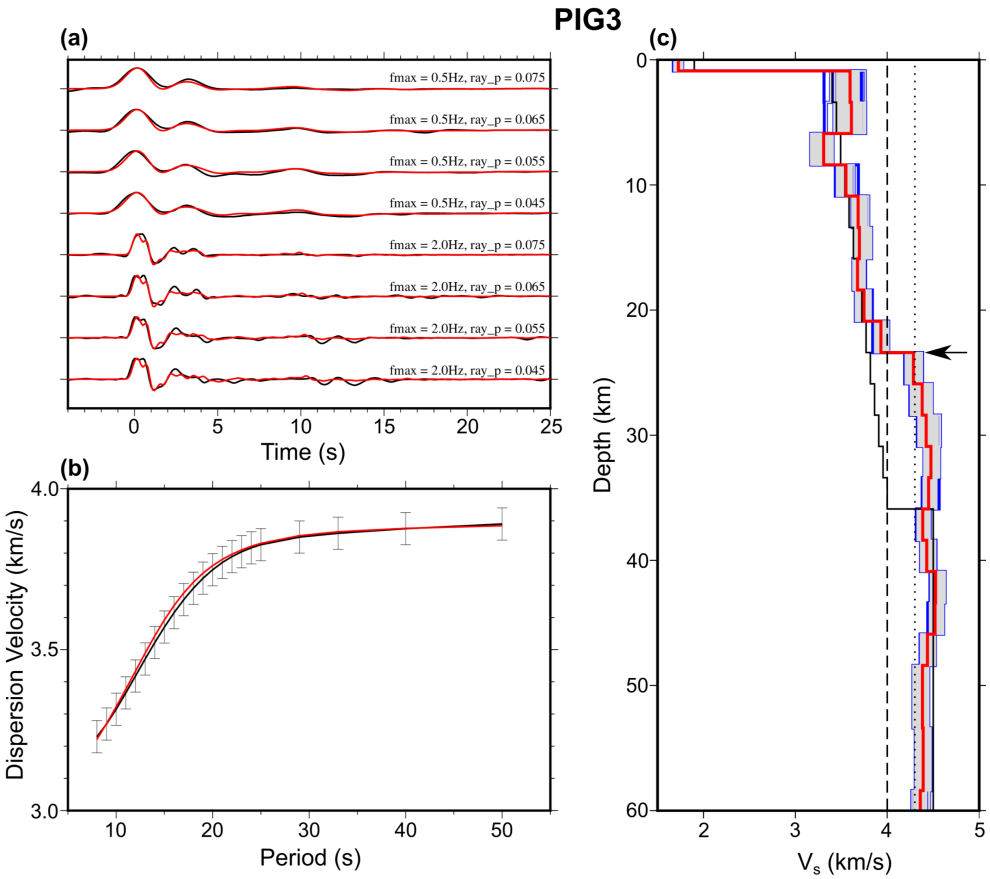

Figure 3.12: Testing running the bootstrapping procedure with 1000 iterations (blue) and 500 iterations (grey). The bootstrap limits of both the 500 and 1000 iteration runs are highly similar, as such running the process with just 500 iterations should be sufficient.

sediments, V_s of 3.2-4.0 km/s represent likely felsic to intermediate crust, whilst a V_s of 4.0-4.3 km/s indicate likely mafic lower crust.

3.4.4 Determining uncertainty

To evaluate uncertainty in the final V_s models I used a bootstrapping procedure which involved repeating the inversion process 200 times each with randomly resampled receiver function stacks (e.g. *Bao et al.*, 2015, *Emry et al.*, 2015). Each bootstrap receiver function stack was produced by randomly selecting receiver functions from the dataset with replacement and then stacking in each ray parameter bin, similar to the forward modelling bootstrapping described in Section 3.3. I would then repeat the joint inversion with the new receiver functions, store the output and repeat the process 500 times. To determine how many iterations are appropriate I tested running the bootstrapping with 500 and 1000 iterations as (Fig. 3.12). The bootstrap limits for the 500 and 1000 iteration runs are highly similar, therefore given the reduced

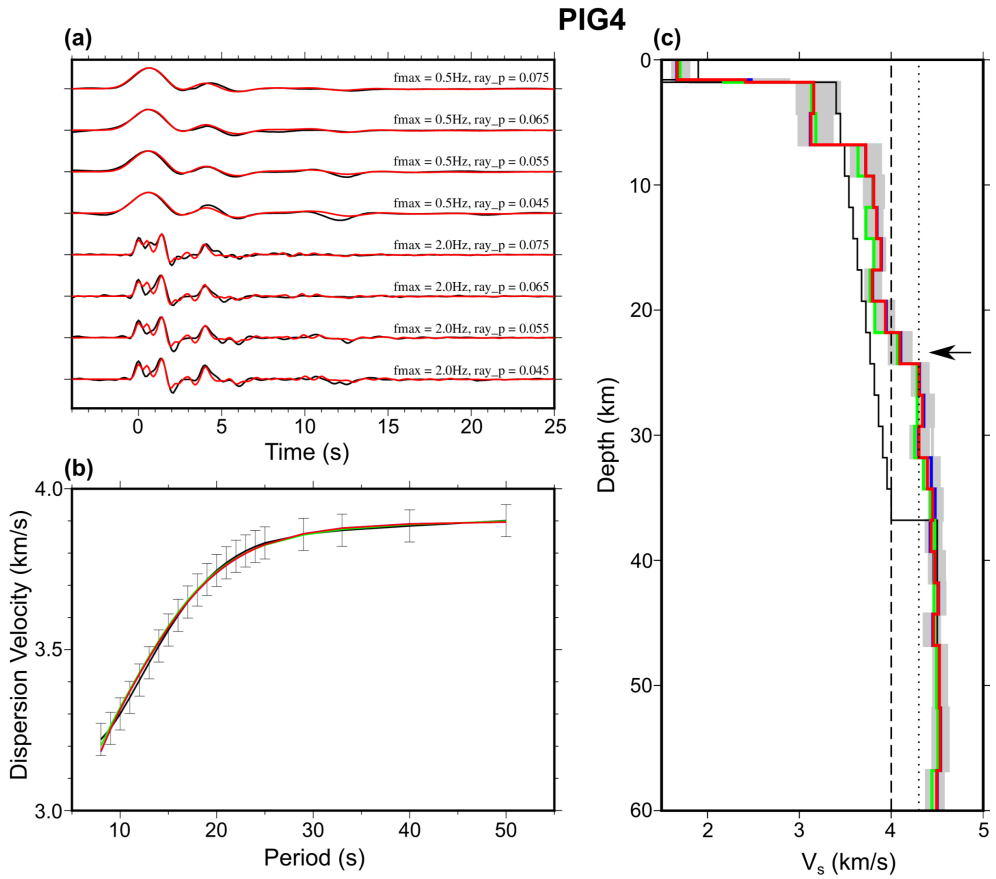

Figure 3.13: Comparison between using various Vp/Vs ratios in the joint inversion. In red is the joint inversion results presented in the manuscript, using the equations defined in (*Brocher*, 2005) to define Vp and density. In green is a joint inversion using a crustal Vp/Vs ratio of 1.80 and in blue a Vp/Vs ratio of 1.70. Although there is a slight difference in the shear wave velocity at each layer between the three models, all three curves agree within the bootstrap error bounds (grey), and the interpreted Moho would remain the same for all three (indicated by a black arrow). All receiver function waveform/dispersion curve model fits are very similar regardless of the Vp/Vs ratio used.

computation time when running this process over all 33 stations I decided to proceed using 500 iterations.

The range of final models could then be used to determine the uncertainty in the modelled V_s-depth structure (Fig. 3.10). To determine the corresponding uncertainty for the crustal thickness value, I inspected the modelled bootstrap shear wave velocity limits of layers neighbouring the interpreted Moho. The error in my velocity models is constrained to ± 0.15 km/s and the Moho depth to $\pm 2.5 - 5$ km at most stations. These uncertainty constraints are comparable to other studies of crustal thickness in the region (e.g. *Chaput et al.*, 2014, *Ramirez et al.*, 2017). Additional, uncertainty in the joint inversion results arises due to the Vp/Vs ratio remaining fixed in the inversion. After

testing the joint inversion with a range of crustal Vp/Vs ratios (1.7-1.8), I found that the uncertainty arising from the Vp/Vs ratio was within the bootstrap error bounds, and the interpreted Moho would remain the same (Fig. 3.13).

3.5 Results

At each station I have produced models of crustal shear wave velocity structure, and interpreted the according crustal thickness (Fig. 3.14). Table 3.2 features all joint inversion and forward modelling results at each station, which are shown in full in Appendix A.

The Antarctic Peninsula and HEW blocks host the thickest crust I interpret in this study, with crustal thickness ranges of 30-38 km and 30-40 km respectively. In both these blocks I also found the largest relative abundance of likely felsic-to-intermediate crust with a V_s from 3.2-3.9 km/s. The thinnest crust I interpreted is within the WARS, with a thickness range of 18-28 km. Given that the Antarctic Peninsula developed as a volcanic arc, and is known to feature widespread granitic volcanism (*Jordan et al.*, 2017, 2020), a predominatly felsic crustal composition is to be expected. Within the WARS I also modelled the overall highest relative proportion of high velocity, likely mafic lower crust to likely felsic/intermediate crust (Fig. 3.14).

Within the HEW block I found the thickest crust at stations HOWD, WILS and UNGL, at 40, 38, and 30 $\pm$ 5 km respectively. All three stations are located within the Ellsworth Mountain section of the block, whilst stations within the Whitmore Mountain and Haag Nunatak sections of the block feature a thinner crust at $\sim$33 km. These results are consistent with the current interpretation of the block being composite in nature (e.g. *Jordan et al.*, 2020). Given that most stations within the HEW and Antarctic Peninsula are situated on the flanks of nunataks and on bedrock, no subglacial sediment was identified within these blocks.

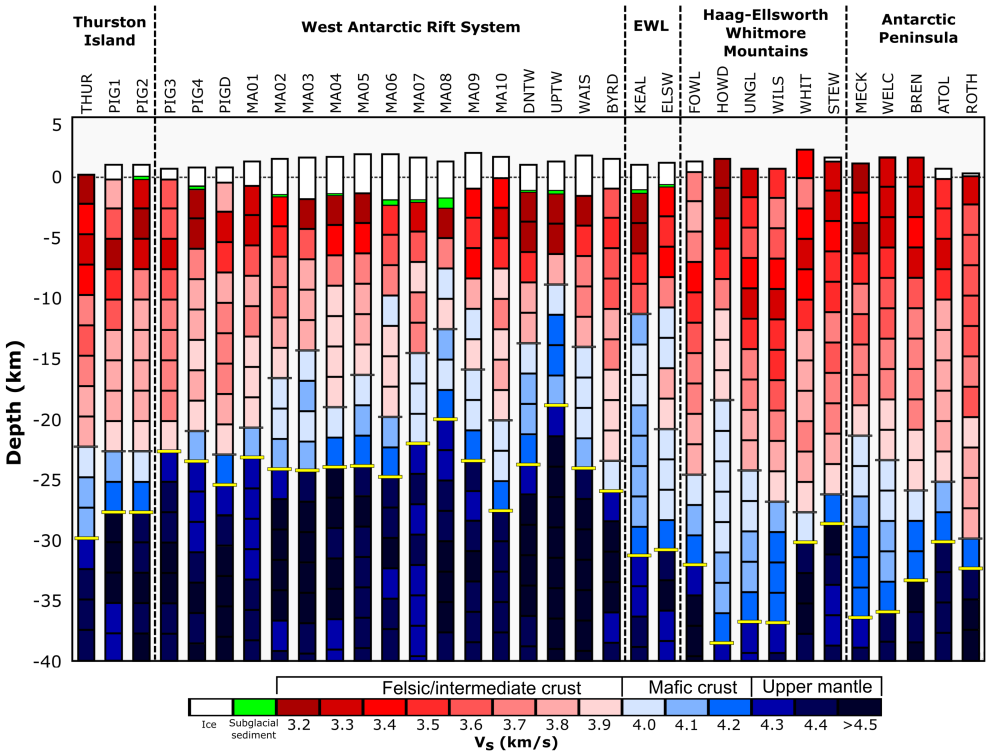

Figure 3.14: A summary of my V_s-depth profiles at each station, grouped by crustal block. I also grouped stations in the Ellsworth Land (EWL) region, given the ambiguity as to which block these stations belong. Each crustal column is coloured by modelled shear wave velocity, with red colours indicating likely felsic-to-intermediate crust and blue representing likely mafic lower crust. Upper mantle is displayed in dark blue, subglacial sediment in green, and ice in white. My interpreted transition from felsic/intermediate crust to mafic lower crust is indicated with a horizontal grey line at each station, and my interpreted Moho with a yellow line. I include the ice thickness from *Fretwell et al.* (2013) and the subglacial sediment thickness identified in the forward modelling stage.

Station	Lat	Lon	Elevation (km)	Ice (km)	Sed (km)	Sed ϵ(± km)	Sed Vs (km/s)	Sed Vs ϵ(± km/s)	Crustal thickness (km)	Crustal thickness ϵ (± km)	Crustal thickness from O'Donnell et al. (2019a) (km)	RFs in stack	Tectonic block/ region
ATOL	-71.3897	-68.8701	0.7	0.86	0.0	N/A	0.0	N/A	30	5.0	33	43	AP
BREN	-72.6750	-63.0210	1.6	0.13	0.0	N/A	0.0	N/A	35	5.0	34	48	AP
BYRD	-80.0170	-119.4738	1.5	2.45	0.0	N/A	0.0	N/A	25	2.5	27	431	WARS
DNTW	-76.4512	-107.7769	1.0	2.11	0.1	0.1	0.8	0.4	23	5.0	24	221	WARS
ELSW	-75.5194	-85.7076	1.2	1.89	0.1	0.1	1.2	0.8	30	5.0	33	41	EWL
FOWL	-76.8928	-79.3011	1.3	0.00	0.0	N/A	0.0	N/A	33	5.0	38	121	HEW
HOWD	-77.5286	-86.7694	1.5	0.00	0.0	N/A	0.0	N/A	40	5.0	38	540	HEW
KEAL	-76.5204	-85.6996	1.0	2.10	0.2	0.1	1.1	0.5	30	5.0	35	63	EWL
MA01	-76.9397	-97.5596	1.3	2.03	0.0	N/A	0.0	N/A	23	2.5	25	203	WARS
MA02	-77.4394	-97.5595	1.5	3.00	0.1	0.1	0.5	0.2	23	2.5	27	166	WARS
MA03	-77.9401	-97.5585	1.6	3.40	0.0	N/A	0.0	N/A	23	2.5	26	163	WARS
MA04	-78.4221	-97.5879	1.7	3.10	0.1	0.1	0.8	0.8	23	2.5	26	154	WARS
MA05	-78.9395	-97.5573	1.9	3.25	0.0	N/A	0.0	N/A	23	2.5	32	164	WARS
MA06	-79.4397	-97.5587	1.9	3.80	0.4	0.2	0.9	0.3	23	2.5	35	142	WARS
MA07	-78.2496	-93.4991	1.6	3.54	0.1	0.2	0.7	0.4	20	2.5	35	159	WARS
MA08	-77.4014	-103.0022	1.3	3.05	0.8	0.2	1.6	0.3	18	5.0	24	171	WARS
MA09	-79.8993	-104.9977	2.0	2.92	0.0	N/A	0.0	N/A	23	5.0	29	200	WARS
MA10	-78.5999	-109.0003	1.7	1.80	0.0	N/A	0.0	N/A	28	5.0	26	90	WARS
MECK	-75.2808	-72.1850	1.1	0.00	0.0	N/A	0.0	N/A	38	5.0	35	351	AP
PIG1	-73.9782	-97.5750	1.0	1.20	0.0	N/A	0.0	N/A	28	5.0	25	134	TI
PIG2	-74.4557	-97.6830	1.0	1.10	0.1	0.2	1.0	1.0	28	5.0	25	84	TI
PIG3	-75.0841	-97.4744	0.7	0.90	0.0	N/A	0.0	N/A	23	2.5	25	146	WARS
PIG4	-75.7599	-97.5830	0.8	1.60	0.2	0.1	1.1	0.4	23	2.5	25	79	WARS
PIGD	-75.8026	-100.2758	0.8	1.25	0.0	N/A	0.0	N/A	25	5.0	25	70	WARS
ROTH	-67.5200	68.1488	0.3	0.17	0.0	N/A	0.0	N/A	33	5.0	N/A	54	AP
STEW	-84.1863	-86.2349	1.6	0.88	0.0	N/A	0.0	N/A	30	2.5	32	316	HEW
THUR	-72.5301	-97.5606	0.2	0.00	0.0	N/A	0.0	N/A	30	5.0	27	293	TI
UNGL	-79.7746	-82.5240	0.7	0.00	0.0	N/A	0.0	N/A	38	5.0	37	379	HEW
UPTW	-77.5781	-109.0374	1.3	2.39	0.3*	N/A	0.5*	N/A	18	10.0	24	356	WARS
WAIS	-79.4181	-111.7779	1.8	3.37	0.0	N/A	0.0	N/A	23	2.5	25	426	WARS
WELC	-70.7318	-63.8274	1.5	0.64	0.0	N/A	0.0	N/A	38	5.0	N/A	42	AP
WHIT	-82.6823	-104.3867	2.3	0.00	0.0	N/A	0.0	N/A	33	2.5	31	534	HEW
WILS	-80.0396	-80.5587	0.7	0.00	0.0	N/A	0.0	N/A	38	2.5	36	81	HEW

Table 3.2: Table of results from all stations used in this study. Ice thickness is from BEDMAP2 (Fretwell et al., 2013). *Subglacial sediment results used from Chaput et al. (2014) at UPTW due to unstable solution in forward modelling. The tectonic block/region acronyms are as follows: Antarctic Peninsula (AP), Ellsworth Land (EWL), Haag-Ellsworth Whitmore (HEW) and West Antarctic Rift System (WARS).

Stations ELSW and KEAL are located close to the northern edge of the HEW block in Ellsworth Land, and feature fundamentally different crust to that seen within the interior of the HEW. The tectonic framework of the Ellsworth Land region is largely unclear, due to it not being clearly linked to any one of West Antarctica's crustal blocks (see Fig. 1.2). I interpreted a shallower Moho at 30 ± 5 km with a seemingly two layer crust. A slow upper crust of ∼3.4 km/s overlies a fast and relatively uniform middle and lower crust with an average V_s of 4.0 km/s. The internal crustal structure at these stations is similar to those in the centre of the WARS, however both feature a deeper Moho. Additionally I identified subglacial sediment at both stations with a thickness of 0.1-0.2 km and V_s of ∼1.0 km/s.

In the center of the WARS I found slow upper crustal layers V_s <3.2 km/s, underlain by 10-15 km of likely felsic crust and a 5-10 km thick, likely mafic, lower crust with a V_s >4.0 km/s. The thinnest crust imaged in this study at 18-20 km come from stations MA07, MA08 and UPTW, all of which lie in the vicinity of either the Byrd Subglacial Basin or Bentley Subglacial Trench. Both subglacial basins are regions in which enhanced Neogene extension is proposed to have occurred (e.g. *Jordan et al.*, 2010), which may have caused the localised thinning I model here.

At station UPTW I used the subglacial sediment thickness and V_s from *Chaput et al.* (2014) to parameterise the initial model, as my forward modelling did not produce a stable solution at this station.

3.6 Discussion

To build on our current knowledge of West Antarctica's crustal framework, I consider my estimates of crustal thickness and shear wave velocity structure in the context of the regional tectonics. Improving our grasp on West Antarctica's tectonic framework is essential for building a comprehensive understanding of the region's evolution. By inspecting the broad crustal structure of each crustal block, I can contrast West Antarctica's tectonic mosaic with analogous regions worldwide.

	Crustal thickness range (km)		
Crustal Block	**This study**	**Other studies**	**Reference**
West Antarctic Rift System	18-28	21-31	Winberry & Anandakrishnan (2004)
		20-25	Jordan et al. (2010)
		20-28	Baranov & Morelli (2013) and references therein
		25-28	O'Donnell & Nyblade (2014)
		21-28	Chaput et al. (2014)
		19-29	Ramirez et al. (2016)
		20-30	Shen et al. (2018)
Thurston Island	28-30	24-26	Jordan et al. (2010)
		24-28	Baranov & Morelli (2013) and references therein
		∼25	O'Donnell & Nyblade (2014)
		28-35	Shen et al. (2018)
Haag-Ellsworth Whitmore	30-40	30-40	Baranov & Morelli (2013) and references therein
		28-36	O'Donnell & Nyblade (2014)
		30-37	Chaput et al. (2014)
		35-38	Ramirez et al. (2017)
		30-43	Shen et al. (2018)
Antarctic Peninsula	30-38	34-44	Baranov & Morelli (2013) and references therein
		29-34	O'Donnell & Nyblade (2014)

Table 3.3: Crustal thickness estimates from present and previous studies.

My crustal thickness estimates from West Antarctica are compatible with other seismic and gravity studies conducted in the region, as summarised by Table 3.3. In the WARS my crustal thickness range of 18-28 km is in good agreement with seismic (*Winberry and Anandakrishnan*, 2004, *Baranov and Morelli*, 2013, *Chaput et al.*, 2014, *Ramirez et al.*, 2016, *Shen et al.*, 2018) and gravity derived crustal thickness estimates (*Jordan et al.*, 2010, *O'Donnell and Nyblade*, 2014). Stations BYRD, DNTW, UPTW and WAIS are featured in previous receiver function (*Chaput et al.*, 2014) and S-wave receiver function (*Ramirez et al.*, 2016) studies. My crustal thickness estimates agree within uncertainty bounds with *Chaput et al.* (2014) at all four stations, but I find 10 km thinner crust at UPTW than *Ramirez et al.* (2016).

3.6.1 Tectonic interpretation of V_s profiles

Fig. 3.15 shows my crustal thickness estimates plotted alongside the ambient seismic noise derived crustal thickness model of *O'Donnell et al.* (2019a). Given the similar input dispersion datasets there is a good general agreement between crustal thickness estimates (Table 3.3), however the inclusion of receiver functions in this study improves resolution of crustal structure and discontinuities at each station. My minimum crustal thickness comes from the Byrd Subglacial Basin, and is ∼5 km thinner than that of *O'Donnell et al.* (2019a). Given that the spatial resolution of the ambient noise crustal model of *O'Donnell et al.* (2019a) is on the order of ∼300 km, it is likely that these narrow rifts are not fully resolved. As such, the combination of both the crustal thickness model of *O'Donnell et al.* (2019a) and the joint inversion results from this study can provide an enhanced image of West Antarctica's crustal mosaic.

I find the thinnest crust in this study in the centre of the West Antarctic Rift System; an area which also hosts the Byrd Subglacial Basin and Bentley Subglacial Trench. In addition in this area I find the highest proportion of fast, likely mafic lower crust as shown by Fig. 3.14. The isostatic impact of the potentially high relative abundance of dense mafic crust may be a contributing factor in the region's extremely low observed bedrock elevation (*Fretwell et al.*, 2013), in combination with the isostatic adjustment of the thick ice overburden. I model a thinner crust and higher proportion of mafic lower crust in comparison to the Mesozoic/Cenozoic extensional type section of *Rudnick and Fountain* (1995); my WARS models are more in line with the active rifts that *Rudnick and Fountain* (1995) analyse. I therefore suggest that the thin crust with a thick mafic lower crustal layer I model in the vicinity of the Byrd Subglacial Basin and Bentley Subglacial Trench is supportive of additional Neogene rifting impacting the central and eastern WARS (e.g. *Jordan et al.*, 2010). My WARS models agree well with the updated antarctic crustal models of *Baranov et al.* (2021), which show an average

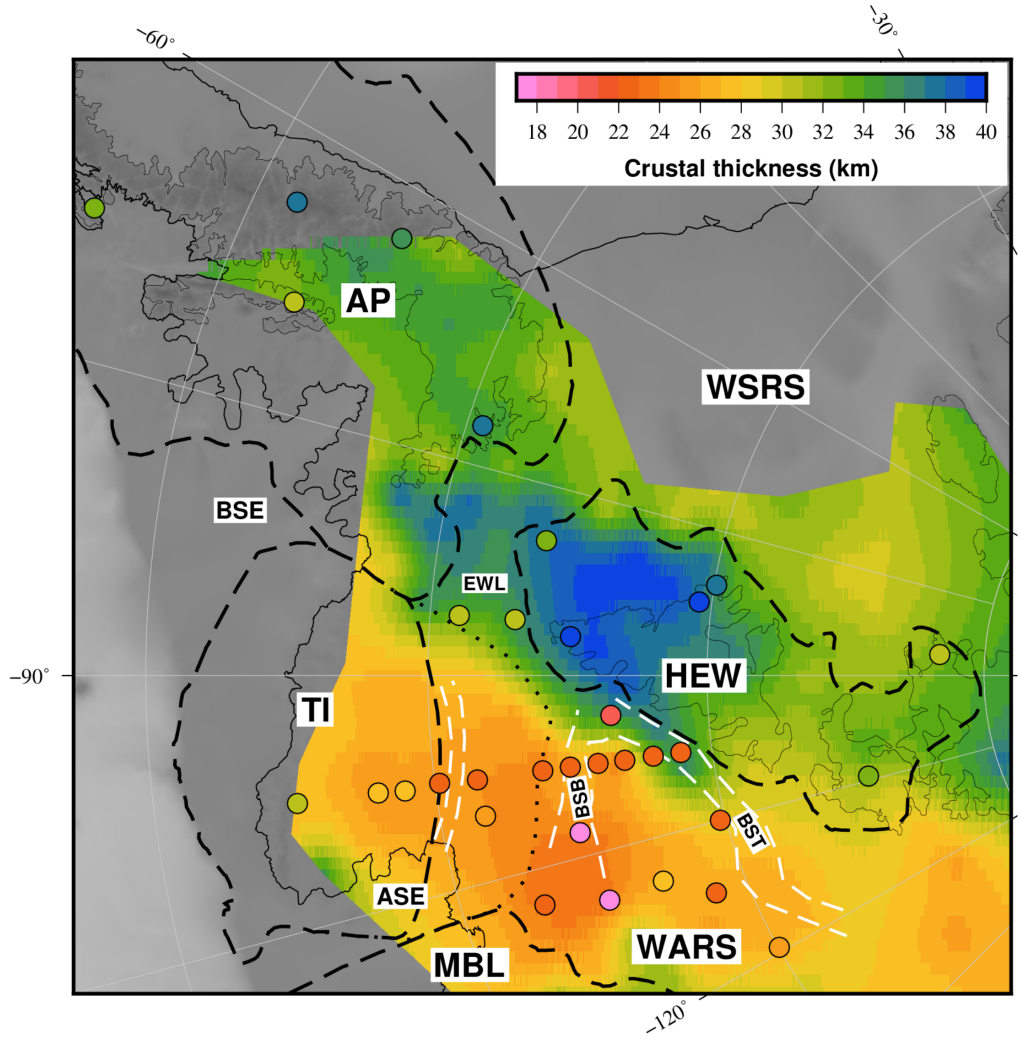

Figure 3.15: A map of my crustal thickness estimates at each station (circles) superimposed on the ambient noise derived crustal thickness map of *O'Donnell et al.* (2019a). The crustal block boundaries of *Dalziel and Elliot* (1982) are in dashed black except for the Thurston Island-WARS boundary which is dotted, here I have redrawn the Thurston Island-WARS boundary to encompass the thinner crust I have imaged at stations PIG3, PIG4 and MA01.

crustal thickness of 22 km with a high velocity lower crust in the vicinity of the Byrd Subglacial Basin.

A comparable rift system to the WARS in terms of scale (but not elevation) is the Cenozoic Basin and Range province, which features crust ranging from 30-35 km thick (*Zandt et al.*, 1995). The thinner WARS crust supports the suggestion that it has undergone enhanced localised thinning relative to the Basin and Range. The highly mafic lower crust I model, in combination with the localised deep subglacial basins of the Byrd Subglacial Basin and Bentley Subglacial Trench, is comparable to the southern section of the Kenya Rift Zone and Baikal Rift Zone (*Thybo and Artemieva*, 2013). In these regions the presence of mafic underplating and sills in the lower crust has lead to magma compensated crustal thinning, and a deep rift graben forming above. The Baikal Rift Zone features an uplifted Moho and an exceptionally high lower crustal seismic velocity (*Thybo and Nielsen*, 2009), showing a clear similarity to the crustal structure I model within the deep subglacial basins of the WARS. Were the high velocity lower crustal structure I model within the central WARS indeed linked to the relatively uplifted Moho, then that would suggest that magmatic activity was occurring in the lower crust during the most recent proposed pulse of WARS extension (e.g. *Jordan et al.*, 2010).

Within the Antarctic Peninsula I find an average crustal thickness of 35 km with $\sim 75\%$ of the crust being composed of lower velocity likely felsic to intermediate material (Fig. 3.14). As such, the crustal thickness and velocity structure that I model in the Antarctic Peninsula is consistent with an arc tectonic environment (e.g. *Christensen and Mooney*, 1995). Models of subglacial heat flux on the Antarctic Peninsula have suggested that the southern and eastern sections of the Peninsula have a high flux, up to 100 mWm^{-2} in places (*Burton-Johnson et al.*, 2017). Areas of elevated heat flux on the Antarctic Peninsula coincide with UKANET stations ATOL, BREN and WELC, all of which show relatively slow upper and mid crustal average shear wave velocities and a thin mafic lower crust with respect to the total crustal thickness (Fig. 3.14). A predominantly felsic to intermediate crustal composition in this region would provide capacity for high radiogenic heat production as suggested by *Burton-Johnson et al.* (2017).

I find along-strike variability in crustal thickness within the HEW block, from the Haag Nunatak section through the Ellsworth Mountains and into the Whitmore Mountains. The thickest crust I model in this study in the Ellsworth Mountain section of the HEW block at 38-40 km at stations HOWD, UNGL and WILS. Stations within

the Whitmore Mountain section of the HEW block image a thinner (30-33 km), and more felsic-like crust than the Ellsworth Mountain section of the block (Fig. 3.14). This spatial variability of crustal thickness and structure within the HEW block has previously been noted by other seismic and aerogravity studies (*Jordan et al.*, 2010, *Chaput et al.*, 2014, *Heeszel et al.*, 2016, *Ramirez et al.*, 2017, *O'Donnell et al.*, 2019a). The UKANET station FOWL is the first to be deployed in the Haag Nunatak section of the HEW block, and here I infer ∼7.5 km thinner crust (33 ±2.5 km), and a contrasting crustal structure to the neighbouring POLENET/ANET stations in the Ellsworth Mountains (HOWD, UNGL, WILS). The fast upper crust I infer at FOWL may be indicative of additional potentially mafic intrusions in the upper crust relative to surrounding stations in Ellsworth Land and the HEW. The basement exposure of the Haag Nunataks is among the oldest sampled in West Antarctica at ∼1 Ga (*Millar and Pankhurst*, 1987), and the crustal thickness I model is ∼10 km thinner than the characteristic seismically imaged Proterozoic crust of *Durrheim and Mooney* (1991). The Proterozoic crust studied in *Durrheim and Mooney* (1991) also includes a thick high velocity layer at the base of the crust which is attributed to basaltic underplating, and at FOWL I infer a 7.5 km thick likely mafic lower crust.

A possible explanation for the reduced crustal thickness I model at FOWL relative to other characteristic Proterozoic crust is through lower crustal flow into neighbouring tectonic blocks. Lower crustal flow from the Haag Nunataks into the Weddell Sea Rift System in the Jurassic has previously been proposed by *Jordan et al.* (2017), which would have acted to enhance Weddell Sea Rift System extension. Lower crustal flow occurs when the middle to lower crust contains a weak ductile zone, often formed via a hot or thick crust, which deforms due to lateral pressure gradient arising from variations in crustal thickness or density (e.g. *Bird*, 1991). Given the distinct crustal composition and thickness of the HEW block relative to the neighbouring regions of Ellsworth Land and the Weddell Sea Rift System, it is possible that a lateral pressure gradient significant enough to produce lower crustal flow could have existed. This would additionally suggest that the HEW block had a mechanically weak lower crust, which given its thick crust and dynamic tectonic evolution, is a possibility. Studying lower crustal flow is difficult, given that any geophysical models only produce a snapshot of the lower crust, and the time scales over which lower crustal flow occurs is not accurately constrained (*Clark et al.*, 2005). Further investigation of lower crustal flow could use models of variation in the regional crustal seismic anisotropy from shear wave splitting measurements (e.g. *Hu et al.*, 2018).

Baranov et al. (2021) produce a P-wave velocity model for the entire Antarctic continent, and extract velocity profiles in specific regions of West Antarctica. *Baranov et al.* (2021) find that lower crustal velocities are much higher than expected for standard continental crust. The high velocities they model in the lower crust suggests a predominantly mafic composition, which is consistent with my findings within the central WARS (Fig. 3.14). The mafic lower crust that *Baranov et al.* (2021) model in the central WARS at the Byrd Subglacial Basin has an average P-wave velocity of 7.3 km/s and a thickness of $\sim$ 8 km. At stations MA02, MA03 and MA08 which are above the Byrd Subglacial Basin I model the thickness of a mafic lower crustal layer to be 7.5 10 and 7.5 km respectively, with an average S-wave velocity of 4.06 km/s. Assuming a lower crustal Vp/Vs ratio of 1.8 (e.g. *Rudnick and Fountain*, 1995) this average S-wave velocity translates to a P-wave velocity of $\sim$ 7.3 km/s, so both the mafic layer thickness and velocities are comparable between my models and that of *Baranov et al.* (2021) in this region. In the Antarctic Peninsula *Baranov et al.* (2021) model a lower crustal layer thickness of $\sim$ 18 km, which is generally greater than the mafic lower crustal thickness that I model in the region, other than at MECK in the southern Antarctic Peninsula where I model a 15 km thick layer (Fig. 3.14). This difference may arise due to my interpretation of mafic lower crust being layers in which the S-wave velocity consistently exceeds 4.0 km/s, as *Baranov et al.* (2021) model an average lower crustal P-wave velocity of 7.1 km/s which is 0.2 km/s slower than they model in the central WARS.

3.6.2 Subglacial sediment thickness modelled beneath the West Antarctic Ice Sheet

Fig. 3.9 features a map of all stations at which I identify low velocity subglacial layers in the forward modelling. Subglacial layers of this thickness (0.1-0.8 km) and shear wave velocity (0.4-1.6 km/s) are indicative of unlithified, soft and possibly saturated sediment (*Winberry and Anandakrishnan*, 2004). I find low velocity subglacial layers at 10 stations within the WARS, Thurston Island and Ellsworth Land, with the majority of stations in the vicinity of the Byrd Subglacial Basin and Bentley Subglacial Trench. These deep subglacial basins could provide ample accommodation space for the accumulation of relatively thick subglacial sediment, which in turn may have provided the basal till to accelerate regional ice flow. The abundance of soft unlithified sediment in the central portion of the WARS could well have been a contributing factor for the fast flow observed in the Thwaites Glacier region (*Rignot et al.*, 2011). Soft deforming till layers have been identified in the upper reaches of Thwaites Glacier using seismic reflection (*Muto et al.*, 2019), much of which may have been sourced from the thick subglacial sediment accumulations I model in the Byrd Subglacial Basin. Subglacial sediment has also been identified within the deep basins of the central WARS by *Pour-*

point et al. (2019), who used a joint inversion of receiver functions, Rayleigh and Love dispersion, and Rayleigh wave horizontal-to-vertical amplitude ratio. *Pourpoint et al.* (2019) modelled sediment to be 1.5 km thick beneath station MA08, and >0.5 km thick at stations DNTW, UPTW, MA06 and MA07. In addition I find 0.1-0.2 km thick subglacial sediment present in the vicinity of the neighbouring Pine Island Glacier at PIG2 and PIG4, another region of fast ice flow.

Another region in which I infer the presence of low velocity subglacial sediment is at stations ELSW and KEAL (Fig. 3.9), both of which lie upstream of the Rutford Ice Stream and Evans Ice Stream. The Rutford Ice Stream flows at a velocity up to ∼400 m a^{-1} (*Gudmundsson*, 2006), yet it has a gentle surface slope relative to other fast flowing West Antarctic ice streams suggesting that the basal driving stress is low (e.g. *MacAyeal et al.*, 1995). To accommodate such a high velocity with a low basal driving stress the basal friction must also be low, implying that soft sediment must be present. A number of studies have confirmed the presence of large scale sedimentary bedforms beneath the Rutford Ice Stream, using both seismic surveying and ice penetrating radar (*King et al.*, 2007, *Smith and Murray*, 2009). In the Evans Ice Stream, *Vaughan et al.* (2003) measured acoustic impedance to reveal that the entire bed of the ice stream consists of dilated sediment. The 0.1-0.3 km thick low velocity sedimentary layer that I model at ELSW and KEAL could have provided an upstream source for the subglacial sediments identified beneath the Rutford Ice Stream and Evans Ice Stream, which has subsequently acted to accelerate flow.

Chapter 4

Local seismicity detected by the UKANET seismic network

4.1 Introduction

The Pine Island Glacier station traverse of the UKANET and POLENET Mini Array seismic networks crosses from the Thurston Island block into the West Antarctic Rift System, therefore studying patterns of seismicity may help to reveal more on the region's tectonic framework. This chapter presents a search for local seismicity detected by the UKANET seismic network and POLENET/ANET stations deployed in West Antarctica from 2015 to 2018. The aim of this chapter is to locate and characterise the local seismicity recorded within the time period of interest, whether that be of tectonic, volcano-tectonic or glacial origin. The distribution of local seismicity across West Antarctica may reveal whether or not any active rift processes are occurring within the WARS. Prior to the deployment of the UKANET seismic network the sparse station coverage in the Amundsen Sea Embayment and Ellsworth Land meant that study of local seismicity in these regions was limited. The denser station coverage provided by the UKANET deployment will therefore mean that smaller magnitude (M_L <1), local events can be detected.

4.1.1 Historic recorded seismicity in Antarctica

Prior to the deployment of major seismic networks within Antarctica, studies of local seismicity were limited to instruments sporadically located around the continent. Earthquakes large enough to produce teleseismically recorded phases originating in Antarctica are sparse; the first confirmed intracontinental event with an accurately

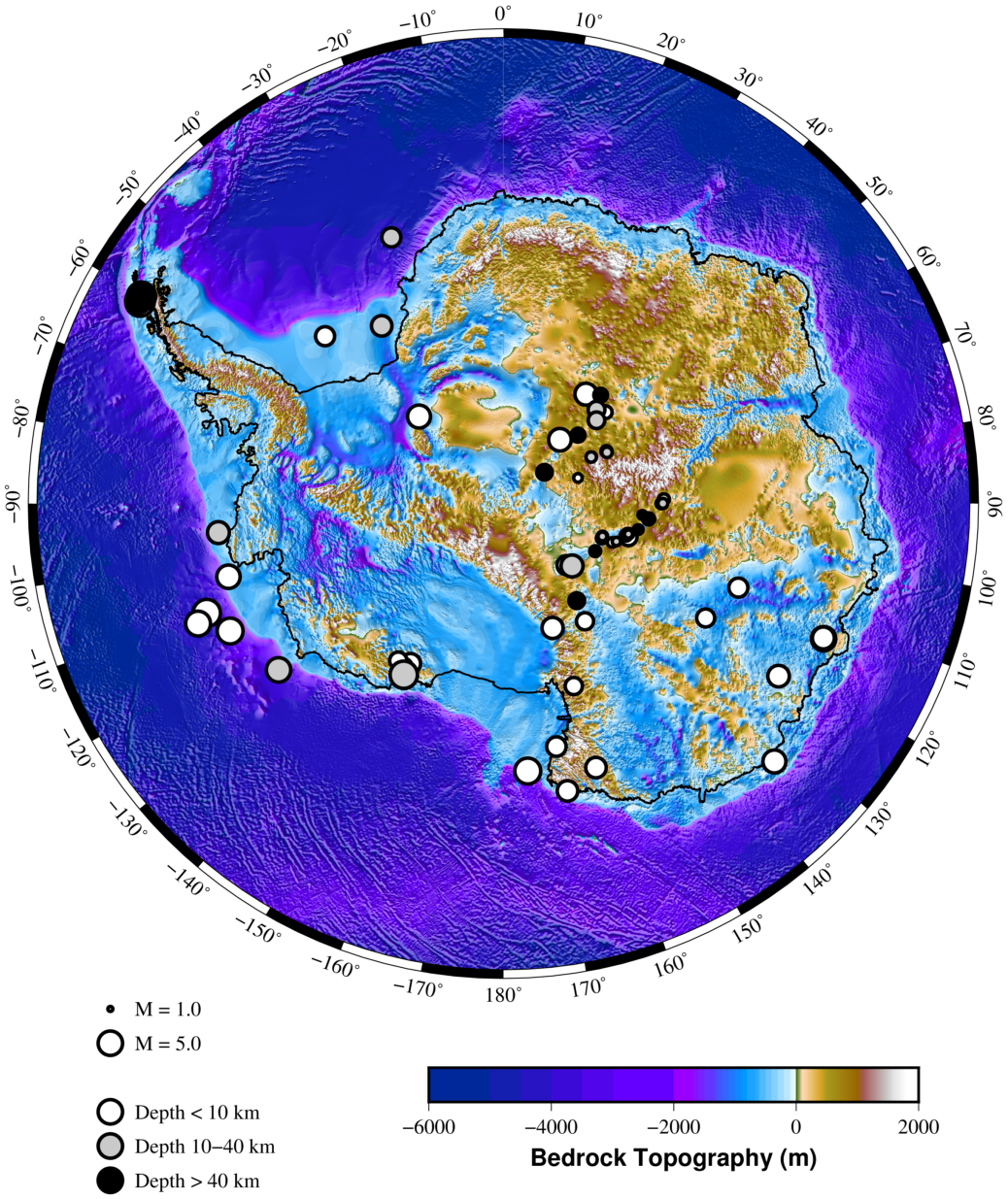

Figure 4.1: Previous intraplate seismicity recorded in Antarctica. Events shown are from the following studies: *Adams et al.* (1985), *Adams and Akoto* (1986), *Lough et al.* (2013, 2018), *O'Donnell et al.* (2017), *Reading* (2007), *Winberry* (2003). Bedrock topography is from *Fretwell et al.* (2013).

constrained origin occurred in 1982 (*Adams et al.*, 1985) (Fig. 4.1). An early study (*Adams and Akoto*, 1986) of Antarctica's seismicity recorded on four instruments deployed around the continent's coastline only identified three events within the continental interior. All four events identified in *Adams et al.* (1985) and *Adams and Akoto* (1986) were located in East Antarctica, with magnitudes (M_b) between 4.4 and 5.0.

The deployment of the TAMSEIS and GAMSEIS seismic networks allowed for the identification of local seismicity in East Antarctica. *Lough et al.* (2018) used GAMSEIS data to identify 27 intraplate tectonic earthquakes at shallow to mid crustal depths in East Antarctica. The authors attribute these local earthquakes to the reactivation of an ancient East Antarctic rift system. In addition, *Lough et al.* (2018) suggest that when considered alongside published catalogues of Antarctic seismicity, these local earthquakes indicate that the seismicity rate in East Antarctica is similar to other stable cratons.

One of the first seismic networks deployed in West Antarctica from 1998-2001 suggested that there was in fact tectonic seismicity located in the region (*Winberry*, 2003). *Winberry* (2003) found clusters of $M_L > 2$ events on the flank of Marie Byrd Land and in the centre of the WARS which the authors interpreted to be of tectonic origin. Were the WARS to still be active then there would likely be associated tectonic seismicity, however seismicity in this region could also be related to regional deglaciation and uplift. Very few intraplate tectonic events have been identified within West Antarctica, both through teleseismic and local studies, largely due to the low rates of intraplate deformation. A magnitude 5.6 intraplate earthquake occurred in Marie Byrd Land in 2012 which was recorded at POLENET/ANET stations and used to model upper mantle velocity and viscosity structure (*O'Donnell et al.*, 2017).

One of the most active regions in West Antarctica for intraplate seismicity (M_b 4-5) are the Transantarctic Mountains and the adjacent Ross Sea Embayment (*Reading*, 2007). *Reading* (2007) suggested that events recorded in the Ross Sea Embayment represent near vertical dip-slip deformation, and are likely associated with the continuing uplift of the Transantarctic Mountains. Whilst *Reading* (2007) suggested that the teleseismically recorded events in the Transantarctic Mountains are tectonic in origin, other studies have shown that smaller events (M_b <4) in this region are ice related (e.g. *Danesi et al.*, 2007, *Zoet et al.*, 2012). Earthquakes have been located along the continental rise offshore of Thurston Island in the Amundsen and Bellingshausen seas (e.g. *Reading*, 2007). The focal mechanisms for these events suggest that compressive deformation is occurring (*Reading*, 2007). Seismic reflection profiles have additionally been

able to image compressional structures in the area (*Gohl et al.*, 1997). The northern Antarctic Peninsula also features compressional tectonics with associated seismicity, relating to subduction in the Bransfield Strait (*Robertson Maurice et al.*, 2003).

Seismicity associated with active volcanism within West Antarctica has also been recorded at stations deployed on the continental interior. A study of seismicity recorded at POLENET/ANET stations identified two swarms of seismicity in Marie Byrd Land, one of the most volcanically active region in West Antarctica (*Lough et al.*, 2013). *Lough et al.* (2013) suggest that these event swarms indicate the presence of an active subglacial complex. Marie Byrd Land features 18 shield volcanoes, many of which are aligned in linear chains (*LeMasurier and Rex*, 1989). Three volcanoes also protrude the ice sheet on the other side of the Amundsen Sea Embayment from Marie Byrd Land in the Hudson Mountains. The Hudson Mountains are located close to Pine Island Glacier, and also feature major subglacial volcanism. Ice-penetrating radar data suggests that massive tephra deposits, thickest at a subglacial topographic high, are indicative of a major subglacial eruption at 207 $_{BC}$ $\pm$ 240 years (*Corr and Vaughan*, 2008). *Corr and Vaughan* (2008) termed this subglacial volcano the Hudson Mountains Subglacial Volcano, and further analysis of the BEDMAP2 dataset has revealed a further 91 potential subglacial volcanoes distributed across the WARS, Marie Byrd Land and Thurston Island (*de Vries et al.*, 2018). This study involved identifying conical structures protruding upwards from a defined digital elevation model, and as such does not give any indication as to whether these potential subglacial volcanoes show any signs of past or present activity. The morphology of many of these cones closely fits that of typical shield volcanoes, which is consistent with rift volcanism (*de Vries et al.*, 2018).

The deployment of major seismic networks in Antarctica's interior also allowed for the study of cryoseismicity across the continent. Given the massive ice volume present across Antarctica there is a range of potential seismic sources arising from ice sheet processes (e.g. *Podolskiy and Walter*, 2016). Seismic sources within the ice sheet can relate to any of the following: surface crevasses, basal stick slip motion, subglacial water flow, hydrofracturing and iceberg calving.

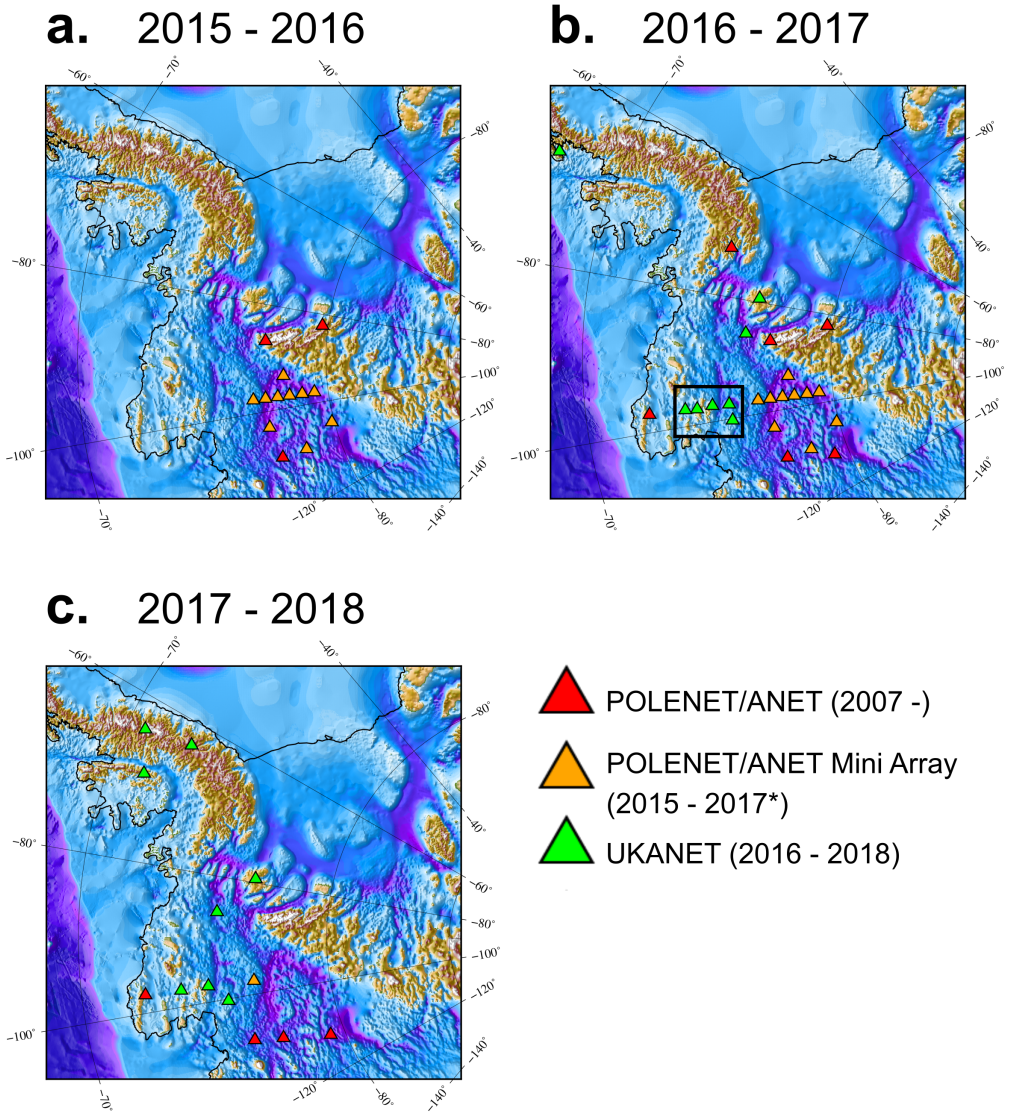

Figure 4.2: Maps of the network configuration for the duration of the local seismicity study. a) 2015-2016 b) 2016-2017 with UKANET Pine Island Glacier stations highlighted by the black box c) 2017-2018. ∗ MA01 was active from 2015-2018.

2015-2016				2016-2017				2017-2018			
Station	**Lat**	**Lon**	**Network**	**Station**	**Lat**	**Lon**	**Netwok**	**Station**	**Lat**	**Lon**	**Network**
HOWD	-77.5286	-86.7694	YT	FOWL	-76.8928	-79.3011	1D	ATOL	-71.3897	-68.8701	1D
MA01	-76.9397	-97.5596	YT	HOWD	-77.5286	-86.7694	YT	BREN	-72.6750	-63.0210	1D
MA02	-77.4394	-97.5595	YT	KEAL	-76.5204	-85.6996	1D	DNTW	-76.4512	-107.7769	YT
MA03	-77.9401	-97.5585	YT	MA01	-76.9397	-97.5596	YT	ELSW	-75.5194	-85.7076	1D
MA04	-78.4221	-97.5879	YT	MA02	-77.4394	-97.5595	YT	FOWL	-76.8928	-79.3011	1D
MA05	-78.9395	-97.5573	YT	MA03	-77.9401	-97.5585	YT	MA01	-76.9397	-97.5596	YT
MA06	-79.4397	-97.5587	YT	MA04	-78.4221	-97.5879	YT	PIG1	-73.9782	-97.5750	1D
MA07	-78.2496	-93.4991	YT	MA05	-78.9395	-97.5573	YT	PIG3	-75.0841	-97.4744	1D
MA08	-77.4014	-103.0022	YT	MA06	-79.4397	-97.5587	YT	PIGD	-75.8026	-100.2758	1D
MA09	-79.8993	-104.9977	YT	MA07	-78.2496	-93.4991	YT	THUR	-72.5301	-97.5606	YT
MA10	-78.5999	-109.0003	YT	MA08	-77.4014	-103.0022	YT	UPTW	-77.5781	-109.0374	YT
UNGL	-79.7746	-82.5240	YT	MA09	-79.8993	-104.9977	YT	WAIS	-79.4181	-111.7779	YT
				MA10	-78.5999	-109.0003	YT	WELC	-70.7318	-63.8274	1D
				MECK	-75.2808	-72.1850	YT				
				PIG1	-73.9782	-97.5750	1D				
				PIG2	-74.4557	-97.6830	1D				
				PIG3	-75.0841	-97.4744	1D				
				PIG4	-75.7599	-97.5830	1D				
				PIGD	-75.8026	-100.2758	1D				
				ROTH	-67.5200	68.1488	1D				
				THUR	-72.5301	-97.5606	YT				
				UNGL	-79.7746	-82.5240	YT				
				UPTW	-77.5781	-109.0374	YT				
				WAIS	-79.4181	-111.7779	YT				

Table 4.1: Stations used in the network coincidence search for local seismicity for each season from 2015-2018. Networks used are POLENET/ANET (YT) and UKANET (1D)

4.2 Data

The stations used in the search for local seismicity are summarised in Fig. 4.2 and Table 4.1. All UKANET stations active from 2016-2018 were used, along with additional coeval POLENET/ANET stations. I used data from the POLENET Mini Array and long term stations UPTW, HOWD and UNGL from 2015-2016, to investigate whether any seismicity was recorded in the central WARS.

The January 2016-January 2017 season featured the densest station deployment in my period of study (Fig. 4.2), and is the only year in which all the UKANET Pine Island Glacier and POLENET/ANET Mini Array stations were active. In addition to the UKANET and Mini Array stations in 2016-2017, POLENET stations MECK, HOWD and UNGL were utilised to study any potential seismicity in the HEW block and surrounding area. Stations THUR, UPTW and WAIS were also used to complement the UKANET Pine Island Glacier and Mini Array stations.

In the January 2017-January 2018 season a reduced number of stations were available in Thurston Island and the central WARS, as two of the UKANET Pine Island Glacier stations and most of the Mini Array stations were removed (Fig. 4.2). Only PIG1, PIG3, PIGD and MA01 remained, and only the vertical component was operational at PIGD, limiting its use in event location. I also used POLENET/ANET stations THUR, DNTW, UPTW and WAIS to complement the remaining Pine Island Glacier/Mini Array stations in the 2017-2018 season. The 2017-2018 season also featured three active UKANET stations in the Antarctic Peninsula; ATOL, BREN, and WELC.

4.2.1 Event detection and location

To get an initial overview for the seismicity present in the UKANET dataset I produced day long helicoder records (Fig. 4.3 - 4.5) at all UKANET stations for the duration of the network deployment (2016-2018). For each day I produced an unfiltered helicoder record, along with one band-pass filtered from 2-15 Hz, and another high-pass filtered at 5 Hz at each station (Fig. 4.3 - 4.5). The unfiltered record tended to only show teleseismic events, as any local seismicity was masked by low frequency noise. The largest high frequency events were visible in both the band-pass and high-pass filtered records (Fig. 4.4 - 4.5), many of which were detectable at three or more stations. In the 2-15 Hz band-pass filtered dayplots at the UKANET Pine Island Glacier stations there was a high proportion of small, frequent events that were not as prominent in the 5 Hz high-pass filtered data. These events were only apparent on stations near

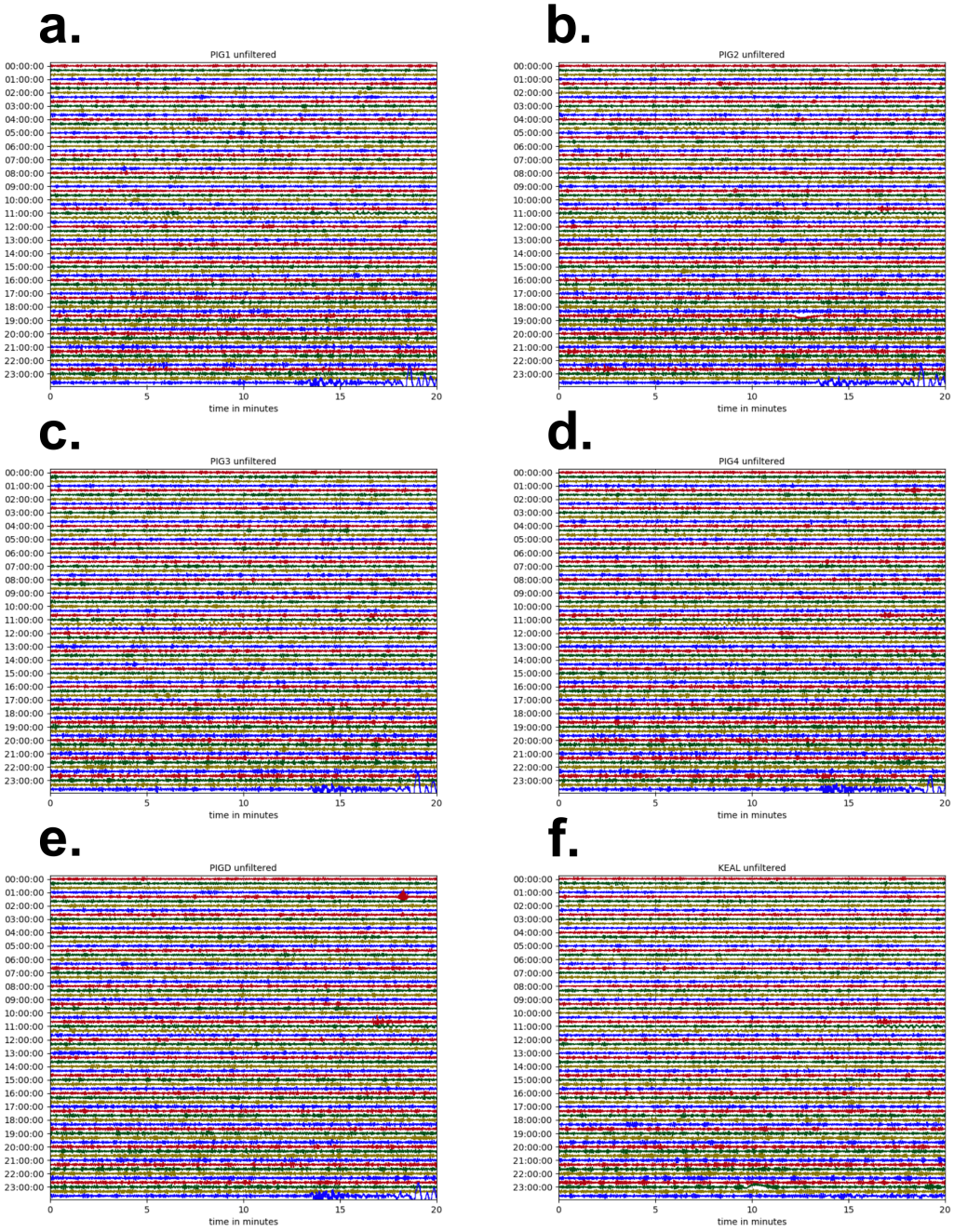

Figure 4.3: Unfiltered vertical component day long records from 16/02/2016 at a. PIG1, b. PIG2, c. PIG3, d. PIG4, e. PIGD and f. KEAL.

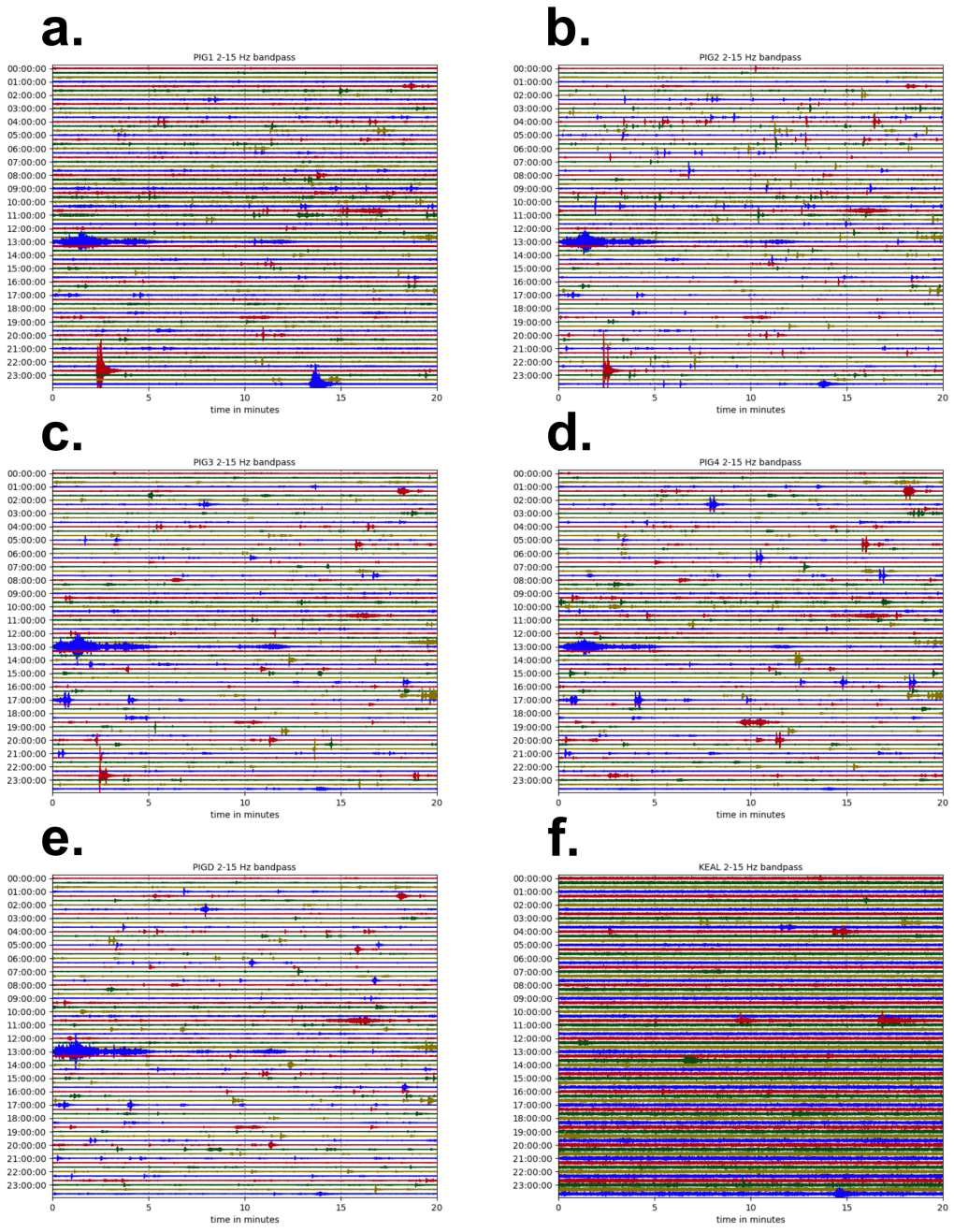

Figure 4.4: Vertical component day long records from 16/02/2016 bandpass filtered from 2-15 Hz at a. PIG1, b. PIG2, c. PIG3, d. PIG4, e. PIGD and f. KEAL.

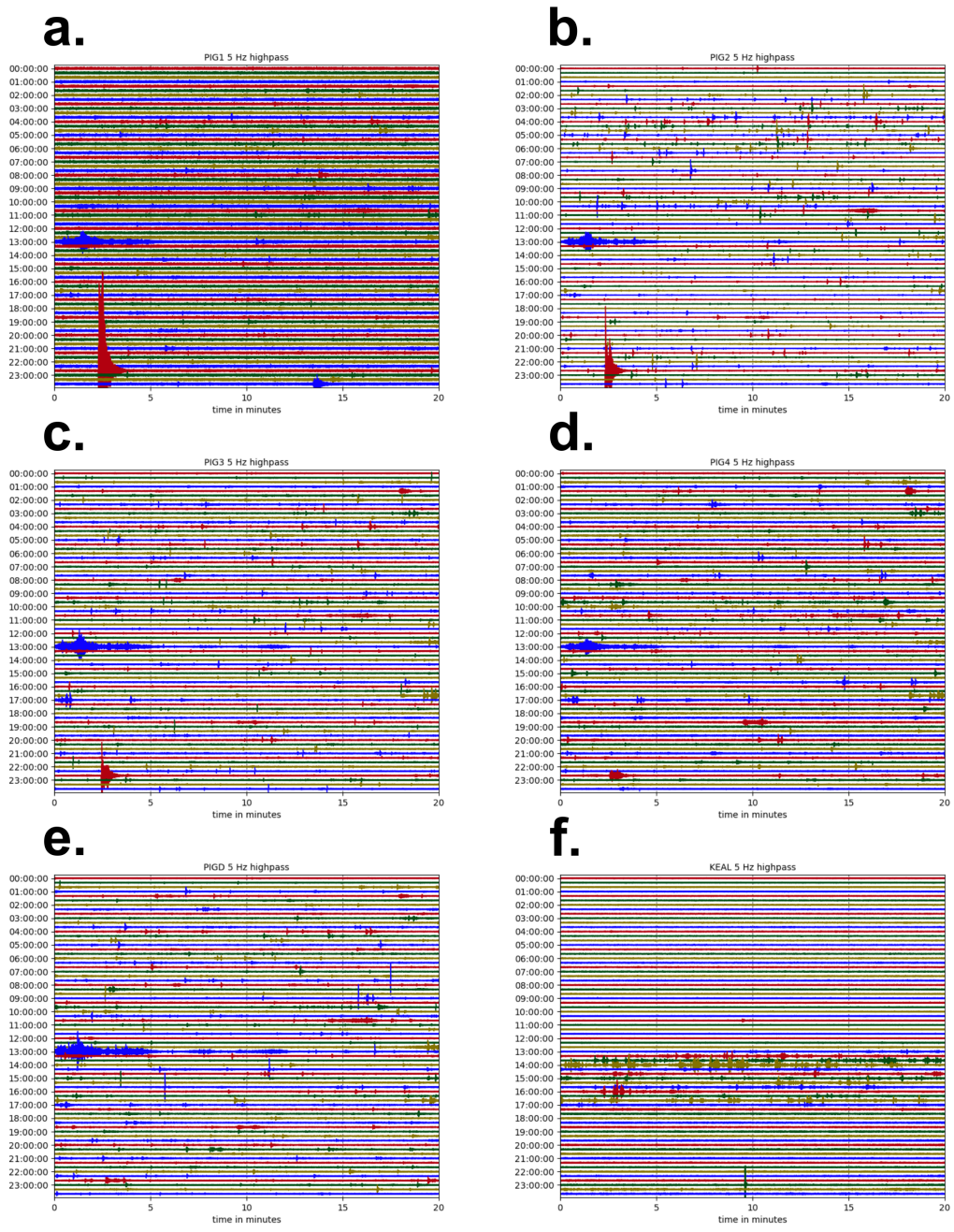

Figure 4.5: Vertical component day long records from 16/02/2016 highpass filtered above 5 Hz at a. PIG1, b. PIG2, c. PIG3, d. PIG4, e. PIGD and f. KEAL.

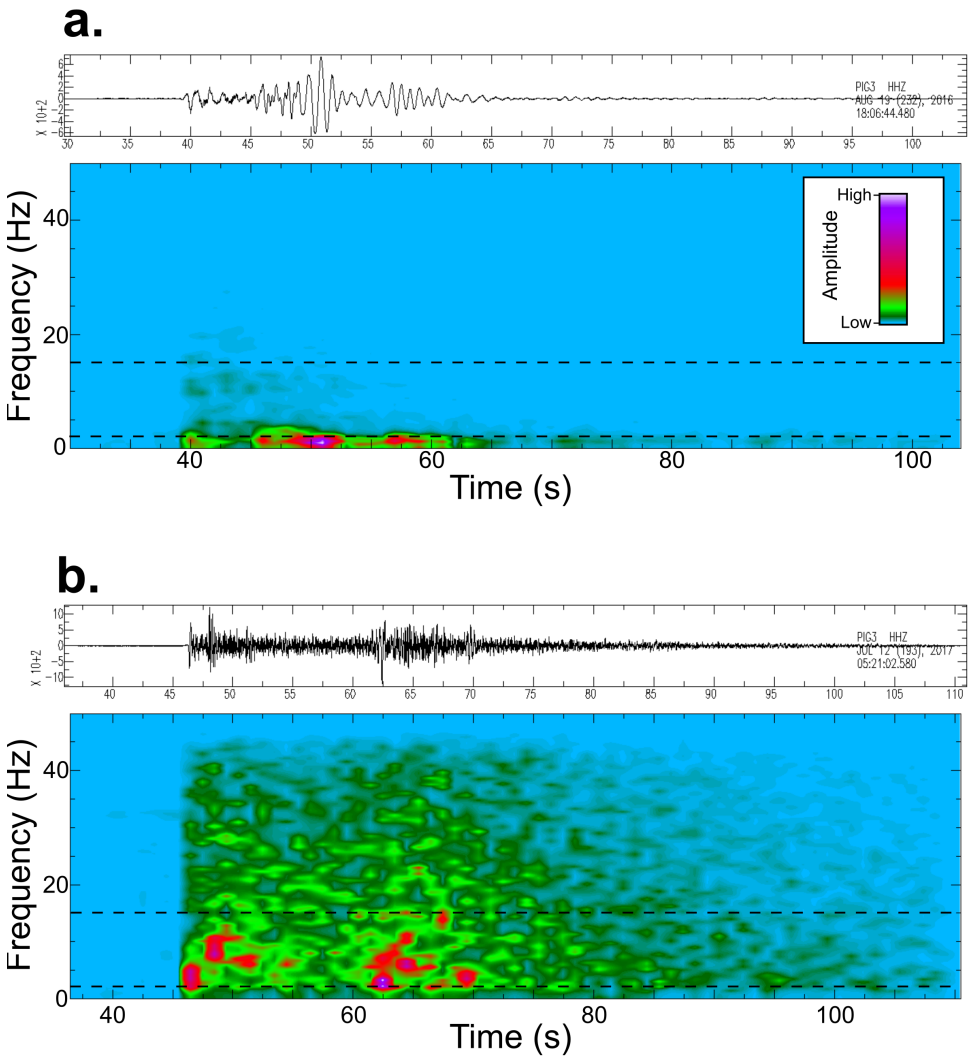

Figure 4.6: a. A vertical component highpass filtered above 1 Hz with a spectrogram from PIG3 of a low frequency event likely produced from the ice sheet. b. A likely local tectonic event recorded at PIG3 and filtered using the same parameters as panel a. featuring frequencies in the 1 - 50 Hz band. Dashed lines are added at 2 and 15 Hz for reference with the network coincidence search.

Pine Island Glacier, and have a frequency content and waveform consistent with a cryoseismic source (e.g. *Podolskiy and Walter*, 2016) (Fig. 4.6). Examples of filter testing are shown in Fig. B.1 - B.2.

4.2.2 Network coincidence search

To automatically detect local events recorded by the stations in Table 4.1 (Fig. 4.2) from 2015-2018 I used a network coincidence trigger algorithm on the continuous miniSEED data included in the Obspy toolbox (*Beyreuther et al.*, 2010). The network coincidence trigger works by reading the vertical component from all active stations for a given day, then applying a recursive short time average (STA)-long time average (LTA) routine trace by trace. The recursive STA/LTA compares the average absolute amplitude within two consecutive sliding windows. The STA window is sensitive to instantaneous spikes in amplitude, such as earthquakes, whilst the LTA window provides the average amplitude of the seismic noise (*Trnkoczy*, 2009). When the ratio of the STA and LTA values exceeds a pre-defined threshold, a trigger is noted for that trace. The trace is 'de-triggered' when the STA/LTA ratio falls below a second lower threshold, and the process can repeat. The network coincidence trigger compiles a chronological list of all single station triggers for each day, then identifies any overlapping triggers from three or more stations.

Selection of the STA/LTA window lengths and network coincidence thresholds was done by a trial and error process. I tested the network coincidence trigger on a week of continuous data, in which I had manually detected events through visual inspection of the helicoder records. The STA was set to 1 s and the LTA to 60 s following *Keir et al.* (2006b), with a trigger noted when the STA/LTA ratio exceeded 25, and de-triggered when it returned to < 2. A STA value of 1 s and a LTA of 60 s provides a good sensitivity to impulsive P-wave arrivals from local events 4.7, and all successfully detects all events identified by visual inspection.

The frequency band in which the continuous data is filtered has a dramatic impact on the style and amount of seismic events flagged by the network coincidence trigger. When run on unfiltered vertical components, only teleseismic events tend to be detected. Frequency filtering is therefore required to provide sensitivity to local seismicity. The impact of which frequency band is used for the network coincidence trigger is most pronounced on the UKANET Pine Island Glacier stations, given their proximity to the shear margins and calving front of the glacier. Running the network coincidence trigger at these stations on vertical components band-pass filtered from 2-15 Hz leads to 2609

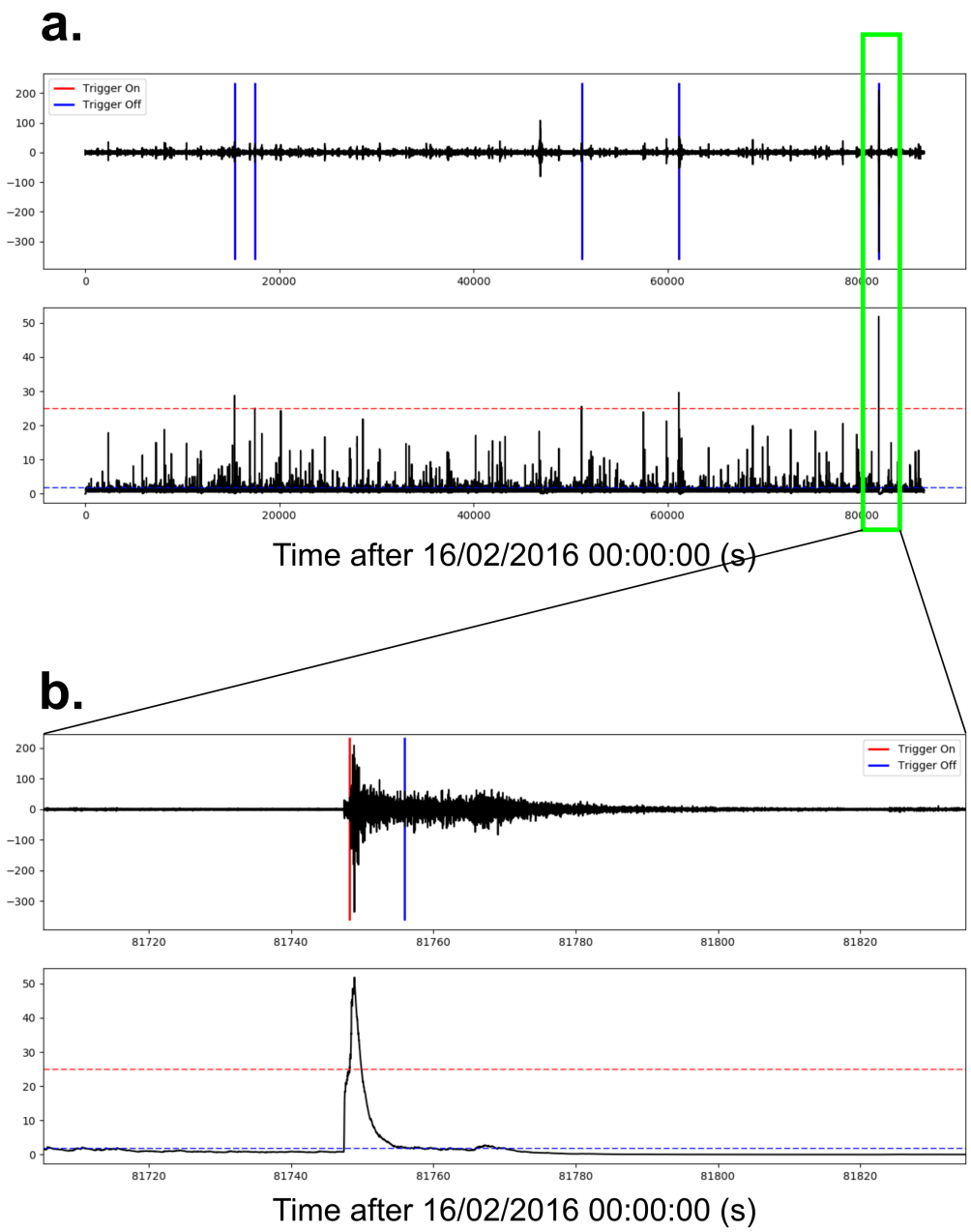

Figure 4.7: a) (Top panel) Day long vertical component highpass filtered above 5 Hz from PIG3 on 16/02/2016 with STA/LTA triggers on and off marked in red and blue lines respectively. (Lower panel) Characteristic function with STA/LTA trigger on threshold marked in red dashed, and trigger off marked in blue dashed. b) A zoom in on one of the events flagged by the STA/LTA search.

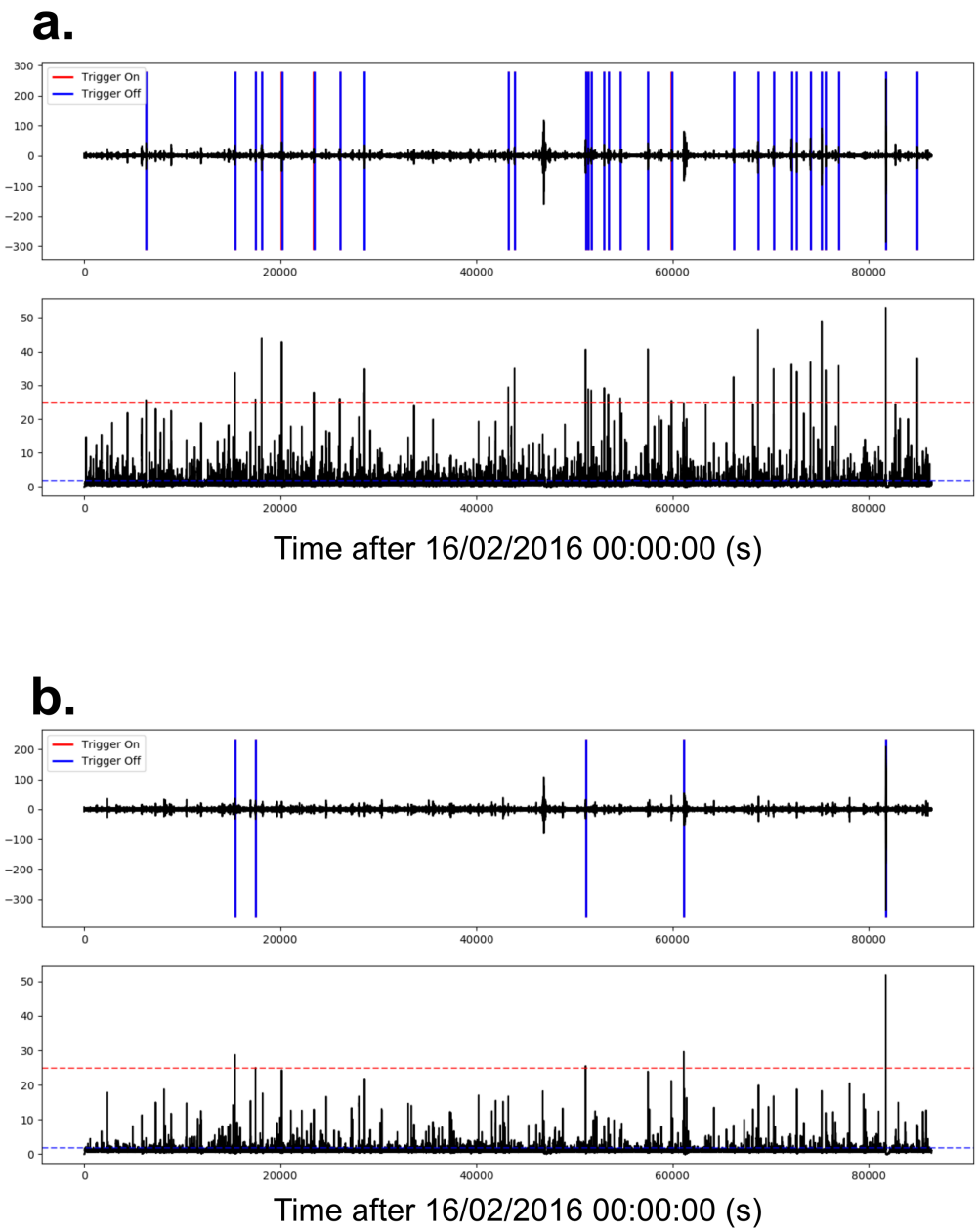

Figure 4.8: a) An STA/LTA search using a vertical component from PIG3 on 16/02/2016 bandpass filtered from 2-15 Hz. Searching in this frequency band returns a high number of detections from likely cryoseismic sources. b) An STA/LTA search using the same data and search parameters as panel a) but having been high-pass filtered above 5 Hz.

detections between 2016 and 2017, whilst using the same data/windows/parameters but with a high-pass filter above 5 Hz leads to 307 detections. This is due to many of the detections within the 2-15 Hz band being likely of cryoseismic origin. An example of a 'likely cryoseismic' and 'likely tectonic' event recorded at PIG3 is shown in Fig. 4.6. The 'likely cryoseismic' event features a predominantly lower frequency content than the 'likely tectonic' event, and a less impulsive P-wave arrival. Low frequency events of this type have been observed in other glaciated regions, often dominated by surface waves with a dominant frequency from 1-5 Hz and M_L <1 (*Thelen et al.*, 2013, *Podolskiy and Walter*, 2016; and references therein). Given that the main aim of this chapter is to detect and locate tectonic seismicity, it was therefore advantageous to tailor the network coincidence trigger parameters to avoid being overwhelmed by cryoseismic events.

To try and minimise the number of cryoseismic events detected by the network coincidence trigger, the algorithm was run on the vertical component data band-pass filtered at 2-15 Hz at all stations excluding the UKANET Pine Island Glacier stations (PIG1, PIG2, PIG3, PIG4, PIGD) for 2016-2017 only. I then ran an additional search using vertical component data high-pass filtered above 5 Hz at all stations including UKANET Pine Island Glacier stations, and merged the event lists from both searches, removing any duplicates in the second instance. Using the 2-15 Hz band-pass filtered data provided the best sensitivity to all local seismicity, whilst using a 5 Hz high-pass on the Pine Island Glacier stations reduced the number of cryoseismic events detected. The combination of both network coincidence searches led to 1304 detections from January 2015-February 2018.

4.2.3 Event quality control and phase picking

Prior to picking P- and S-wave first arrival times, I visually inspected all seismograms available for each event which triggered the network coincidence algorithm. For an event to be approved for phase picking it had to show resolvable P- and S- wave arrivals on at least three stations. Any non-seismogenic or teleseismic events were discarded at this stage. This quality control reduced the number of events from 1304 to 207. The majority of discarded events were either teleseismic detections, or did not show P- and S- wave arrivals which could be accurately picked at more than three stations.

First arrival times for P- and S- phases were picked on data zero phase band pass filtered from 2-15 Hz. Band-pass filtering in any lower frequency bands retained some

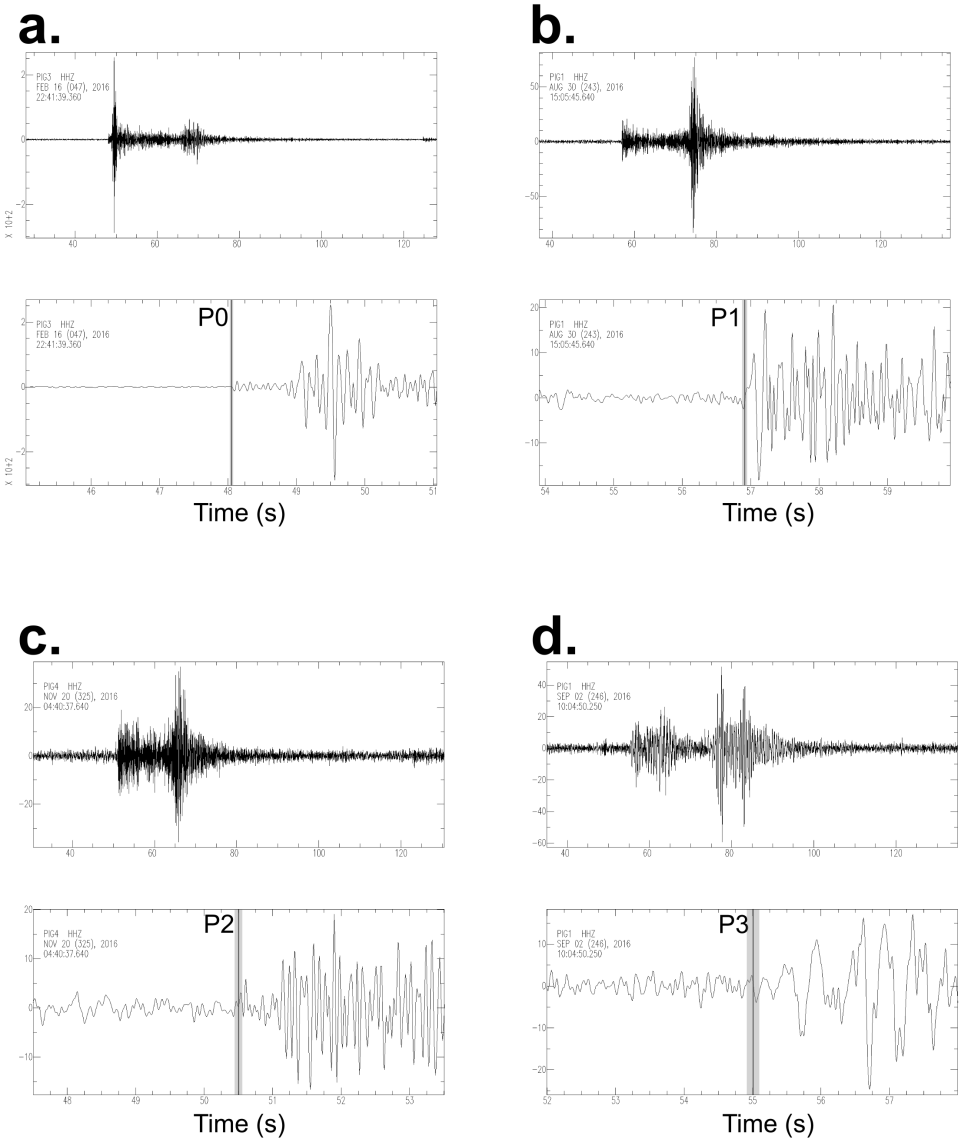

Figure 4.9: Examples of P-wave picking uncertainty. P-wave quality factors of P0 (a), P1 (b), P2 (c) and P3 (d) were assigned to a picking uncertainty of 0.05 s, 0.1 s, 0.15 s and 0.2 s respectively

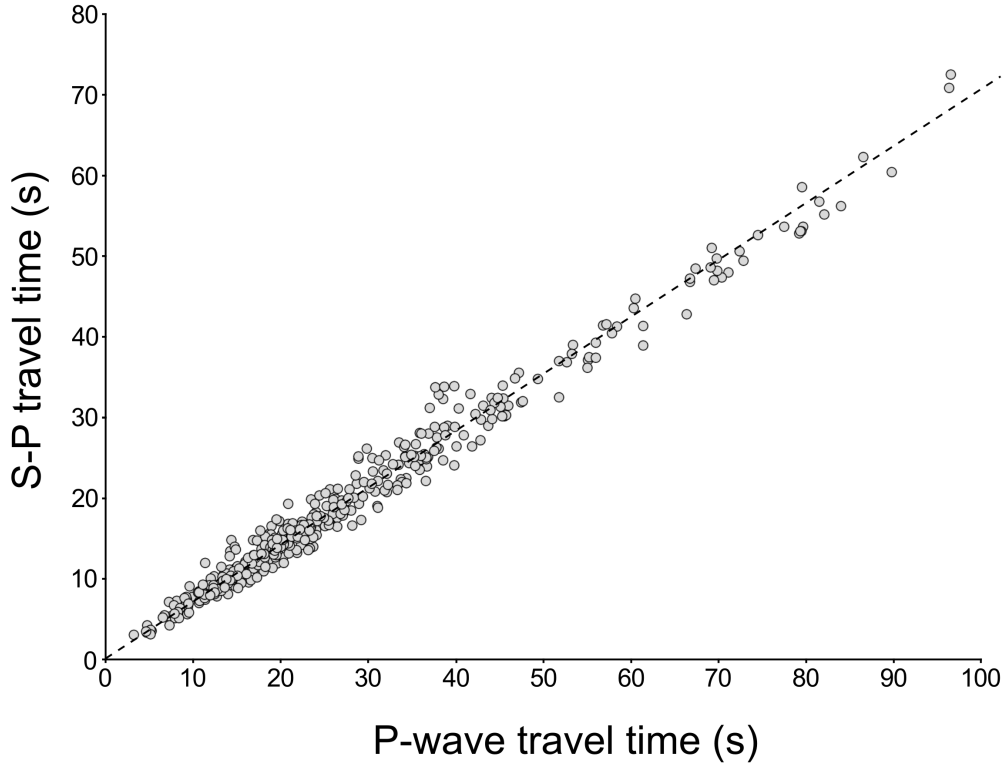

Figure 4.10: Wadati diagram of all S-to-P and P-wave arrival times from this study, which correspond to a Vp/Vs ratio of 1.72.

low frequency noise throughout the record, making picking more difficult. Each P- and S- phase pick was assigned a quality factor based on the pick uncertainty, which were later used in the event location procedure. P-wave quality factors of 0, 1, 2 and 3 were assigned to a picking uncertainty of 0.05 s, 0.1 s, 0.15 s and 0.2 s respectively (Fig. 4.9). 9 % of P-wave picks were assigned a quality factor 0, 66.6 % a factor 1, 11.6 % a factor 2, and 12.8 % a factor 3. For S-wave picks the quality factors of 0, 1, 2 and 3 were assigned to a picking uncertainty of 0.1 s, 0.2 s, 0.25 s and 0.3 s respectively. 0.7 % of S-wave picks were assigned a quality factor 0, 62.3 % a factor 1, 28.1 % a factor 2, and 8.9 % a factor 3. Any events with P- and S- arrival quality factors of worse than 3 were discarded at this stage. A Wadati diagram of all picks in this study is shown in Fig. 4.10, the best fit line of which represents a Vp/Vs ratio of 1.72.

4.2.4 Event location

The Hypoinverse algorithm (*Klein*, 1989) was used for event location. Hypoinverse works by iteratively converging on the event hypocentre by minimising the root-mean-square (RMS) residual between the predicted and measured arrival times for a given velocity model. For initial event location I used a simple velocity model based on the AK135 continental model (*Kennett*, 2005), with the average ice thickness from all stations from BEDMAP2 (*Fretwell et al.*, 2013). Arrival times used by Hypoinverse were weighted by the quality factor assigned in the picking process. P-wave arrivals with a quality factor of 0, 1, 2 and 3 were given a 1, 0.75, 0.5, 0.25 weighting respectively, and S-wave arrivals given half the weighting of a P-wave arrival of the same pick quality. The event locations produced using the AK135 model are shown in Fig. 4.11. Many events are clustered in the Pine Island Bay region, with isolated events further into the WARS and towards Marie Byrd Land. Eight events are also to be located in the Haag-Nunatak sector of the HEW block.

Given that the travel time of a seismic wave is a function of both the hypocentral parameters and the velocity structure encountered along the ray-path from source to receiver, it is often advantageous to locate events whilst simultaneously inverting for velocity structure. Using only one velocity model in the hypocentral location process can introduce a bias due to over or under predicting the Earth's velocity structure. In an attempt to simultaneously solve for both the hypocentral locations and a 1D velocity model, I tested the VELEST algorithm (*Kissling et al.*, 1995). Given the event distribution shown in Fig. 4.12, only 19 events were suitable for use in VELEST within the Pine Island Bay region. An ideal event for use in VELEST should have P-wave arrivals at numerous stations, with an azimuthal gap of less than 180°. The 19 events shown in Fig. 4.12 satisfy these criteria, but an additional issue for most events is the hypocentral distance to the nearest station is too great, which ideally should be less than twice the focal depth (*Kissling et al.*, 1995). The RMS residual for events relocated using VELEST was rarely able to fall beneath that achieved using the AK135 velocity model with Hypoinverse. The large epicentral distances and poor ray-path coverage for the 19 events used in testing VELEST is not sufficient (Fig. 4.12), and as such I decided not to invert for a 1D velocity model during the event relocation process.

In an attempt to reduce the RMS residuals and refine the hypocentral locations, I relocated events using a station dependent velocity model in Hypoinverse (Fig. 4.13). I produced a velocity model at each station based on the S-wave velocity models generated in Chapter 3, and used a Vp/Vs ratio of 1.72 derived from the P- and S- wave travel times (Fig. 4.10). The crust was split into two or three layers depending on

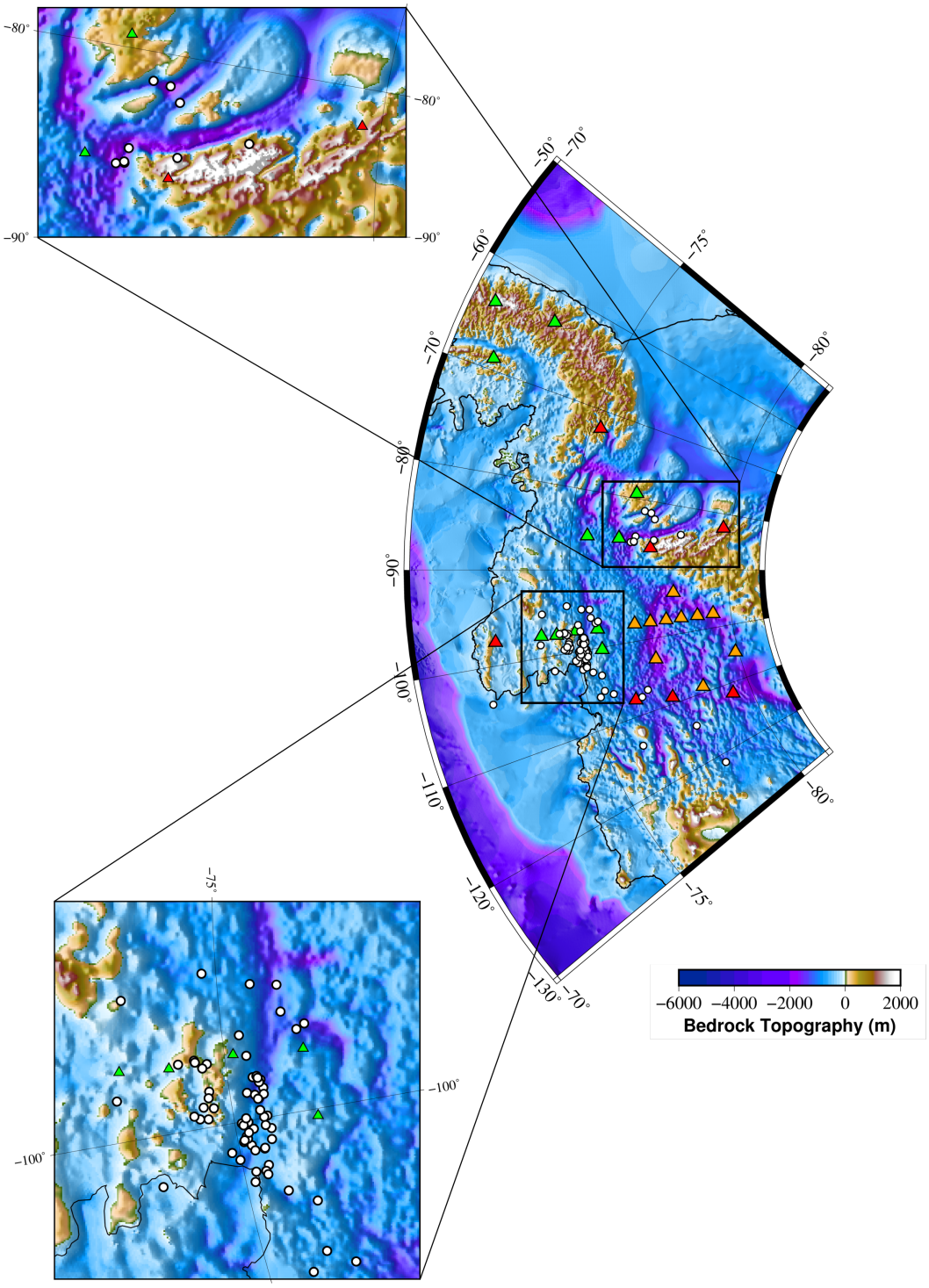

Figure 4.11: All picked events from 2015-2018 located using a crustal velocity model based on AK135. Event epicentres are shown in white circles, and inset maps are included of the Haag-Nunatak and Pine Island Bay regions where most seismicity is concentrated.

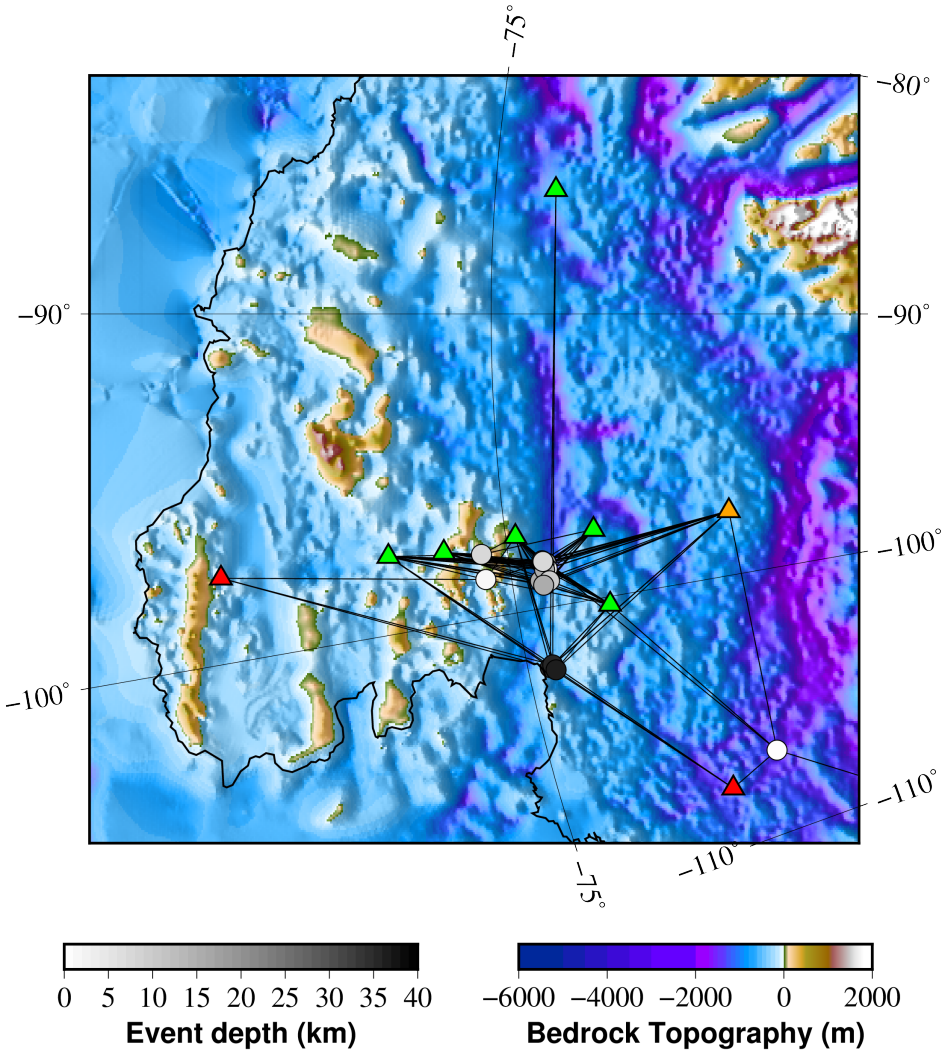

Figure 4.12: Events deemed suitable for inversion for a 1D velocity model, located using the AK135 model. Events are coloured by depth, and raypaths from each event-station pair are shown in black lines.

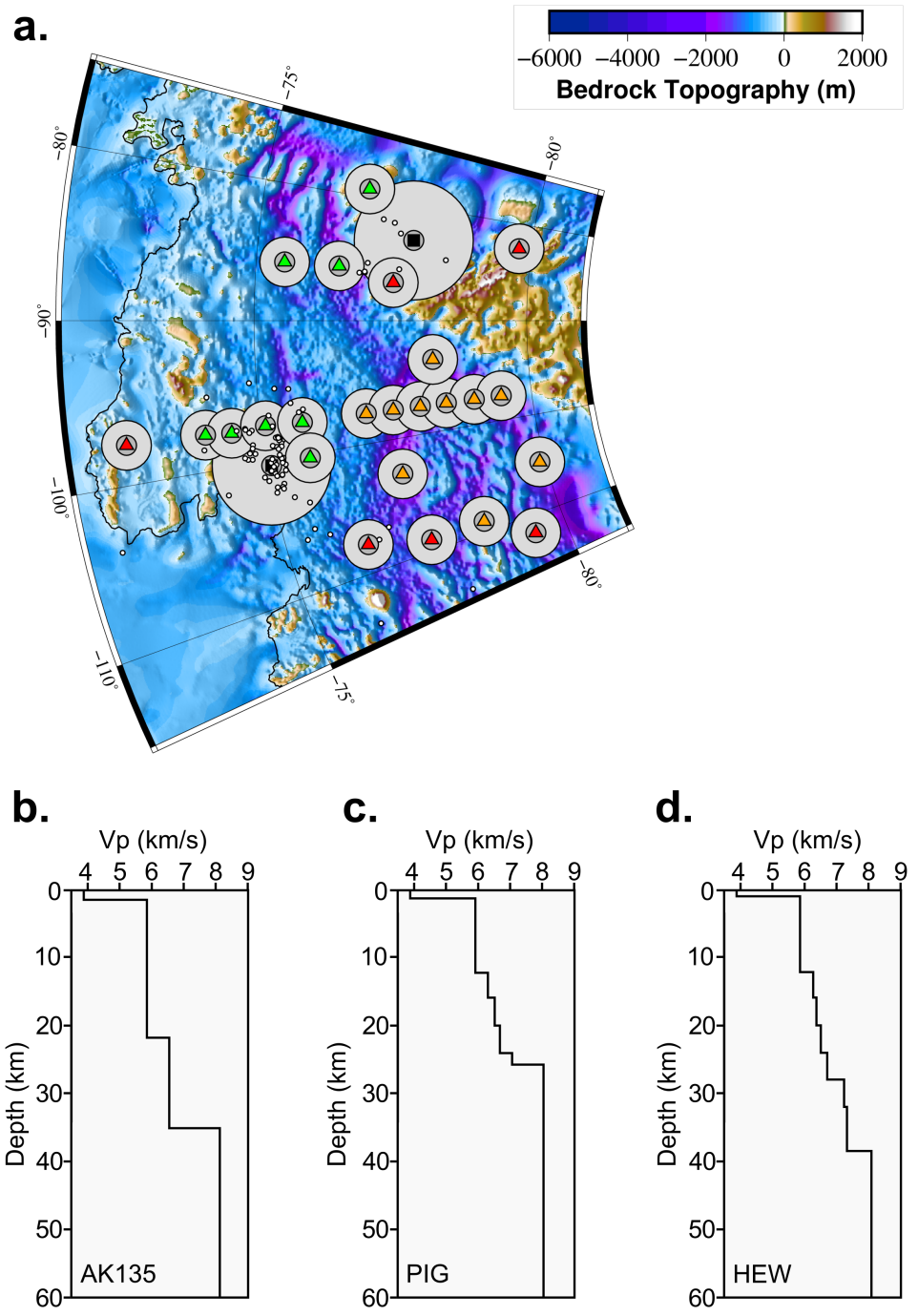

Figure 4.13: a) A map showing the nodes used in the station dependent velocity model used in Hypoinverse. Dark grey circles surrounding a node show the area in which the velocity model from a given station is used exclusively, and light grey the area in which overlapping models are used transitionally. The additional PIG and HEW nodes are shown by black squares. b) The AK135 background P-wave velocity model. c) The PIG P-wave velocity model based on the *O'Donnell et al.* (2019a) model. d) The HEW P-wave velocity model based on the *O'Donnell et al.* (2019a) model.

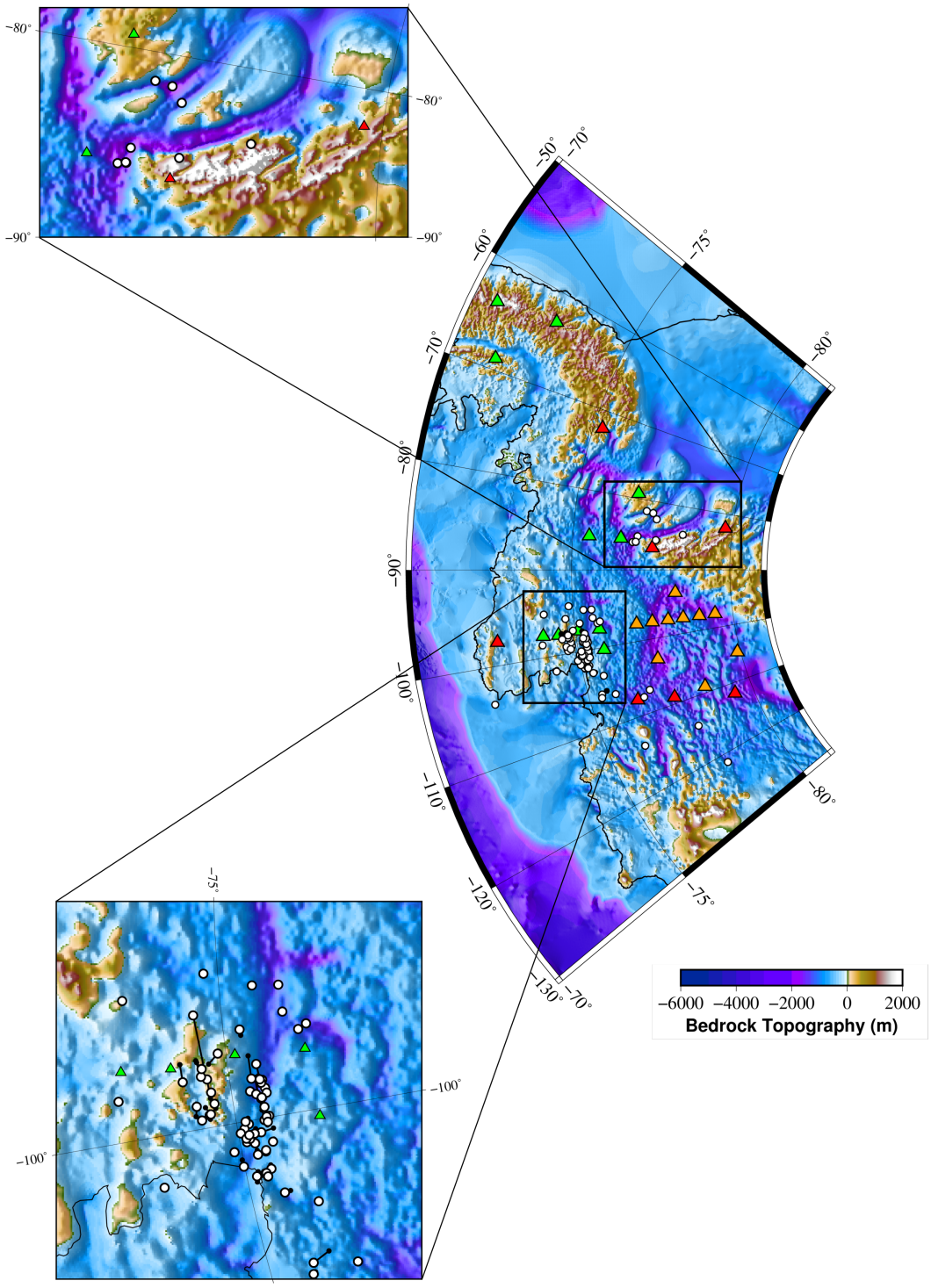

Figure 4.14: Maps of the relocated event hypocentres. Event hypocentres relocated using the station dependent velocity model are shown in white, and old locations solely using the AK135 model in black, with black lines showing how each event has moved.

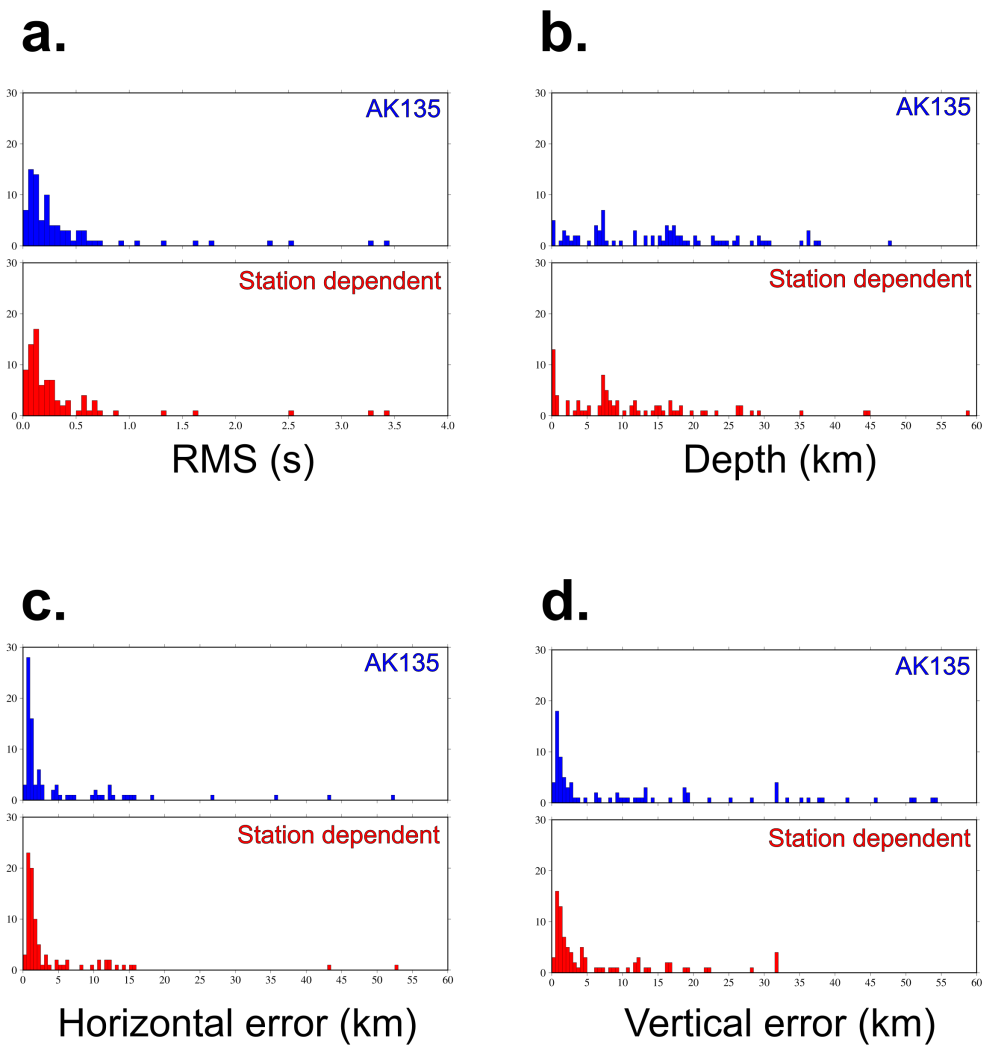

Figure 4.15: Histograms of event statistics based on location using the AK135 velocity model (blue) and station dependent model (red). a) Root-mean-square (RMS) residual. b) Hypocentre depths. c) Horizontal location error. d) Vertical location error.

the overall crustal thickness, and the average velocity from each layer was taken from the joint inversion S-wave model. The minimum thickness for a crustal layer was 7.5 km, such that at least three layers from the joint inversion model were averaged. At each station the ice thickness was extracted from BEDMAP2 (*Fretwell et al.*, 2013) and velocities from (*Kohnen*, 1974). Each station would act as a node, with a 20 km radius circle surrounding it. If an event was located within a 20 km radius of a station, then the velocity model from that station would be used exclusively. Surrounding the 20 km radius circle at each station was a 30 km wide transition zone, in which that station's velocity model would be used in combination with other overlapping velocity models. Two additional nodes were added, with velocities taken from *O'Donnell et al.* (2019a) (Fig. 4.13). The first node was in the centre of Pine Island Bay, and the second in the Haag-Nunataks. These two nodes were added as they would encompass many of the events located in the initial search, and would be more appropriate for the local velocity structure than the background model. For the additional PIG and HEW nodes a 20 km radius inner circle with a 100 km outer transition zone was used. Any events located outside of station based models was located solely using the background AK135 model.

The relocated hypocentres are shown in Fig. 4.14, which also shows the movement of each event from solely using the AK135 model to the station dependent model. The average RMS residual from all events was reduced from 0.54 using only AK135 to 0.46 using the station dependent model, though the overall distribution of the RMS misfit was roughly similar (Fig. 4.15). The average horizontal and vertical error produced by Hypoinverse is also reduced when using a station dependent velocity model versus one based on AK135 (Fig. 4.15). The average horizontal and vertical error for all events located using the AK135 model are ± 5.3 km and ± 11.9 km respectively, whilst the corresponding error values for the station dependent velocity model are ± 4.9 km and ± 6.4 km respectively.

4.3 Determining event magnitudes

To compute the local magnitude of all events in this study I use the equation of *Richter* (1935, 1958) as:

$$M_L = log(A_{WA}) - log(A_0) + S \tag{4.1}$$

A_{WA} is the zero-to-peak amplitude on a horizontal component of a Wood Anderson

instrument in mm, $log(A_0)$ is a distance correction term which describes an attenuation curve for the region, and S is a correction for each station. Given that I have only located 86 events spread over a relatively large area, it is not possible to determine an attenuation curve and station corrections for the region. To do this a denser seismic network with a higher event detection/location rate would be required. To calculate the local magnitude I instead tested using attenuation curves from three tectonically comparable regions: Ethiopia (*Keir et al.*, 2006a), Southern California (*Hutton and Boore*, 1987) and Tanzania (*Langston et al.*, 1998) (Fig. 4.16). The distance correction terms for each region are as follows.

For Ethiopia (*Keir et al.*, 2006a):

$$-log(A_0) = 1.19699log(R/17) + 0.001066(R - 17) + 2 \tag{4.2}$$

For Southern California (*Hutton and Boore*, 1987):

$$-log(A_0) = 1.11log(R/100) + 0.00189(R - 100) + 3 \tag{4.3}$$

For Tanzania (*Langston et al.*, 1998):

$$-log(A_0) = 0.776log(R/17) + 0.000902(R - 17) + 2 \tag{4.4}$$

R is the hypocentral distance in kilometers. Event magnitude was calculated for each event by initially converting both horizontal components with a picked S-wave to a Wood Anderson response. I then picked the maximum zero-to-peak amplitude for each component and computed the local magnitude using each of the three distance correction terms listed above. The median local magnitude from all East and North components was taken respectively for each event, then the two values were averaged to give a final local magnitude value.

Fig. 4.16b shows the distribution of local magnitude values calculated using each of the three distance corrections listed above for each individual horizontal component, whilst Fig. 4.16c shows distribution of final local magnitude values. The local magnitude scales for Ethiopia and Southern California produce a very similar distribution of local magnitude results, whilst the Tanzanian scale generally computes a lower value of local magnitude. Given that many of the stations used in the *Langston et al.* (1998)

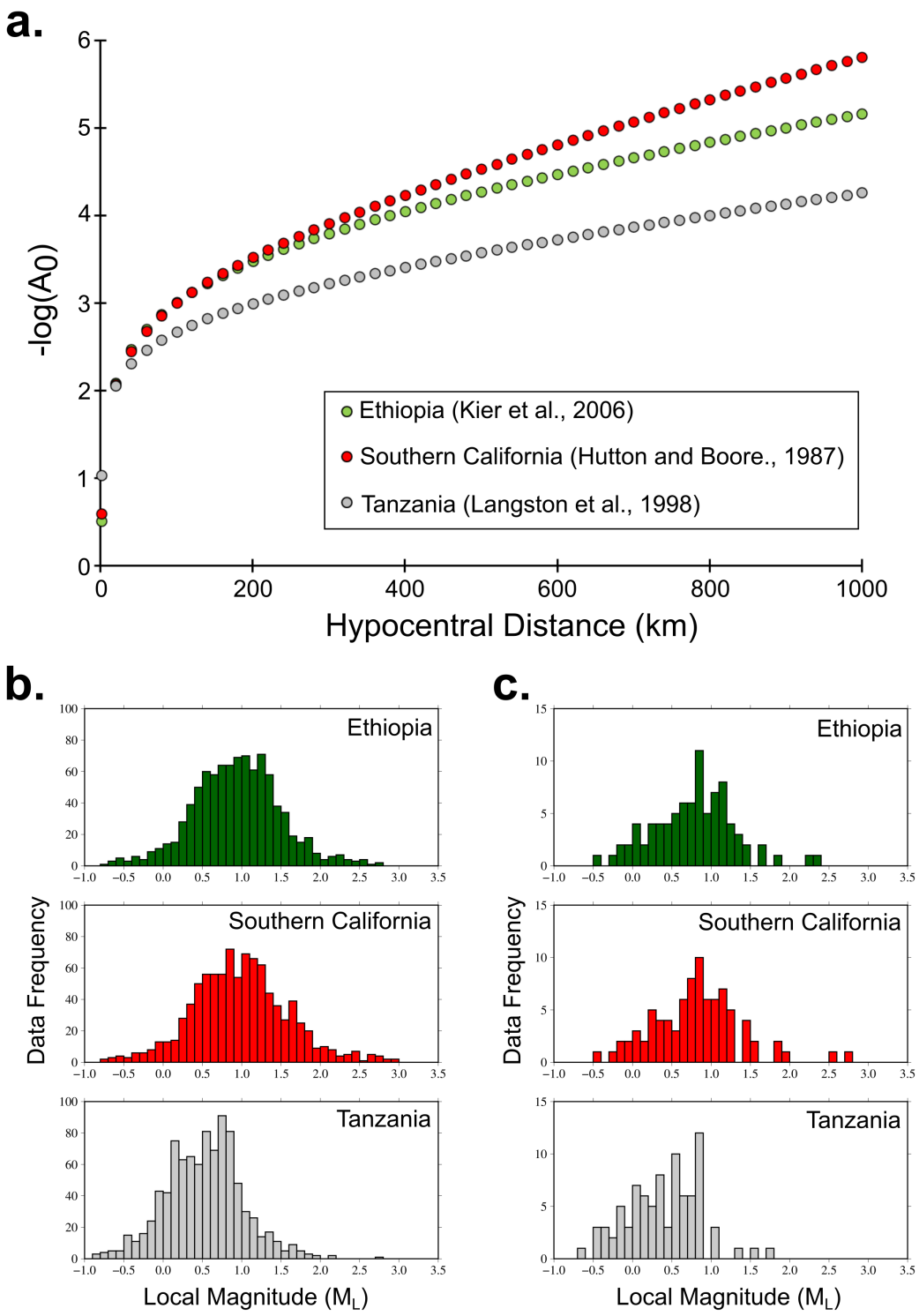

Figure 4.16: a) The three attenuation curves tested in this study. In green is the curve for Ethiopia (*Keir et al.*, 2006a), Southern California is in red (*Hutton and Boore*, 1987), and Tanzania in grey (*Langston et al.*, 1998). b) Histograms of the computed local magnitude for all available horizontal components using each of the three distance corrections shown in a). c) Histograms of the final computed local magnitude for each event.

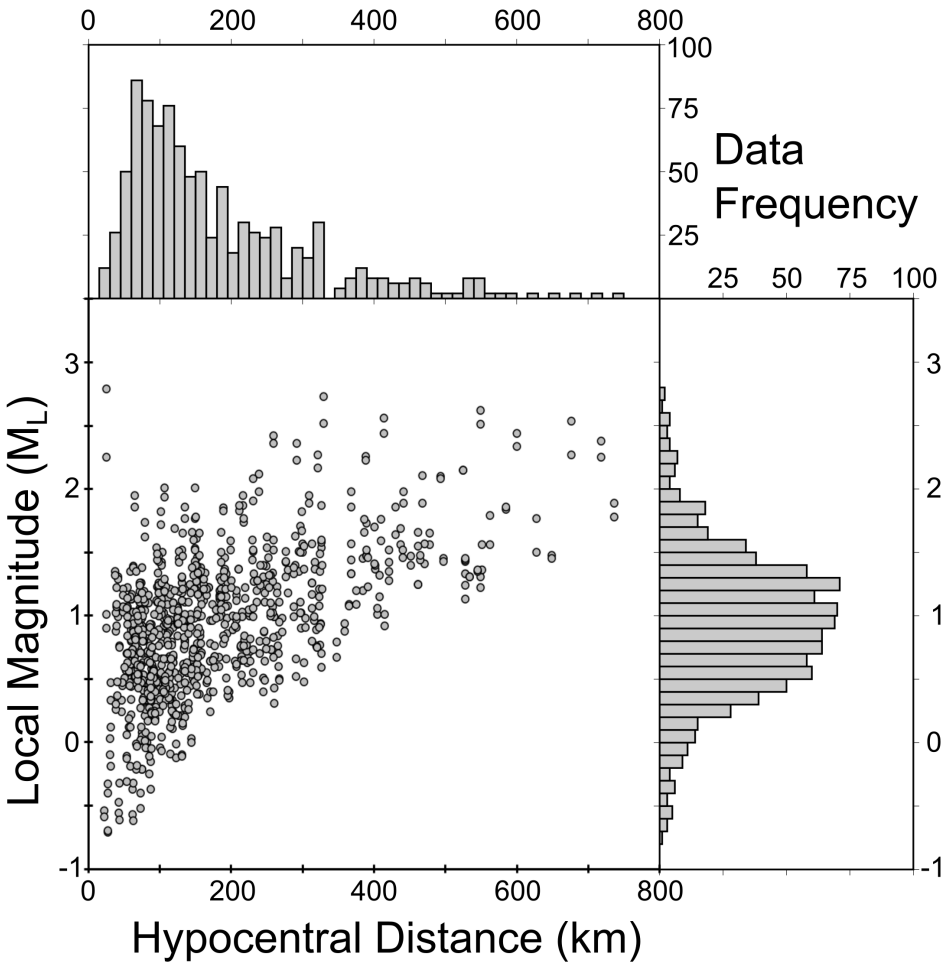

Figure 4.17: Distribution of the hypocentral distance and local magnitude computed using the distance correction terms of *Keir et al.* (2006a) for all available horizontal components.

study were on the Tanzanian Craton rather than in the neighbouring rift zone, this magnitude scale may not be appropriate for West Antarctica. Therefore I decided use the local magnitude equation for Ethiopia (*Keir et al.*, 2006a), given the similar tectonic framework with regards to the Amundsen Sea Embayment region, which hosts the majority of events I located. Given that the magnitude scale I am using is not calibrated for West Antarctica and is instead from an analogous region, all local magnitude results should be compared relatively, though the absolute values should be roughly appropriate. Fig. 4.17 shows the hypocentral distance and local magnitude distribution for all picked horizontal components computed using the distance correction terms of *Keir et al.* (2006a). The majority of local magnitude values computed using the Ethiopian scale are $M_L \approx 1$, with the best represented hypocentral distance range being 50-200 km.

Figures B.3 - B.6 show the distribution of local magnitude values calculated using the distance correction term of *Keir et al.* (2006a) at each station, for each component. UKANET PIG stations have the most calculated local magnitudes, and show a good consistency from station to station. Similarly the POLENET Mini Array stations in the centre of the WARS are very similar from station to station, but some of these stations only have a few values of local magnitude calculated. Stations FOWL, HOWD, KEAL and UNGL, which all where all situated either within or close to the HEW block show generally lower values of calcuated local magnitude than stations further towards the Amundsen Sea Embayment. This could be due to the fact that the events detected at stations in the Thurston Island/WARS region are not detected here, and as such the population of calculated magnitudes are not directly comparable. Another possibility is that the older, thicker crust of the HEW block means that the distance correction term of *Keir et al.* (2006a) is not as suitable here as it is for stations closer to the WARS.

4.4 Event categorisation

Despite attempting to reduce the number of cryoseismic events detected by the network coincidence trigger routine, it is still likely that some of the 86 located events are of a cryoseismic rather than tectonic source. To discriminate likely cyroseismic from possible tectonic events I used a categorisation scheme based on the event depth and location as well as via a visual inspection of each picked waveform style and frequency content. An event was flagged as a 'possible ice-quake' if the event depth was <7.5 km and the location was in the vicinity of a fast flowing ice stream (e.g. Pine Island Glacier, Rutford Ice Stream). Given that many events were only pickable at a handful of stations, often with a poor azimuthal coverage, the depth uncertainty is relatively

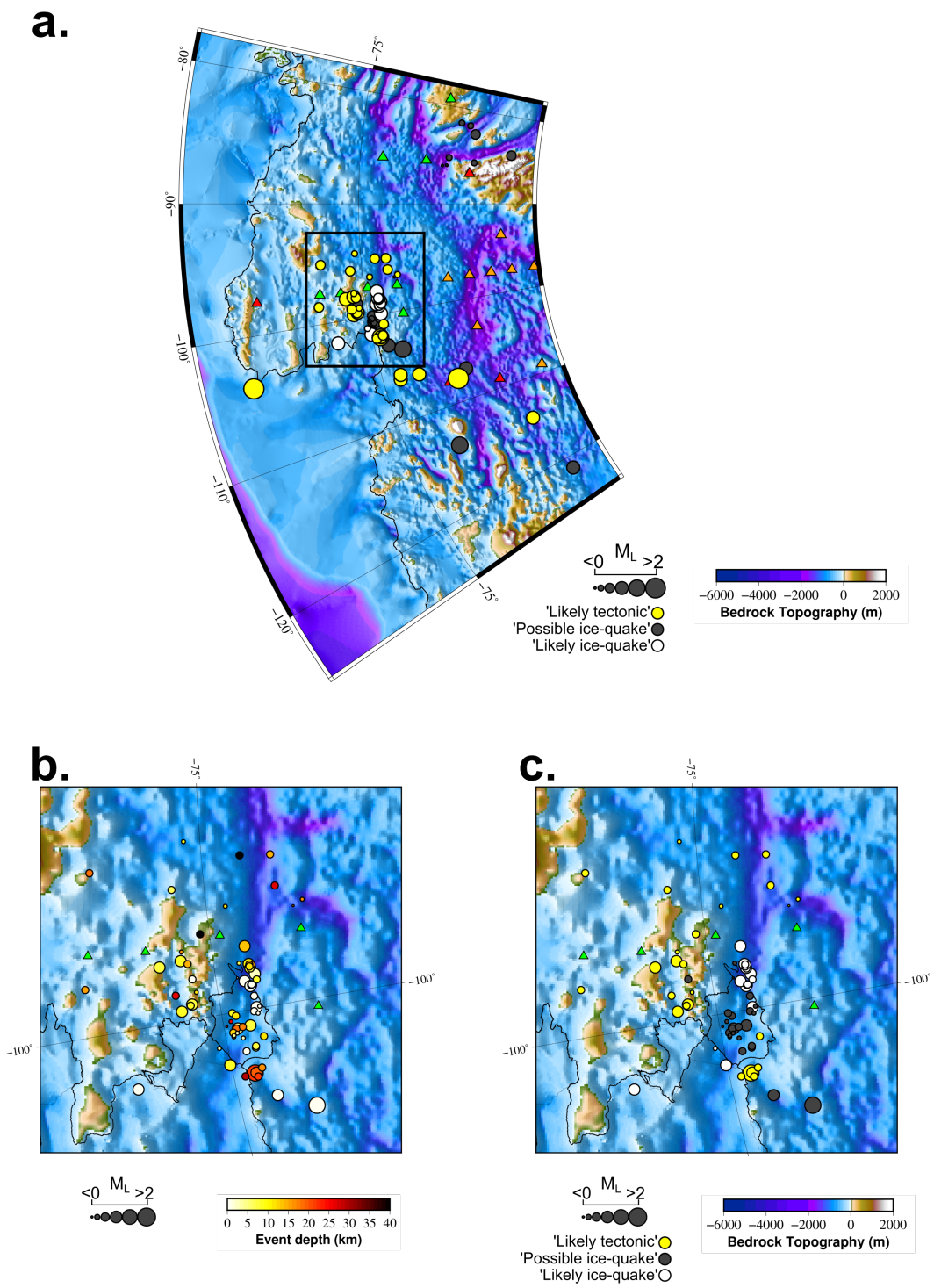

Figure 4.18: a) A map of all located events categorised into 'likely tectonic' (yellow), 'likely ice-quake' (white), and 'possible ice-quake' (grey), sized by local magnitude. b) A closer view of the Pine Island Bay region (black box in panel a.), with events coloured by depth and sized by local magnitude. c) A map of the same region with the events coloured by classification in the same format as panel a.

high (Fig. 4.15). As such if the event depth was <7.5 km, or if the vertical uncertainty could put the event within the ice layer, I considered it as a 'possible ice-quake'.

An event was then flagged as a 'likely ice-quake' if the waveforms and associated spectrograms from all picked stations showed the event was dominantly low frequency (<5 Hz) as shown in Fig. 4.6a. Low frequency events of this type have been observed in other glaciated regions, with a dominant frequency from 1-5 Hz and M_L <1 (*Thelen et al.*, 2013). Studies of these low frequency events originating from glaciers on the Cascade volcanoes in North America show clusters of many events with a high degree of similarity, suggestive of a repetitive shear rupture on the glacier bed (*Thelen et al.*, 2013). Whilst I have only located a few ice-quakes of this style, many more are present within the UKANET record, and were beneath the detection threshold of the network coincidence trigger or only detectable at <2 stations. Local tectonic events tend to produce energy at much higher frequencies (1-50 Hz). It is also possible for ice-quakes to produce frequencies in the 1-50 Hz range via surface crevassing (*Podolskiy and Walter*, 2016; and references therein), though these events tend to have a negative M_L.

If an event was not located on a fast flowing ice stream with a shallow hypocentral depth, and it featured peak frequencies >5 Hz with a positive M_L then it was flagged as a 'likely tectonic' event. This categorisation scheme resulted in 32 'likely tectonic' events, 17 'likely ice-quakes' and 37 'possible ice-quakes'. All of the 'possible ice-quakes' featured waveforms with a frequency content consistent with a local tectonic event, but the hypocentral location was in a region likely to produce substantial cryoseismicity. Events of this type could be from a shallow tectonic source, or have been generated by a cryospheric process which produces high frequencies, such as surface crevassing. Given the potential similarity between cryoseismic and tectonic seismicity it is possible that events could be misclassified.

4.5 Determining focal mechanisms

In an attempt to estimate the source parameters of the located events, I computed focal mechanisms using P-wave polarities, assuming that all sources are a pure double couple mechanism. Focal mechanisms are a useful tool for estimating fault geometry based on the radiation pattern of seismic waves generated during a slip event. A focal mechanism can be determined by measuring the P-wave polarity on vertical components of seismic stations with differing azimuths and hypocentral distances from an event. The polarity of a P-wave first motion indicates whether the fault movement was towards or away from each seismic station, with the assumption being that the fault is a planar

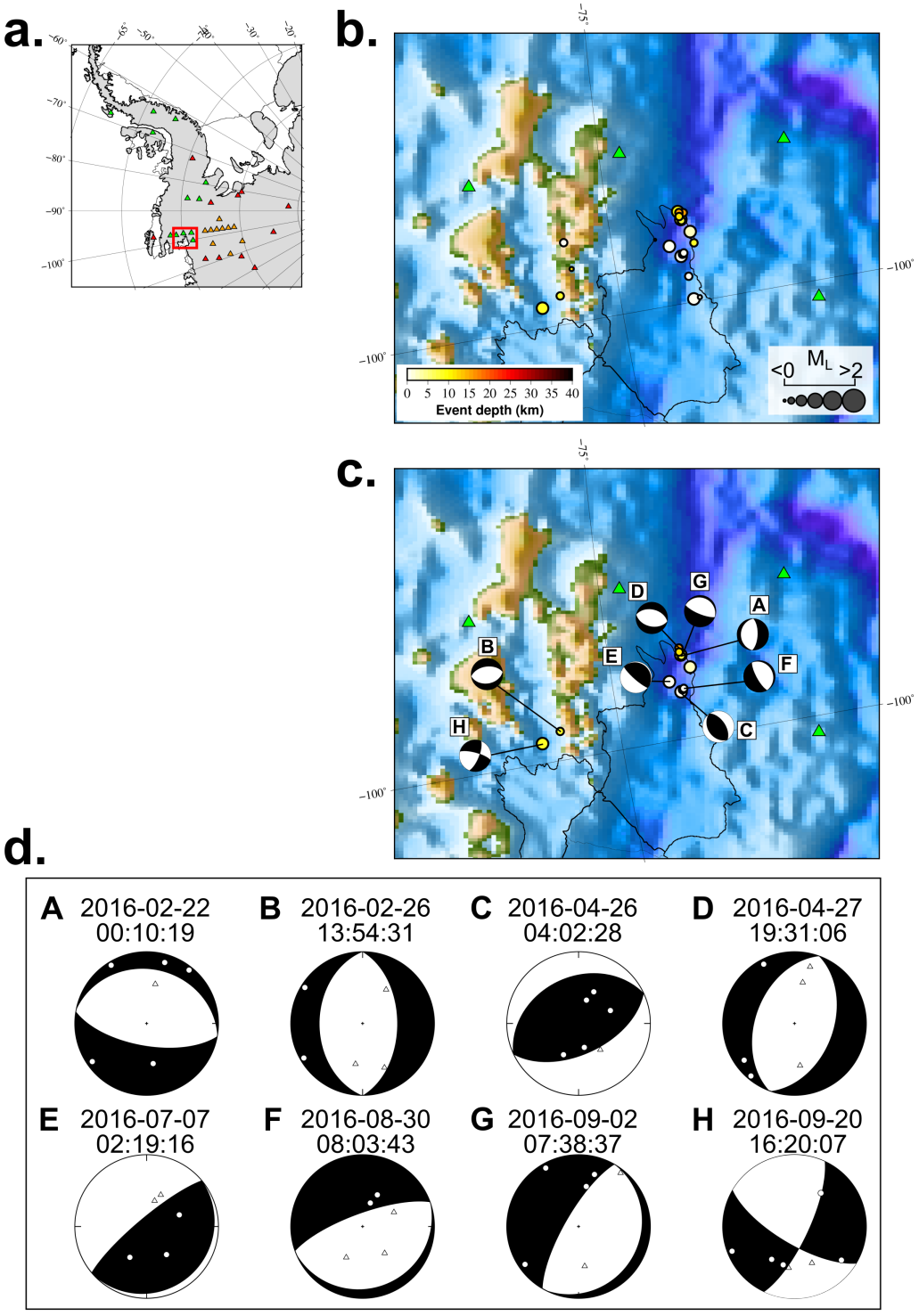

Figure 4.19: a) Map showing location of panels b. and c. b) A map showing the 19 events with a suitable azimuthal coverage for attempting focal mechanism determination coloured by event depth. c) Events with determinable focal mechanisms labelled chronologically. d) The focal mechanisms shown in panel c. with the P-wave polariry picks added. Dilations are marked with triangles and compressions with circles.

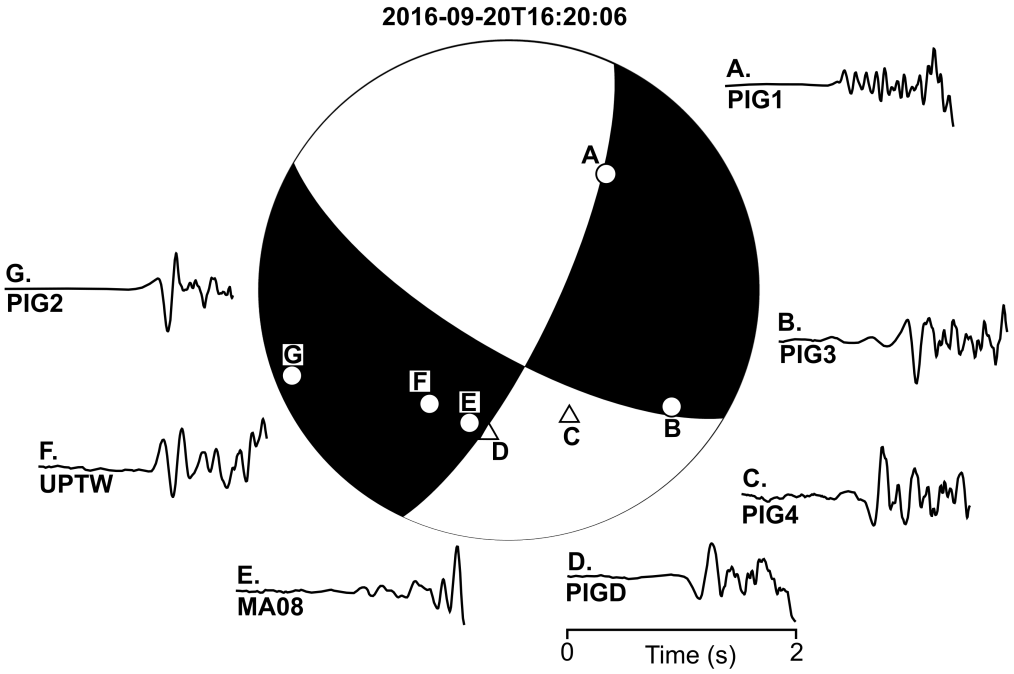

Figure 4.20: The focal mechanism for the 20/09/2016 'likely tectonic' event with P-wave polarity picks at each station shown. Dilations are marked by triangles and compressions by circles.

surface. For a given event the P-wave polarities at each station are marked on a lower hemispheric projection using each respective azimuth and take-off angle. Quadrants of compressive or dilational polarity can then be separated using perpendicular nodal planes, which reveal the fault geometry. Without additional information however it is not possible to tell which nodal plane represents the actual fault based on the P-wave first motion. I used the FOCMEC software package for focal mechanism determination (*Snoke*, 2003), which performs a systematic search of the focal sphere for suitable nodal planes, given the picked P-wave polarities for each event.

Of the 86 event I located in West Antarctica only 19 were suitable for focal mechanism estimation, based on the limited azimuthal coverage and relatively large hypocentral distances (Fig. 4.19). Accurate determination of a focal mechanism requires measurement of P-wave polarity at multiple stations, ideally plotting in each quadrant of the focal sphere. Given the station coverage in this study, only events located in the Pine Island Bay region in 2016 were suitable. The small L-shaped UKANET station array in 2016 provided the azimuthal coverage for events located inside the array to plot in at least three quadrants of the focal sphere. As such the P-wave polarity of each of these events had to be determinable at all UKANET PIG stations for a focal mechanism to be produced. The P-wave polarity at 11 of the 19 total suitable events was not clearly defined at all PIG stations, leading to a ambiguous focal mechanism. As such the focal mechanisms for these events were discarded. SH-waves can also be used to determine focal mechanisms, however despite rotation of the North and East components to a radial-transverse system the uncertainty in the SH- polarity at these events was unsuitable for use.

Two of the suitable events were classified as 'likely tectonic' (events B and H in Fig. 4.19), whilst the other six were either 'possible' or 'likely' ice-quakes given their vicinity to Pine Island Glacier. Due to the station distribution there would only be 5-8 P-wave polarity picks available for each event, and therefore the orientation of the nodal planes was often only loosely constrained. Despite this, the estimated focal mechanisms could still give an indication of the fault sense. Fig. 4.20 shows the most tightly constrained focal mechanism, produced by the 20/09/2016 'likely tectonic' event, which displays oblique-slip.

4.6 Discussion

I have located 86 events across West Antarctica from January 2015 to December 2017. The large interstation distances, varied network configuration each season,

and potential for detection of cryoseismicity mean that determination of a Gutenburg-Richter magnitude-frequency distribution is not possible. All of the events recorded in this study have a $\sim M_L$ <3, which is consistent with the historically low rates of intraplate seismicity observed across the continent (*Reading*, 2002). All event information is summarised in Table B.1.

4.6.1 Uplift as a driving mechanism for seismicity

73 of the 86 events I have located in this chapter are clustered in the region surrounding the Amundsen Sea Embayment (Fig. 4.18). By contrast, just 4 events have been located within the neighbouring central WARS, with no events being located in the vicinity of major WARS structures such as the Bentley and Byrd subglacial basins. It is possible that seismicity is present in the central WARS and was not detected by my network coincidence search, however the POLENET Mini Array station distribution and instrumentation is similar to the UKANET PIG stations, where the highest density of events are located. In addition the network coincidence search parameters were the same for both regions. Neglecting the 'possible ice-quakes', the disparity between the number of events located in the Amundsen Sea Embayment region versus the central WARS therefore suggests a difference in the regional stress field between the two areas.

All events I have located in West Antarctica have a relatively small local magnitude of M_L <3. The low magnitude and lack of events concentrated along potential tectonic structures suggests that there is little tectonic forcing currently occurring within the study area. The only seismicity corresponding with large scale existing tectonic structures are the events located within the Pine Island Rift, however it is difficult to separate which of these events are tectonic and which are cyroseismic (Fig. 4.18). Were there to be any active rifting occurring within the WARS, it would be likely that seismicity would be produced along fault systems distributed across a wider section of the rift system.

The overall pattern of more abundant seismicity in the Pine Island Rift region relative to the central WARS corresponds well with modelled uplift rates in West Antarctica (Fig. 4.21) (*Barletta et al.*, 2018). The rapidly decreasing ice volume observed in the Amundsen Sea Embayment has lead to enhanced uplift rates across the region. Models of both the elastic uplift and uplift from Glacial Isostatic Adjustment (GIA) show forebulges across the Amundsen Sea Embayment, the region in which I have located the majority of seismic events. Uplift rates within the central WARS are lower and more

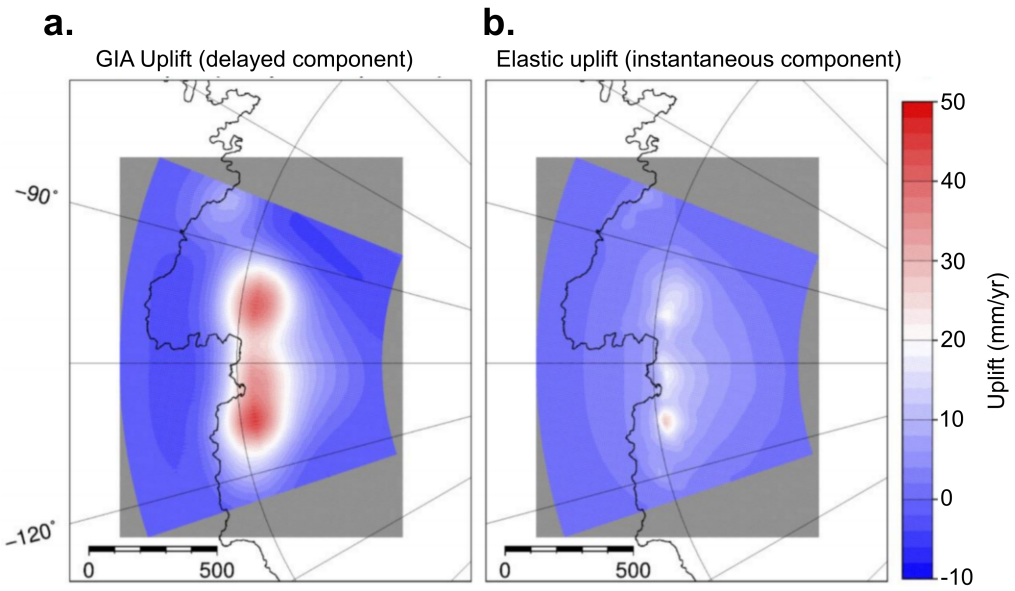

Figure 4.21: Maps of modelled GIA (a) and elastic uplift (b) rates in the Amundsen Sea Embayment. Modified from *Barletta et al.* (2018)

stable, and similarly I have detected and located little seismicity in this region. Given that the events I have located in the area surrounding the Amundsen Sea Embayment are low magnitude, and the available focal mechanisms from potentially tectonic events show a generally normal sense, it is likely that regional uplift is the driving mechanism for much of the observed seismicity.

4.6.2 Patterns of seismicity in the Amundsen Sea Embayment

Given the ability of a fast flowing ice stream such as Pine Island Glacier to produce significant seismicity, it is difficult to determine which of the events located within the Pine Island Rift were produced within the crust versus the ice stream. Fig 4.22b. shows a profile of all events located within the Pine Island Rift coloured by the depth error. The majority of the hypocentres are located at depths of <5 km, or have a depth error which could theoretically move the event to the surface. As such almost all of these events are flagged as 'likely' or 'possible' ice-quakes. Much of the seismicity located at depths of <5 km with a relatively small depth error occurs close to the glacier's grounding line and trends in a similar direction. Tidal flexure of the ice sheet as it transitions from grounded to floating ice is likely to be the cause for the shallow seismicity located in this region. Events C, E and F shown in Fig. 4.19 are likely

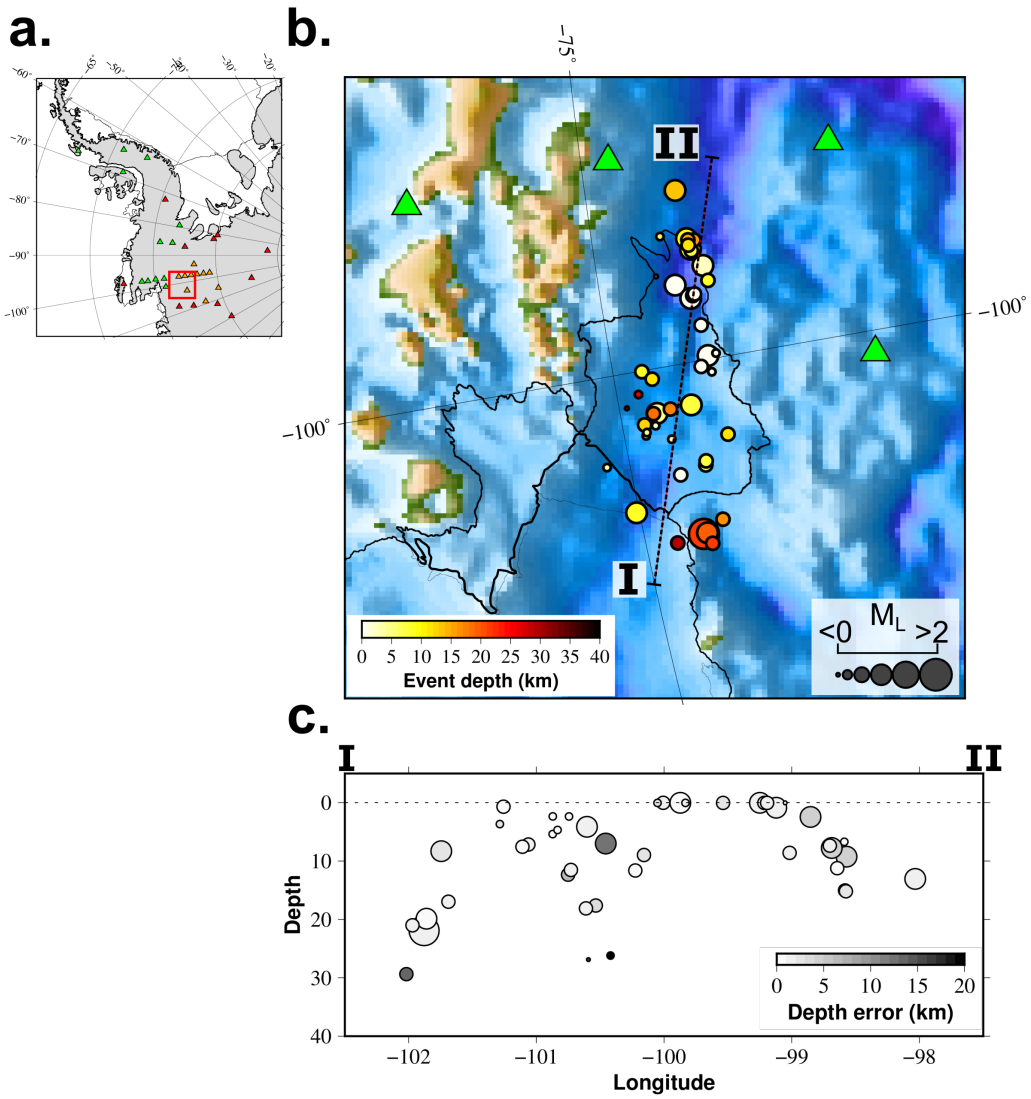

Figure 4.22: b) Events located within the Pine Island Rift coloured by hypocentral depth. The profile line for panel c. is shown in dotted black. c) A depth profile of the events shown in panel b. Events are coloured by the depth error produced by Hypoinverse (*Klein*, 1989)

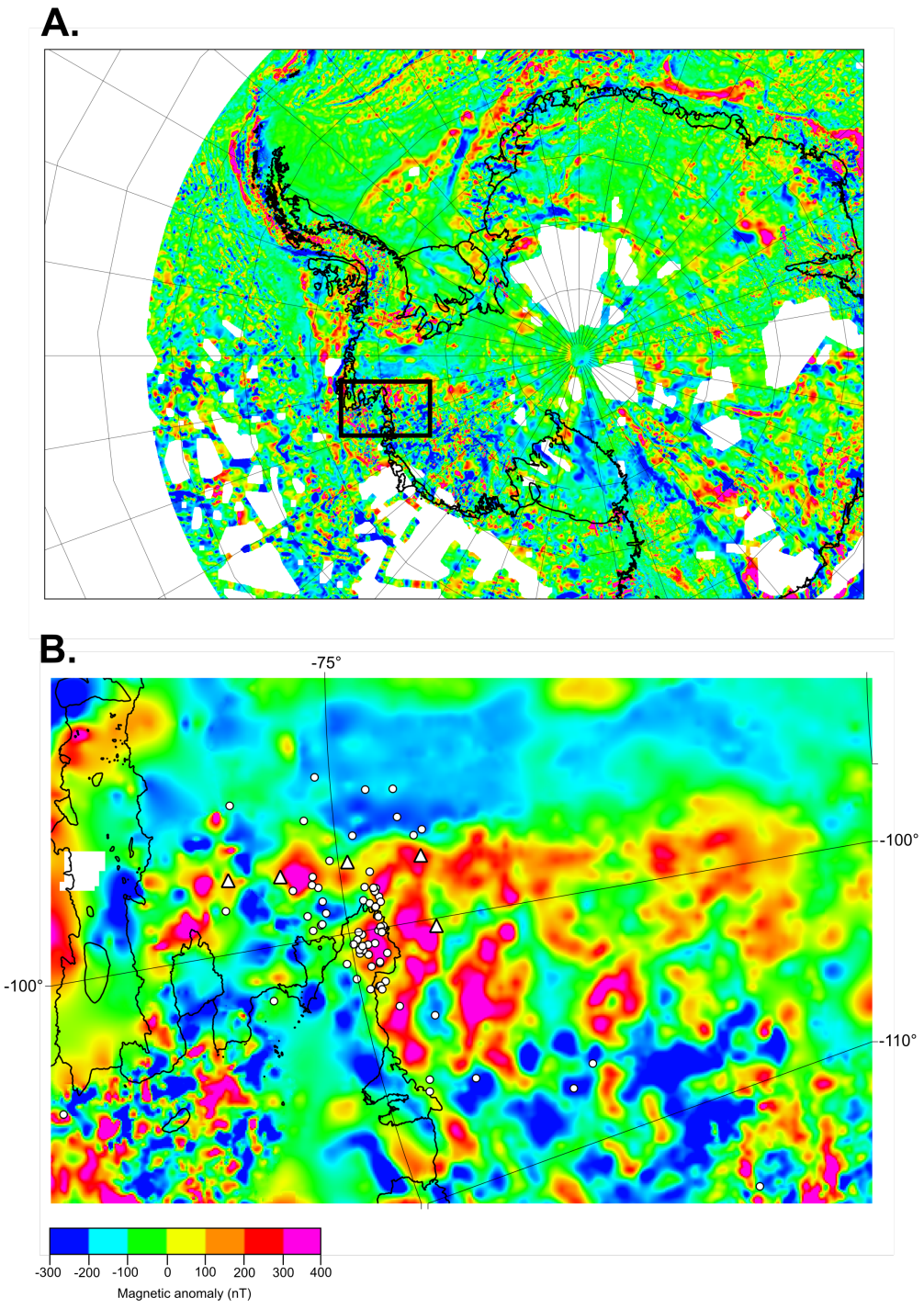

Figure 4.23: a) The ADMAP2 map of the magnetic anomaly across Antarctica developed by *Golynsky et al.* (2018). The black square shows the location of panel b. b) A zoom in on the ADMAP2 dataset in the Amundsen Sea Embayment, showing magnetic highs trending roughly north-south and east-west. The events I have located in this chapter are shown in white circles and the UKANET PIG stations in white triangles.

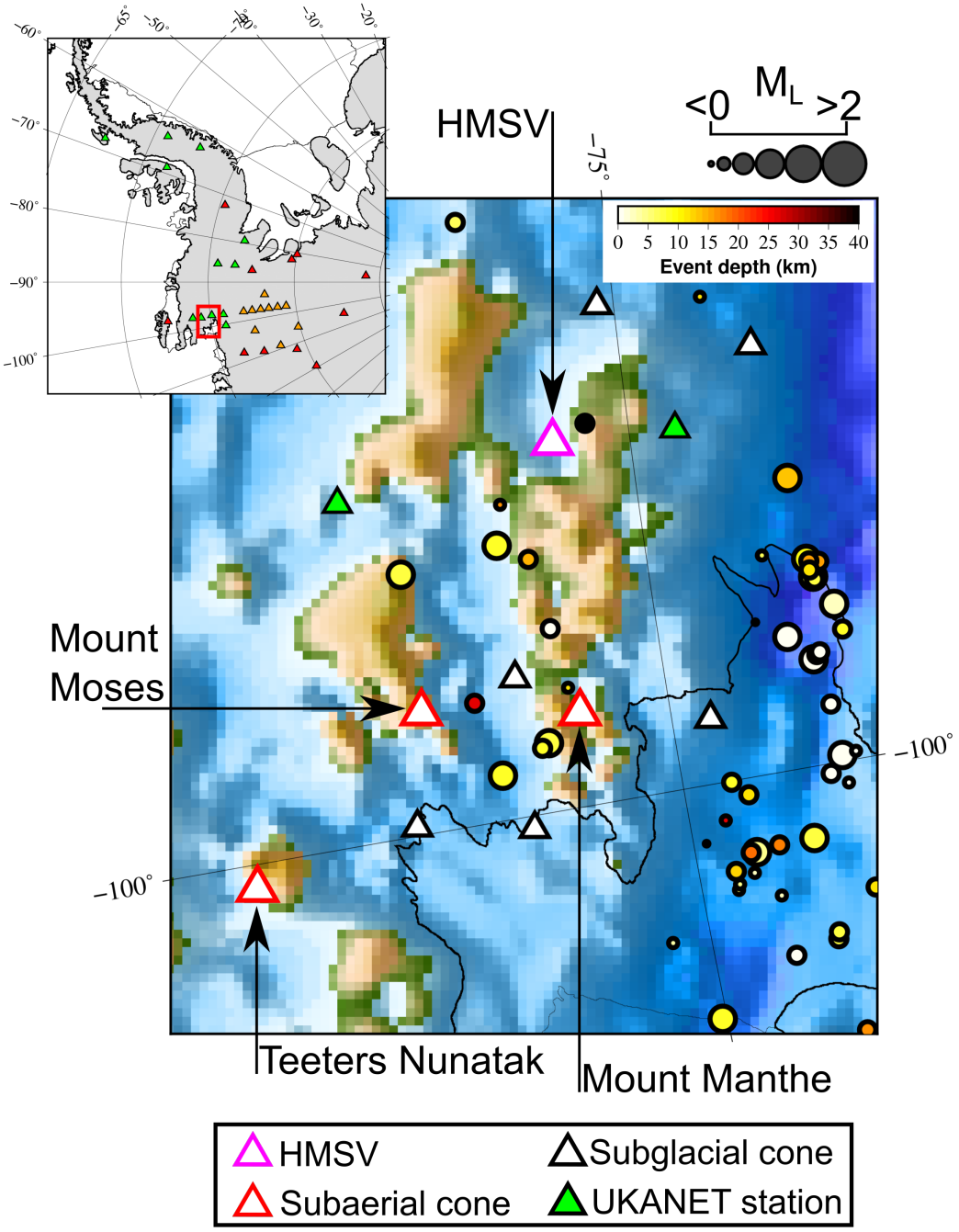

Figure 4.24: A map of the events located in the vicinity of the Hudson Mountains coloured by depth, with possible volcanoes added. Subaerial cones are in red outlined triangles, subglacial cones identified in *de Vries et al.* (2017) in black outlined triangles and the Hudson Mountains Subglacial Volcano (HMSV) (*Corr and Vaughan*, 2008) in a pink outlined triangle.

located within the ice layer (depths <1 km) close to the grounding line, and display near vertical and horizontal nodal planes with possible reverse motion. Compressive forcing occuring within the ice sheet in this region is likely due to tidal flexure at the grounding line. Ice-quakes relating to tidal flexure at the grounding line of Ice Stream C in the Ross Sea Embayment have been observed at similar hypocentral distances (*Anandakrishnan and Alley*, 1997).

Despite many of the events shown in Fig. 4.22 having likely been produced due to active ice sheet processes, it is also possible that some of the deeper events did occur within the crust. The relatively high uplift rates in this region could have caused the reactivation of existing fault structures within the Pine Island Rift. Were the seismicity to be related to active rifting, it may be expected that there would be more events distributed across a longer section of the Pine Island Rift. The focal mechanisms A, D and G in Fig. 4.19 are from events within the Pine Island Rift which occurred at 7-15 km depth and all show a normal sense. Fig. 4.23 shows the events located in this chapter plotted over the ADMAP2 magnetic anomaly dataset of *Golynsky et al.* (2018) in the Amundsen Sea Embayment. Though ADMAP2 shows magnetic highs trending roughly north-south and east-west in the vicinity of the Amundsen Sea Embayment, there is no obvious overlap between these features and the seismic events I have located in this chapter.

Within the wider Amundsen Sea Embayment area there are also subaerial and potentially subglacial volcanic structures present (Fig. 4.24). The Hudson Mountains, which flank the Pine Island Rift feature a chain of subaerial parasitic cones topping three eroded Miocene volcanoes, these are Teeters Nunatak, Mount Moses and Mount Manthe (*Rowley et al.*, 1986) (Fig. 4.24). The nunataks of the Hudson Mountains generally trend east-west or north-south, suggesting that eruptive centres may have been controlled by orthogonal fractures (*Rowley et al.*, 1986). The events that I have located in the Hudson Mountains do not show any north-south trends, however seven events that I have located close to Mount Manthe trend roughly east-west at ∼10 km depth (Fig. 4.24). Recent studies of ice-penetrating radar data have also revealed possible subglacial volcanoes nearby (*Corr and Vaughan*, 2008, *de Vries et al.*, 2017). The subglacial volcano database of *de Vries et al.* (2017) was developed simply by interpreting conical structures in the BEDMAP2 dataset, and as such does not provide any evidence for potential volcanic activity at these subglacial cones. *Corr and Vaughan* (2008) however were able to identify tephra layers within the ice sheet indicative of a large eruption at 207 BC ± 204 years. These tephra layers are thickest above a subglacial high in the Hudson Mountains which the authors term the 'Hudson Mountains Subglacial Volcano'

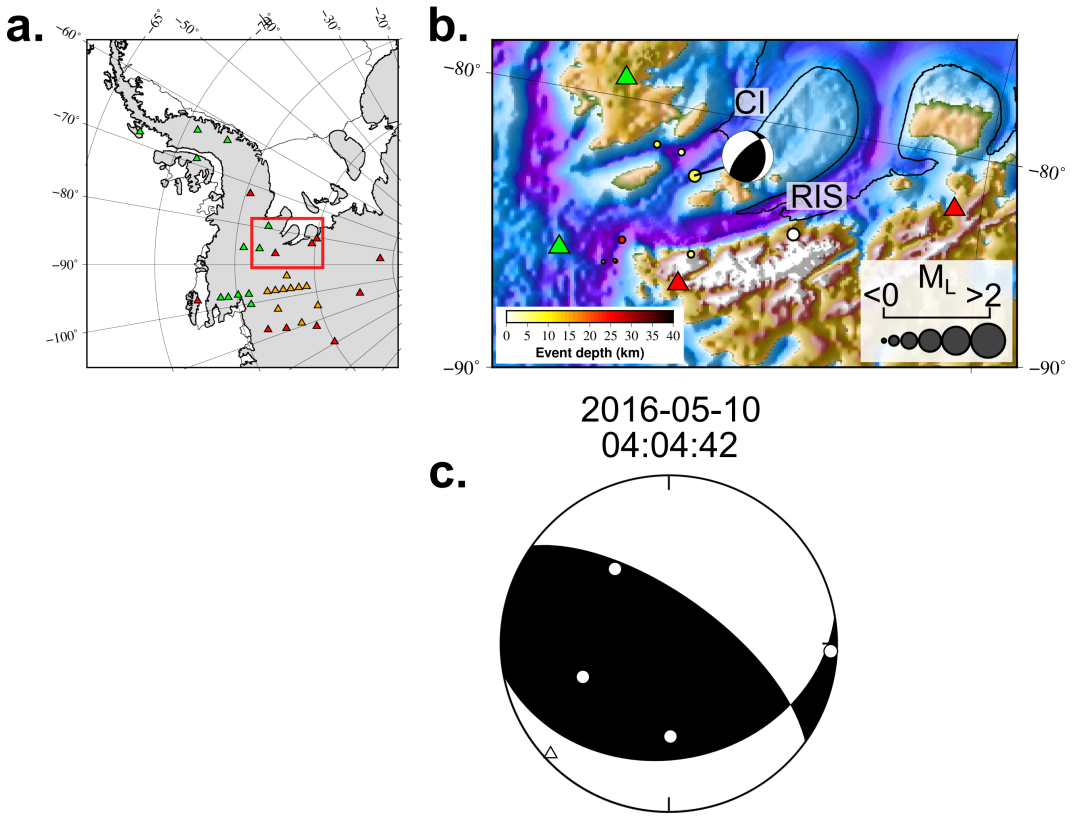

Figure 4.25: a) Map showing the location of panel b. in the red box. b) Events located in the Haag-Nunatak region close to the Rutford Ice Stream (RIS) and Carlson Inlet (CI), coloured by depth and sized by local magnitude. Only one event had a suitable azimuthal coverage for focal mechanism determination, which is shown in panel c. c) Focal mechanism estimated for the 10/05/2016 event located on the southern flank of the Carlson Inlet. Dilations are marked by triangles and compressions by circles

(HMSV). The events I have located within the Hudson Mountains do not correlate well with the subglacial cones identified in *de Vries et al.* (2017), however there is one ∼45 km deep event which is located ∼5 km from the HMSV. This event occured on the 29th of January 2016, when only two of the UKANET PIG stations were active, and as such the horizontal error is relatively high (13 km). Despite this, the event depth combined with the proximity to the relatively recently eruptive HMSV, suggests that this event could be related to volcano-tectonic activity.

4.6.3 Seismicity in the Haag Nunataks

Eight events were located in the Haag Nunatak sector of the HEW block 4.25; a region which features sharp changes in topography from the Ellsworth Mountains into the glacial troughs of the Rutford Ice Stream and Carlson Inlet. Given the regional station distribution, the horizontal and vertical uncertainties (10 - 20 km) for the HEW

hypocentres are much higher than the events located in the Amundsen Sea Embayment. It is therefore difficult to provide a meaningful discussion of the distribution of these events. In general, the events are distributed close to the flanks of the Rutford Ice Stream and Carlson Inlet. All HEW events feature frequency content consistent with a local tectonic event in the 1-50 Hz band, and no events appear similar to the low frequency grounding line ice-quakes identified at Pine Island Glacier. Previous study of seismicity in this region focused on the tidally modulated basal microseismicity on the Rutford Ice Stream using a closely spaced seismic network (*Adalgeirsdóttir et al.*, 2008). Microseismicity of this type is likely too small to be detectable at the hypocentral distances in this study. The events located in this study could relate to faulting along the flanks of the deep subglacial troughs through which the Rutford and Carlson ice streams flow, however given the large uncertainty in the hypocentral locations it is not possible to rule out that the events are cryoseismic. Only one event had an azimuthal coverage suitable for focal mechanism determination and showed an oblique-reverse motion (Fig. 4.25). However, the uncertainty in the polarity picks for this event are too large to give a reliable focal mechanism.

4.7 Summary

86 M_L <3 local seismic events have been located in West Antarctica from 2015-2018. In an attempt to distinguish between seismicity relating to processes in the ice-sheet and in the crust I have categorised events, resulting in 32 'likely tectonic' events, 17 'likely ice-quakes' and 37 'possible ice-quakes'. The event classification scheme was based on the hypocentral location and visual inspection of the recorded waveforms and corresponding frequency content. The majority of events are located in the area surrounding the Amundsen Sea Embayment, a region featuring high uplift rates (*Barletta et al.*, 2018), the fast flowing Pine Island Glacier as well as possible subaerial and subglacial volcanism. Very few events are detected within the central WARS, supporting the suggestion that active rifting is no longer taking place.

Chapter 5

Cryoseismicity produced by Pine Island Glacier

5.1 Introduction

Whilst differentiating tectonic seismicity from local sources in Chapter 4 it became apparent that recordings of cryoseismicity from the UKANET sensors could provide additional information on the dynamic processes of the rapidly changing West Antarctic Ice Sheet. In this chapter I focus on the UKANET stations in the vicinity of Pine Island Glacier, with the aim of investigating how the temporal patterns of recorded cryoseismicity correlate with the glacier's active processes and conditions. Prior to the deployment of UKANET the nearest long term passive seismometer was ∼250 km from Pine Island Glacier's calving front. The UKANET stations deployed closer to the glacier (∼100 km from the calving front) will therefore allow for the detection of smaller (M_L <1) cryoseismic events. Correlating the temporal patterns of automatically detected seismicity rates at these stations with changes in Pine Island Glacier's velocity may provide additional constraints on it's basal environment and flow characteristics. I also aim to investigate the cryoseismicity associated with iceberg calving and destruction of ice melánge at the glacier's calving front. Passive recording of calving seismicity could provide valuable insight into the propagation of rifts in the floating ice tongue that lead to calving (*Jeong et al.*, 2016), and the style of seismicity produced during the generation of a major iceberg (e.g. *Winberry et al.*, 2020).

Studying the processes associated with ice loss at Pine Island Glacier is of global significance, given that it is is one of the largest Antarctic contributors to global sea level rise at ∼0.12 mm/yr, and is responsible for 20% of ice lost from the West Antarctic

Station	No. of detections	Days active	Average detections per day	Distance to PIG calving front
PIGD	4949	321	15.4	96
PIG3	8672	329	26.4	105
PIG2	9360	332	28.2	115
PIG4	6759	325	20.8	130
PIG1	2149	334	6.4	150
MA01	505	364	1.4	240
MA08	315	352	0.9	274
MA03	638	357	1.8	340
MA04	323	343	0.9	390
MA07	450	347	1.3	400
KEAL	629	328	1.9	430
MA05	372	343	1.1	450
MA10	331	359	0.9	450
MA06	374	347	1.1	500
MA09	366	363	1.0	560
FOWL	732	303	2.4	610

Table 5.1: Automatic single station detection statistics for broadband stations active in 2016

Ice Sheet (*Rignot et al.*, 2008, *Wingham et al.*, 2009, *Rignot et al.*, 2011, *Medley et al.*, 2014). At the glacier's grounding line the rate of ice thinning has been accelerating since the 1980s, and ice velocity increased by 34 % from 1996 to 2006 (*Rignot et al.*, 2008, 2011). In recent years Pine Island Glacier has seen a dramatic retreat of tens of kilometers in both the calving front and grounding line (*Park et al.*, 2013, *Favier et al.*, 2014). When looking at the day long records of seismicity at UKANET Pine Island Glacier stations, it is apparent that numerous small events are present throughout the dataset (Fig. 4.4). Given the proximity of these stations to Pine Island Glacier, it is likely that many of these small events, often recorded at only one station, are produced via glacial processes. In addition to providing insight into Pine Island Glacier's ice dynamics, improving our understanding of the distribution and styles of seismicity produced by the glacier can improve the ability to discriminate between ice-quakes and any tectonic seismicity present in the region.

5.2 Rates of seismicity recorded at Pine Island Glacier

To investigate the overall rates of seismicity recorded at UKANET stations close to Pine Island Glacier I used an STA/LTA automatic detection algorithm. As noted in Chapter 4, running a network coincidence search in the 2-15 Hz band using UKANET stations close to Pine Island Glacier (PIG1, PIG2, PIG3, PIG4, PIGD) led to a significant number of detections. It is likely that the majority of these detections are produced by active processes related to Pine Island Glacier, as stations located far

from the glacier do not display similar events (Fig. 4.4). To test if the stations closest to Pine Island Glacier do feature the highest rate of seismicity in this frequency band I ran an STA/LTA detection at all UKANET and POLENET Mini Array stations active in 2016. I used the same STA/LTA parameters as in the network coincidence search in Chapter 4, an STA window of 1 s, LTA window of 60 s, and detection threshold of 25/1. The number of detections at each station are summarised in Table 5.1 and Fig. 5.1, with stations closest to Pine Island Glacier featuring significantly more detections than distal stations.

Stations FOWL, PIG1 and PIG3 were active through both UKANET seasons, from 2016-2018 and as such at these stations I ran the STA/LTA search for their full duration (Fig. 5.2). Between 2016 and 2018 there were 1439 detections at FOWL, 4019 at PIG1 and 17063 at PIG3. FOWL and PIG1 record a fairly constant, low level of seismicity over their duration, although there is a spike in the number of events detected at PIG1 in January 2017. Given that this spike is in the days following the station redeployment, it is likely that these events may have been caused by activity from the field party.

PIG3 shows the highest rates of detected seismicity, which fluctuates over the two year deployment (Fig. 5.2), peaking in the Austral autumn in both years. Fig. 5.3 shows the temporal distribution of detected seismicity at PIG3 plotted against both the average ice velocity of Pine Island Glacier (*Hogg et al.*, 2015) (b) and average monthly temperature at McMurdo (c). The average ice velocity was extracted along a flow-perpendicular profile close to the grounding line, derived from ice velocity estimates using Sentinel-1b data (*Hogg et al.*, 2015). The peak in event detections in 2016 corresponds closely to a period of acceleration in the modelled ice velocity data, following a $\sim$10 % reduction in the glacier's velocity over a $\sim$two week period (Fig. 5.3). A similar reduction in modelled ice velocity corresponding with an increase in event detections occurs in late April 2017, however this reduction is based on only one averaged profile. The event detections also show a pattern roughly anti-correlated with the trends in average monthly temperature, with peak seismicity occurring as temperatures fall in the Austral autumn (Fig. 5.3). The average monthly temperature profile in Fig. 5.3 is from McMurdo, which is $\sim$2000 km away from Pine Island Glacier, but is at a roughly similar latitude and elevation, and as such the overall trends in monthly temperature ought to be similar. There is a gradual buildup in the number of event detections over the two month period prior to the B-44 calving event, which is indicated by the dashed red line in Fig. 5.3b. In the month following the calving of B-44 there is an acceleration in the modelled ice velocity at the grounding line, which also corresponds with an increase in detected events (Fig. 5.3).

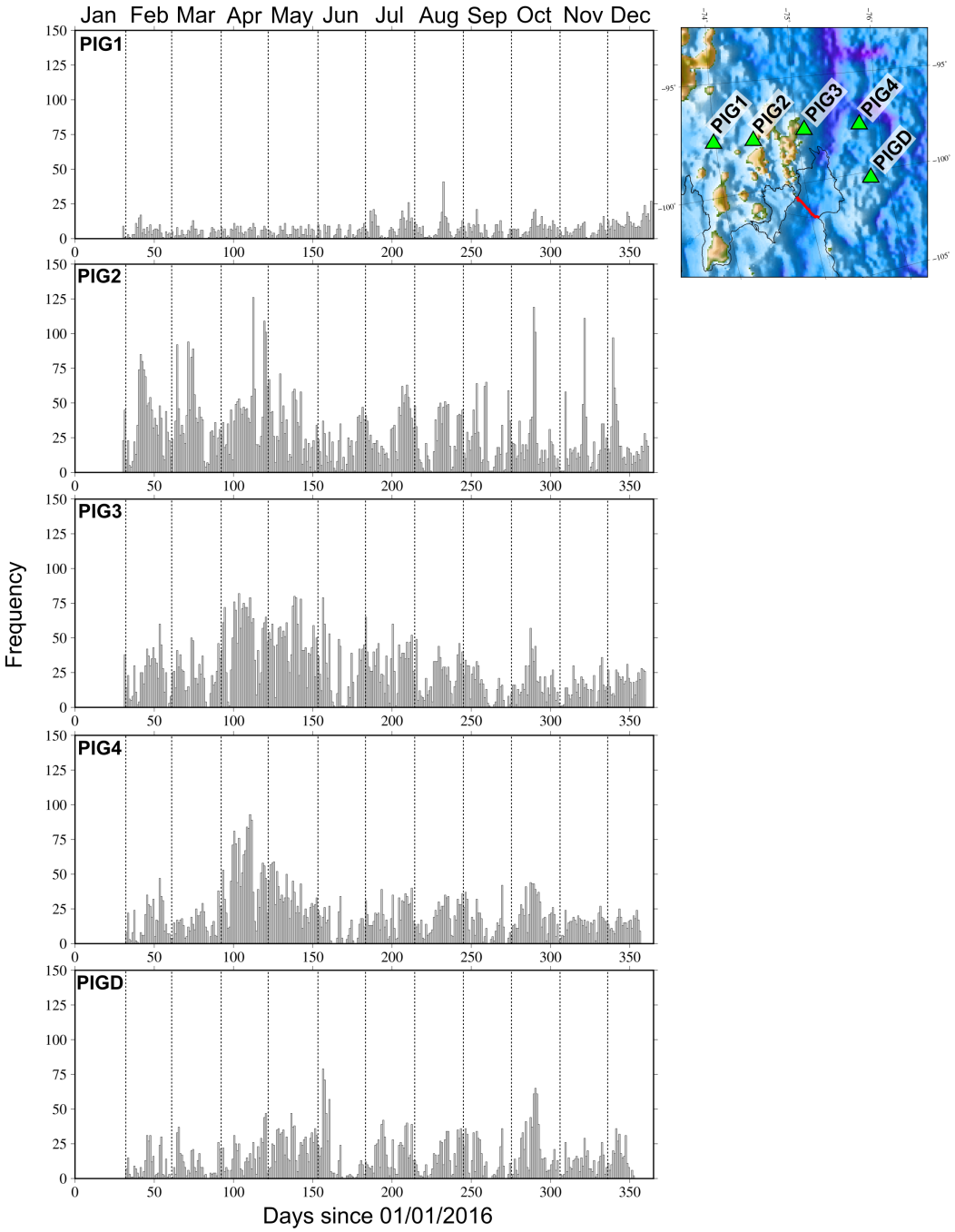

Figure 5.1: Histograms showing the number of events detected per day using the STA/LTA algorithm at each of the UKANET PIG stations in 2016. The Pine Island Glacier calving front is shown in the inset map in red.

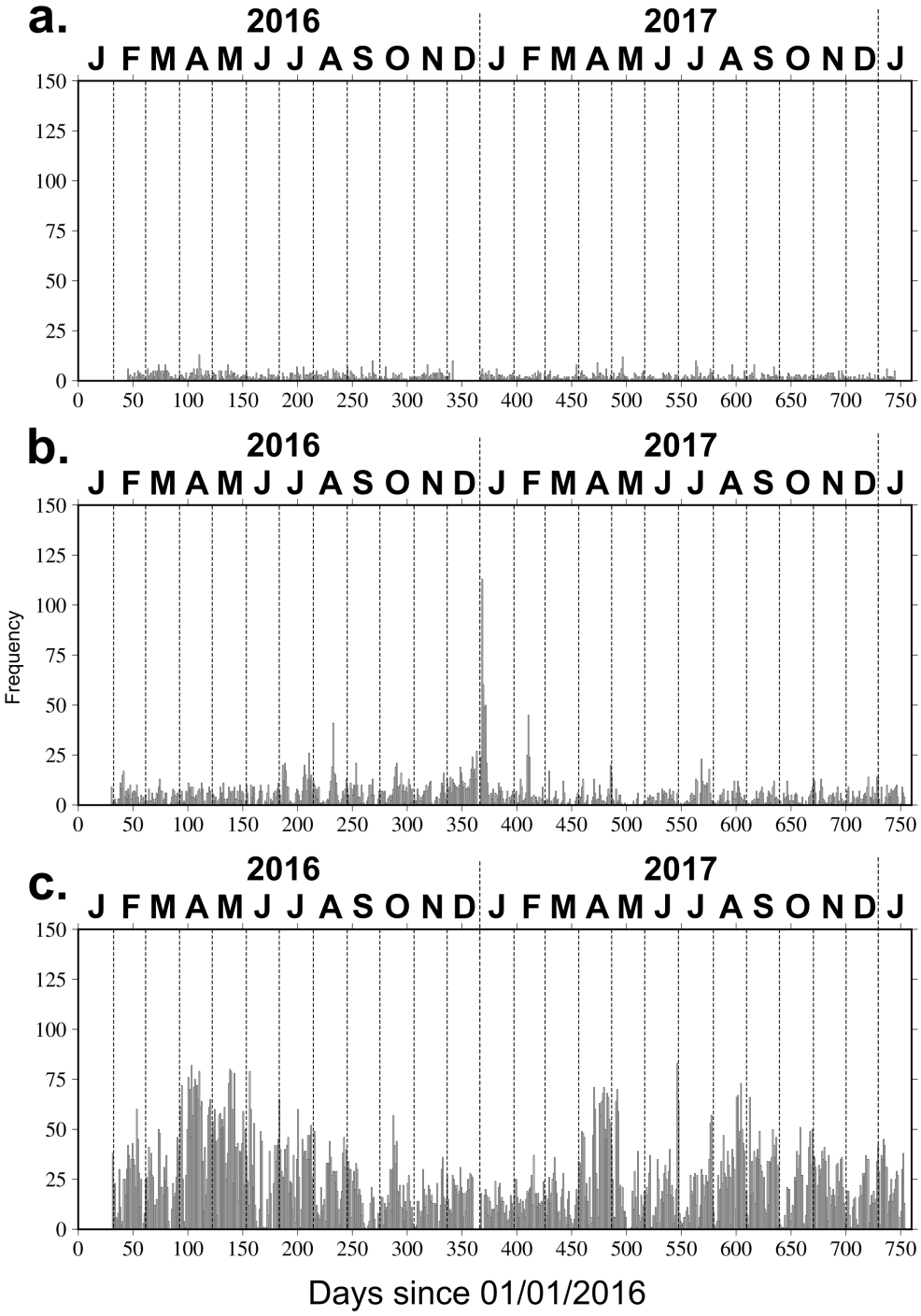

Figure 5.2: Histograms showing the number of events detected per day using the STA/LTA algorithm at (a) FOWL, (b) PIG1 and (c) PIG3 from 2016-2018.

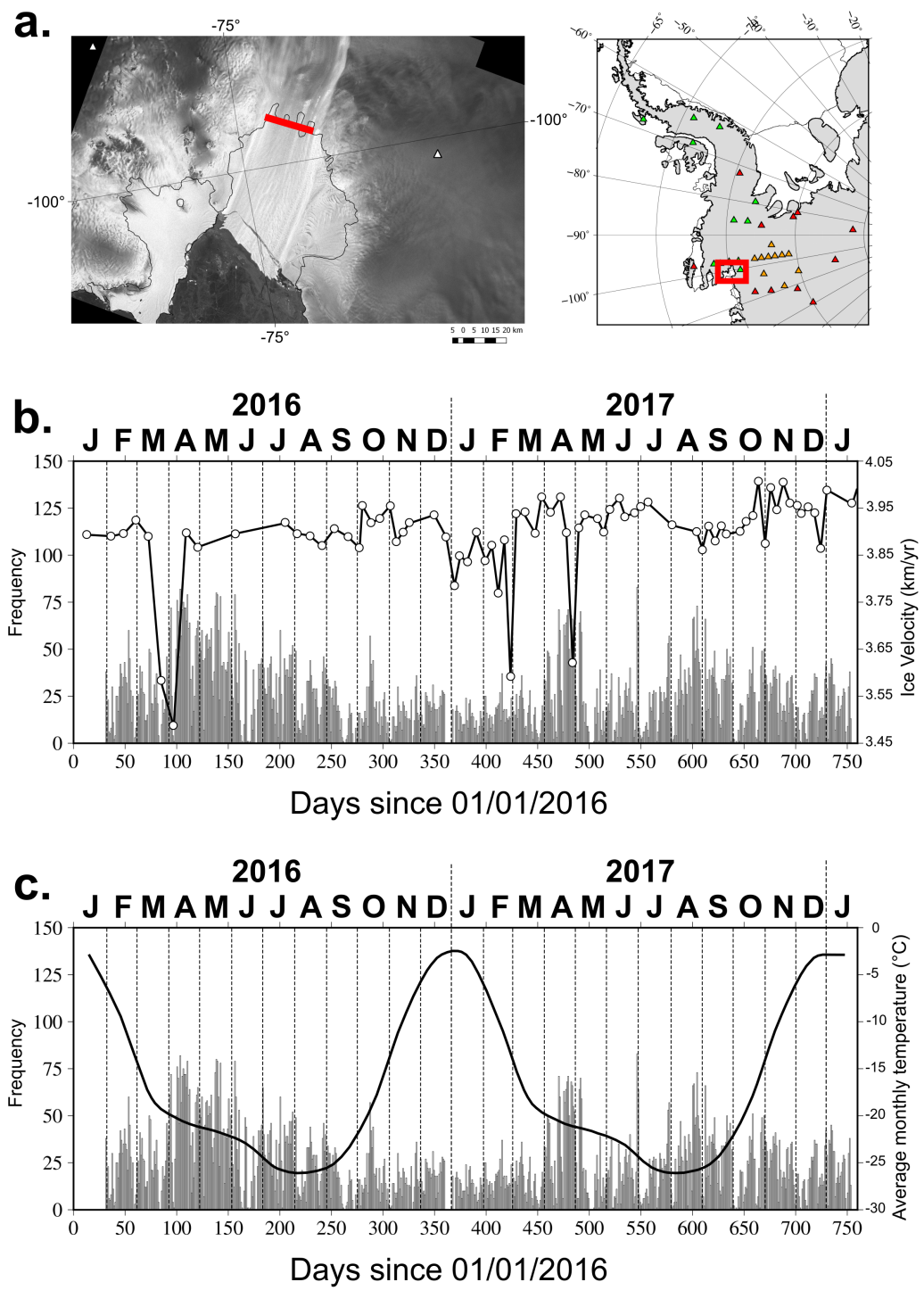

Figure 5.3: Histograms showing the number of events detected per day using the STA/LTA algorithm at PIG3 from 2016-2018 plotted alongside the average ice velocity at the grounding line (*Hogg et al.*, 2015) (b) and average monthly temperature at McMurdo. The profile along which the average grounding line velocity was determined is shown in red line in (a).

5.3 Seismicity produced at the calving front

One major calving event occurred on Pine Island Glacier during the UKANET deployment, producing an iceberg with an area of 54 square nautical miles designated B-44 (Fig. 5.4). Calving events have the capacity to produce a range of styles of seismicity depending on the source-to-station distance. Long period (30 - 150 s) surface waves with moment magnitudes of M_w ~5 can be detected thousands of km away (*Ekström et al.*, 2003), whilst complex high frequency (>1 Hz) signals can be detected at source-to-station distances of tens to hundreds of km (e.g. *Köhler et al.*, 2015, *Winberry et al.*, 2020). The B-44 iceberg was first imaged by Sentinel-1 satellite data on the 23rd of September 2017 and reported by the U.S. National Ice Center, though the preceding Sentinel-1 pass was on the 18th of September 2017. As such, the calving event could have occurred at any time in this six day interval. Calving of the B-44 iceberg was the preceded by the propagation of major fracture in the centre of the floating ice shelf, which first appeared on Sentinel-1 imagery in December 2015.

5.3.1 Repetitive seismicity detected at PIG2

Given PIG2 detected the highest local seismicity rates (Fig. 5.1), with a slightly different temporal distribution of events, I decided to have a closer look at the events detected at this station. Whilst inspecting the day long 2-15 Hz band-pass filtered vertical components in Chapter 4, I additionally noted a number of highly similar waveforms appearing at PIG2 throughout the station's deployment (Fig. 5.5). To investigate if these events are responsible for the slightly varied temporal pattern in events detected at PIG2 relative to neighbouring stations, I utilised a cross correlation detection algorithm. The cross correlation detector required a template event, which would then be cross correlated with the entire seismic record at PIG2. A detection was noted when the cross correlation exceeded a pre-defined similarity threshold. Fig. 5.6 shows an example of the events flagged by the cross correlation detector on a 2-15 Hz bandpass filtered vertical component dayplot from PIG4. The event labelled T was selected as the template, and 7 other similar events were flagged by the cross correlation detector for this day, each with a similarity value of >0.7 (1.0 is an exact match).

The choice of template event will introduce a bias into the number of events detected by the cross correlation technique, as evolution in the source conditions will alter the style of waveform produced through time, assuming that all repetitive events are produced by the same mechanism. I tested four different template events selected throughout 2016, and used a similarity threshold of 50 % for all runs (Fig. 5.7). The 13/03/2016 and 21/04/2016 templates produced 1527 and 929 detections respectively

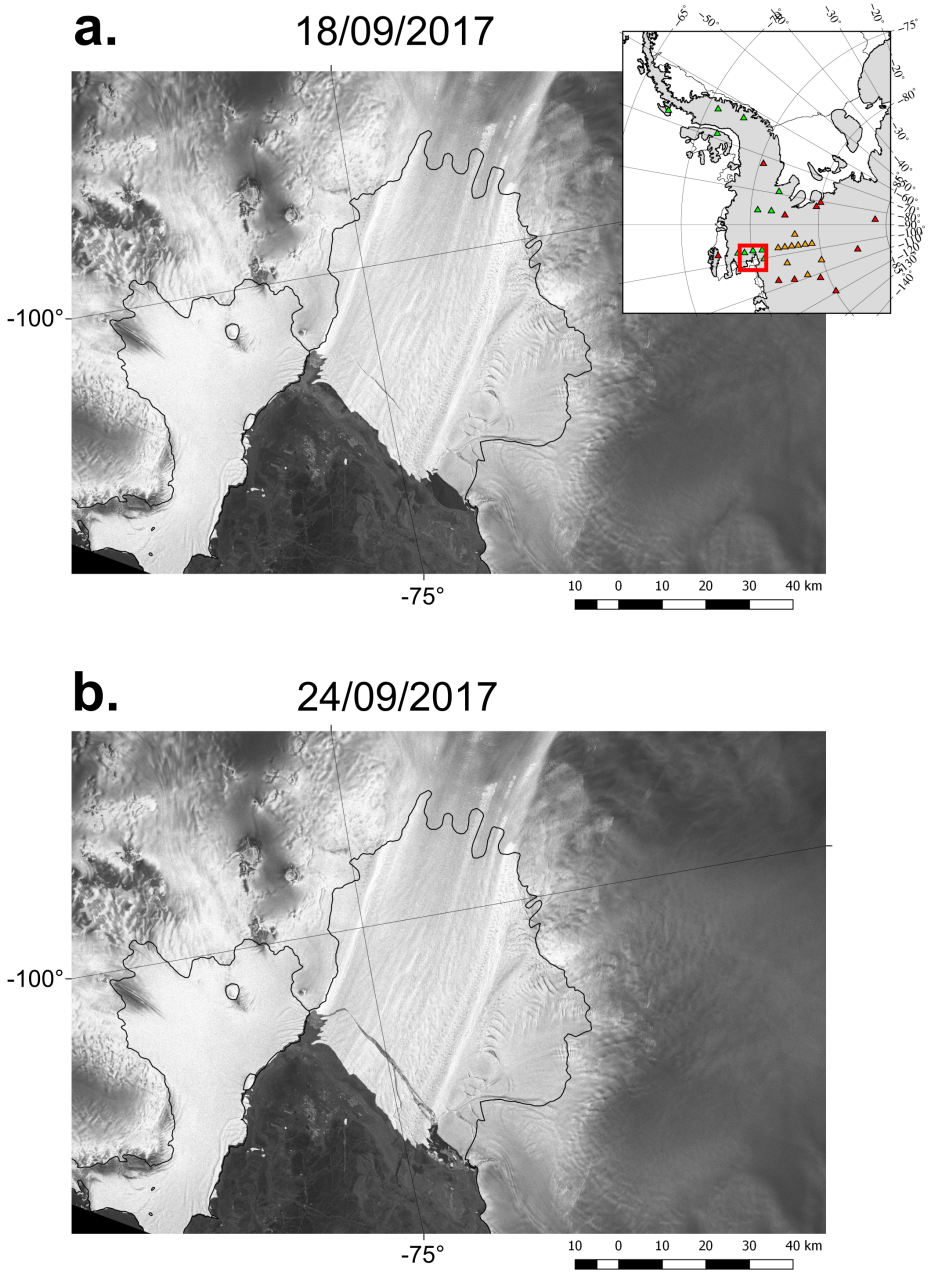

Figure 5.4: Sentinel 1 Sythentic Aperture Radar imagery of Pine Island Glacier from (a) 18/09/2017 and (b) 24/09/2017, showing the calving of the B-44 iceberg.

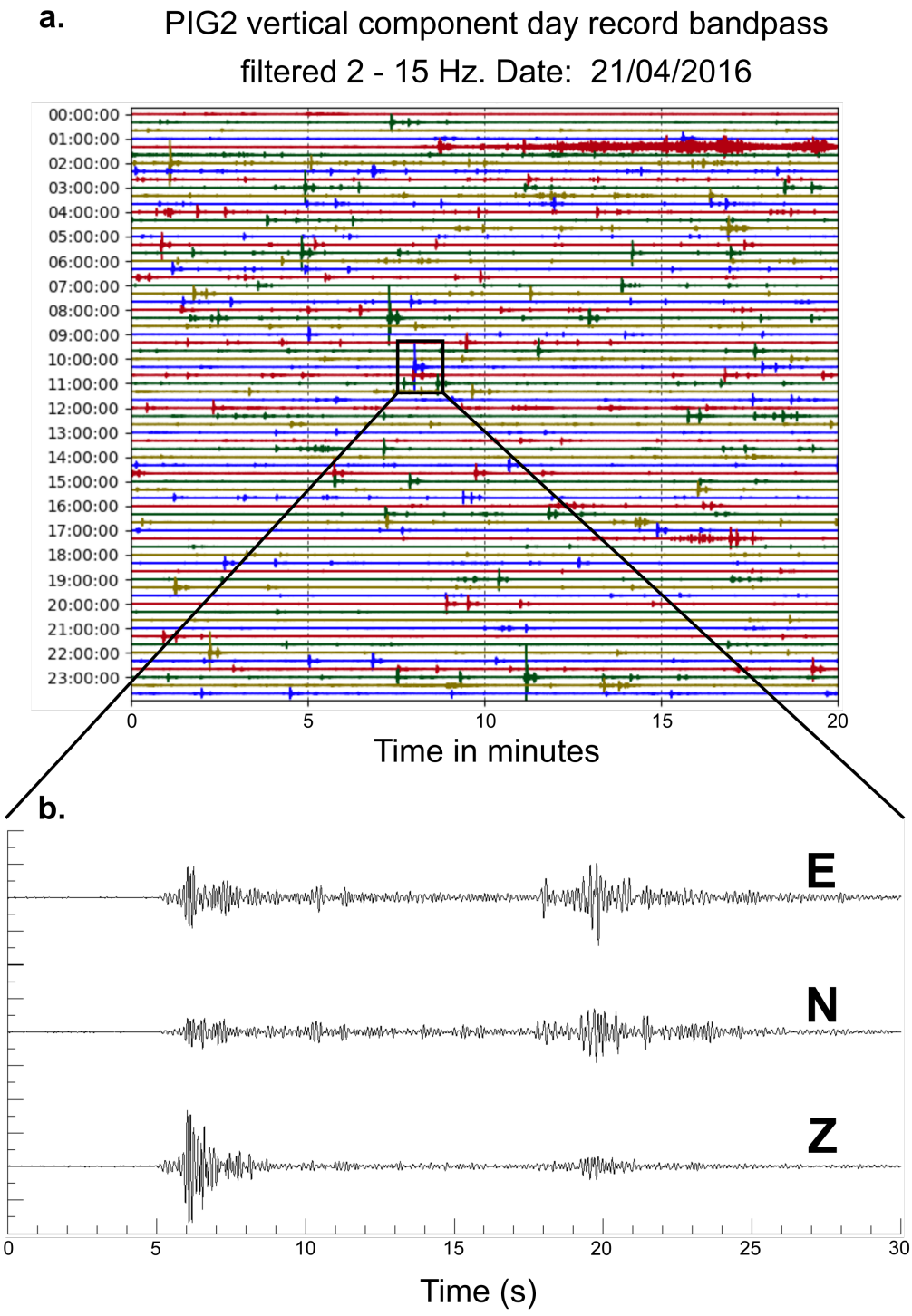

Figure 5.5: (a) A dayplot of the seismicity recorded on the vertical component of PIG2 bandpass filtered from 2-15 Hz, showing multiple highly similar small events occurring throughout the day. (b) The east, north and vertical component seismograms from one of the repetitve events, filtered from 2-15 Hz. The event is shown in the black box in panel (a) in blue.

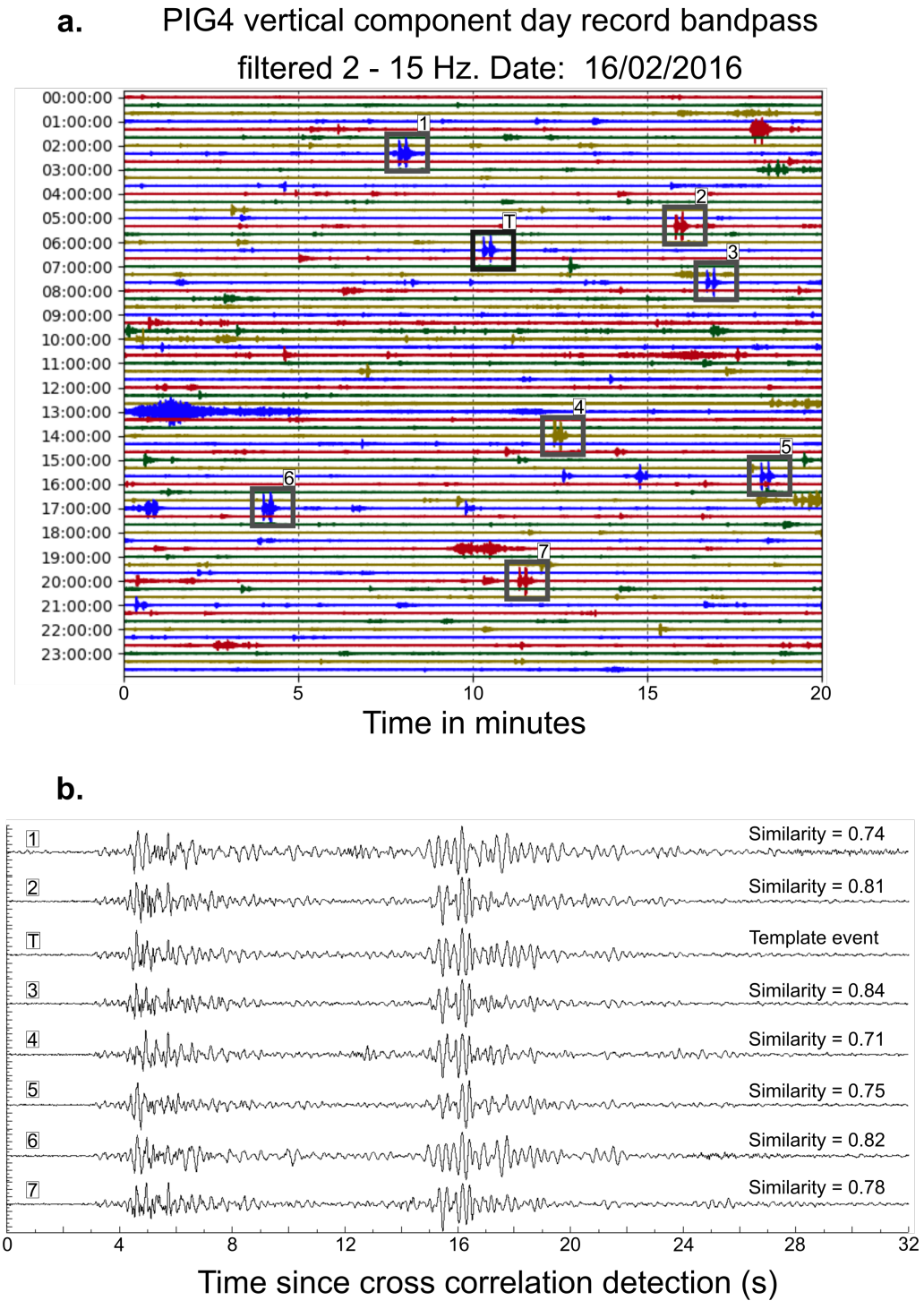

Figure 5.6: (a) A dayplot of the seismicity recorded on the vertical component of PIG4 bandpass filtered from 2-15 Hz, showing multiple highly similar events which have been identified using the cross correlation detector. Events flagged by the cross correlation detector are shown in a black box and numbered, with the template event labelled T, the corresponding waveforms are shown in panel b. On panel b. the similarity produced by the cross correlation detector is also shown for each event.

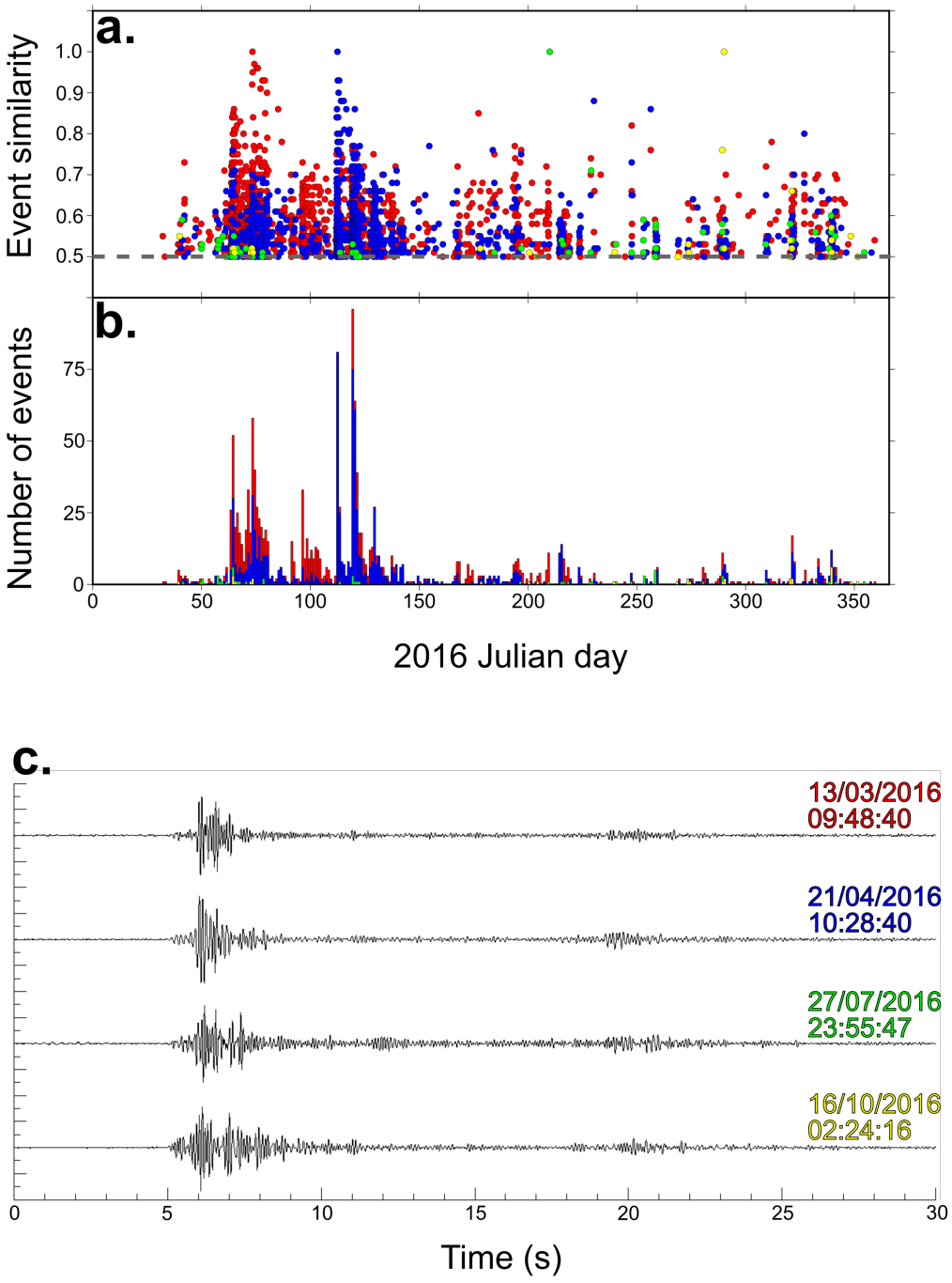

Figure 5.7: The temporal distribution of events detected at PIG2 using the cross correlation detector. Four template events were used which are shown in panel (c): 13/03/2016 09:48:40 in red, 21/04/2016 10:28:40 in blue, 27/07/2016 23:55:47 in green, and 16/10/2016 02:24:16 in yellow. (a) Each event detected using the cross correlation detector plotted in terms of its similarity to the template, coloured by the template event used. (b) A histogram of all events detected using each of the four templates, binned by day and coloured by template.

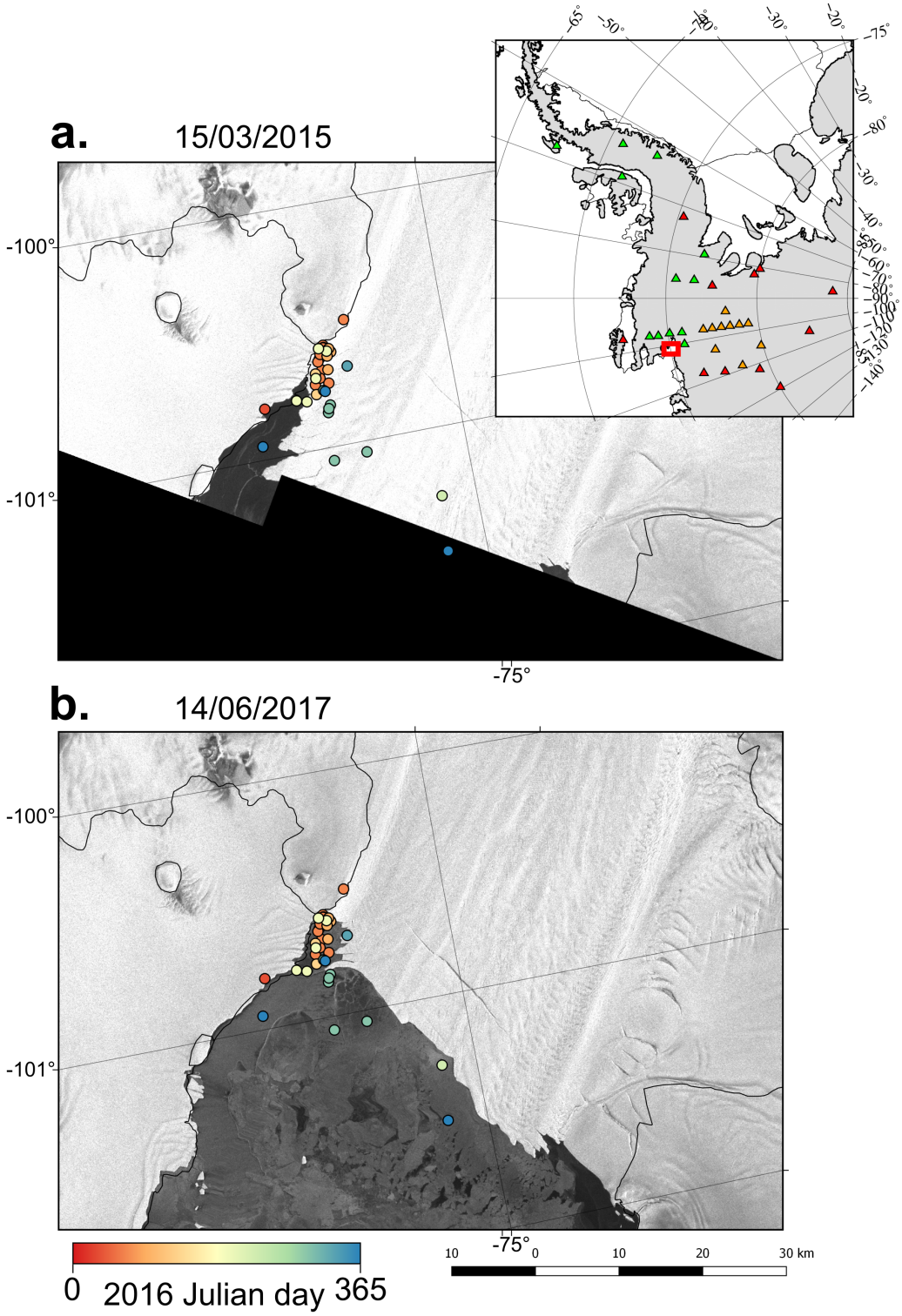

Figure 5.8: Sentinel 1 imagery of the Pine Island Glacier calving front on (a) 15/03/2015 and (b) 14/06/2017, with events detected using the cross correlation detector and located in Hypoinverse plotted. The shear margin in which most of the similar seismicity is located has experienced a dramatic retreat between the two Sentinel images. No Sentinel data was available for the region between the two dates shown.

(Fig. 5.7), both predominantly clustered from February to May 2016. The 27/07/2016 and 16/10/2016 templates produced 62 and 31 detections respectively (Fig. 5.7), however these events do not reproduce large clusters of detections around the template date. This suggests that most of the seismicity of this type occurred in the early portion of 2016, as the template events later in the year do not show significant rates of detection close to the respective template date.

Events produced by the cross correlation detection algorithm were visually inspected, and P- and S- wave phases were manually picked where possible. Given that many of these events were barely resolvable at stations other than PIG2, which generally showed a highly impulsive P-wave arrival, only 34 events were picked (Table C.1). These events were then located using the same station dependent velocity model in Hypoinverse as in Chapter 4, revealing that the majority of events were clustered along the northern shear margin/melánge of Pine Island Glacier at the calving front (Fig. 5.8). Fig. 5.8 shows the location of the 34 events coloured by 2016 Julian day, which shows that the majority of locatable events occurred in the early portion of 2016 (February to May), and were clustered along a section of the glacier's melánge which experienced a dramatic retreat between 2015 and 2017 (e.g. *Jeong et al.*, 2016). The event depths produced by Hypoinverse are all <10 km, which combined with the associated vertical error and hypocentral location close to the shear margin suggests that these events were produced by the glacier. No satellite imagery is available for the northern shear margin at the calving front of Pine Island Glacier in 2016, however given the calving front's dramatic retreat and previously highly complex melánge, it is possible that these events were produced as the shear margin was destroyed (Fig. 5.8).

5.3.2 Seismicity produced by the B-44 calving event

To investigate whether the seismicity produced by the calving of the B-44 iceberg was recorded by the active UKANET stations close to Pine Island Glacier, I looked at the continuous data recorded during the interval between the 18/09/2017 and 23/09/2017 Sentinel 1b passes (Fig. 5.9). Fig. 5.9 shows the vertical component of PIG3 band-pass filtered from 1-5 Hz, split into day long segments from 17/09/2017 to 26/09/2017, revealing a ∼8 hour long episode of high frequency seismicity on the 22nd of September. *Winberry et al.* (2020) observed a very similar signal in the 1-5 Hz band at station DNTW during a calving event at Thwaites Glacier ∼125 km from the station, which was well constrained by Landsat 8 and Sentinel 2 optical imagery. The sustained high frequency tremor on the 22nd of September 2017 was recorded at stations DNTW, ELSW, MA01, PIG1, PIG3, THUR and UPTW distributed ∼100 to 450 km away from the calving front (Fig. 5.10), and was likely produced by the calving

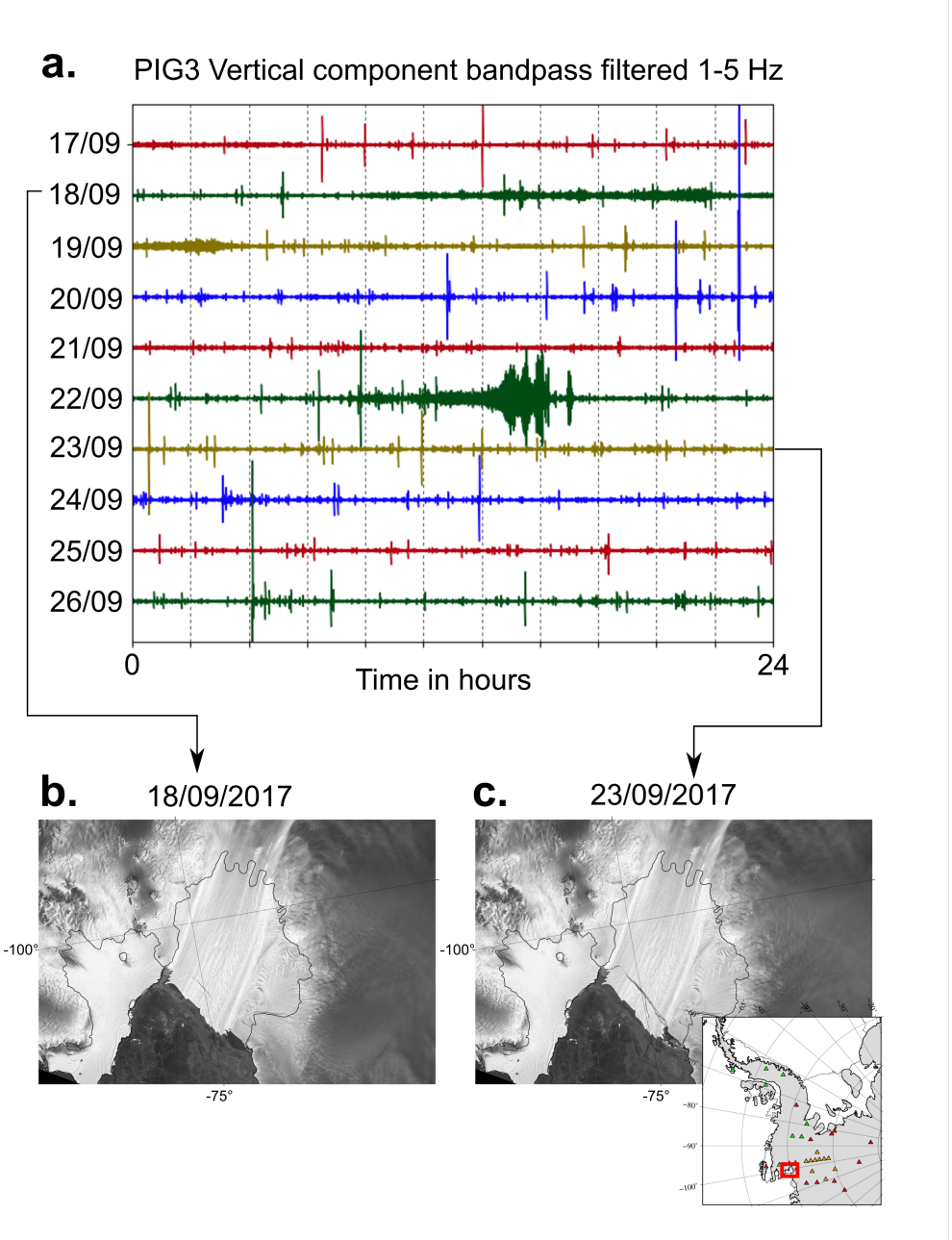

Figure 5.9: (a) Vertical component from PIG3 band-pass filtered from 1-5 Hz for the days surrounding the B-44 calving event. Sustained high frequency tremor is present on the 22/09/2017, consistent with that observed by *Winberry et al.* (2020) at Thwaites Glacier, and between the Sentinel 1 passes on 18/09/2017 (b) and 23/09/2017 (c).

of the B-44 iceberg.

The initial 1-2 hours of high frequency seismicity prior to the main calving event features a gradual build up of high frequency noise (Fig. 5.10). This build up in noise is then followed by a ∼1 hour long period featuring a pulsing signal. In-between each pulse the noise level drops near to the pre-event level, with a ∼6 minute interval between the peak of each pulse (Fig. 5.10). The pulsing signal is then lost as the main section of high frequency seismicity occurs, lasting for ∼3 hours, similar to the calving seismicity observed at Thwaites Glacier by *Winberry et al.* (2020).

The *Winberry et al.* (2020) study of seismicity associated with a Thwaites calving event provides the most appropriate comparison for the calving seismicity recorded in this study, given the location and similarly sparse station distribution. Whilst the overall style and duration of the high frequency seismicity produced by the B-44 calving event is similar to that shown in *Winberry et al.* (2020), there are also some notable differences. *Winberry et al.* (2020) do not observe a high frequency pulsing signal prior to the main calving event, which suggests a possible difference in the inital mechanisms of iceberg calving between the two glaciers. *Winberry et al.* (2020) also detect two (M_s ∼3) long period (10-30 s) seismic events, in addition to the high frequency seismicity. The authors suggest that these events could have been produced due to the generation of small tabular icebergs as part of the calving event, or be due to the capsizing of icebergs. To check if similar long period events are present during the B-44 calving, I band-pass filtered the vertical component data from 10-50 s at all stations which recorded the high frequency seismicity. No long period events were present in the days surrounding the B-44 event. The absence of long period seismicity produced during the B-44 calving is therefore supports the hypothesis that it was produced by capsizing icebergs at Thwaites, given the massive upright B-44 iceberg (Fig. 5.9), versus the complex production of smaller blocks by Thwaites Glacier (*Winberry et al.*, 2020).

Following the calving event on the 22nd of September 2017, there were subsequent Sentinel 1 passes on the 30th of September and 6th of October (Fig. 5.11). In between the 23/09/2017 and 30/09/2017 Sentinel images the B-44 iceberg is fairly stationary, however between 30/09/2017 and 06/10/2017 the iceberg moves ∼5 km to the south. The 06/10/2017 also shows that in addition to moving ∼5 km, the B-44 iceberg was again in contact with Pine Island Glacier. Fig. 5.11 shows the vertical component from PIG3 band-pass filtered from 1-5 Hz in day-long traces for the days surrounding the 30/09/2017 and 06/10/2017 Sentinel 1 images. There is a ∼30 hour long period of sustained high frequency tremor, with a dominant frequency of ∼1 Hz recorded from

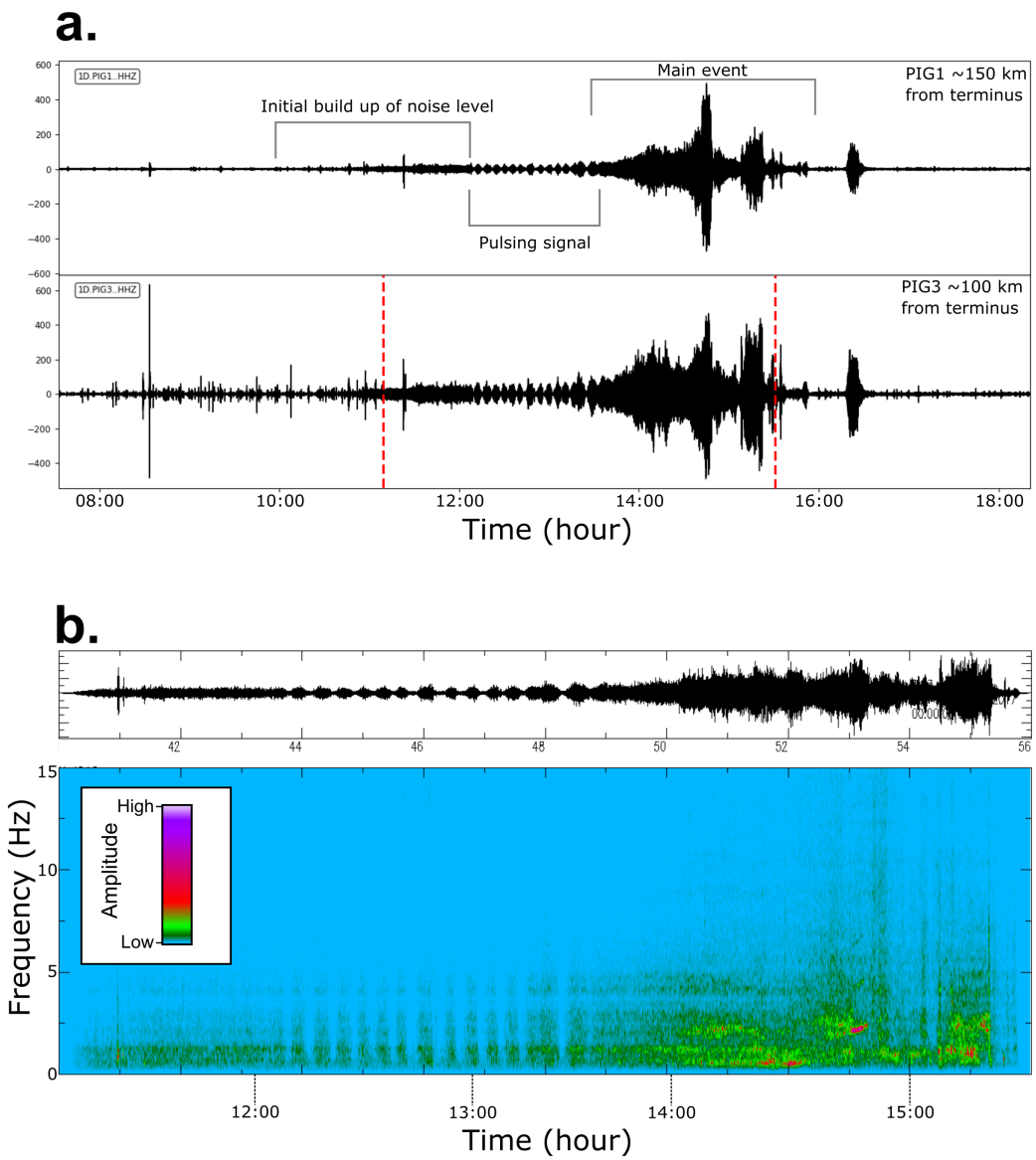

Figure 5.10: (a) Vertical component seismograms band-pass filtered from 1-5 Hz from PIG1 (top) and PIG3 (bottom) over a ~10 hour interval surrounding the likely B-44 calving event. (b) A spectrogram of the main section of the high frequency tremor event at PIG3 with a 0.5 Hz high-pass filter applied, showing the drop off in background noise inbetween the pulsing signal prior to the main calving event. Possible spectral gliding lines are also visible at 14:45. The start and end of the trace in (b) are marked by the red dashed lines in panel (a).

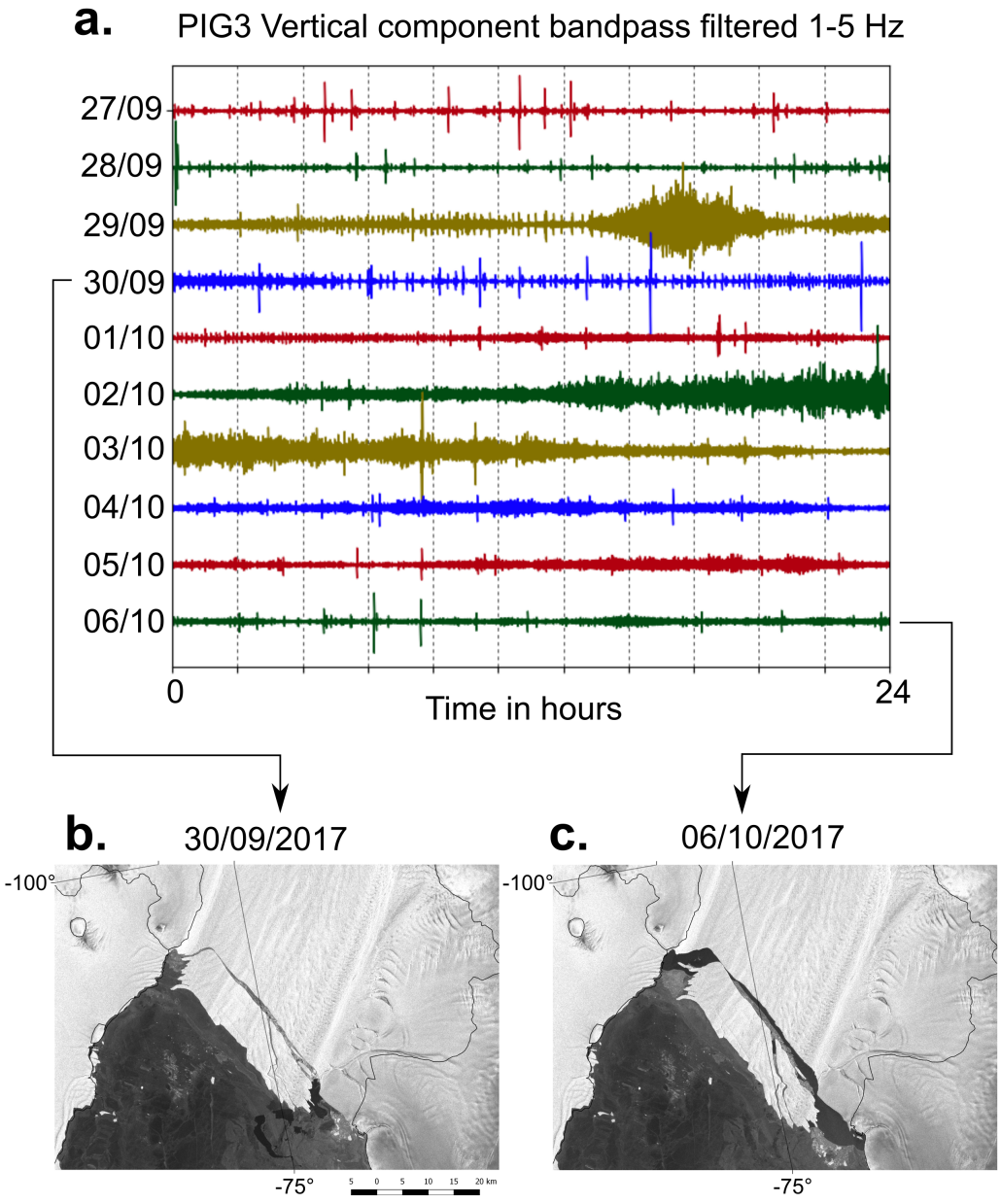

Figure 5.11: (a) Vertical component from PIG3 band-pass filtered from 1-5 Hz for the days surrounding 30/09/2017 (b) and 06/10/2017 (c) Sentinel 1 images. Sustained tremor with a peak frequency of 1 Hz is present from 02/10/2017-03/10/2017, roughly coinciding with a ∼5 km southerly movement of the B-44 iceberg.

the 2nd to the 3rd of October (Fig. 5.11). This sustained tremor may correspond to the B-44 iceberg scraping against the floating ice of Pine Island Glacier, as it drifted to the south.

5.4 Discussion

The rates of automatically detected seismicity at PIG3 over a two year period can be used to infer more detail on Pine Island Glacier's ice dynamics. The increased number of events detected during periods of relatively slow ice flow at the grounding line could be indicative of some basal stick slip seismicity occurring (Fig. 5.2). The Whillans Ice Stream in the Ross Sea sector of the WARS displays a characteristic stick slip behaviour with associated seismicity, and as such has been the subject of focused study (e.g. *Bindschadler et al.*, 2003, *Wiens et al.*, 2008). The Whillans Ice Stream flows at $\sim$300 m a^{-1} from the Transantarctic Mountains into the Ross Ice Shelf over a region with minimal surface topography. The ice stream flows in short 20-30 minute bursts in which total displacements of 0.2 - 0.5 m can occur within 1 minute (*Bindschadler et al.*, 2003), producing associated seismicity (*Wiens et al.*, 2008). Slip events are usually followed by 6 - 25 hour periods of dormancy. A particularly interesting feature of the stick-slip seismicity from the Whillans Ice Stream is that it matches the temporal cadence of the Ross Ice Shelf ocean tides (*Bindschadler et al.*, 2003). In addition there is a positive correlation between the magnitude of a slip event and the length of the preceding quiescent interval (*Winberry et al.*, 2009). No obvious tidal signal is present in the automatically detected seismicity from 2016-2018, and in addition the satellite based estimates of ice velocity have a relatively long interval between passes. As such it is difficult to make definitive interpretations on the relationship between the tides, ice velocity and seismicity produced given the instrumentation currently available around the glacier. This would be possible if denser seismic and GPS networks were deployed on/close to the glacier, however the seismicity rates recorded by UKANET stations do show some relationship with the ice velocity and temperature (Fig. 5.3).

Without additional seismic stations closer to the glacier it is very difficult to infer whether the majority of the seismicity produced by Pine Island Glacier was produced by basal, internal, or surface ice processes. Despite this, the higher rates of seismicity recorded at PIG2 and PIG3, which are situated closer to the northern shear margin versus PIG4 and PIGD - situated closer to the southern shear margin (Fig. 5.1, suggests that there may be a variable level of seismicity produced by either side of the glacier. Were the majority of the detected seismicity produced by basal processes, then I would expect that the seismicity rates to be similar at all UKANET PIG stations. Ice sheet modelling has suggested that Pine Island Glacier features a weak bed, given the

departure in the patterns of driving stress along the glacier with regards to a typical ice profile (*Joughin et al.*, 2003). The glacier's weak bed is likely due to the potentially widespread presence of subglacial sediment (e.g. *Brisbourne et al.*, 2017), and the receiver function models I show in Chapter 3 (Fig. 3.9) suggest that there is potential for thick subglacial sediment accumulation near the glaciers main tributaries. A weak bed and generally high glacial driving stress (e.g. *Joughin et al.*, 2003) would suggest that it is unlikely for stick slip basal seismicity to occur at a detectable level given the hypocentral distances in this study.

If much of the detected seismicity was produced by the growth of surface crevasses, a slightly different temporal pattern of seismicity than that shown in Figs.5.1 and 5.2 may be expected. Crevassing occurs when strain rates exceed a depth-dependent fracture criterion, usually growing near the surface as there is little pressure provided from the ice overburden (e.g. *Colgan et al.*, 2016). It is possible that much of the seismicity I have detected which originates from the floating section of the glacier could have been produced by a combination of basal and surface crevassing, such as that observed by *Vaughan et al.* (2012). *Vaughan et al.* (2012) used ice penetrating radar and acoustic data to image a network of sinuous subglacial channels at the base of the floating ice, the location of which have in turn determined which regions feature the highest concentration of surface crevasses.

The majority of the detected cryoseismicity described in this chapter is likely produced by deformation along Pine Island Glacier's extensive shear margins and ice melánge (Fig. 5.8). Disintegration of the northern ice melánge was proposed to be closely linked to the calving of a major iceberg at Pine Island Glacier in 2015 (*Jeong et al.*, 2016), and it is likely that further disintegration accelerated the calving of the B-44 iceberg in 2017. In both the 2015 and 2017 calving events at Pine Island Glacier, a substantial flow transverse rift was produced in the centre of the glacier, close to the grounding line, months before the actual calving occurred. It has been suggested that the 2015 rift was initiated by basal crevassing at the grounding line (*Jeong et al.*, 2016), and remained relatively stationary until ice detachment occurred from the damaged northern margin, driving the rift to rapidly propagate across the glacier. Given the similar nature of the flow transverse rift produced in the months prior to the B-44 calving, and the further destruction of the northen melánge, which produced much of the seismicity recorded in this study (Figs. 5.1, 5.5 and 5.8), it is likely that the overall mechanisms for the 2015 and 2017 calving events were similar. Additionally *Arndt et al.* (2018) suggest that interaction between the ice shelf and baythmetric ridges close to the northern melánge may have been responsible for rift propagation leading to calving

events in 2015 and 2017. It is therefore additionally possible that much of the repetitive seismicity I observe in this region (Figs. 5.5, 5.8) was produced by the floating ice colliding with these submarine highs.

In the Sentinel 1 image on 18/09/2017, the rift that led to calving of the B-44 iceberg was ∼20 km long; between 18/09/2017 and 23/09/2017 it therefore propagated ∼15 km. Fig. 5.9 shows a very low level of high frequency tremor on 18/09/2017-19/09/2017 which could be related to rift propagation, however the overall levels of seismicity prior to 22/09/2017 are fairly low. It is therefore possible that much of the 15 km of rupture along the rift either occurred aseismically, or during the ∼10 hours of high frequency tremor recorded on 22/09/2017 (Fig. 5.10). An interesting feature of the seismicity recorded at PIG3 which corresponds with the B-44 calving is the pulsing signal prior to the main calving event. Given that the large tabular nature of the B-44 iceberg, it is likely that the flow transverse rift grew rapidly due to longitudinal extension (e.g. *Benn and Åström*, 2018). The pulsing signal therefore may relate to the oscillation of seawater within the propagating basal rift. Within the main calving seismicity there is also some evidence for gliding spectral lines (Fig. 5.10). Gliding spectral lines of this type have been observed as icebergs scrape against the ocean floor (*Dziak et al.*, 2013), or against each other (*MacAyeal et al.*, 2008). The high frequency seismicity observed on 02/10/2017-03/10/2017 which corresponds with a ∼5 km movement of the B-44 iceberg does not show any evidence of gliding spectral lines. Given that spectral lines produced by iceberg scraping can correlate with the speed of the moving iceberg (*MacAyeal et al.*, 2008), and the signal shown in Fig. 5.11 displays a constant ∼1 Hz tremor, this may indicate that the iceberg was scraping against Pine Island Glacier at a roughly constant speed of ∼0.2 km/hour. Further investigation of the mechanisms that led to calving of the B-44 iceberg could use waveform modelling, particularly on the pulsing signal that preceded the main calving event. The timing, duration, frequency content and periodicity of the pulsing signal could reveal more about how the large rift in the ice shelf grew in the hours prior to calving. I have suggested that this signal is likely due to seawater oscillating in the large basal fracture as it grew prior to calving, which may be supported or refuted by further waveform modelling.

5.5 Summary

This chapter demonstrates how studying long term records of passive seismic data from stations in the vicinity of major ice streams can provide additional constraints on the glacial dynamics. The patterns and rates of seismicity detected at stations deployed close to Pine Island Glacier suggest that much of the seismicity is produced along the glacier's substantial shear margins and floating melánge. There is some evidence for

correlation between the rates of detected seismicity and the glacier's average velocity (Fig. 5.3), though without more frequent estimates of the flow speed it is difficult to define the exact relationship between the two features. Seismometers located at distances of up to 450 km from the glacier's calving front were able to record ∼10 hours of high frequency tremor, which was likely produced by the calving of the B-44 iceberg on 22/09/2017. All stations used in this study were at distances of >100 km from the glacier's calving front, and as such a denser, longer term seismic deployment located closer to the glacier could reveal much more information on Pine Island Glacier's ice dynamics and processes.

Chapter 6

Discussion

In this chapter I discuss the findings of my thesis with regards to three key themes in West Antarctica. The first is using the results from the joint inversion in Chapter 3 and the local 'likely tectonic' seismicity results from Chapter 4 to build a more comprehensive understanding of the bounds of the WARS, along with other geophysical studies in the region. The second theme I discuss in this chapter is the implications of my findings of crustal structure and composition for the geothermal heat flow in West Antarctica, in the context of the wider literature. The third theme I discuss is the impact of the potential Glacial Isostatic Adjustment processes occurring in West Antarctica, particularly in the rapidly changing Amundsen Sea Embayment. I finally make a recommendation for future seismic investigation in West Antarctica.

6.1 Refining the bounds of the West Antarctic Rift System

Given that the geology of the WARS is largely obscured by the overlying West Antarctic Ice Sheet, its exact bounds are difficult to define. How far the WARS progressed towards the Amundsen and Bellingshausen sea embayments is unclear, as is any possible linkage between the WARS and neighbouring Weddell Sea Rift System through Ellsworth Land (Fig. 6.1). *Dalziel and Elliot* (1982) are often referred to when discussing the bounds of the WARS, and in regions where the change in topography and crustal thickness between the WARS and neighbouring blocks is clearly pronounced, such as the HEW and Marie Byrd Land, the bounds proposed by *Dalziel and Elliot* (1982) are appropriate. Regions in which the *Dalziel and Elliot* (1982) bounds are potentially in need of updating are the more gradual transitions between the WARS and Thurston Island, and the rift system's possible termination towards Ellsworth Land

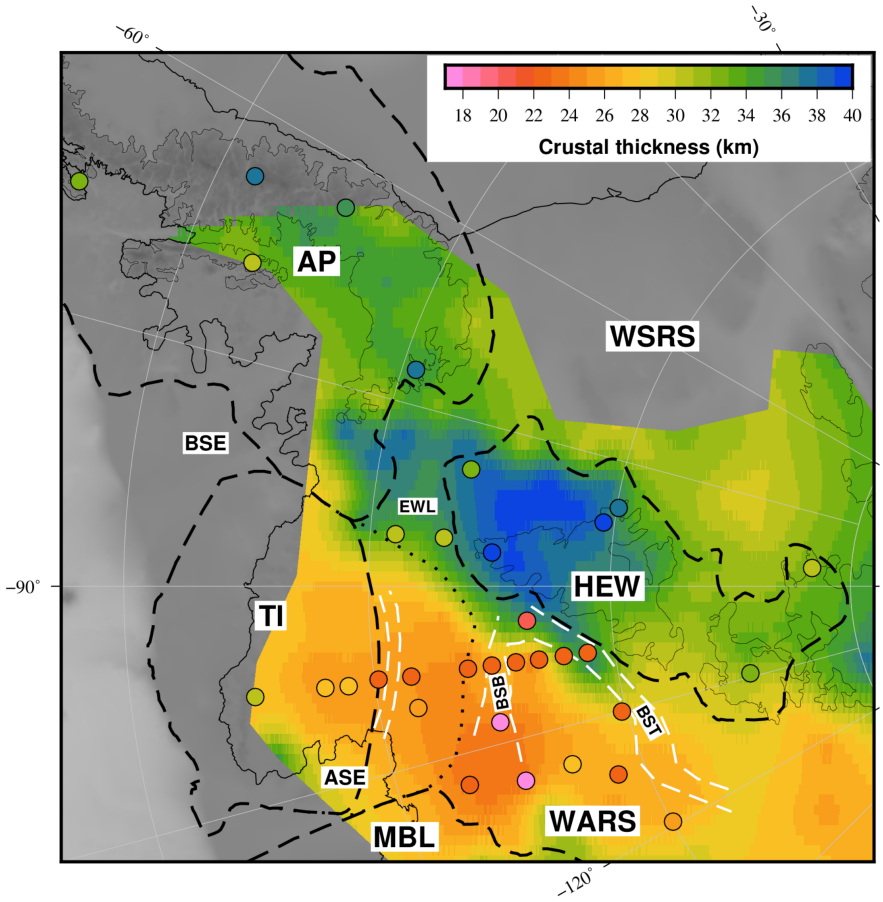

Figure 6.1: Crustal thickness estimates from this study at each station (circles) superimposed on the ambient noise derived crustal thickness map of *O'Donnell et al.* (2019a). The crustal block boundaries of *Dalziel and Elliot* (1982) are in dashed black except for the Thurston Island-WARS boundary which is dotted, here I have redrawn the Thurston Island-WARS boundary as dashes to encompass the thinner crust I have imaged at stations PIG3, PIG4 and MA01.

(Fig. 6.1).

According to the crustal block boundaries of *Dalziel and Elliot* (1982), the tectonic block in which UKANET stations ELSW and KEAL are situated is indeterminate (Fig. 6.1). This region of Ellsworth Land is crucial for revealing any possible connectivity with the Weddell Sea Rift System. The overall modelled crustal thickness at the Ellsworth Land stations from the joint inversion in Chapter 3 (30 ± 2.5 km) is comparable to the neighbouring Haag Nunataks, yet the modelled internal crustal structure features a thicker (10-20 km thick) high-velocity likely mafic lower crust. As noted in Chapter 3, the potential abundance of dense mafic lower crust may be responsible for the deep bedrock elevations in the region, whilst the overall thicker crust suggests that Ellsworth Land has undergone less extension than the central WARS. The presence of extensive mafic underplating in the neighbouring Weddell Sea Rift System has been attributed to plume related Jurassic magmatism by *Jordan et al.* (2017); a similar mechanism may have been responsible for the thick mafic lower crust which I have modelled in Ellsworth Land. An alternative interpretation is that lower crustal flow from the Haag Nunataks transferred mafic material not only to the Weddell Sea Rift System but also into Ellsworth Land. Were this to be the case then a lateral pressure gradient in the lower crust would have to have been present to facilitate upper crustal extension, suggesting that the region has been subject to some stretching. The disparity in both crustal thickness and structure with regards to the central WARS suggests that the rift system did not substantially propagate into Ellsworth Land. I therefore suggest that there is not a direct linkage between the WARS and Weddell Sea Rift System, and that the WARS instead propagated in the direction of the Bellingshausen and Amundsen Sea embayments. The UKANET - POLENET Mini Array traverse (PIG1 - MA06) crosses from Thurston Island into the West Antarctic Rift System, and as such can be utilised to better constrain the northern boundary of the WARS. A number of previous studies have proposed that the Pine Island Rift is a branch of the WARS (*Gohl et al.*, 2007, *Jordan et al.*, 2010, *Gohl*, 2012, *Damiani et al.*, 2014), and that the region between the Pine Island Rift and the Byrd Subglacial Basin is a transitional crustal boundary zone (*Diehl*, 2008). Fig. 6.2 shows the shear wave velocity-depth profiles from the UKANET-POLENET Mini Array station traverse. At stations in the centre of the West Antarctic Rift System (PIG3 - MA05) I modelled crust with a consistent thickness of 23-25 km, whilst at Thurston Island stations (THUR - PIG2) I found a thicker crust of 28-30 km. My findings therefore support the suggestion that the WARS - Thurston Island block boundary lies in the vicinity of the Pine Island Rift. Fig. 6.3 shows crustal thickness estimates along the UKANET-POLENET Mini Array traverse from *Jordan et al.* (2010), *O'Donnell et al.* (2019a) and the joint inversion in Chapter 3. The gravity derived crustal thickness estimates of *Jordan et al.* (2010)

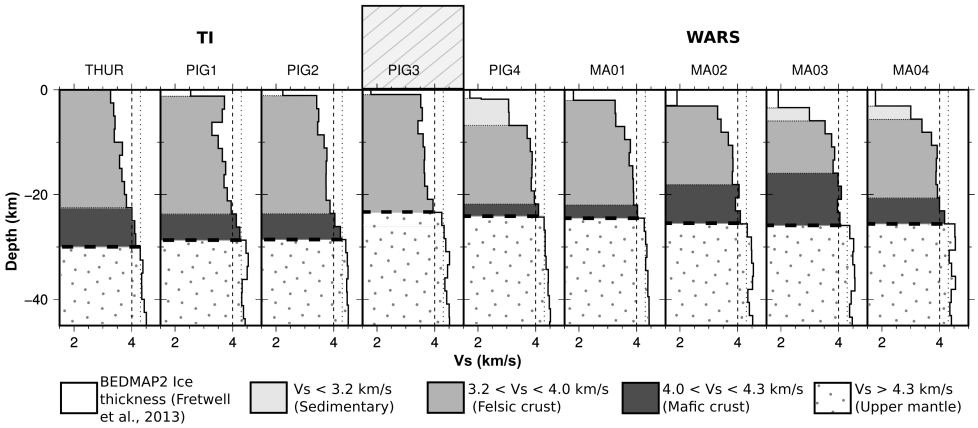

Figure 6.2: Shear wave velocity structure from the UKANET-POLENET/ANET Mini Array traverse stations which sample the transition from the Thurston Island (TI) block into the WARS. My interpreted Moho is shown by a horizontal dashed black line at each station, and I add vertical dashed and dotted lines at 4.0 and 4.3 km/s respectively to indicate the transition from lower crustal to upper mantle velocities. I interpret the Thurston Island-WARS transition to lie in the vicinity of PIG3 as shown by the dashed box. Within Thurston Island I find a $\sim$28 km thick crust, whilst in the WARS I find a $3-5$ km thinner crust with a higher proportion of fast (4.0-4.3 km/s) lower crust

shows a more gradual trend of increasing crustal thickness towards Thurston Island, with the authors suggesting that the Thurston Island-WARS boundary is further north than suggested by *Dalziel and Elliot* (1982). At the southern end of the profile, the ambient noise derived estimates of *O'Donnell et al.* (2019a) show crustal thickening towards the HEW block much earlier than my joint inversion estimates, and that of *Jordan et al.* (2010). This may be related to the ambient noise technique being less sensitive to relatively short wavelength structure, such as the sharp increase in crustal thickness and topography between the WARS and HEW block. The sharp change in crustal character and bedrock elevation between the WARS and HEW block suggests that this boundary may instead be more fault controlled than the gradual Thurston Island-WARS flank.

Gohl (2012) and *Bingham et al.* (2012) both suggest that major ice streams in West Antarctica exploit tectonic lineaments created by rifting. My estimates of crustal thickness in the vicinity of the Pine Island Rift support the suggestion that Pine Island

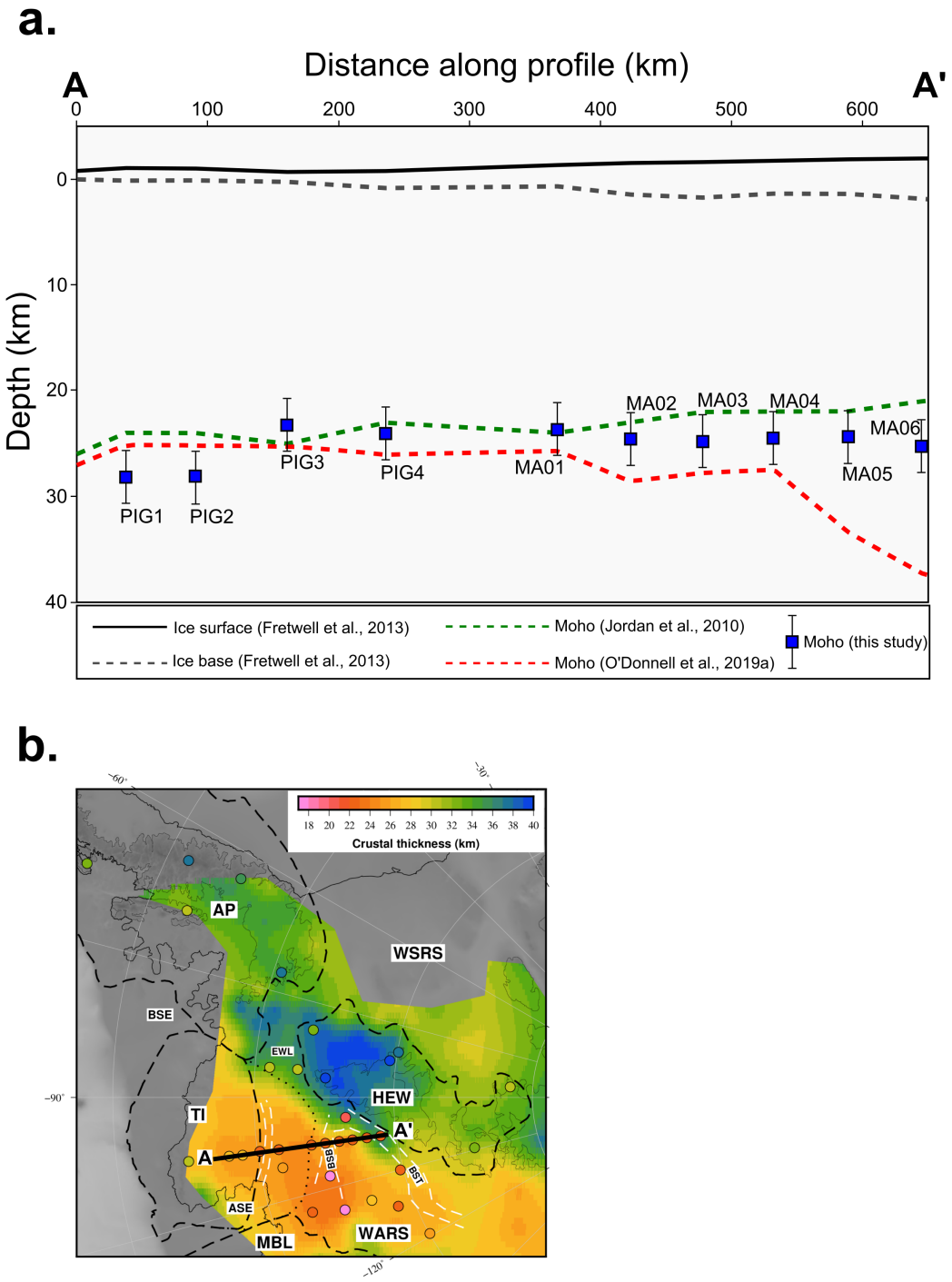

Figure 6.3: (a) A profile of crustal thickness from Thurston Island into the WARS modelled in three studies: the gravity derived estimates of *Jordan et al.* (2010) in green, ambient seismic noise derived estimates from *O'Donnell et al.* (2019a) in red, and my joint inversion estimates from Chapter 3 in blue squares. (b) A map of my crustal thickness estimates at each station (circles) superimposed on the ambient noise derived crustal thickness map of *O'Donnell et al.* (2019a), with the profile line in panel (a) shown in solid black line.

Glacier may have been steered by WARS rift structures, given the Thurston Island-WARS boundary is likely towards this region. Were the Thurston Island-WARS boundary to be in the vicinity of the Pine Island Rift then that would imply a ∼200 km shift from its previously accepted position in *Dalziel and Elliot* (1982). If the WARS is indeed 200 km wider, then there are implications for modelling plate circuit closure and for the total amount of extension encompassed by the WARS. The updated boundary also suggests that the WARS extends further towards both the Amundsen Sea and Bellingshausen Sea embayments than previously accepted in *Dalziel and Elliot* (1982) (Fig. 6.1). A shift in the Thurston Island-WARS boundary would also mean that the Thurston Island block is smaller than previously though based on the boundaries of *Dalziel and Elliot* (1982). Either the Thurston Island block did not extent as far south as previously accepted, or the rift system propagated into Thurston Island crust. Fig. 1.3, which is modified from *Jordan et al.* (2020), suggests that at ∼ 175 Ma the Thurston Island and HEW blocks were relatively close prior to WARS extension. Were the Thurston Island block to in fact be smaller than previously thought, then this may have implications for West Antarctic block reconstructions of this type. Although much of the likely tectonic seismicity located in Chapter 4 lies within this transitional zone between WARS and Thurston Island crust, the events are relatively sparse and do not seem to align with any likely rift structures, supporting the suggestion that the WARS is no longer active.

6.2 Geothermal heat flow in West Antarctica

The thin crust and possible magmatism occurring in West Antarctica has implications for the region's geothermal heat flux. Geothermal heat flux plays a key role in the stability of Antarctica's ice sheet, as high heat flow can lead to enhanced basal melting (*Blankenship et al.*, 1993). An increase in basal melting can lead to the saturation of subglacial sediment and a reduction in basal friction, further promoting fast ice flow. However given the thick ice cover across the majority of the continent, directly measuring geothermal heat flux becomes very difficult. The seismically slow upper mantle of West Antarctica (e.g. *Ritzwoller et al.*, 2001, *O'Donnell et al.*, 2019b) suggests that it is warm relative to East Antarctica. The global surface heat flux model of *Shapiro and Ritzwoller* (2004) extrapolated from seismic wavespeeds was additionally supportive of augmented heat flux in West Antarctica, with a maximum value of ∼120 $\mathrm{mWm^{-2}}$ in the WARS (Fig. 6.4d.). *Maule et al.* (2005) further modelled heat flux in Antarctica using satellite magnetic data, finding heat flux elevated to ∼80 $\mathrm{mWm^{-2}}$ along the Siple Coast, but not as high within the central WARS (Fig. 6.4b.). *Martos et al.* (2017) also modelled geothermal heat flux across Antarctica, but instead used spectral analysis of airborne magnetic data, finding heat flux to be elevated up to ∼120 $\mathrm{mWm^{-2}}$ in the

central WARS and along the Antarctic Peninsula (Fig. 6.4a.). The warm upper mantle beneath the WARS (*Ritzwoller et al.*, 2001, *O'Donnell et al.*, 2019b), and thin crust across much of the region, as shown in Chapter 3 (Fig. 6.1) and other studies (e.g. *Chaput et al.*, 2014, *Shen et al.*, 2018, *O'Donnell et al.*, 2019a), supports the suggestion that geothermal heat flux into the base of the West Antarctic Ice Sheet is likely to be elevated.

Thanks to drilling into Subglacial Lake Whillans in the vicinity of the Siple Coast *Fisher et al.* (2015) were able to take direct measurements of geothermal heat flux, finding it as high as 285±80 $\mathrm{mWm^{-2}}$. *Begeman et al.* (2017) used the same method as *Fisher et al.* (2015) near the grounding line of the Whillans Ice Stream, ∼100 km from the site of *Fisher et al.* (2015). *Begeman et al.* (2017) found a geothermal heat flow of 88±7 $\mathrm{mW/m^{-2}}$, and attribute the spatial variability to either the advection of heat via crustal fluids, or shallow magmatic intrustions. Ice sheet modelling has additionally suggested that a geothermal heat flux of >150 $\mathrm{mW/m^{-2}}$ would have been necessary to produce the subglacial lakes found in the vicinity of the Whillans Ice Stream (*Seroussi et al.*, 2017).

High geothermal heat flux up to ∼200 $\mathrm{mWm^{-2}}$ with a minimum average of ∼114 ±10 $\mathrm{mWm^{-2}}$ was additionally inferred beneath Thwaites Glacier using radar and hydrologic modelling (*Schroeder et al.*, 2014). These elevated values exceed the regional and continental scale models, which the authors attribute to likely localised volcanism. In addition *Loose et al.* (2018) analysed seawater helium isotopes ratios in Pine Island Bay to propose that a volcanic heat source is present upstream of Pine Island Ice Shelf, towards the boundary of Thurston Island and the WARS. This heat source could be related to subglacial volcanism in the Hudson Mountains (e.g. *Corr and Vaughan*, 2008), a region in which many of the 'likely tectonic' events I detected in Chapter 4 are located. It is possible that some of these events could be related to magmatic activity, however without a denser seismic network deployed in the region it is difficult to accurately distinguish between tectonic and volcanic events. In the nearby Amundsen Sea Embayment, *Dziadek et al.* (2019) model geothermal heat flow from in situ shipborne temperature measurements, finding heat flow to range from 65 to 95 $\mathrm{mWm^{-2}}$. The potentially elevated geothermal heat flow in the region surrounding Pine Island Glacier could have been a contributing factor for the glacier's rapid acceleration over recent decades. High geothermal heat flux in combination with the possible nearby accumulations of subglacial sediment (Fig. 3.9) may have acted to reduce the glacier's basal friction and accelerate flow. I modelled 0.1-0.2 km thick subglacial sediment in the vicinity of Pine Island Glacier at PIG2 and PIG4. Large-scale sedimentary deposits

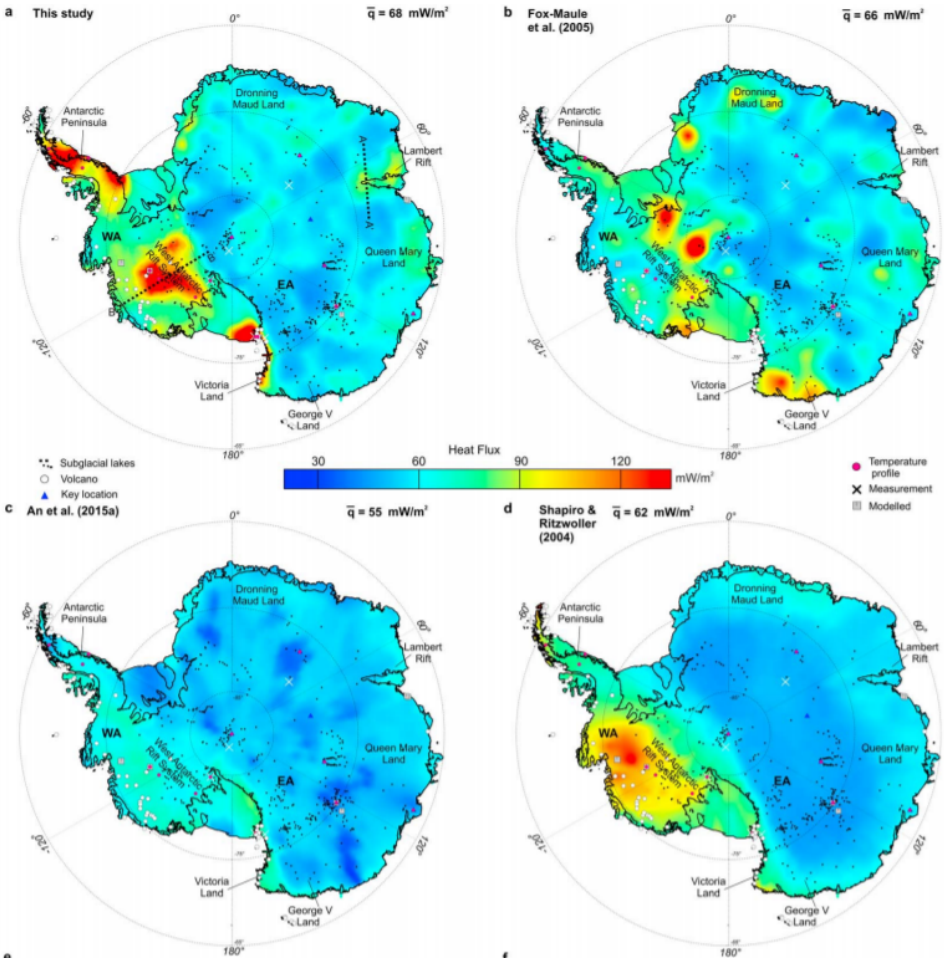

Figure 6.4: Maps of modelled geothermal heat flux variation across Antarctica from *Martos et al.* (2017). a) The heat flux map of *Martos et al.* (2017) derived from spectral analysis of airborne magnetic data. *Martos et al.* (2017) find geothermal heat flux to be higher in West Antarctica than East Antarctica, particularly in the central WARS and Antarctic Peninsula. b) The *Maule et al.* (2005) heat flux model produced using satellite magnetic data. c) The seismically derived heat flux map of *An et al.* (2015). d) Another seismically derived heat flux map from *Shapiro and Ritzwoller* (2004), again finding heat flux to be higher in West Antarctica than East Antarctica. Figure taken from *Martos et al.* (2017).

have previously been identified using seismic reflection (*Brisbourne et al.*, 2017), and aerogravity models indicate there could be ∼0.8 km thick sediments near the glacier's grounding line (*Muto et al.*, 2016).

O'Donnell et al. (2019b) also propose surface geothermal heat flux values that best explain their modelled lithospheric mantle velocities across West Antarctica. Within the southern Antarctic Peninsula, Thurston Island and WARS they suggest a surface heat flux of ∼60 mW m^{-2}, and ∼50 mW m^{-2} within the HEW block. The surface heat flux estimates of *O'Donnell et al.* (2019b) are regional averages over hundreds of

km, and have a limited sensitivity to upper crustal composition. Within the Antarctic Peninsula and HEW blocks, my shear wave velocity profiles produced by the joint inversion in Chapter 3 suggest a predominatly felsic/intermediate crustal composition (Fig. 3.14). If these blocks do indeed feature a largely felsic/intermediate composition, then there could be potentially enhanced radiogenic heat produced within the crust, as previously suggested in the southern Antarctic Peninsula by *Burton-Johnson et al.* (2017).

6.3 Glacial Isostatic Adjustment processes in West Antarctica

The dramatic loss of ice mass in the Amundsen Sea Embayment over recent decades (*Rignot et al.*, 2008, 2011) will have had a significant influence on the Glacial Isostatic Adjustment processes occurring across the region (*Barletta et al.*, 2018) (Fig. 6.5). As previously noted in Chapter 4, I suggest that much of the 'likely tectonic' seismicity I classified in the vicinity of the Amundsen Sea Embayment was produced within the crust, as a result of the high uplift rates in the region (*Barletta et al.*, 2018). Rates of bedrock uplift in glaciated regions are influenced by both the instantaneous elastic response to current changes in ice mass, as well as the viscoelastic response to historic changes in ice mass (e.g. *Barletta et al.*, 2018, *Nield et al.*, 2018). The timing of the viscoelastic response is a function of the lithospheric viscosity and thickness; parameters which show spatial variation across West Antarctica (*O'Donnell et al.*, 2017, *Nield et al.*, 2018, *O'Donnell et al.*, 2019b). Regions which overly a low-viscosity upper mantle will be more sensitive to the recent ice history, whilst a high-viscosity upper mantle will show a more significant response to more ancient changes in ice mass. Recent studies of West Antarctica's upper mantle indicate that its viscosity is much lower than the global average, at $\sim 10^{18}$-10^{19} Pa s, suggesting that Glacial Isostatic Adjustment processes may be occurring on a decadal scale (*O'Donnell et al.*, 2017, *Barletta et al.*, 2018). The relatively fast response to the recent deglaciation history in the Amundsen Sea Embayment, and the overall pattern of regional uplift (Fig. 6.5) support the suggestion that much of the seismicity I detect in Chapter 4 was associated with bedrock deformation from Glacial Isostatic Adjustment. Seismicity related to Glacial Isostatic Adjustment processes has been observed in other regions which have experienced substantial deglaciation such as Fennoscandia (*Keiding et al.*, 2015) and northeastern Canada (*Steffen*, 2013). Seismicity produced by uplift in Fennoscandia is mostly low intensity and located in the upper 20 km of the crust (*Keiding et al.*, 2015), which is consistent with the seismicity detected in the Amundsen Sea Embayment in Chapter 4.

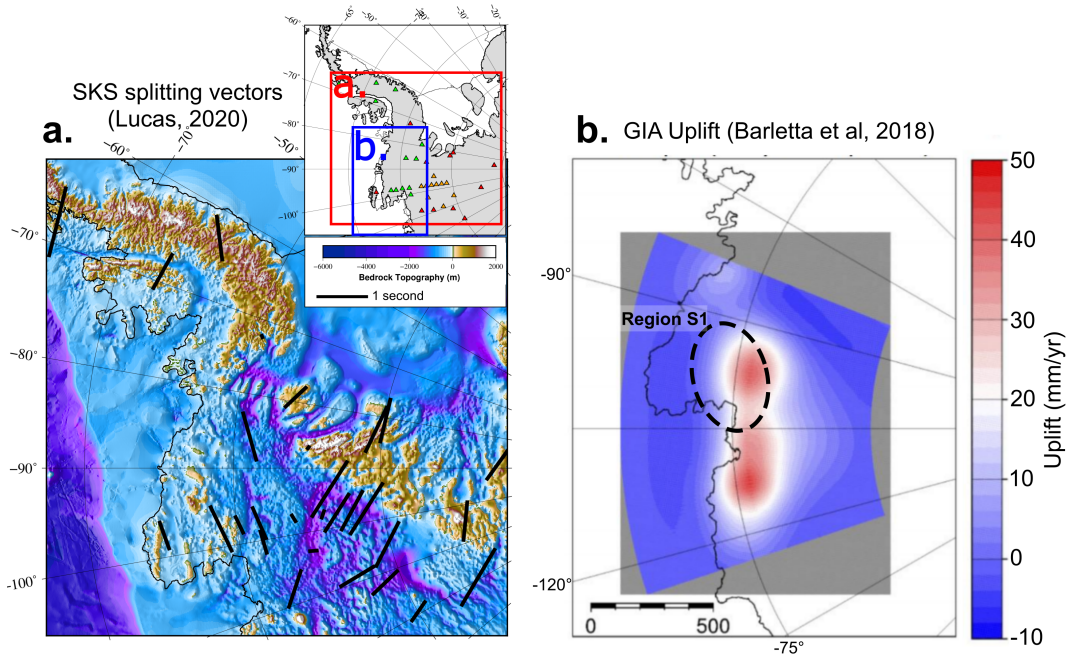

Figure 6.5: (a) A map of West Antarctica with the shear wave splitting vectors from *Lucas et al.* (2020) in black, over bedrock topography (*Fretwell et al.*, 2013). (b) Modelled Glacial Isostatic Adjustment uplift in the Amundsen Sea Embayment modified from *Barletta et al.* (2018). The region S1 is marked in black dashed line in panel (b) which encompasses the majority of the 'likely tectonic' seismicity located in Chapter 4 (Fig. 4.18) Panel (a) and (b) are drawn with different projection centres, so the bounds of each plot are shown in red (a) and blue (b) in the inset location map.

Nield et al. (2018) suggested that lateral variations in lithospheric thickness have an impact on the ability to accurately model Glacial Isostatic Adjustment in West Antarctica. Discarding lateral variation in lithospheric thickness leads to peak uplift and subsidence estimates produced from Glacial Isostatic Adjustment being biased low in West Antarctica, and short wavelength deformation cannot be accurately resolved (*Nield et al.*, 2018). Additionally, Earth models used when modelling Glacial Isostatic Adjustment generally only include a constant thickness, purely elastic crustal layer (*Kaufmann et al.*, 2005, *Nield et al.*, 2018). Given the variety in crustal thickness and composition shown in Chapter 3 and other studies (e.g. *Chaput et al.*, 2014, *O'Donnell et al.*, 2019a), neglecting lateral variation in the crustal layer may also introduce an additional, albeit smaller bias in the Glacial Isostatic Adjustment models.

Teleseismic shear wave splitting has been utilised on POLENET/ANET data to investigate azimuthal anisotropy in the upper mantle (*Accardo et al.*, 2014). Measuring seismic anisotropy has proven to be a powerful tool for inferring mantle flow and defor-

mation. Deformation in the mantle can lead to both the lattice preferred orientation (LPO) of anisotropic minerals such as olivine, and shape preferred orientation (SPO) of parallel structure. Models that account for seismic anisotropy in the mantle include: LPO of olivine induced by ongoing extension or compression, SPO caused by the alignment of parallel dikes or lenses of melt, and fossilised LPO anisotropy from past tectonic forcing. *Accardo et al.* (2014) find upper mantle seismic anisotropy varies between East and West Antarctica, suggesting that the anisotropic signature of the WARS results from asthenospheric mantle strain from the final pulse of Miocene extension. The fast axes in the WARS are sub-parallel to the direction of extension (Fig. 6.5), which *Accardo et al.* (2014) attribute to ductile shearing rather than magmatic intrusion.

Lucas et al. (2020) have further investigated upper mantle anisotropy in Antarctica by studying shear wave splitting at additional stations, including the UKANET-POLENET Mini-Array station traverse (Fig. 6.5). POLENET Mini-Array stations MA02-MA06 show fast axes roughly consistent with the central WARS (*Accardo et al.*, 2014), whilst stations surrounding the Amundsen Sea Embayment show a ∼130° shift in fast splitting direction. This change in fast direction combined with a reduction in the splitting time at stations between Thurston Island-WARS suggests a transitional change in the style of upper mantle deformation experienced by the two regions. *Accardo et al.* (2014) suggest that this shift in splitting direction may be related to the more complex tectonic history of the Amundsen Sea Embayment, as *Granot et al.* (2013) propose that the region experienced convergent motion during the Eocene-Ogliocene. It is also possible that the change in fast splitting direction in the Amundsen Sea Embayment is due to upper mantle flow from the uplift driven by Glacial Isostatic Adjustment (*Barletta et al.*, 2018) (Fig. 6.5). Fig. 6.5 shows the modelled Glacial Isostatic Adjustment uplift signal in the Amundsen Sea Embayment, which closely correlates with the densest region of 'likely tectonic' events located in Chapter 4 (Region S1 - Fig. 6.5b). The high rate of modelled uplift surrounding the Amundsen Sea Embayment (*Barletta et al.*, 2018), combined with the low upper mantle viscosity (*O'Donnell et al.*, 2017, *Barletta et al.*, 2018), could mean that resulting upper mantle flow has overprinted any pre-existing anisotropic fabric relating to WARS extension.

6.4 Recommendation for future work

In this study, one of the main limitations was the sparse station distribution. This was particularly pertinent when attempting to study the local seismicity in Chapters 4 and 5, as accurate determination of an event's location and source parameters relies on having a good azimuthal station coverage. Despite this, both Chapters 4 and 5

demonstrate that a lot of insight that can be gained into some of the regional tectonic and glacial processes occurring, particularly in the area surrounding the Amundsen Sea Embayment. A denser, and longer term seismic network deployed around the Amundsen Sea Embayment could provide even more detail on the ice dynamics of the region's fast flowing ice streams, as well as the pattern of seismicity produced by isostatic rebound and possible subglacial volcanism. Given that the already high rates of regional uplift in the Amundsen Sea Embayment are projected to accelerate over the coming decade (*Barletta et al.*, 2018), it would be interesting to see how this influences the distribution and volume of local seismicity in the area. It is likely that rates of seismicity related to Glacial Isostatic Adjustment processes will accelerate with the increasingly rapid regional uplift, and it is also possible that these processes could lead to even larger seismic events. It has been suggested that Glacial Isostatic Adjustment was a significant factor in the M_w 8.1 Balleny Island earthquake within the Antarctic oceanic crust (*Reading*, 2007; and references therein), as such monitoring changes in the patterns of seismicity with uplift in the Amundsen Sea Embayment could be of value.

A dense network of broadband seismometers and GPS stations distributed around Pine Island Glacier could help to further investigate the glacier's ice dynamics. As shown in Chapter 5, valuable information can be gleaned by correlating patterns in detected seismicity with some of the glacier's physical processes. The main limitation in Chapter 5 is both the short network duration surrounding Pine Island Glacier (<2 years), and the distances from the glacier to each station (>95 km). Were there to be a denser network of stations distributed for a longer time period around the glacier, then more detail could be revealed on the glacier's basal environment, calving mechanisms, and grounding line retreat. Many of the substantial rifts in the floating ice-shelf that lead to major calving events at Pine Island Glacier have been proposed to have initiated due to basal crevassing close to the grounding line *Jeong et al.* (2016). Detecting and accurately locating any seismicity close to the grounding line as these rifts are initiated could therefore provide a crucial insight into the evolution of Pine Island Glacier. In addition, studying seismicity produced during calving events could shed more light on how these substantial rifts in the ice shelf quickly propagate before breaking off, and the potential hydraulics involved during calving (Fig. 5.10).

An additional aspect of Pine Island Glacier which could be further investigated with passive seismometers is the relationship between the glacier's velocity and seismicity. A similar investigation as that carried out on the Whillans Ice Stream (*Winberry et al.*, 2009), involving a short term dense network of GPS and seismic stations could be

carried out to do this, and further investigate the glacier's basal processes. Fig. 5.3 shows some relationship between a decrease in ice velocity at the grounding line, and increasing rates of detected seismicity. In this study however I am only able to estimate ice velocity using satellite based estimates, with >6 day intervals between each pass. A co-located network of seismic and GPS instruments deployed close to the grounding line could therefore investigate these patterns on a shorter timescale, and possibly reveal if there is any tidal influence on the glacier's flow rate and associated seismicity.

Another region which could benefit from the deployment of additional seismometers is the region of Ellsworth Land towards the Bellingshausen Sea Embayment. Given that the shear wave velocity models produced via the joint inversion in Chapter 3 suggest that the Thurston Island-WARS boundary is further north than previously accepted in *Dalziel and Elliot* (1982), it would be good to follow this transitional region, and therefore the extent of the WARS, towards the Bellingshausen Sea Embayment (Fig. 6.1).

The work that I have presented in this thesis could also be further built upon using the existing data from UKANET and POLENET. The transverse receiver functions could be studied in more depth to investigate anisotropy in the crust, and possibly in the ice layer. Using the transverse receiver functions could build on other studies of seismic anisotropy in West Anarctica, which have predominantly focused on SKS-splitting (e.g. *Accardo et al.*, 2014, *Lucas et al.*, 2020). The work I presented in Chapter 4 could benefit from further work on both the event classification and further refinement of the velocity models used in event location. Waveform modelling could be utilised to more accurately separate cryoseismic from tectonic events, which would drastically improve the accuracy in event classification in this region.

Chapter 7

Conclusions

This thesis features a study of West Antarctica's crustal structure and seismicity using 33 stations from the recently deployed UKANET seismic network (2016-2018) and longer term POLENET/ANET seismic network (2008-). By jointly inverting receiver functions with Rayleigh wave phase velocity dispersion curves I was able to model shear wave velocity structure beneath each station. Interpreting these shear wave velocity models then allowed for determination of crustal thickness and structure. I modelled crustal thicknesses of 30-38 km in the Antarctic Peninsula, 30-40 km in the HEW block, 28-30 km in Thurston Island and 18-28 km in the WARS. The thinner crust modelled at UKANET stations in the vicinity of Pine Island Glacier suggests that the WARS has extended further towards the Amundsen Sea Embayment than previously accepted in *Dalziel and Elliot* (1982). Within the Ellsworth Land region I found crust to be $\sim$5 km thicker than the central WARS, suggesting that there is no direct connectivity between the WARS and neighbouring Weddell Sea Rift System.

I additionally modelled the presence of layers of subglacial low velocity, likely soft sediment at all ice-situated stations using high frequency receiver functions. The forward modelling approach involved a grid search over sediment thickness and shear wave velocity, and I inferred subglacial sediment to be present at 10 stations in West Antarctica. Six stations at which subglacial sediment appears to be present are within the central WARS, and lie close to the rift systems major subglacial basins, the Byrd Subglacial Basin and Bentley Subglacial Trench. Both basins provide ample space for sediment accumulation, and may have been used as source regions for the basal till identified beneath the fast flowing Thwaites Glacier. Similarly the subglacial sediment layers I infer at stations in Ellsworth Land could have provided a source region for the basal till beneath the nearby Rutford and Evans ice streams, as well as station PIG4

near Pine Island Glacier.

By studying the continuous records of seismicity at 29 stations from the UKANET and POLENET/ANET networks from 2015-2018 I was able to locate 86 local-to regional scale events in West Antarctica. All events are low magnitude (M_L<3), and are predominantly clustered around the Amundsen Sea Embayment. I classified each event into three categories to separate the more obvious cryoseismic events from possible tectonic seismicity, based on the hypocentral location, waveform style and frequency content. This categoristaion scheme resulted in 32 'likely tectonic' events, 17 'likely ice-quakes' and 37 'possible ice-quakes'. The distribution of local seismicity I have detected across West Antarctica closely correlates with the high uplift rates produced by deglaciation and Glacial Isostatic Adjustment modelled by *Barletta et al.* (2018). I therefore suggest that the majority of the non-cryoseismic seismicity produced in the Amundsen Sea Embayment region is related to the rapid regional uplift, rather than active tectonic forcing. A number of the 'likely tectonic' events located within the Hudson Mountains lie close to possibly subglacial and subaerial volcanic cones, though determining whether or not these events were produced by volcanic activity would require a denser seismic network to be deployed in the region.

To further study the cryoseismicity produced by Pine Island Glacier, and see if the recorded seismicity correlates with the glacier's flow characteristics, I looked at the rates of automatically detected seismic events at UKANET stations from 2016-2018. Stations close to Pine Island Glacier (100-150 km away) detect ∼10 times as many events as distal stations (>200 km away). The temporal pattern of events detected over a two year period at station PIG3 shows some correlation with the average velocity at the grounding line, but more frequent estimates of the glacier's velocity are required for an accurate interpretation to be made. I also detected ∼1000 highly similar events using a cross correlation detector, located within the glaciers northern shear margin/melánge, which was destroyed between 2015 and 2017. UKANET and POLENET/ANET stations were also able to record ∼10 hours of high frequency tremor, which was likely produced by the calving of the 54 square nautical mile B-44 iceberg on the 22nd of September 2017. The tremor features a regular pulsing signal prior to the main calving event, which may relate to seawater oscillating in the propagating basal crevasse that triggered the calving event.

This thesis shows just some of the insight into West Antarctica's tectonic framework and active processes that can be gleaned from studying records from long term passive broadband seismic networks. Many of the stations used in this study were the first

deployed in their respective region of West Antarctica, and there are still various areas of the continent that lack seismic coverage. Seismic investigation within the interior of West Antarctica is still in its early stages relative to other continents worldwide.

Appendix A

Appendix for Chapter 3

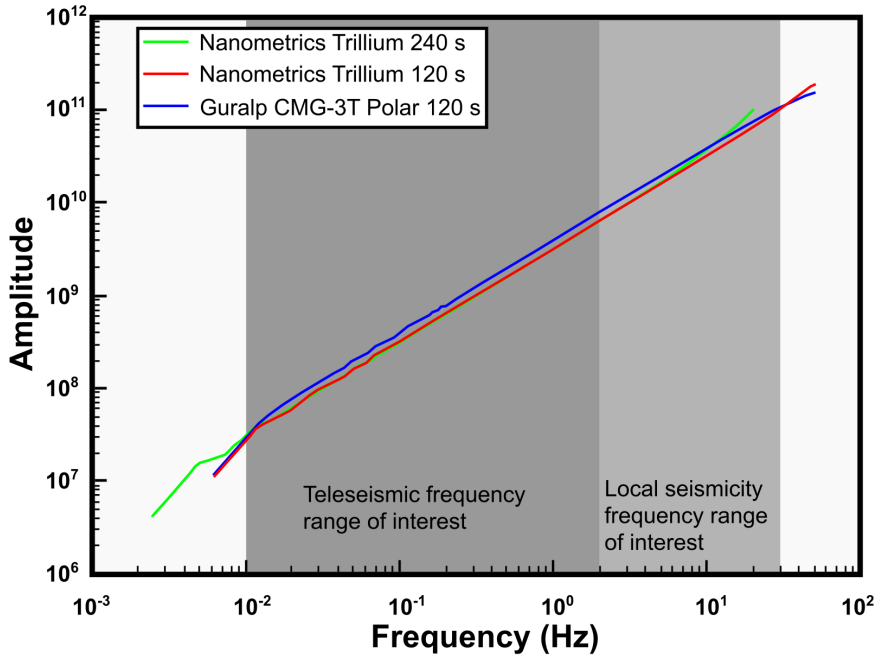

Figure A.1: Instrument responses from the three seismometer types used in this study.

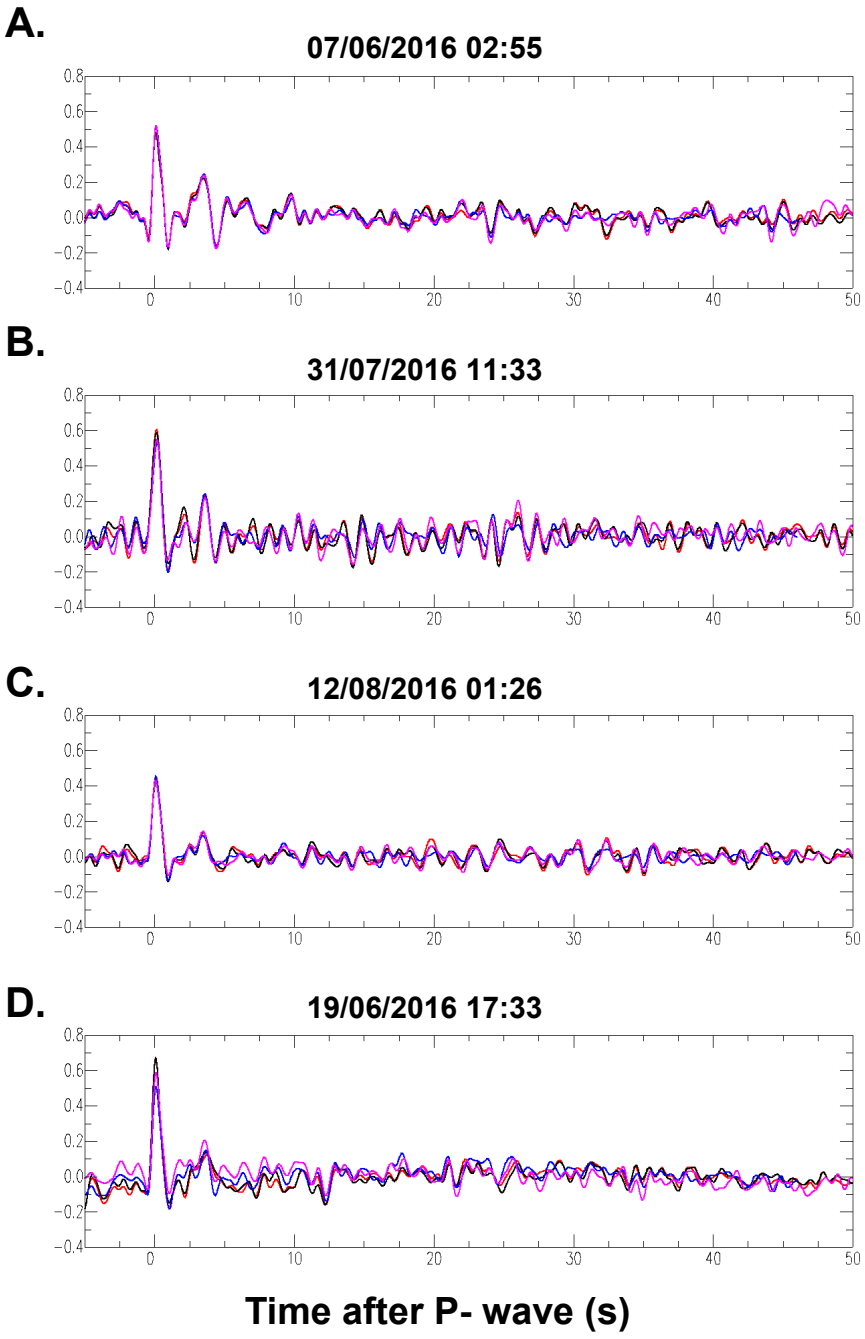

Figure A.2: Examples of testing the length of windows used on traces prior to generating receiver functions. Panels a. to d. show four separate events recorded at PIG1, each with four receiver functions generated after cutting traces with different window lengths. The windows used are: 10 s prior to the P-wave arrival to 40 s after (blue), 10 s prior to the P-wave arrival to 60 s after (magenta), 10 s prior to the P-wave arrival to 100 s after (red), 10 s prior to the P-wave arrival to 120 s after (black).

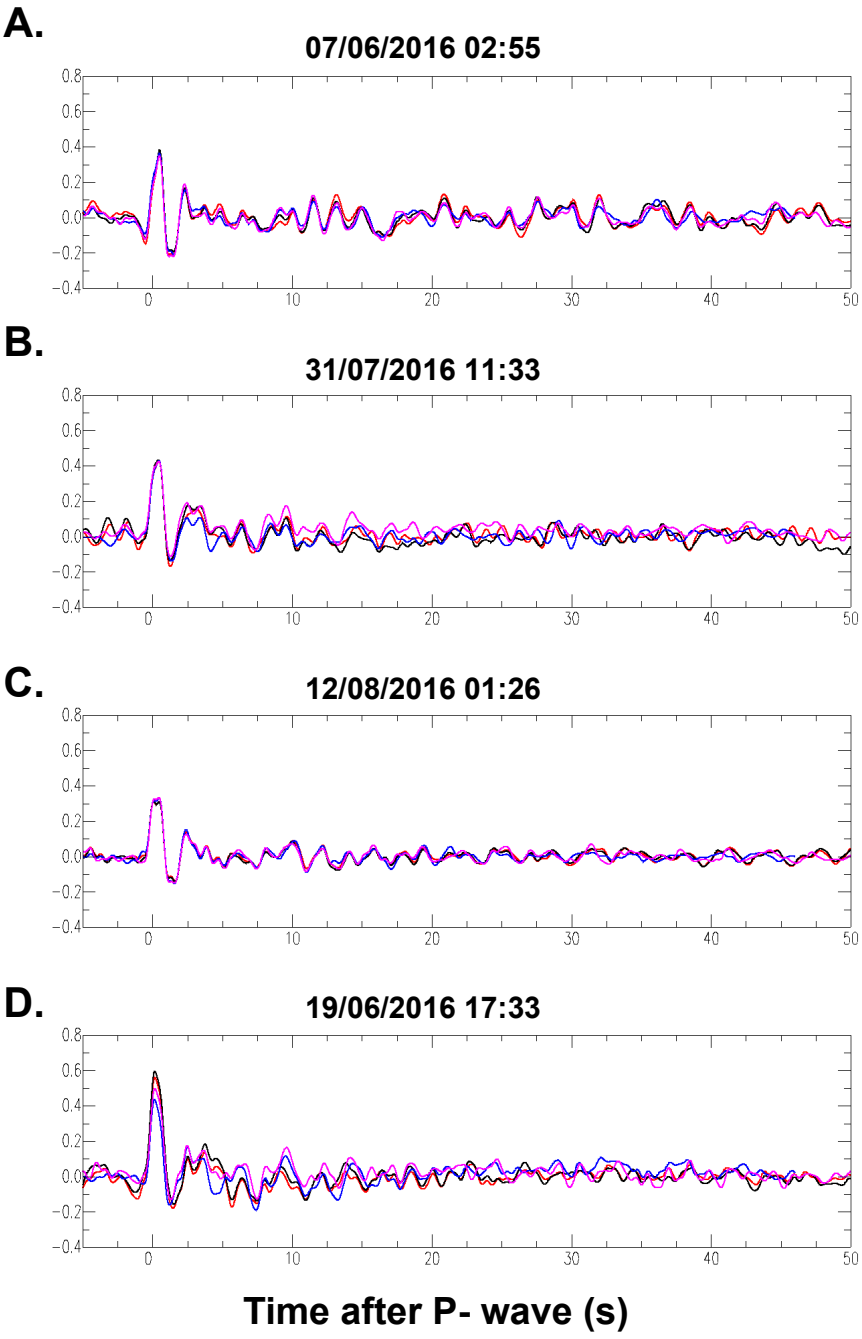

Figure A.3: Examples of testing the length of windows used on traces prior to generating receiver functions. Panels a. to d. show four separate events recorded at PIG3, each with four receiver functions generated after cutting traces with different window lengths. The windows used are: 10 s prior to the P-wave arrival to 40 s after (blue), 10 s prior to the P-wave arrival to 60 s after (magenta), 10 s prior to the P-wave arrival to 100 s after (red), 10 s prior to the P-wave arrival to 120 s after (black).

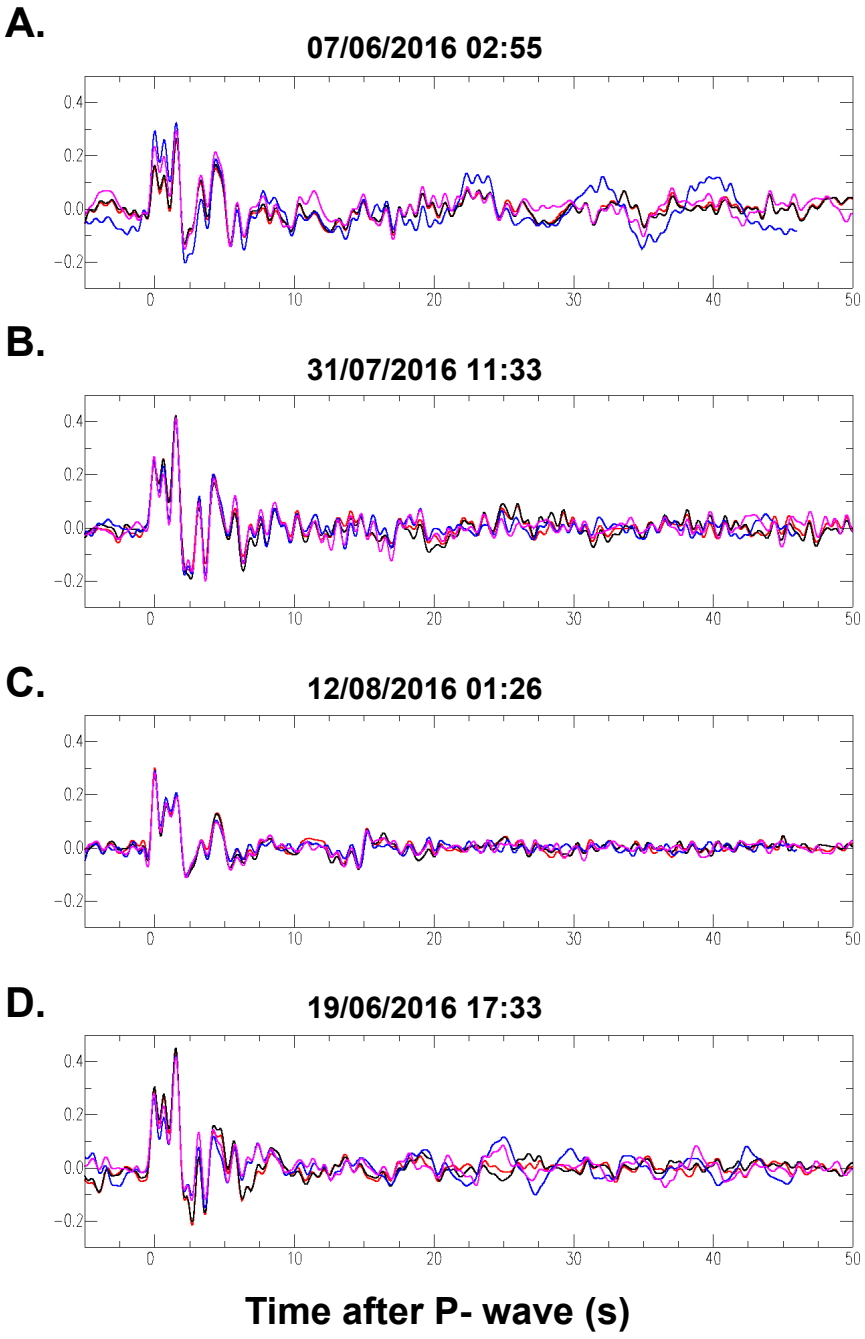

Figure A.4: Examples of testing the length of windows used on traces prior to generating receiver functions. Panels a. to d. show four separate events recorded at MA01, each with four receiver functions generated after cutting traces with different window lengths. The windows used are: 10 s prior to the P-wave arrival to 40 s after (blue), 10 s prior to the P-wave arrival to 60 s after (magenta), 10 s prior to the P-wave arrival to 100 s after (red), 10 s prior to the P-wave arrival to 120 s after (black).

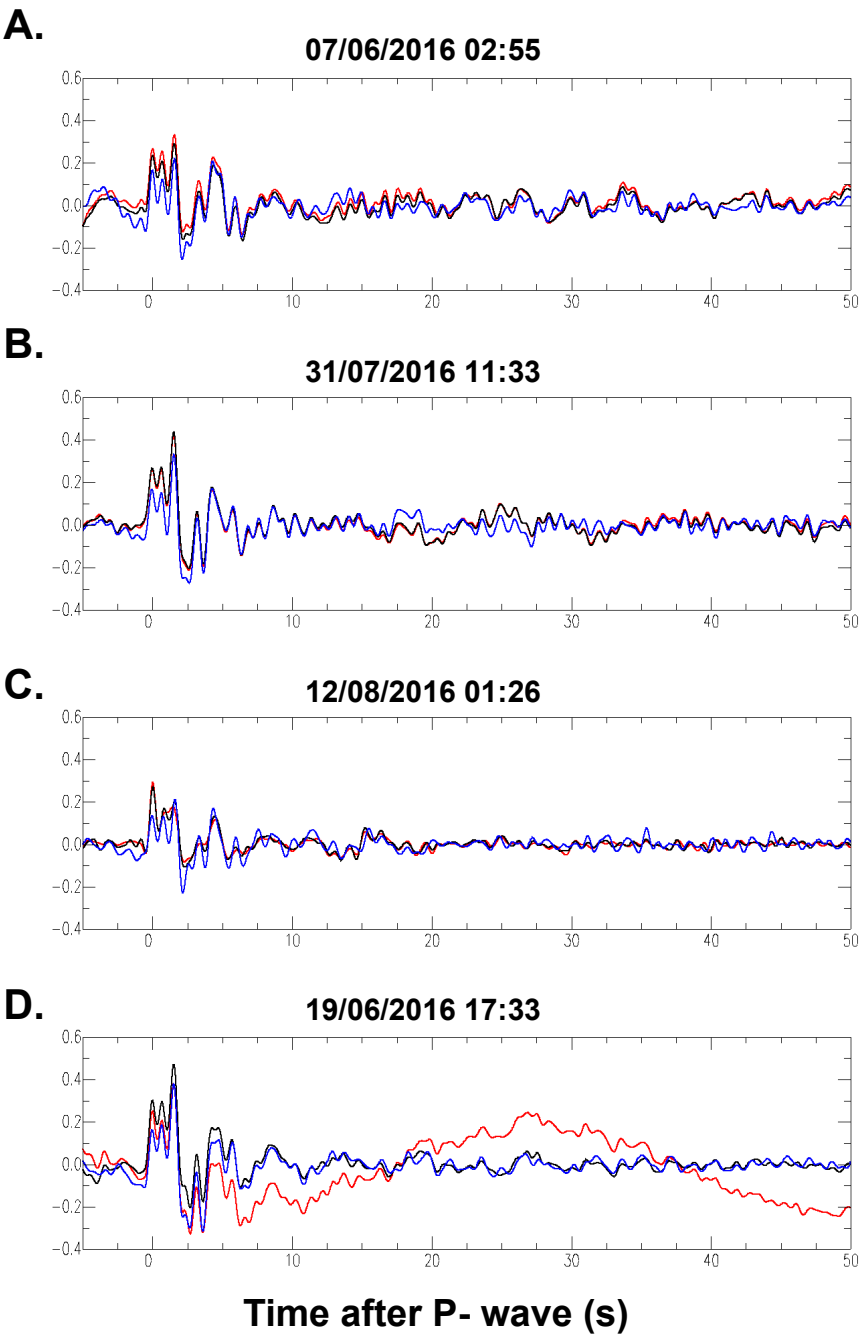

Figure A.5: An example of testing bandpass filters applied prior to receiver function generation. Panels a. to d. show four separate events recorded at MA01, each with three receiver functions generated after high pass filtering at 0.01 Hz (red) 0.05 Hz (black) and 0.5 Hz (blue).

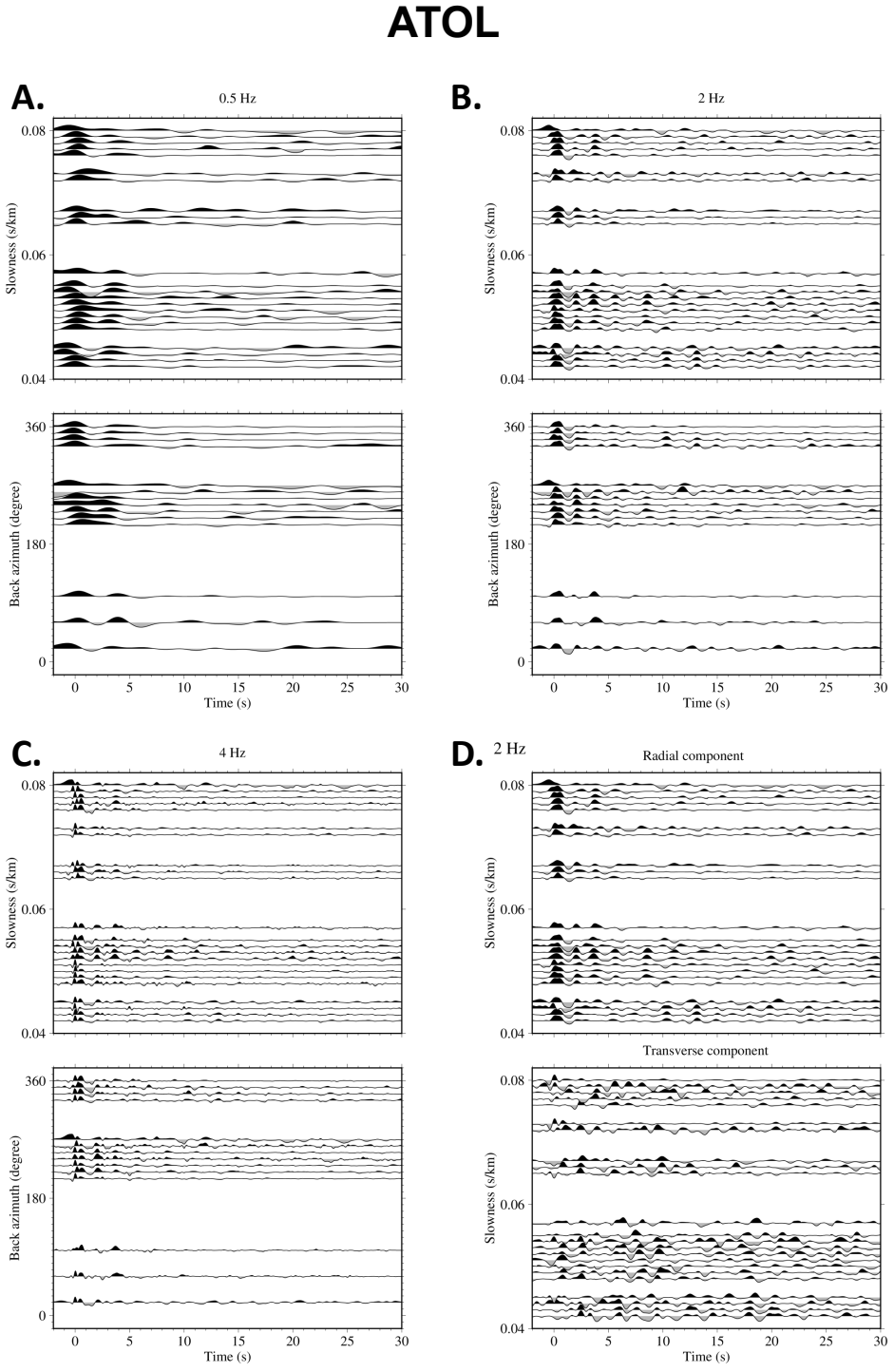

Figure A.6: Receiver functions computed at ATOL plotted by back azimuth and slowness. Receiver functions are binned by back azimuth every 10°and by slowness every 0.001 s/km. a) Receiver functions calculated with a maximum frequency of 0.5 Hz. b) Receiver functions calculated with a maximum frequency of 2 Hz. c) Receiver functions calculated with a maximum frequency of 4 Hz. d) 2 Hz maximum frequency radial and transverse receiver functions plotted by slowness.

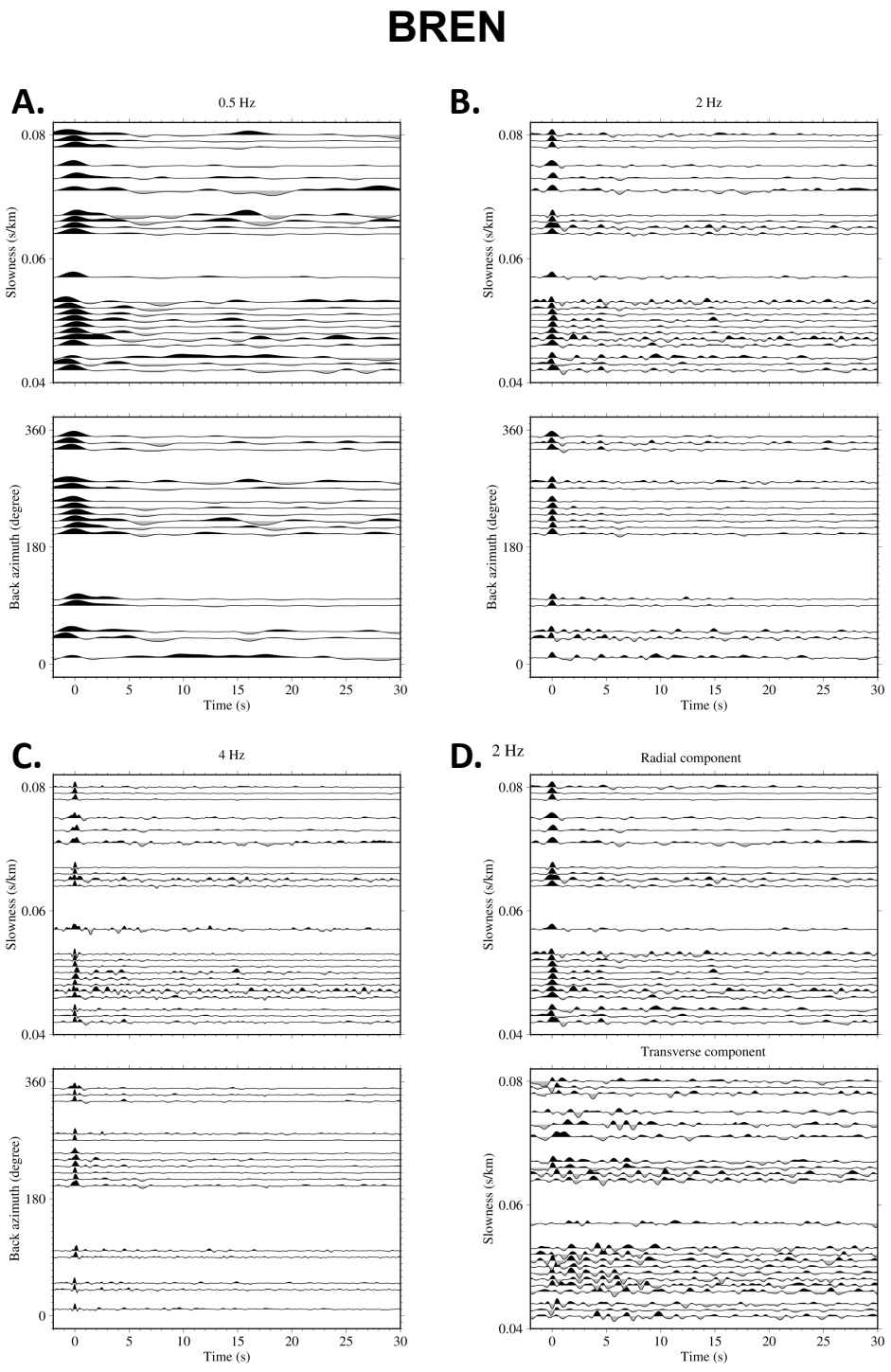

Figure A.7: Receiver functions computed at BREN plotted by back azimuth and slowness. Receiver functions are binned by back azimuth every 10°and by slowness every 0.001 s/km. a) Receiver functions calculated with a maximum frequency of 0.5 Hz. b) Receiver functions calculated with a maximum frequency of 2 Hz. c) Receiver functions calculated with a maximum frequency of 4 Hz. d) 2 Hz maximum frequency radial and transverse receiver functions plotted by slowness.

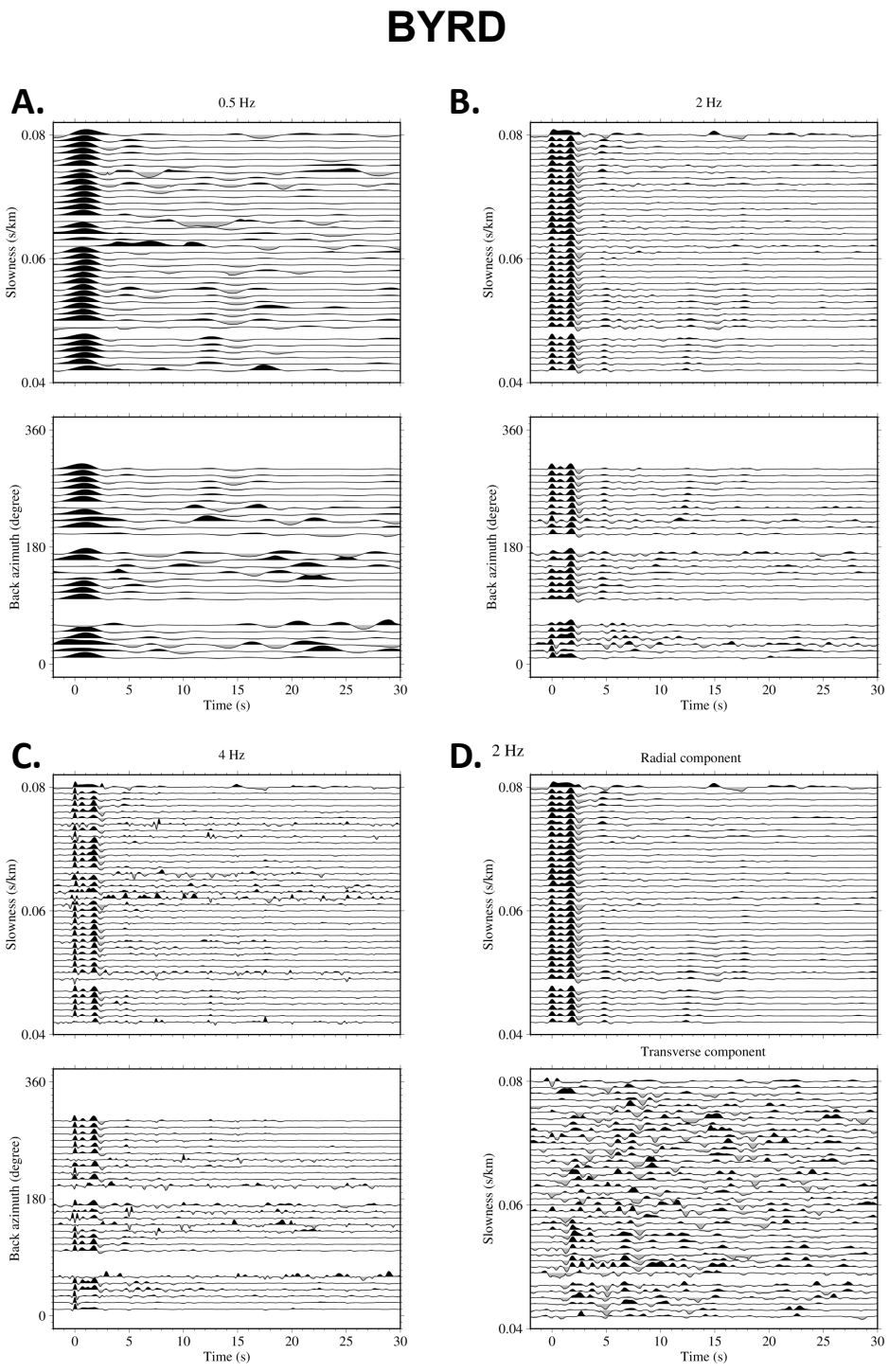

Figure A.8: Receiver functions computed at BYRD plotted by back azimuth and slowness. Receiver functions are binned by back azimuth every 10°and by slowness every 0.001 s/km. a) Receiver functions calculated with a maximum frequency of 0.5 Hz. b) Receiver functions calculated with a maximum frequency of 2 Hz. c) Receiver functions calculated with a maximum frequency of 4 Hz. d) 2 Hz maximum frequency radial and transverse receiver functions plotted by slowness.

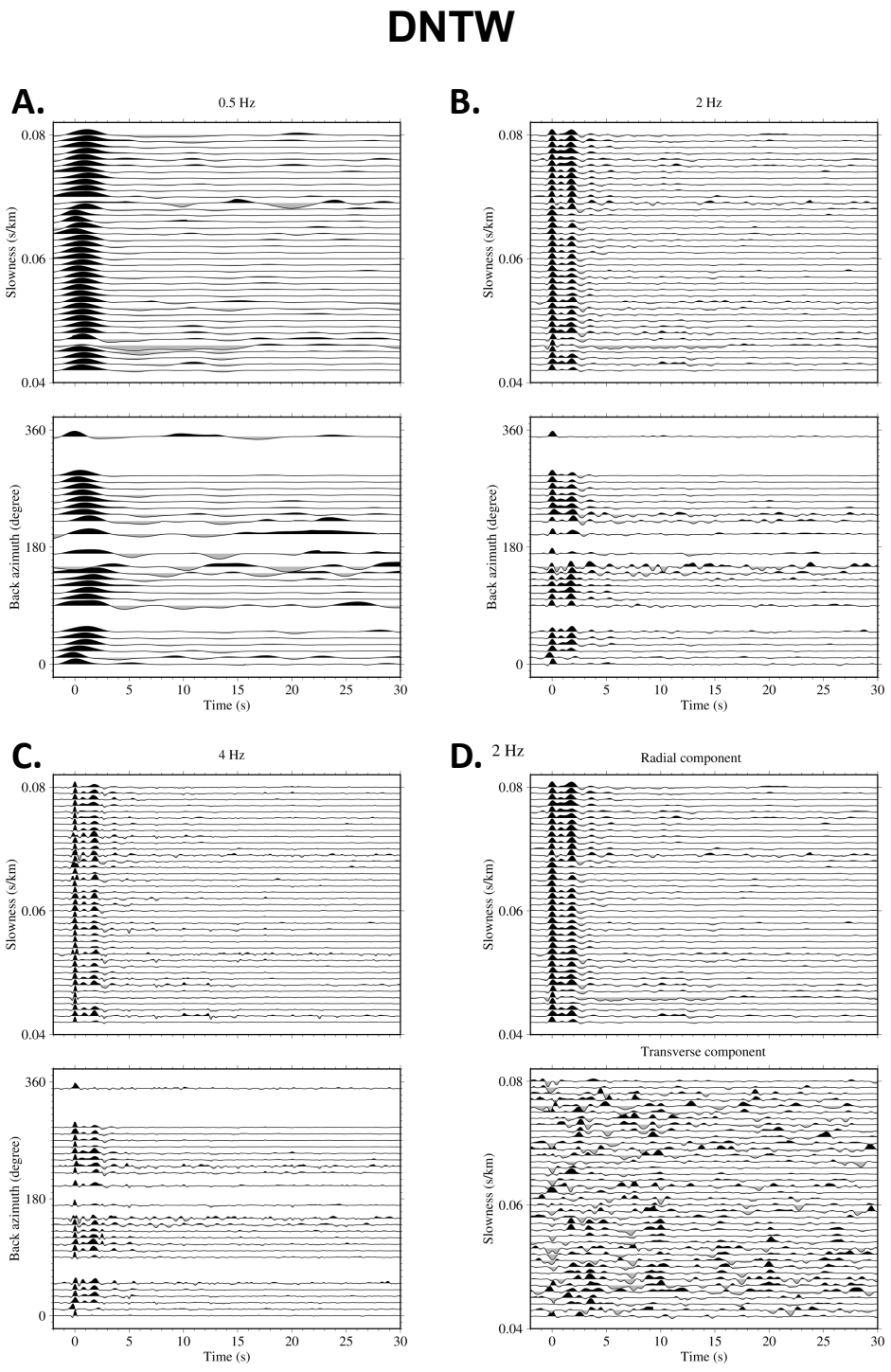

Figure A.9: Receiver functions computed at DNTW plotted by back azimuth and slowness. Receiver functions are binned by back azimuth every 10°and by slowness every 0.001 s/km. a) Receiver functions calculated with a maximum frequency of 0.5 Hz. b) Receiver functions calculated with a maximum frequency of 2 Hz. c) Receiver functions calculated with a maximum frequency of 4 Hz. d) 2 Hz maximum frequency radial and transverse receiver functions plotted by slowness.

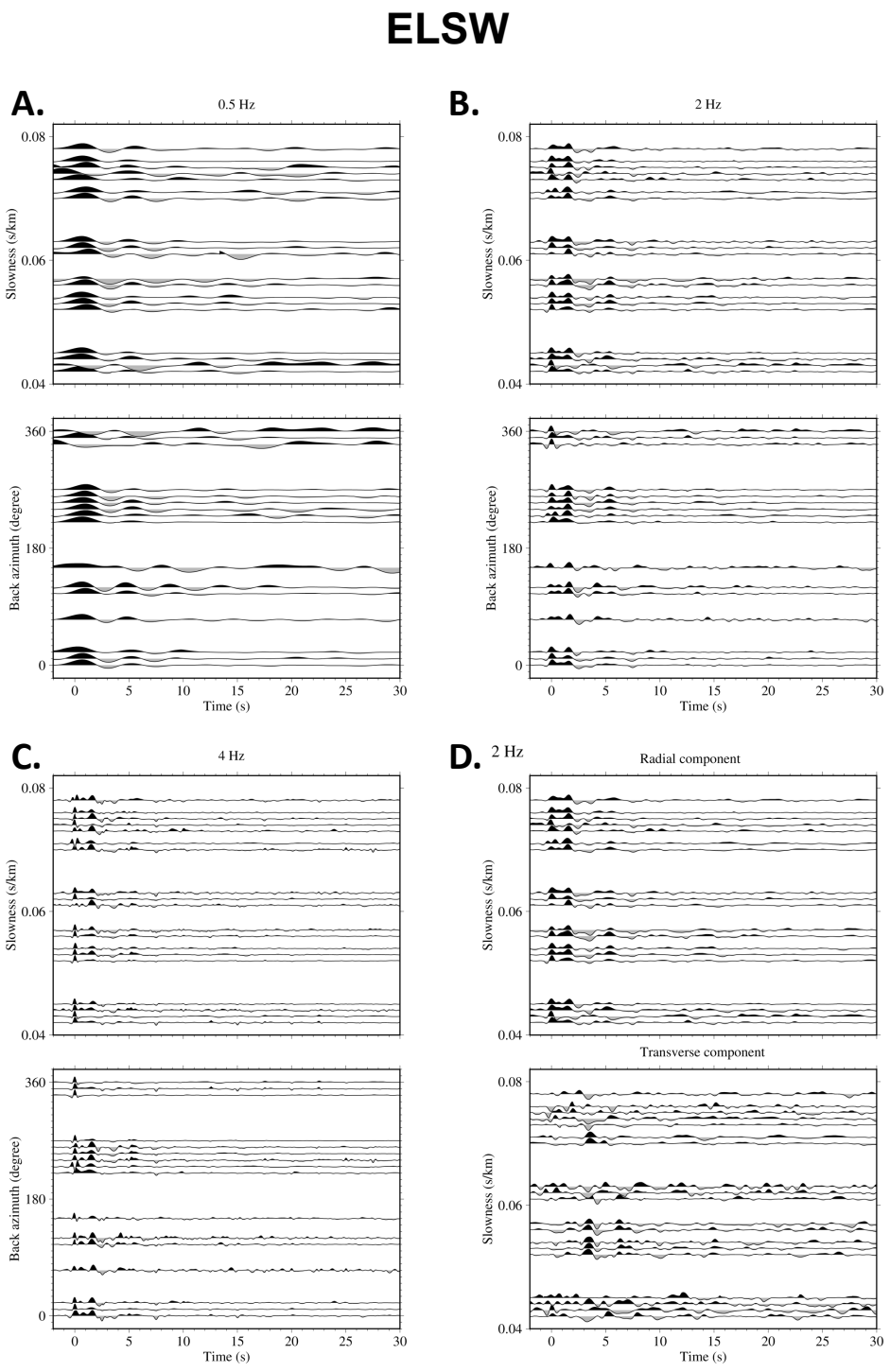

Figure A.10: Receiver functions computed at ELSW plotted by back azimuth and slowness. Receiver functions are binned by back azimuth every 10°and by slowness every 0.001 s/km. a) Receiver functions calculated with a maximum frequency of 0.5 Hz. b) Receiver functions calculated with a maximum frequency of 2 Hz. c) Receiver functions calculated with a maximum frequency of 4 Hz. d) 2 Hz maximum frequency radial and transverse receiver functions plotted by slowness.

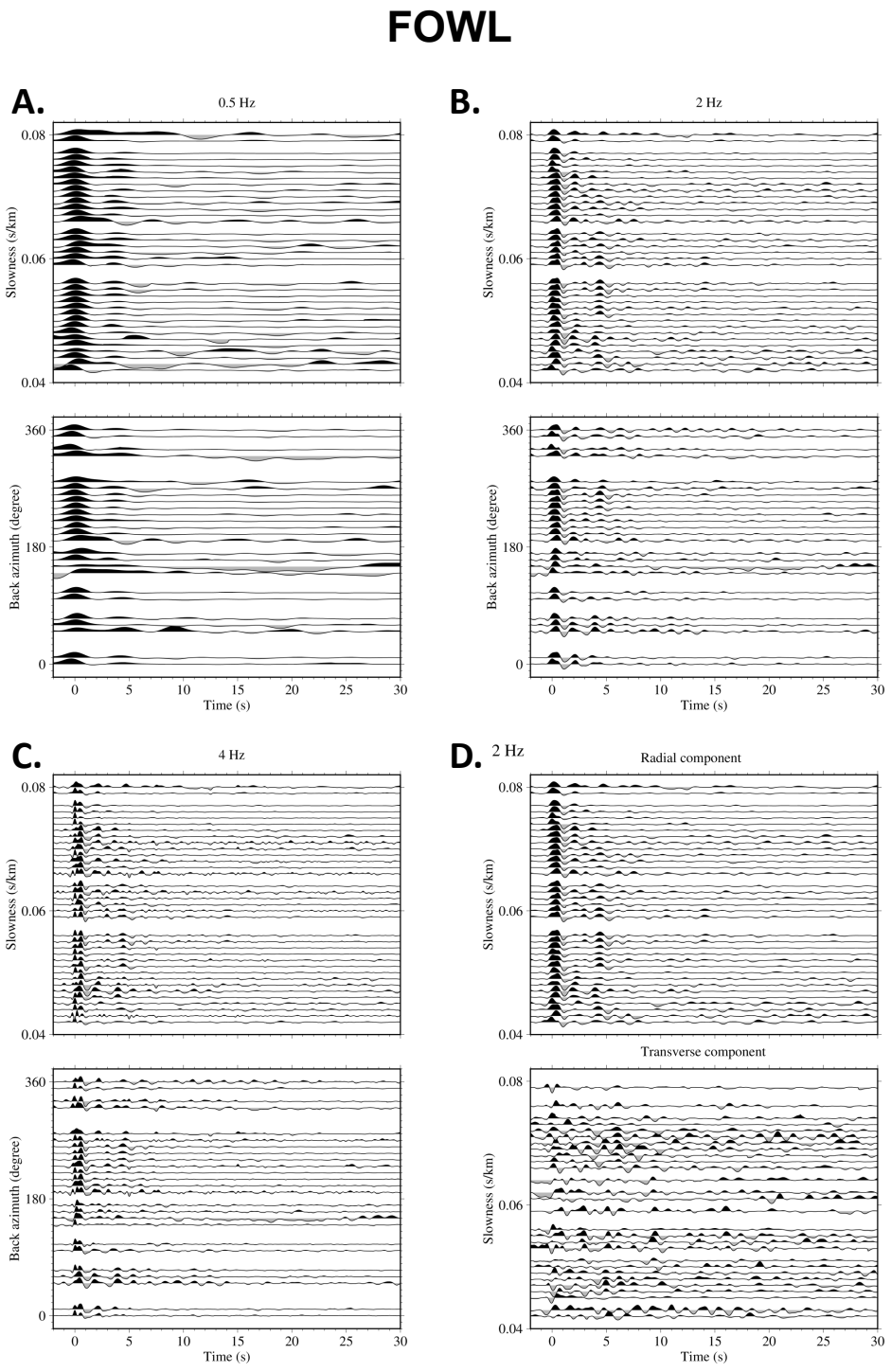

Figure A.11: Receiver functions computed at FOWL plotted by back azimuth and slowness. Receiver functions are binned by back azimuth every 10°and by slowness every 0.001 s/km. a) Receiver functions calculated with a maximum frequency of 0.5 Hz. b) Receiver functions calculated with a maximum frequency of 2 Hz. c) Receiver functions calculated with a maximum frequency of 4 Hz. d) 2 Hz maximum frequency radial and transverse receiver functions plotted by slowness.

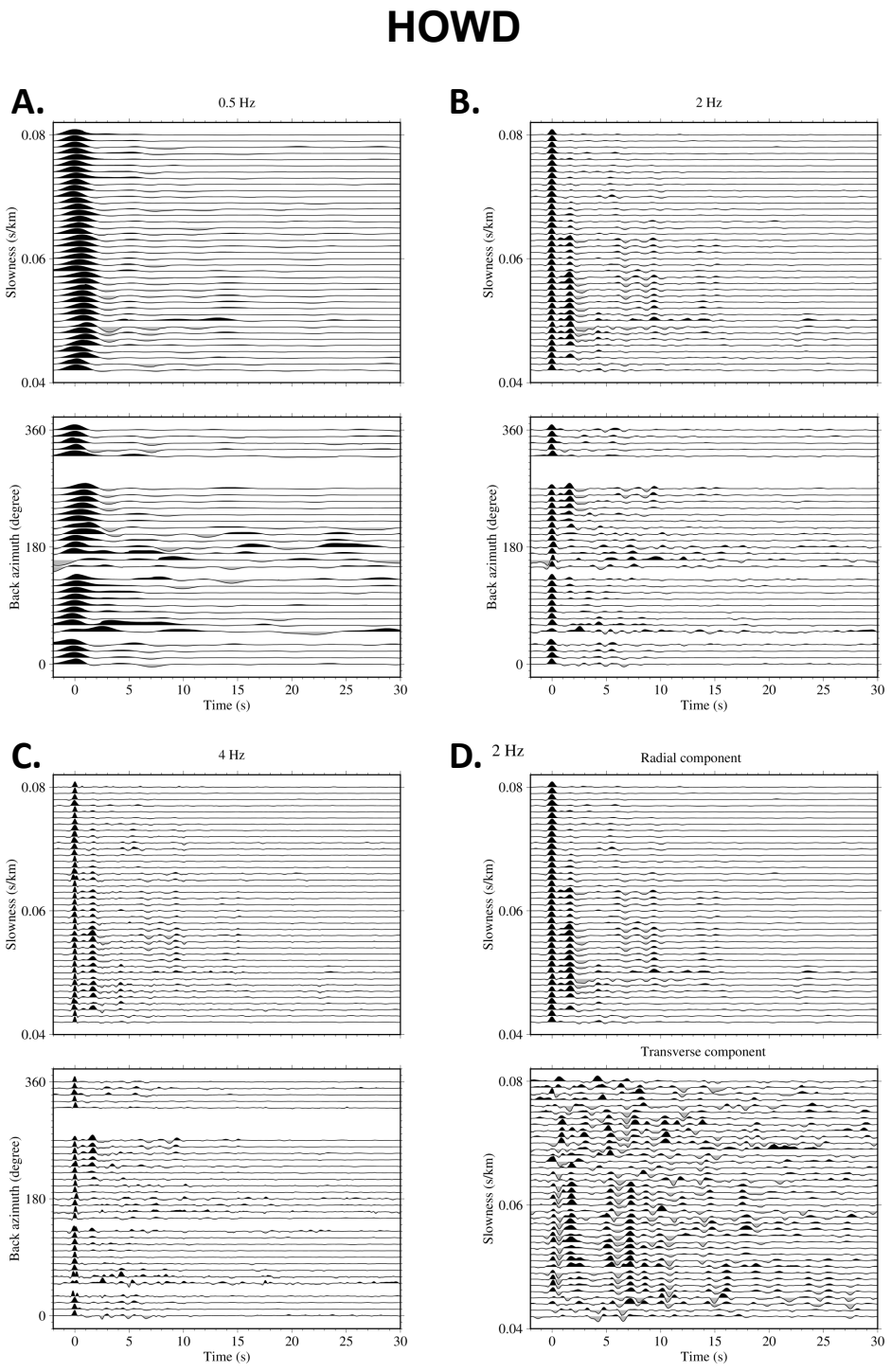

Figure A.12: Receiver functions computed at HOWD plotted by back azimuth and slowness. Receiver functions are binned by back azimuth every 10°and by slowness every 0.001 s/km. a) Receiver functions calculated with a maximum frequency of 0.5 Hz. b) Receiver functions calculated with a maximum frequency of 2 Hz. c) Receiver functions calculated with a maximum frequency of 4 Hz. d) 2 Hz maximum frequency radial and transverse receiver functions plotted by slowness.

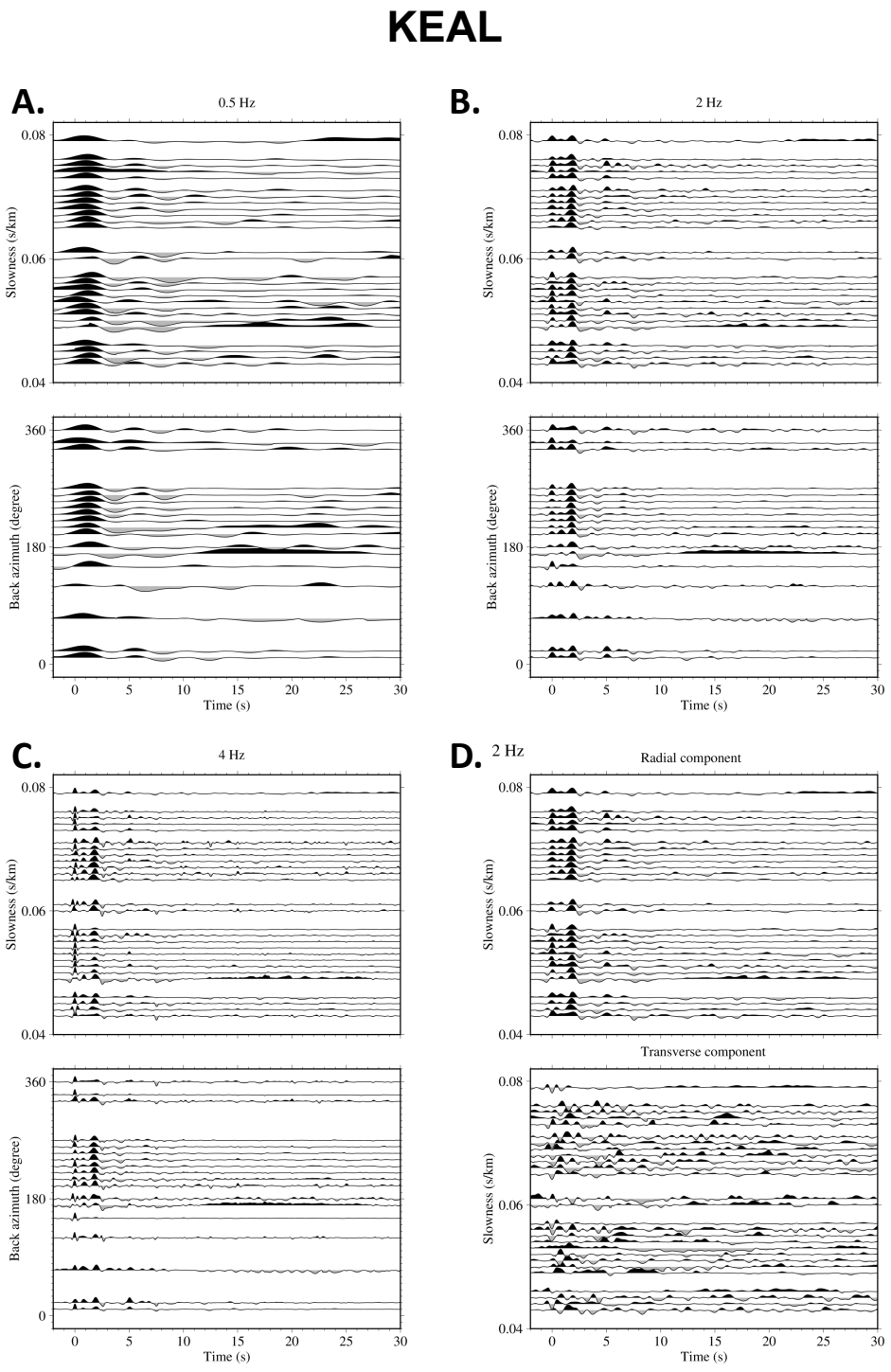

Figure A.13: Receiver functions computed at KEAL plotted by back azimuth and slowness. Receiver functions are binned by back azimuth every 10°and by slowness every 0.001 s/km. a) Receiver functions calculated with a maximum frequency of 0.5 Hz. b) Receiver functions calculated with a maximum frequency of 2 Hz. c) Receiver functions calculated with a maximum frequency of 4 Hz. d) 2 Hz maximum frequency radial and transverse receiver functions plotted by slowness.

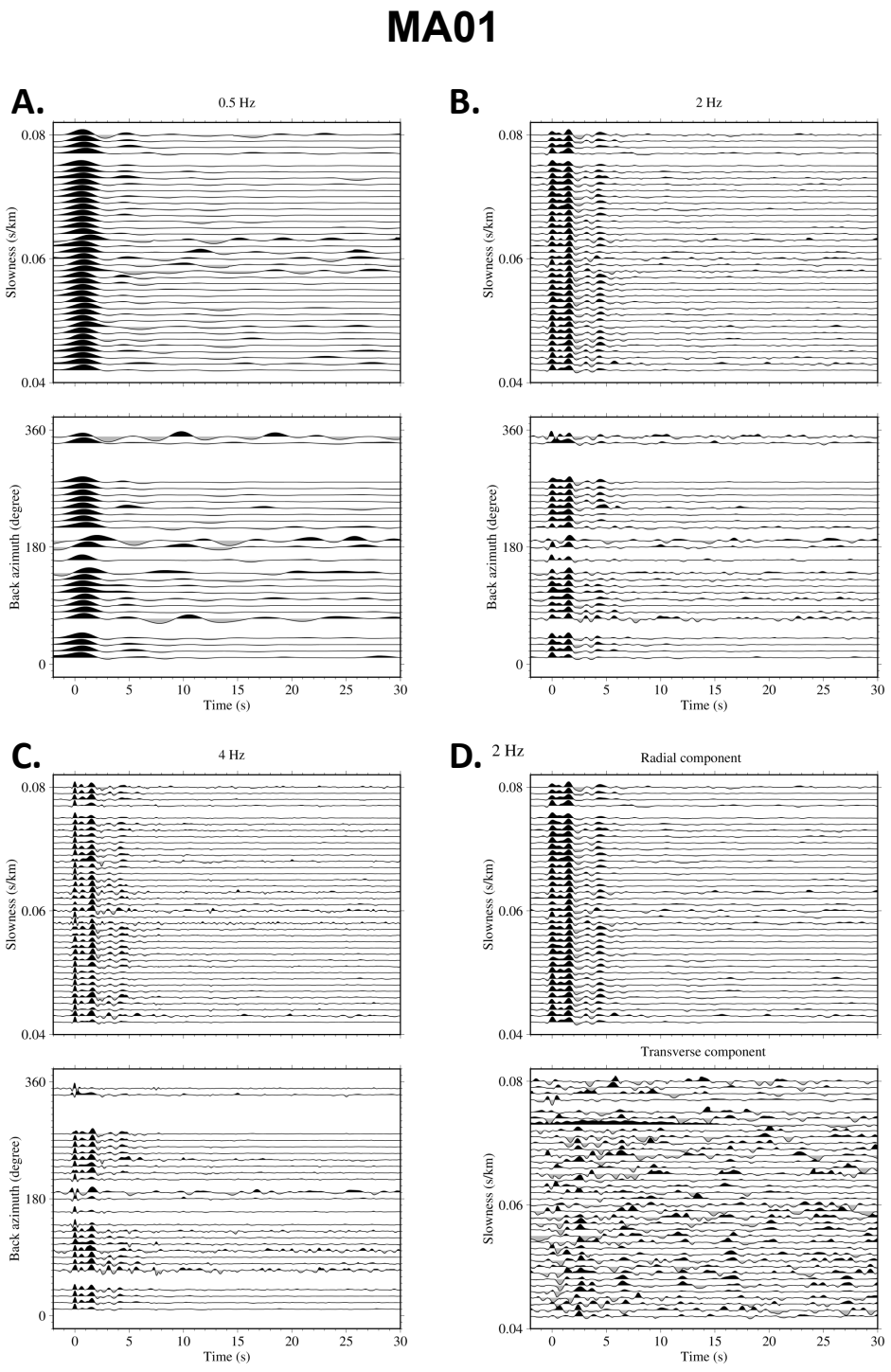

Figure A.14: Receiver functions computed at MA01 plotted by back azimuth and slowness. Receiver functions are binned by back azimuth every 10°and by slowness every 0.001 s/km. a) Receiver functions calculated with a maximum frequency of 0.5 Hz. b) Receiver functions calculated with a maximum frequency of 2 Hz. c) Receiver functions calculated with a maximum frequency of 4 Hz. d) 2 Hz maximum frequency radial and transverse receiver functions plotted by slowness.

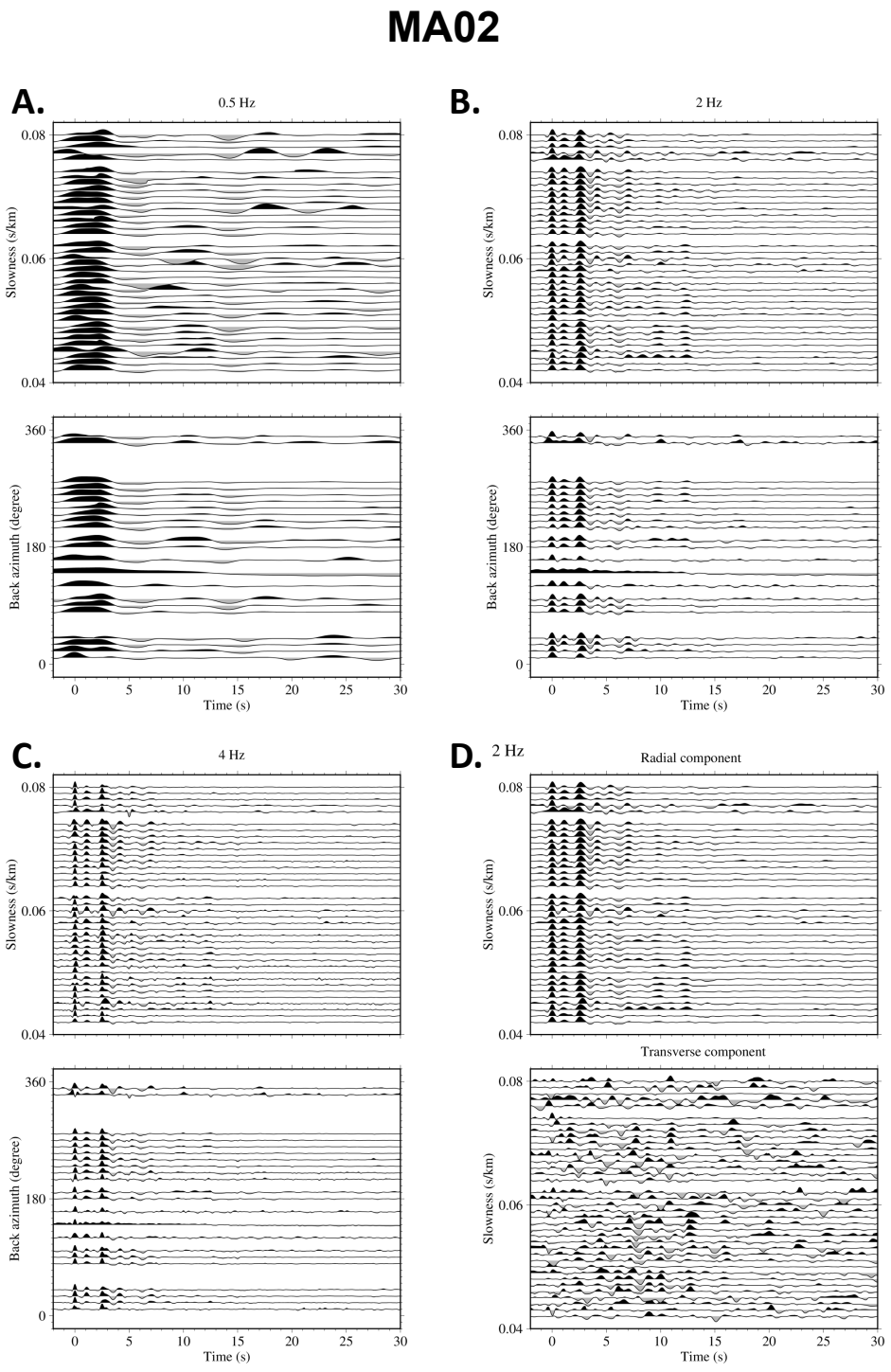

Figure A.15: Receiver functions computed at MA02 plotted by back azimuth and slowness. Receiver functions are binned by back azimuth every 10°and by slowness every 0.001 s/km. a) Receiver functions calculated with a maximum frequency of 0.5 Hz. b) Receiver functions calculated with a maximum frequency of 2 Hz. c) Receiver functions calculated with a maximum frequency of 4 Hz. d) 2 Hz maximum frequency radial and transverse receiver functions plotted by slowness.

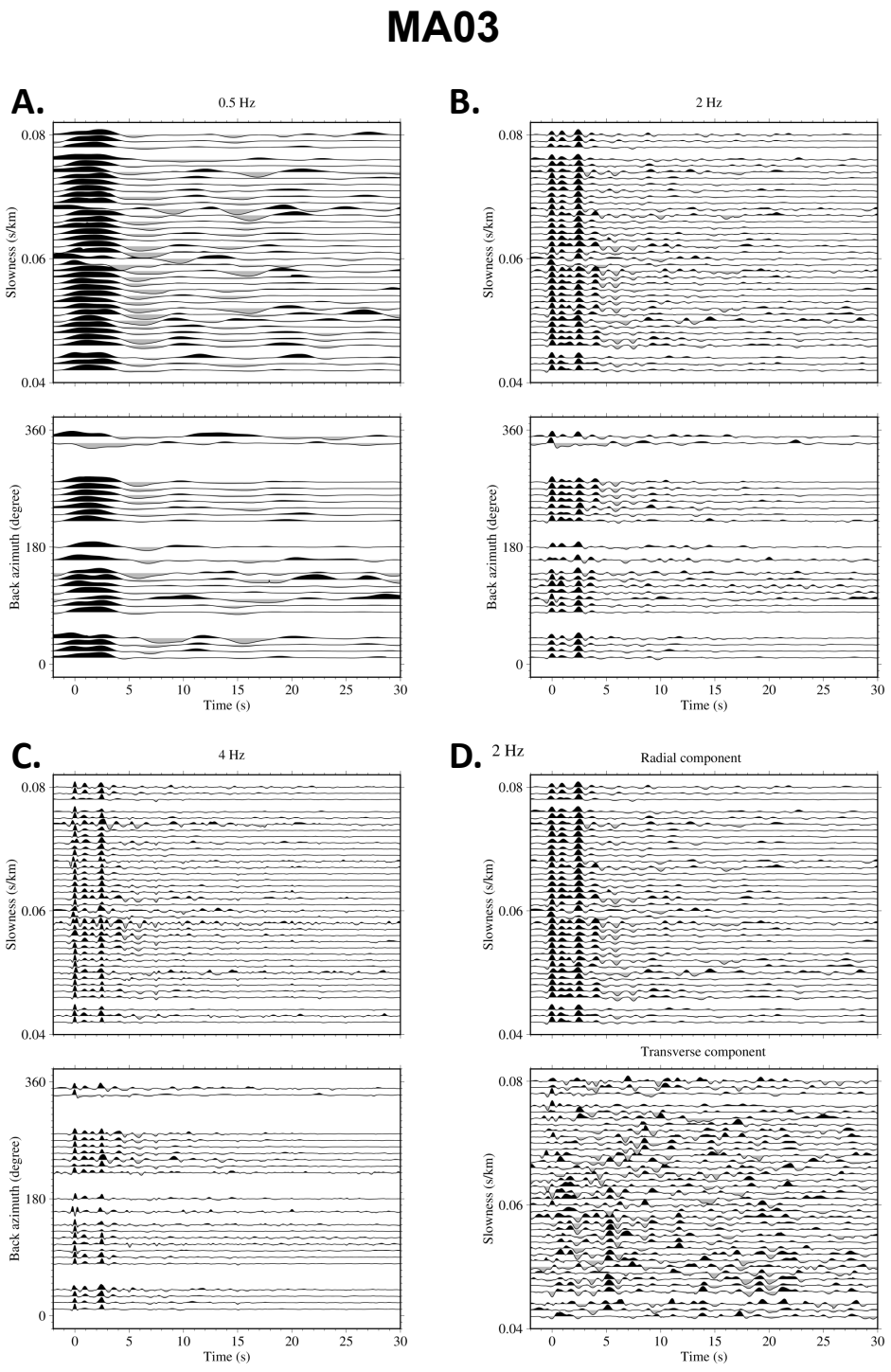

Figure A.16: Receiver functions computed at MA03 plotted by back azimuth and slowness. Receiver functions are binned by back azimuth every 10°and by slowness every 0.001 s/km. a) Receiver functions calculated with a maximum frequency of 0.5 Hz. b) Receiver functions calculated with a maximum frequency of 2 Hz. c) Receiver functions calculated with a maximum frequency of 4 Hz. d) 2 Hz maximum frequency radial and transverse receiver functions plotted by slowness.

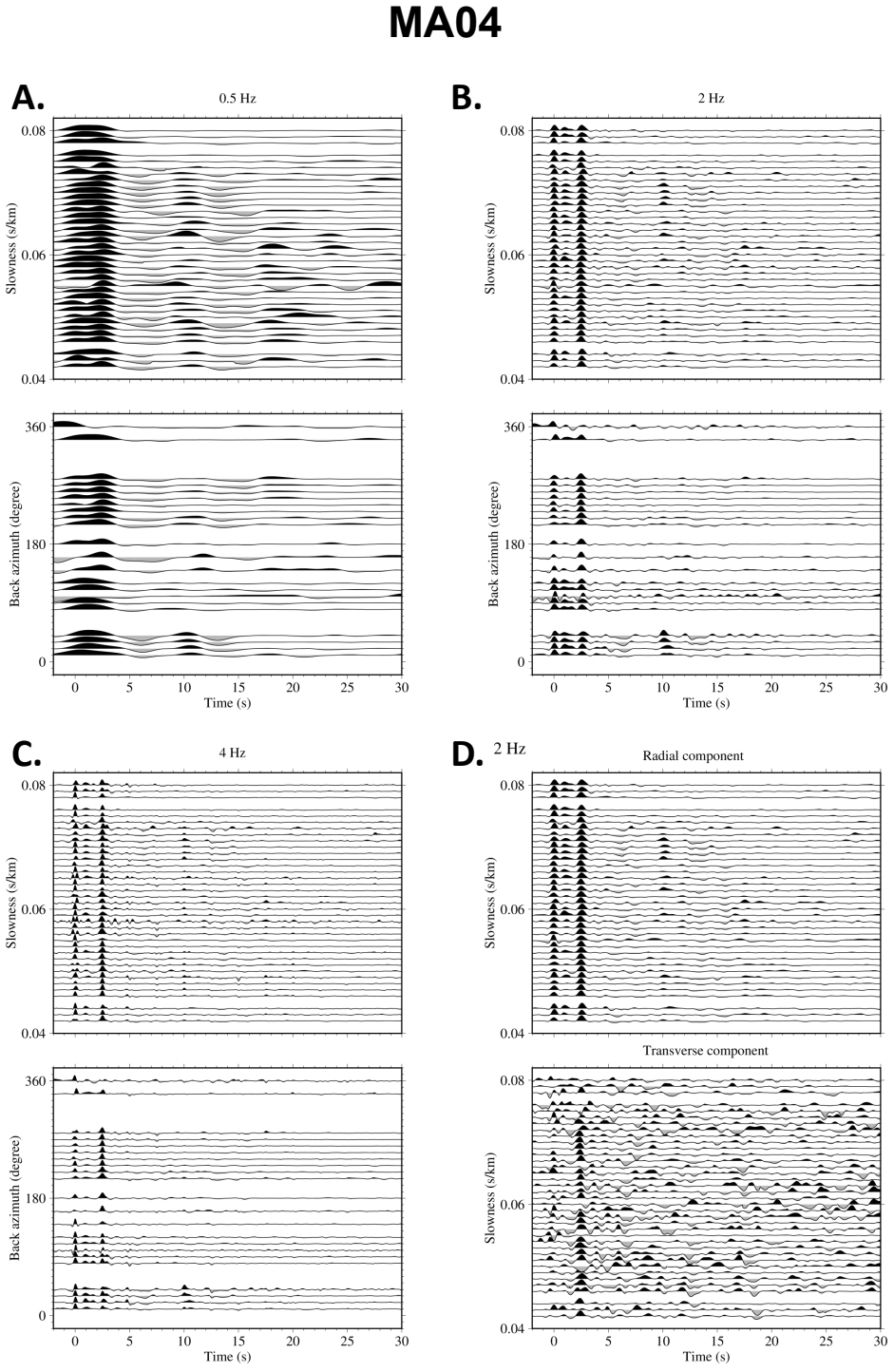

Figure A.17: Receiver functions computed at MA04 plotted by back azimuth and slowness. Receiver functions are binned by back azimuth every 10°and by slowness every 0.001 s/km. a) Receiver functions calculated with a maximum frequency of 0.5 Hz. b) Receiver functions calculated with a maximum frequency of 2 Hz. c) Receiver functions calculated with a maximum frequency of 4 Hz. d) 2 Hz maximum frequency radial and transverse receiver functions plotted by slowness.

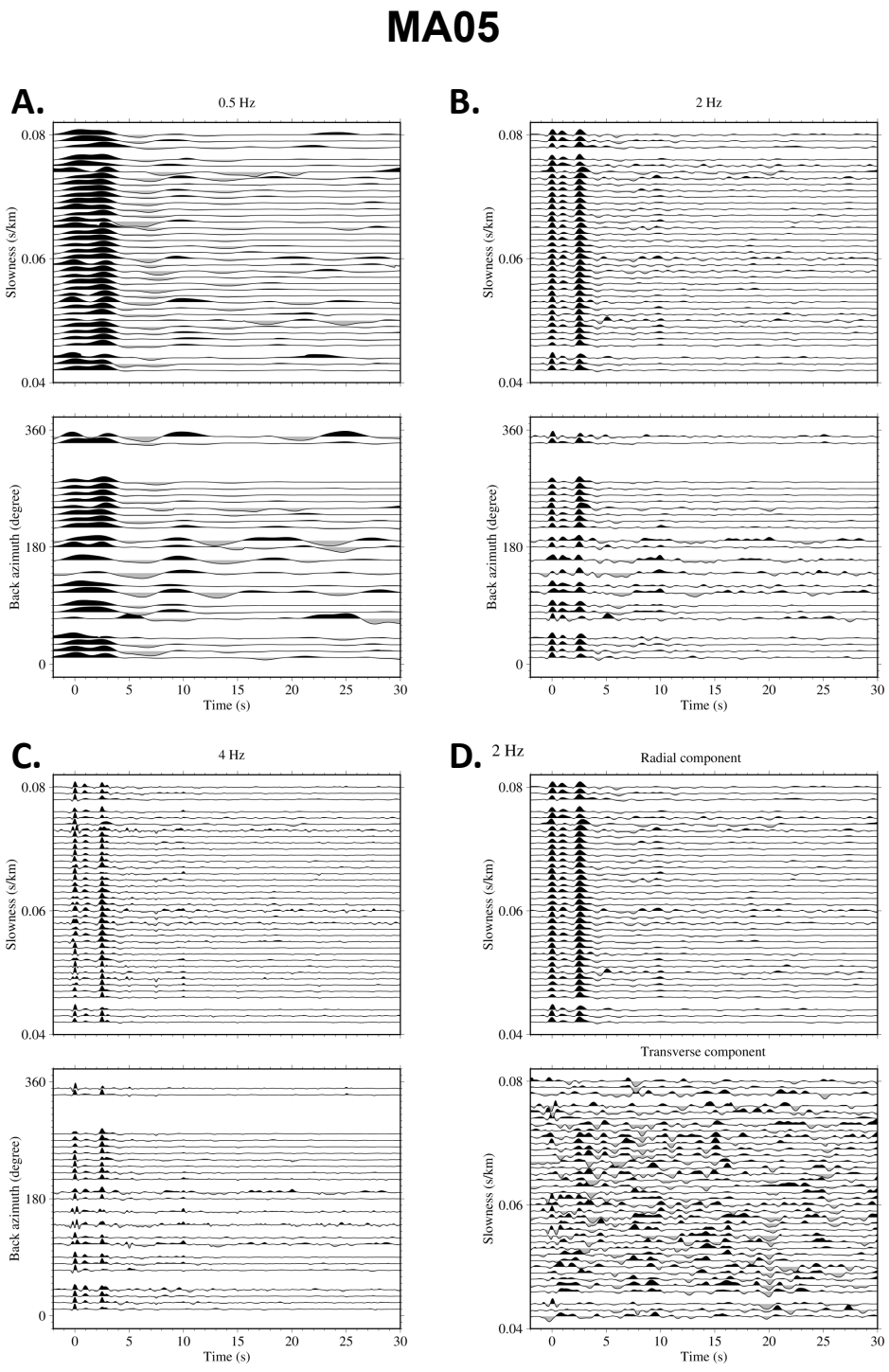

Figure A.18: Receiver functions computed at MA05 plotted by back azimuth and slowness. Receiver functions are binned by back azimuth every 10°and by slowness every 0.001 s/km. a) Receiver functions calculated with a maximum frequency of 0.5 Hz. b) Receiver functions calculated with a maximum frequency of 2 Hz. c) Receiver functions calculated with a maximum frequency of 4 Hz. d) 2 Hz maximum frequency radial and transverse receiver functions plotted by slowness.

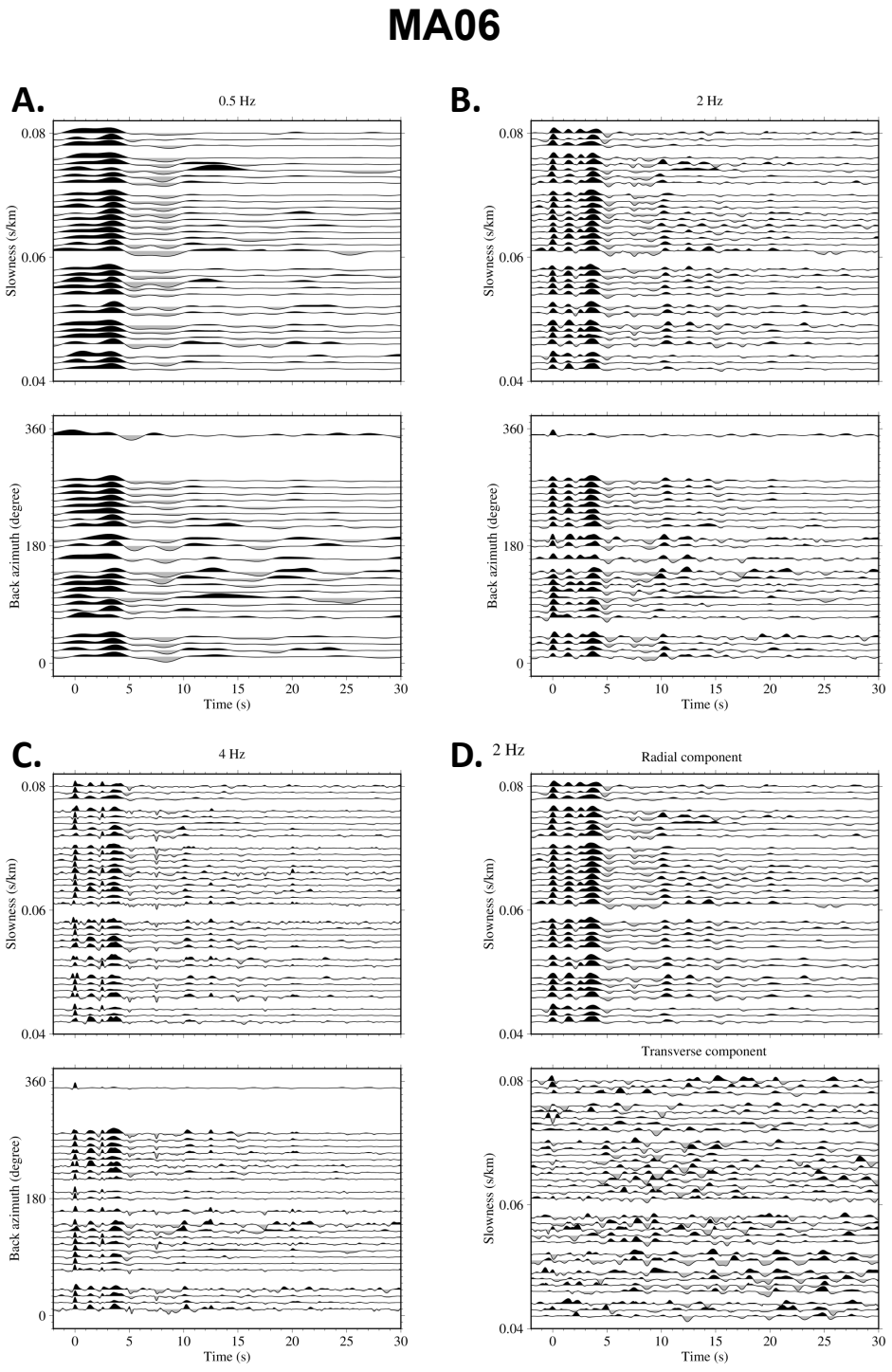

Figure A.19: Receiver functions computed at MA06 plotted by back azimuth and slowness. Receiver functions are binned by back azimuth every 10°and by slowness every 0.001 s/km. a) Receiver functions calculated with a maximum frequency of 0.5 Hz. b) Receiver functions calculated with a maximum frequency of 2 Hz. c) Receiver functions calculated with a maximum frequency of 4 Hz. d) 2 Hz maximum frequency radial and transverse receiver functions plotted by slowness.

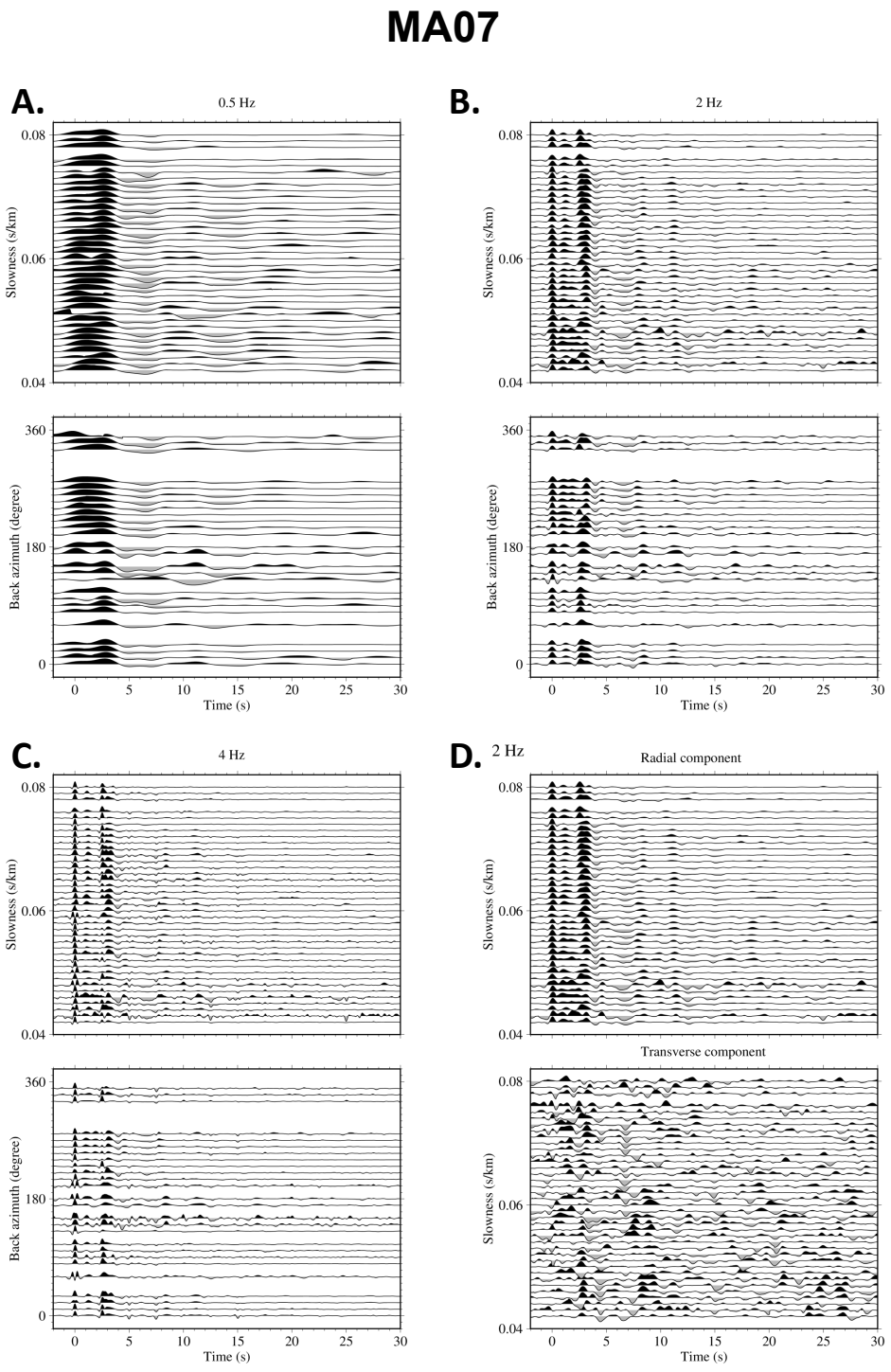

Figure A.20: Receiver functions computed at MA07 plotted by back azimuth and slowness. Receiver functions are binned by back azimuth every 10°and by slowness every 0.001 s/km. a) Receiver functions calculated with a maximum frequency of 0.5 Hz. b) Receiver functions calculated with a maximum frequency of 2 Hz. c) Receiver functions calculated with a maximum frequency of 4 Hz. d) 2 Hz maximum frequency radial and transverse receiver functions plotted by slowness.

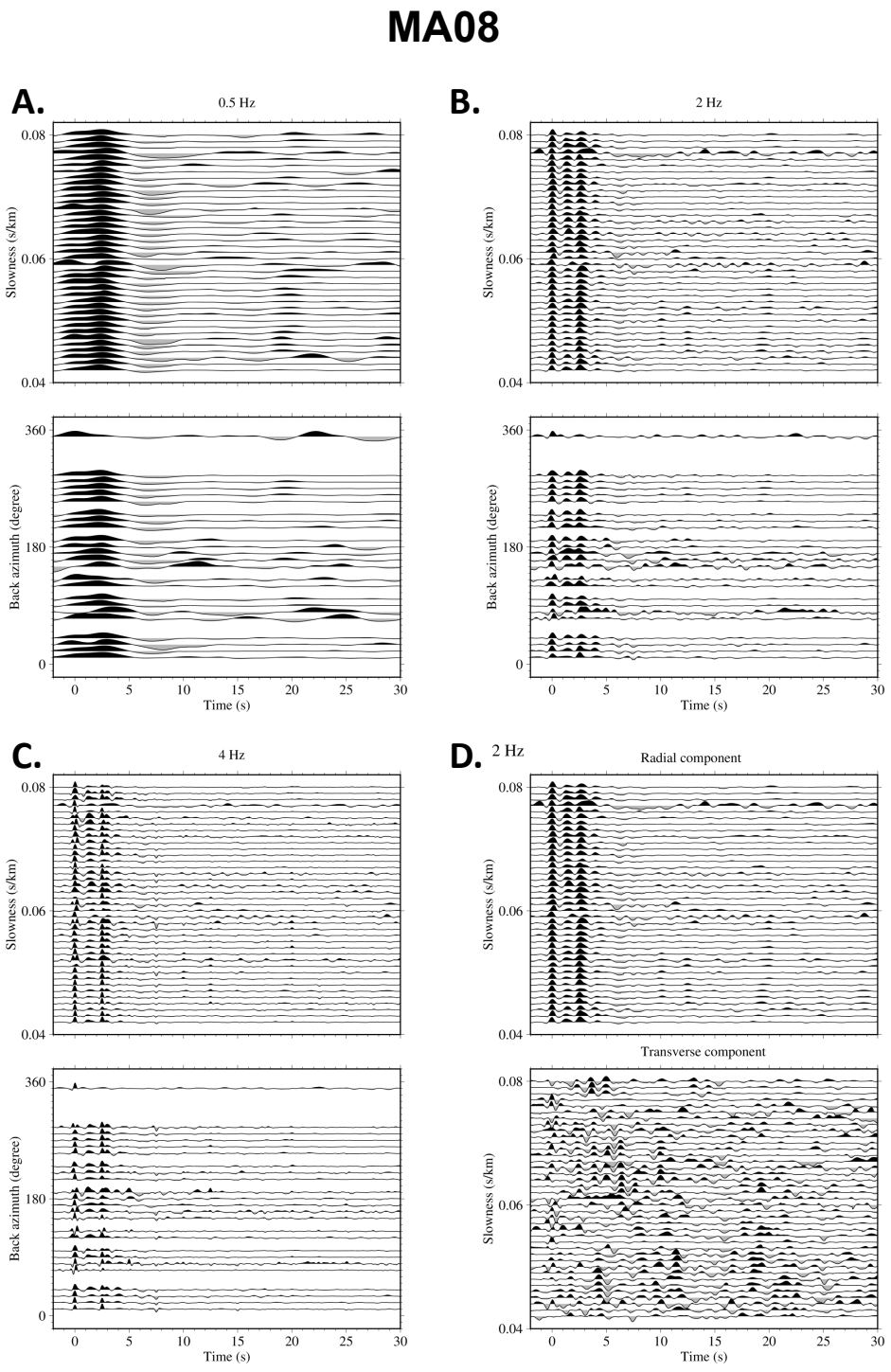

Figure A.21: Receiver functions computed at MA08 plotted by back azimuth and slowness. Receiver functions are binned by back azimuth every 10°and by slowness every 0.001 s/km. a) Receiver functions calculated with a maximum frequency of 0.5 Hz. b) Receiver functions calculated with a maximum frequency of 2 Hz. c) Receiver functions calculated with a maximum frequency of 4 Hz. d) 2 Hz maximum frequency radial and transverse receiver functions plotted by slowness.

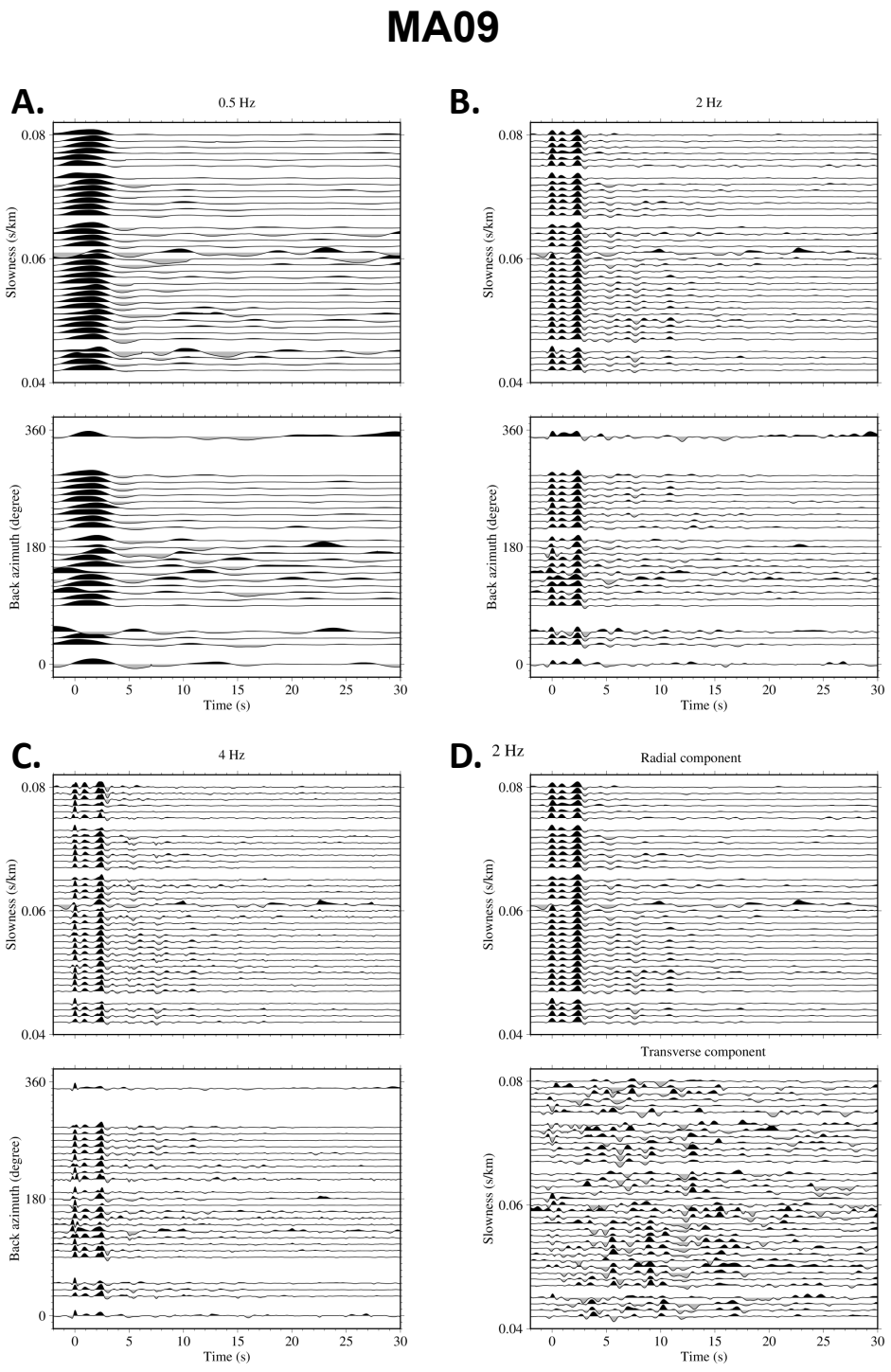

Figure A.22: Receiver functions computed at MA09 plotted by back azimuth and slowness. Receiver functions are binned by back azimuth every 10°and by slowness every 0.001 s/km. a) Receiver functions calculated with a maximum frequency of 0.5 Hz. b) Receiver functions calculated with a maximum frequency of 2 Hz. c) Receiver functions calculated with a maximum frequency of 4 Hz. d) 2 Hz maximum frequency radial and transverse receiver functions plotted by slowness.

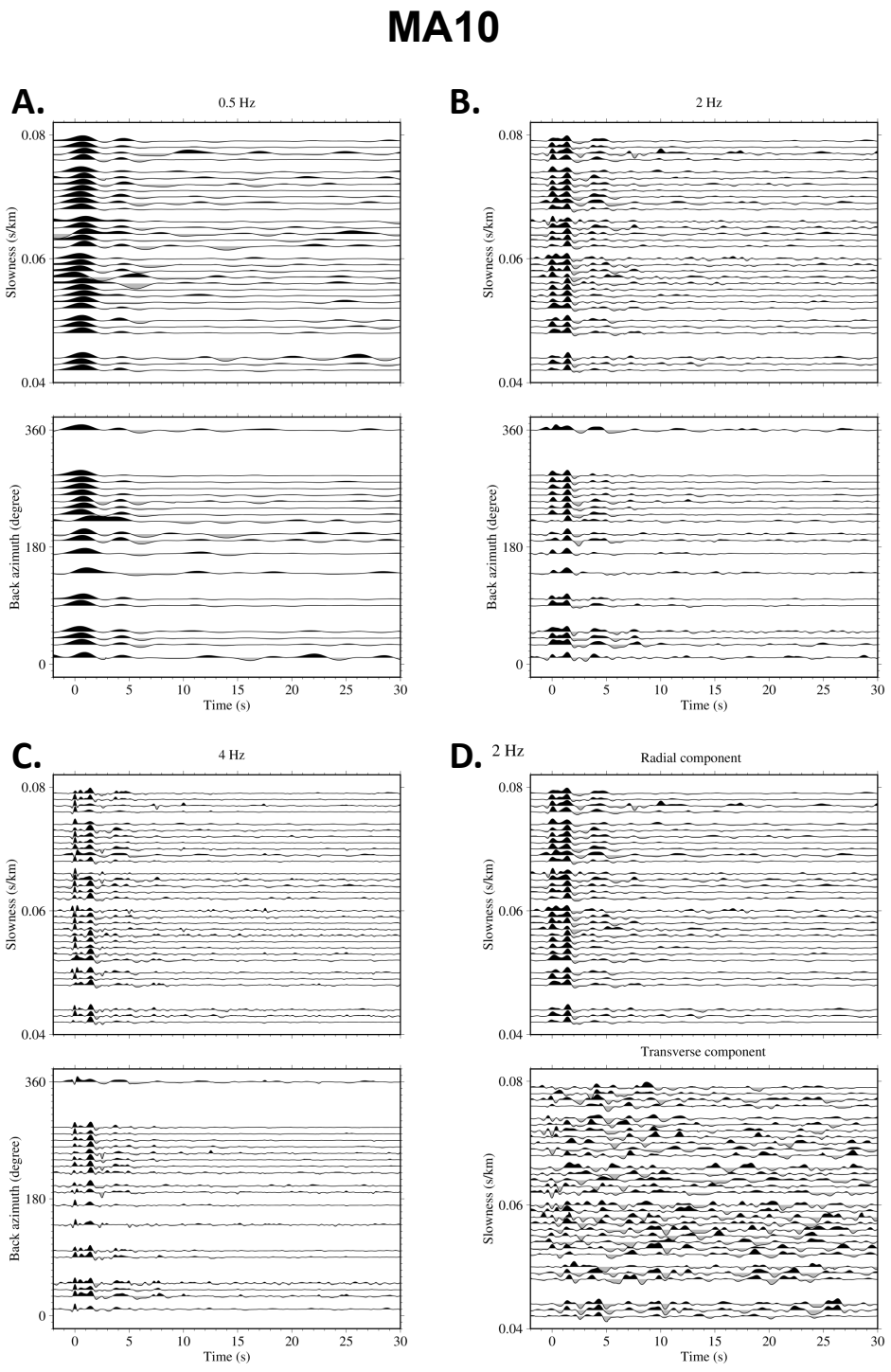

Figure A.23: Receiver functions computed at MA10 plotted by back azimuth and slowness. Receiver functions are binned by back azimuth every 10°and by slowness every 0.001 s/km. a) Receiver functions calculated with a maximum frequency of 0.5 Hz. b) Receiver functions calculated with a maximum frequency of 2 Hz. c) Receiver functions calculated with a maximum frequency of 4 Hz. d) 2 Hz maximum frequency radial and transverse receiver functions plotted by slowness.

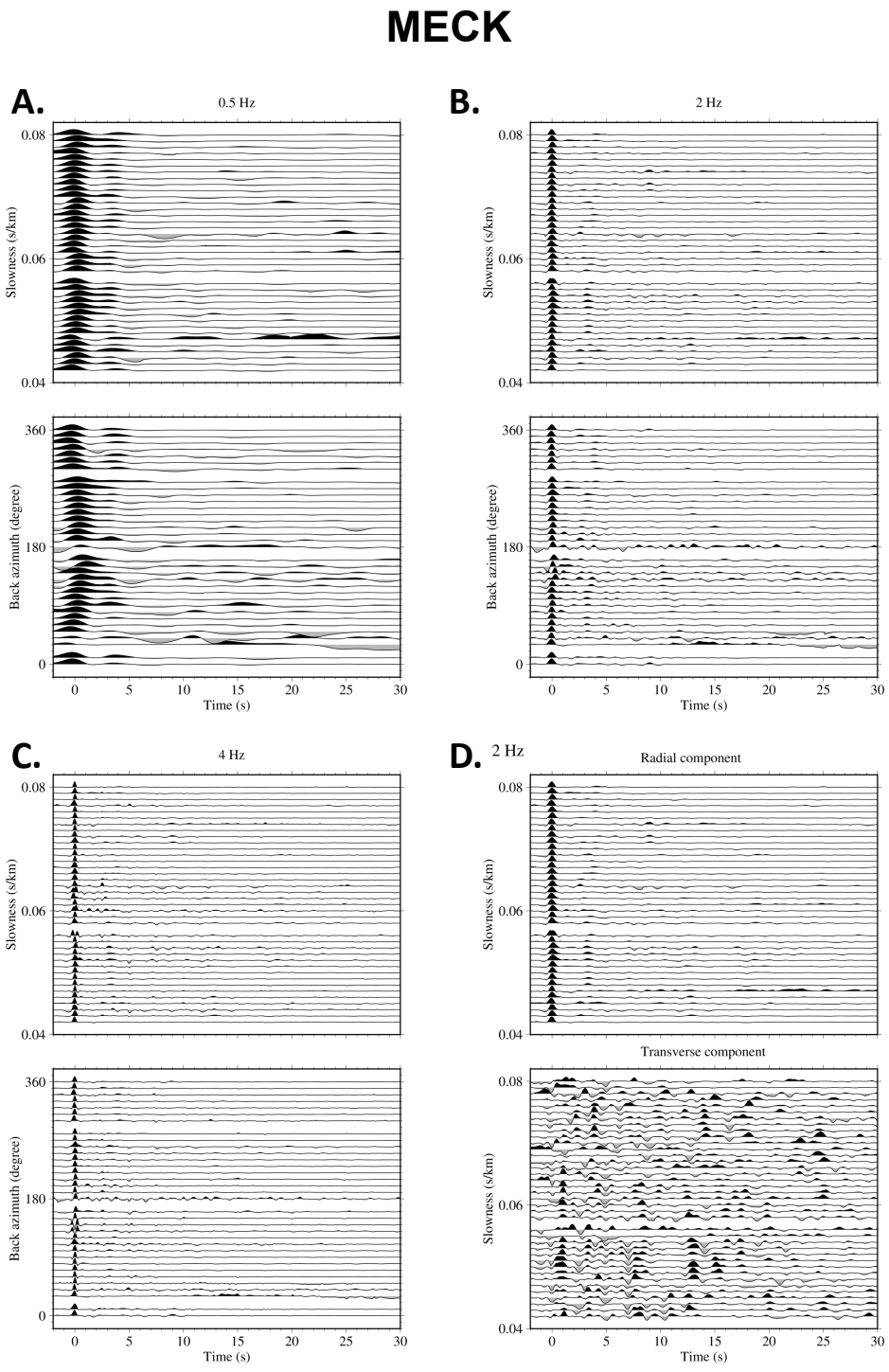

Figure A.24: Receiver functions computed at MECK plotted by back azimuth and slowness. Receiver functions are binned by back azimuth every 10°and by slowness every 0.001 s/km. a) Receiver functions calculated with a maximum frequency of 0.5 Hz. b) Receiver functions calculated with a maximum frequency of 2 Hz. c) Receiver functions calculated with a maximum frequency of 4 Hz. d) 2 Hz maximum frequency radial and transverse receiver functions plotted by slowness.

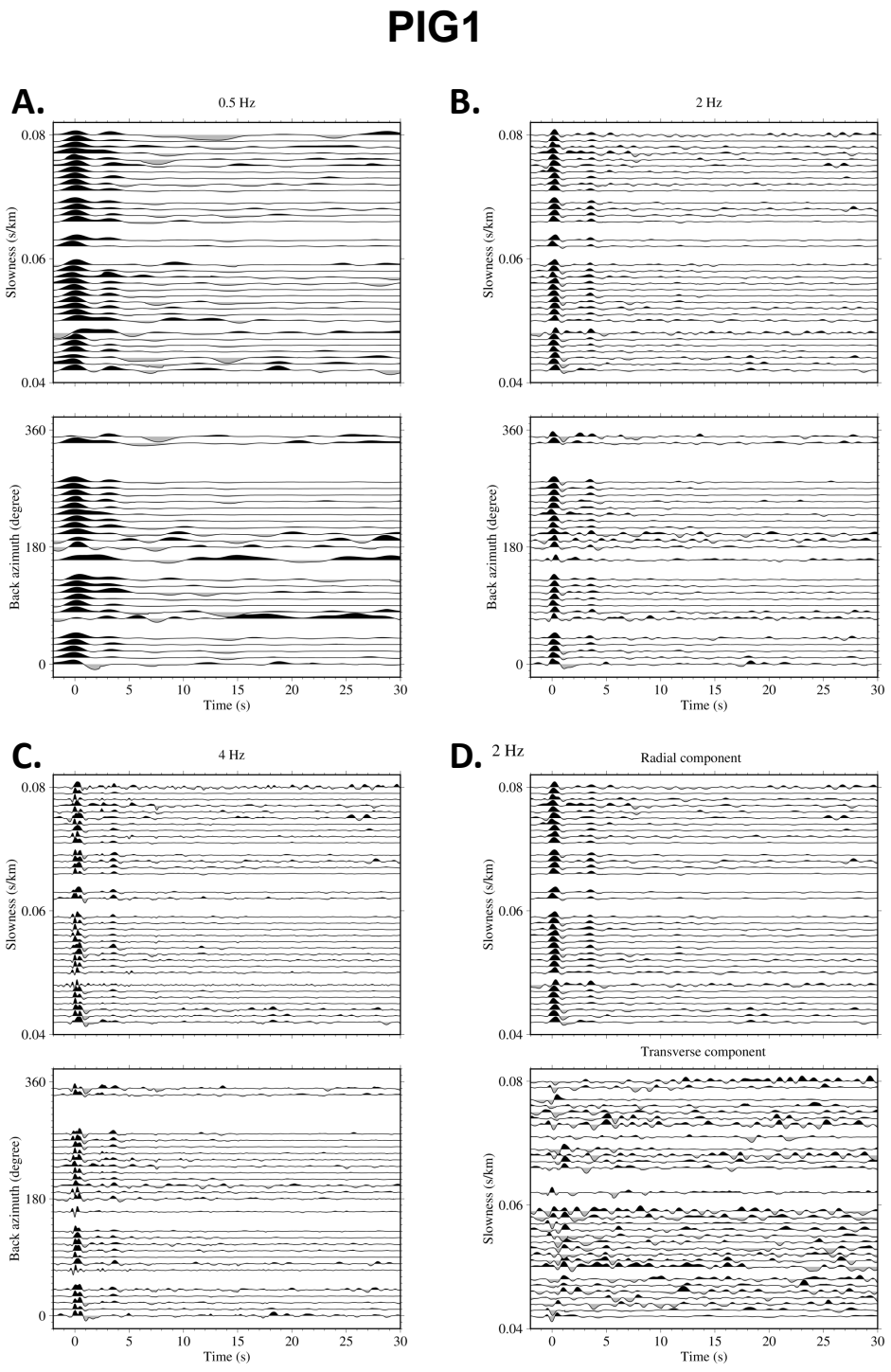

Figure A.25: Receiver functions computed at PIG1 plotted by back azimuth and slowness. Receiver functions are binned by back azimuth every 10°and by slowness every 0.001 s/km. a) Receiver functions calculated with a maximum frequency of 0.5 Hz. b) Receiver functions calculated with a maximum frequency of 2 Hz. c) Receiver functions calculated with a maximum frequency of 4 Hz. d) 2 Hz maximum frequency radial and transverse receiver functions plotted by slowness.

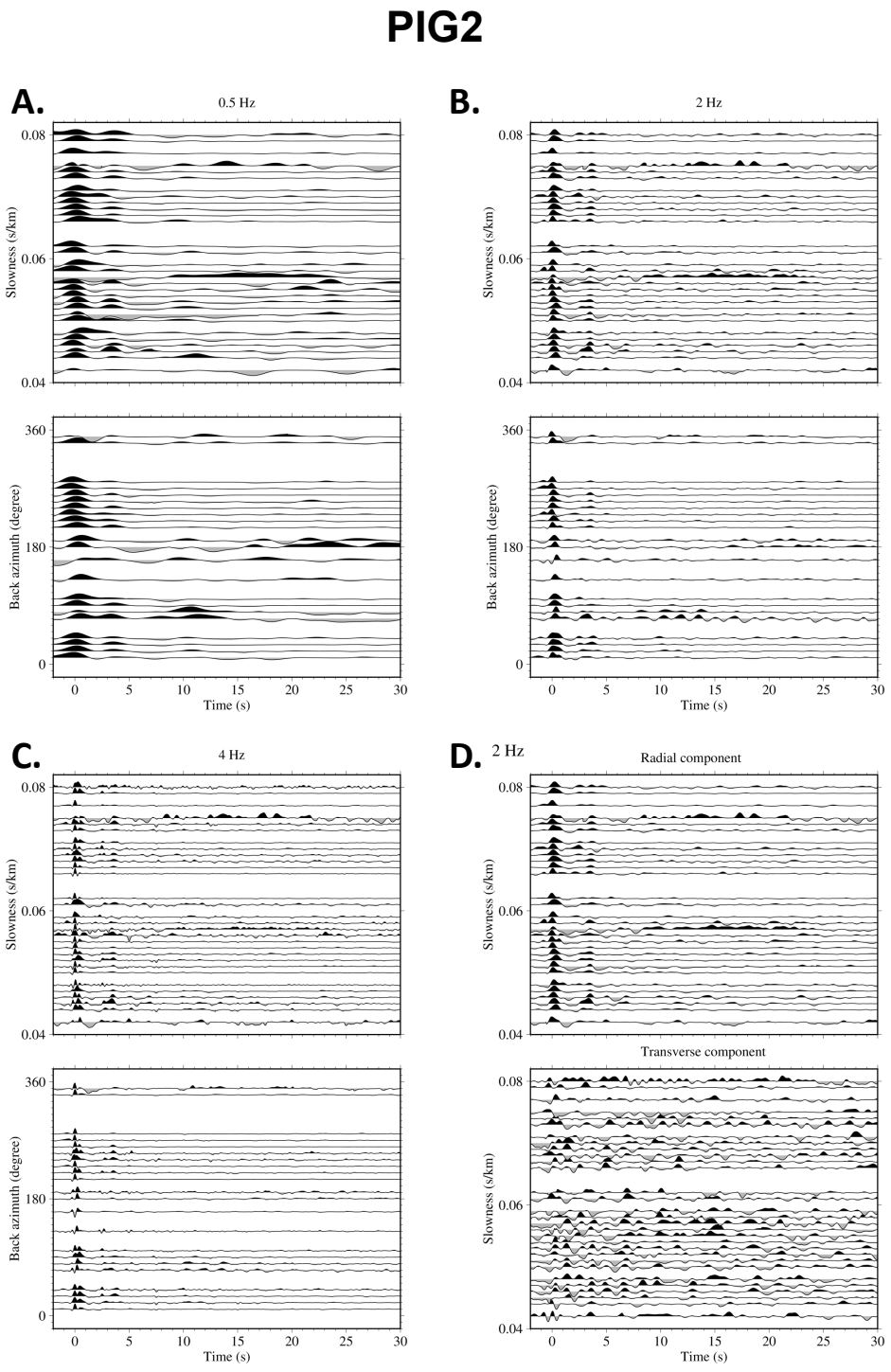

Figure A.26: Receiver functions computed at PIG2 plotted by back azimuth and slowness. Receiver functions are binned by back azimuth every 10°and by slowness every 0.001 s/km. a) Receiver functions calculated with a maximum frequency of 0.5 Hz. b) Receiver functions calculated with a maximum frequency of 2 Hz. c) Receiver functions calculated with a maximum frequency of 4 Hz. d) 2 Hz maximum frequency radial and transverse receiver functions plotted by slowness.

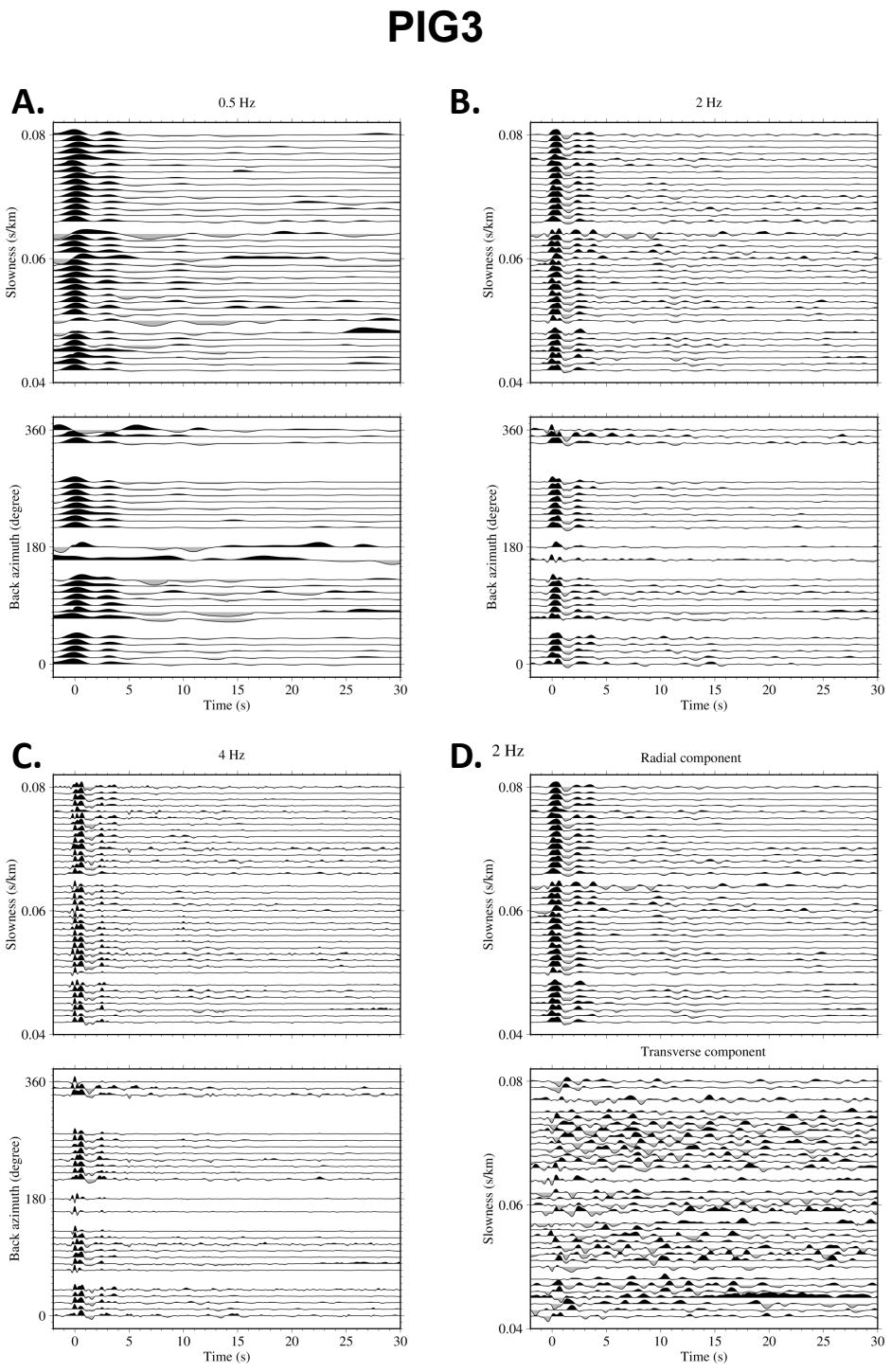

Figure A.27: Receiver functions computed at PIG3 plotted by back azimuth and slowness. Receiver functions are binned by back azimuth every 10°and by slowness every 0.001 s/km. a) Receiver functions calculated with a maximum frequency of 0.5 Hz. b) Receiver functions calculated with a maximum frequency of 2 Hz. c) Receiver functions calculated with a maximum frequency of 4 Hz. d) 2 Hz maximum frequency radial and transverse receiver functions plotted by slowness.

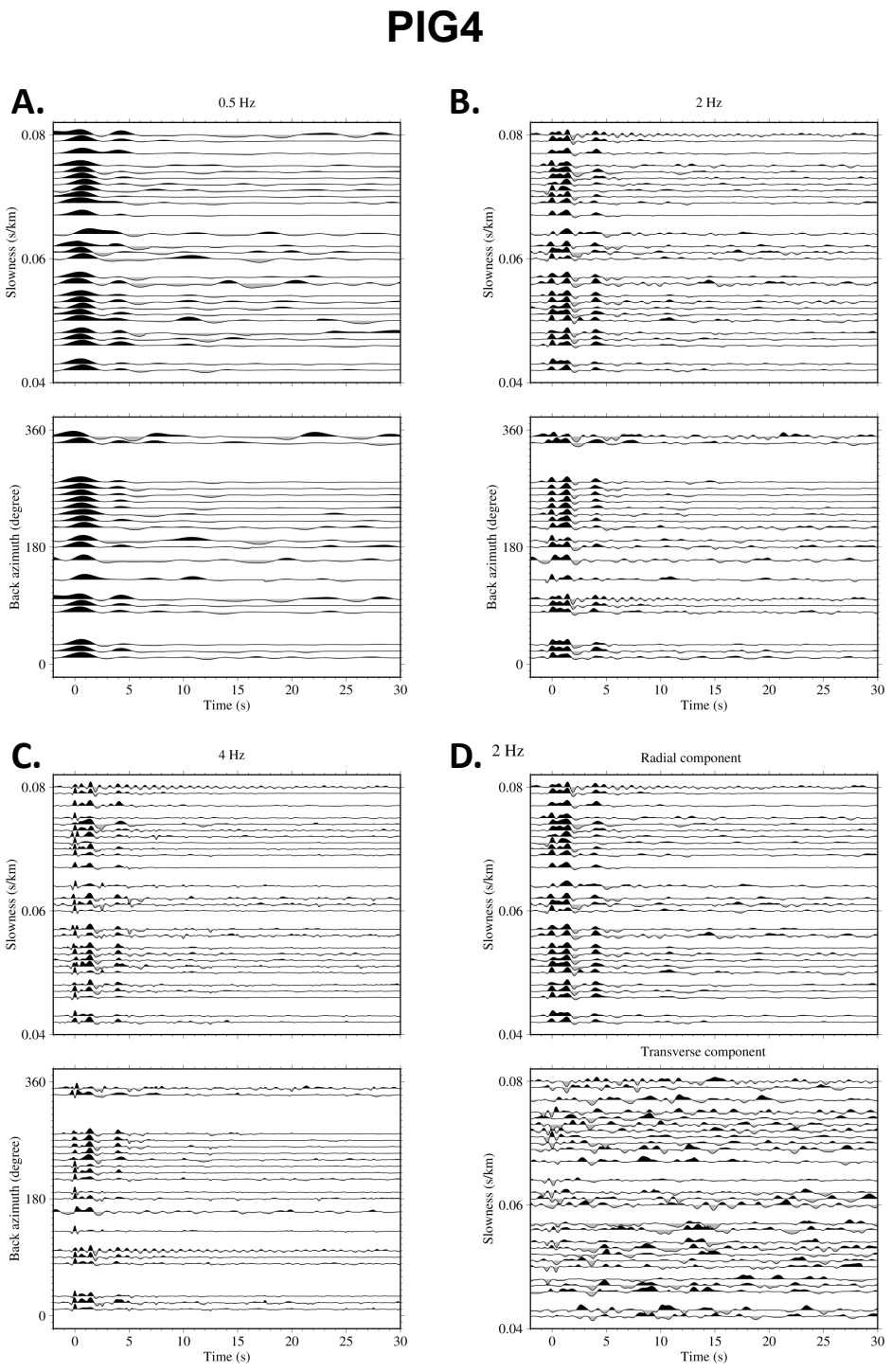

Figure A.28: Receiver functions computed at PIG4 plotted by back azimuth and slowness. Receiver functions are binned by back azimuth every 10°and by slowness every 0.001 s/km. a) Receiver functions calculated with a maximum frequency of 0.5 Hz. b) Receiver functions calculated with a maximum frequency of 2 Hz. c) Receiver functions calculated with a maximum frequency of 4 Hz. d) 2 Hz maximum frequency radial and transverse receiver functions plotted by slowness.

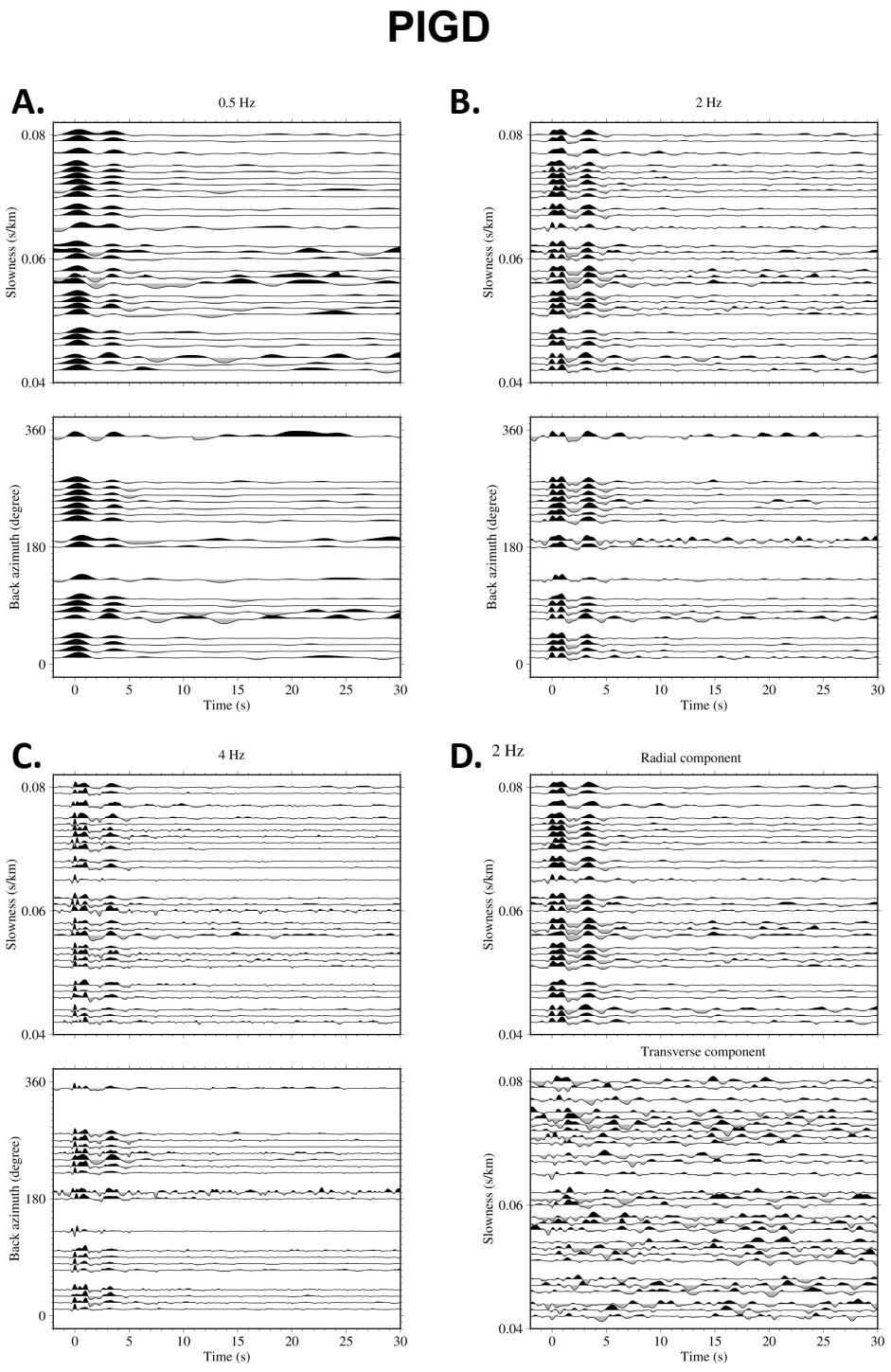

Figure A.29: Receiver functions computed at PIGD plotted by back azimuth and slowness. Receiver functions are binned by back azimuth every 10°and by slowness every 0.001 s/km. a) Receiver functions calculated with a maximum frequency of 0.5 Hz. b) Receiver functions calculated with a maximum frequency of 2 Hz. c) Receiver functions calculated with a maximum frequency of 4 Hz. d) 2 Hz maximum frequency radial and transverse receiver functions plotted by slowness.

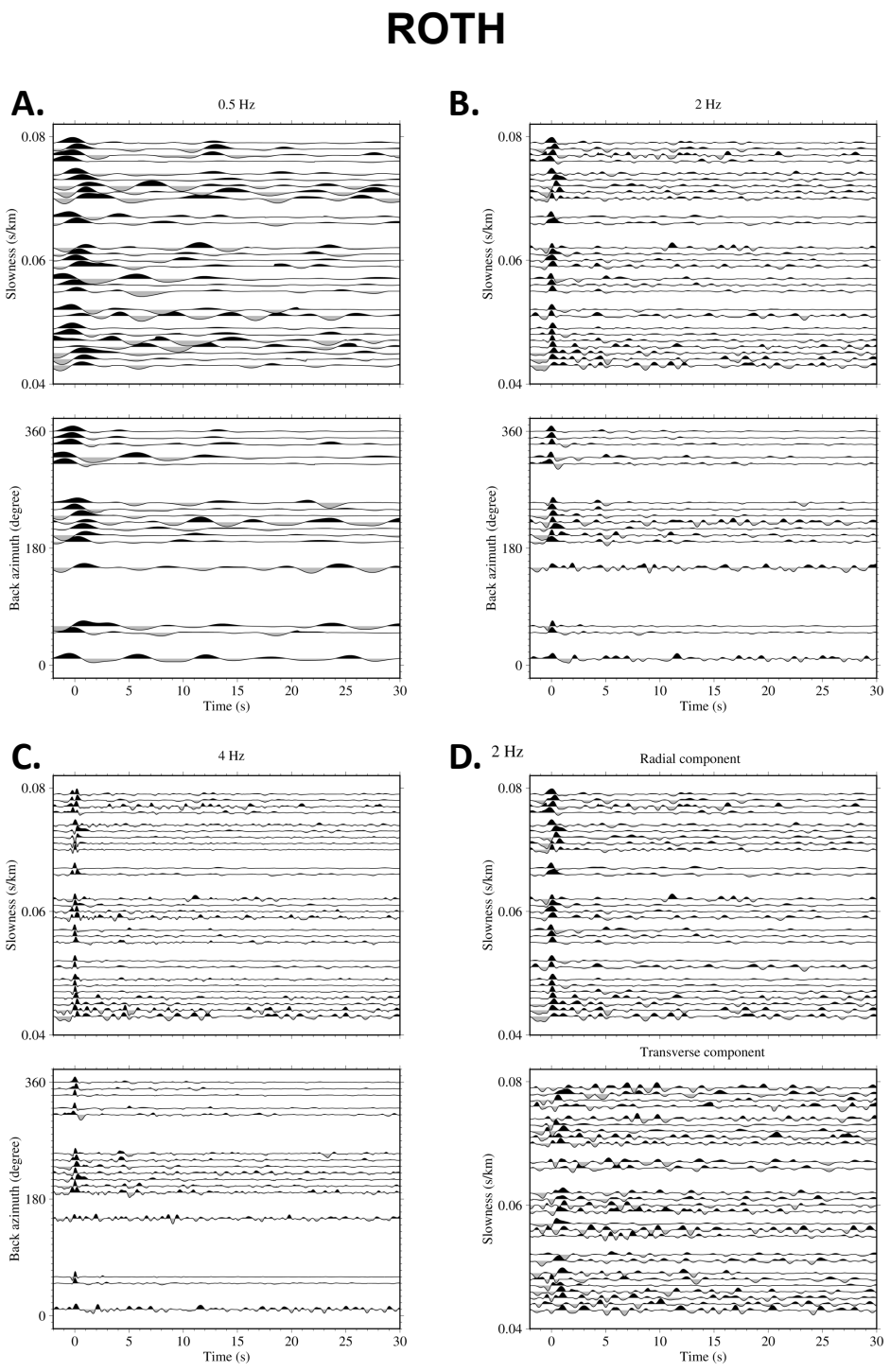

Figure A.30: Receiver functions computed at ROTH plotted by back azimuth and slowness. Receiver functions are binned by back azimuth every 10°and by slowness every 0.001 s/km. a) Receiver functions calculated with a maximum frequency of 0.5 Hz. b) Receiver functions calculated with a maximum frequency of 2 Hz. c) Receiver functions calculated with a maximum frequency of 4 Hz. d) 2 Hz maximum frequency radial and transverse receiver functions plotted by slowness.

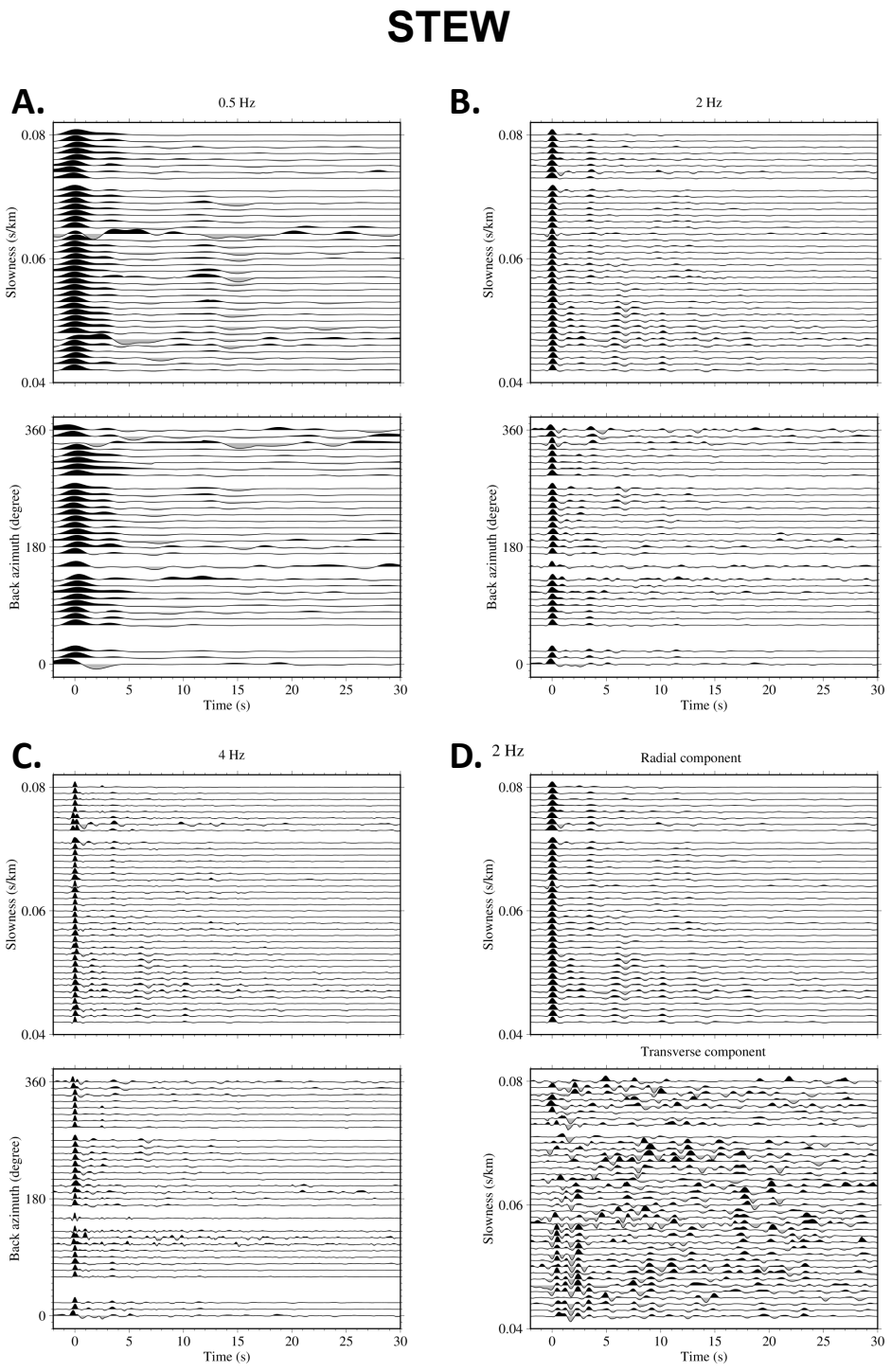

Figure A.31: Receiver functions computed at STEW plotted by back azimuth and slowness. Receiver functions are binned by back azimuth every 10°and by slowness every 0.001 s/km. a) Receiver functions calculated with a maximum frequency of 0.5 Hz. b) Receiver functions calculated with a maximum frequency of 2 Hz. c) Receiver functions calculated with a maximum frequency of 4 Hz. d) 2 Hz maximum frequency radial and transverse receiver functions plotted by slowness.

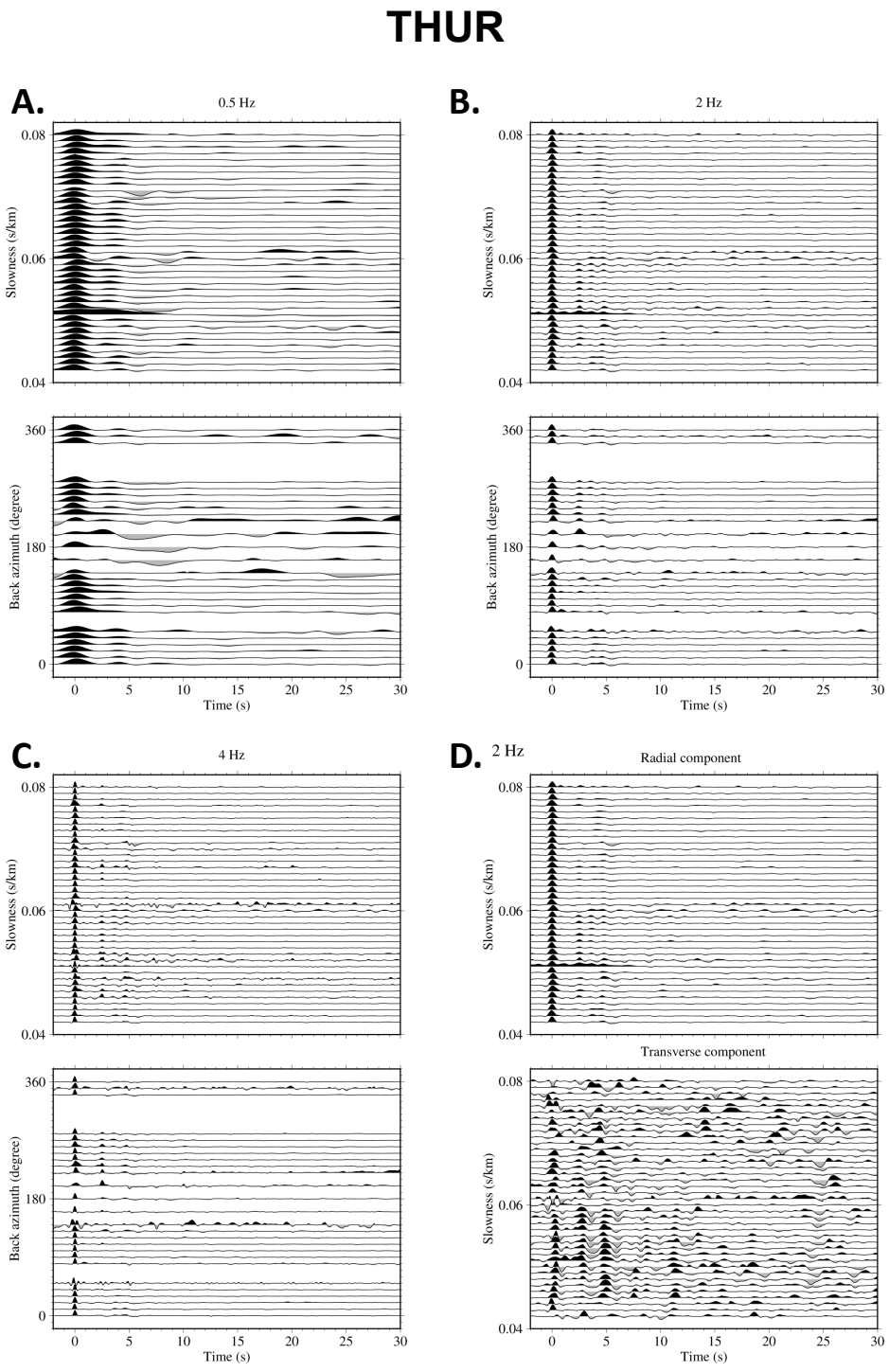

Figure A.32: Receiver functions computed at THUR plotted by back azimuth and slowness. Receiver functions are binned by back azimuth every 10°and by slowness every 0.001 s/km. a) Receiver functions calculated with a maximum frequency of 0.5 Hz. b) Receiver functions calculated with a maximum frequency of 2 Hz. c) Receiver functions calculated with a maximum frequency of 4 Hz. d) 2 Hz maximum frequency radial and transverse receiver functions plotted by slowness.

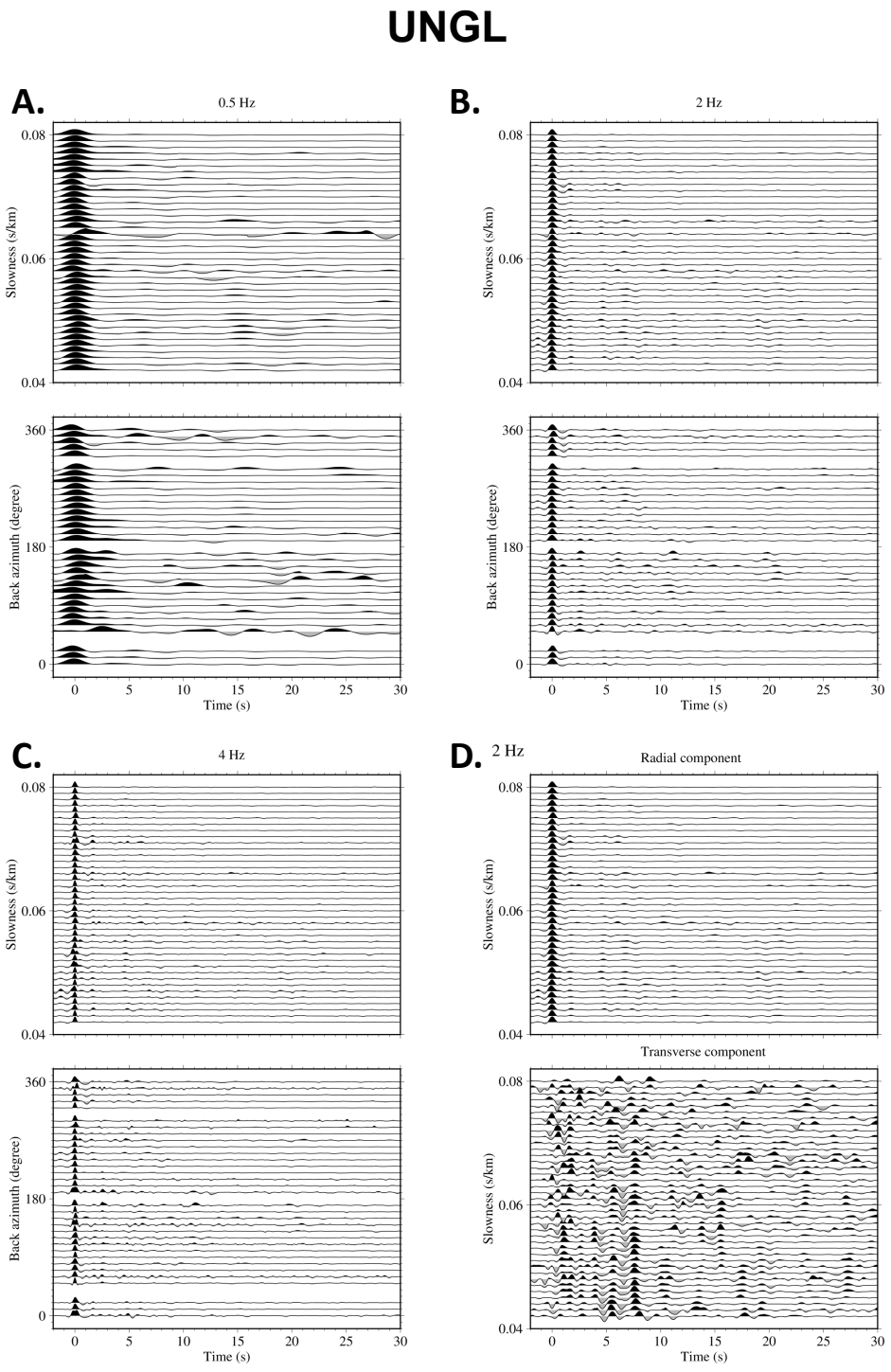

Figure A.33: Receiver functions computed at UNGL plotted by back azimuth and slowness. Receiver functions are binned by back azimuth every 10°and by slowness every 0.001 s/km. a) Receiver functions calculated with a maximum frequency of 0.5 Hz. b) Receiver functions calculated with a maximum frequency of 2 Hz. c) Receiver functions calculated with a maximum frequency of 4 Hz. d) 2 Hz maximum frequency radial and transverse receiver functions plotted by slowness.

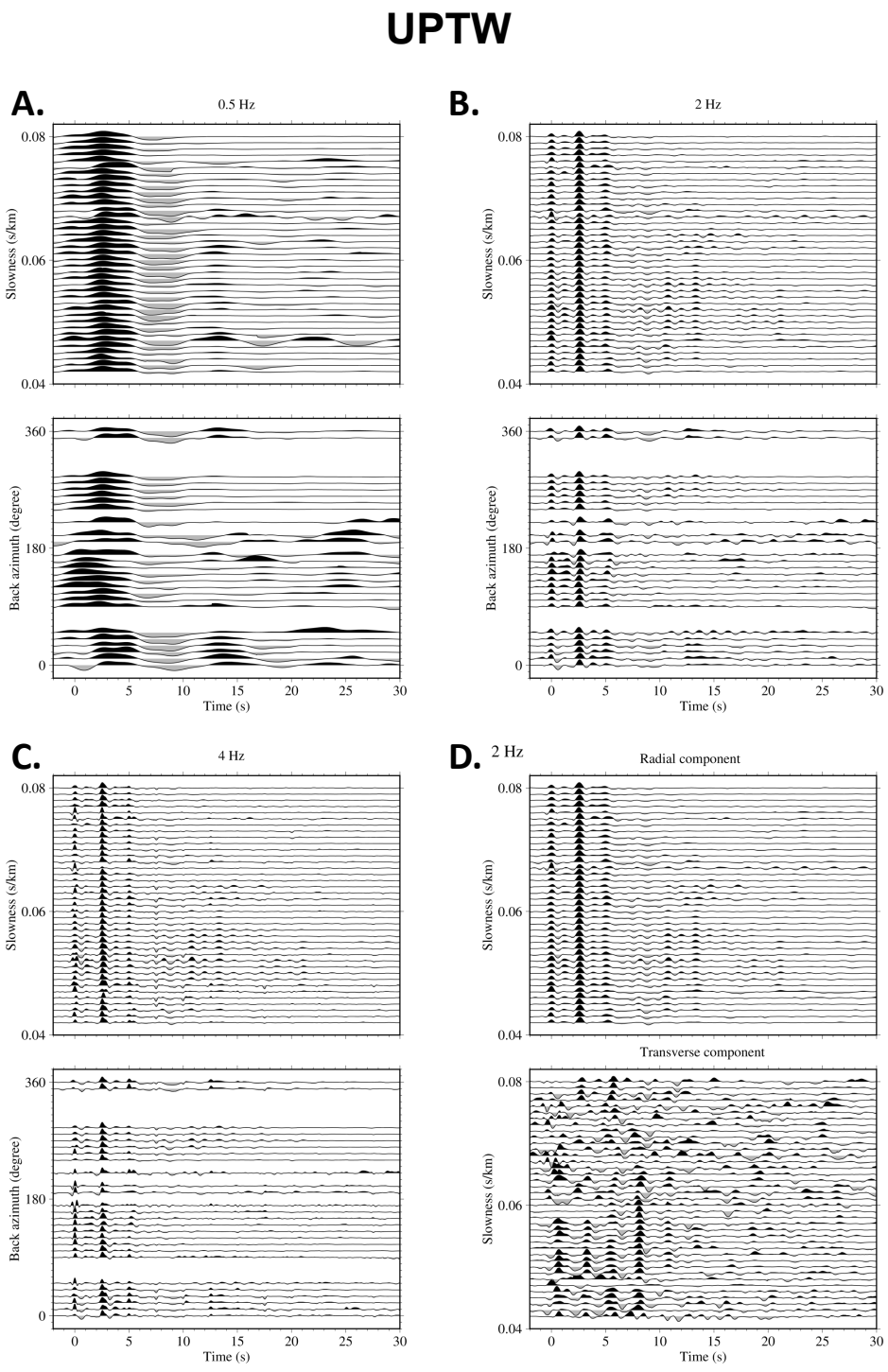

Figure A.34: Receiver functions computed at UPTW plotted by back azimuth and slowness. Receiver functions are binned by back azimuth every 10°and by slowness every 0.001 s/km. a) Receiver functions calculated with a maximum frequency of 0.5 Hz. b) Receiver functions calculated with a maximum frequency of 2 Hz. c) Receiver functions calculated with a maximum frequency of 4 Hz. d) 2 Hz maximum frequency radial and transverse receiver functions plotted by slowness.

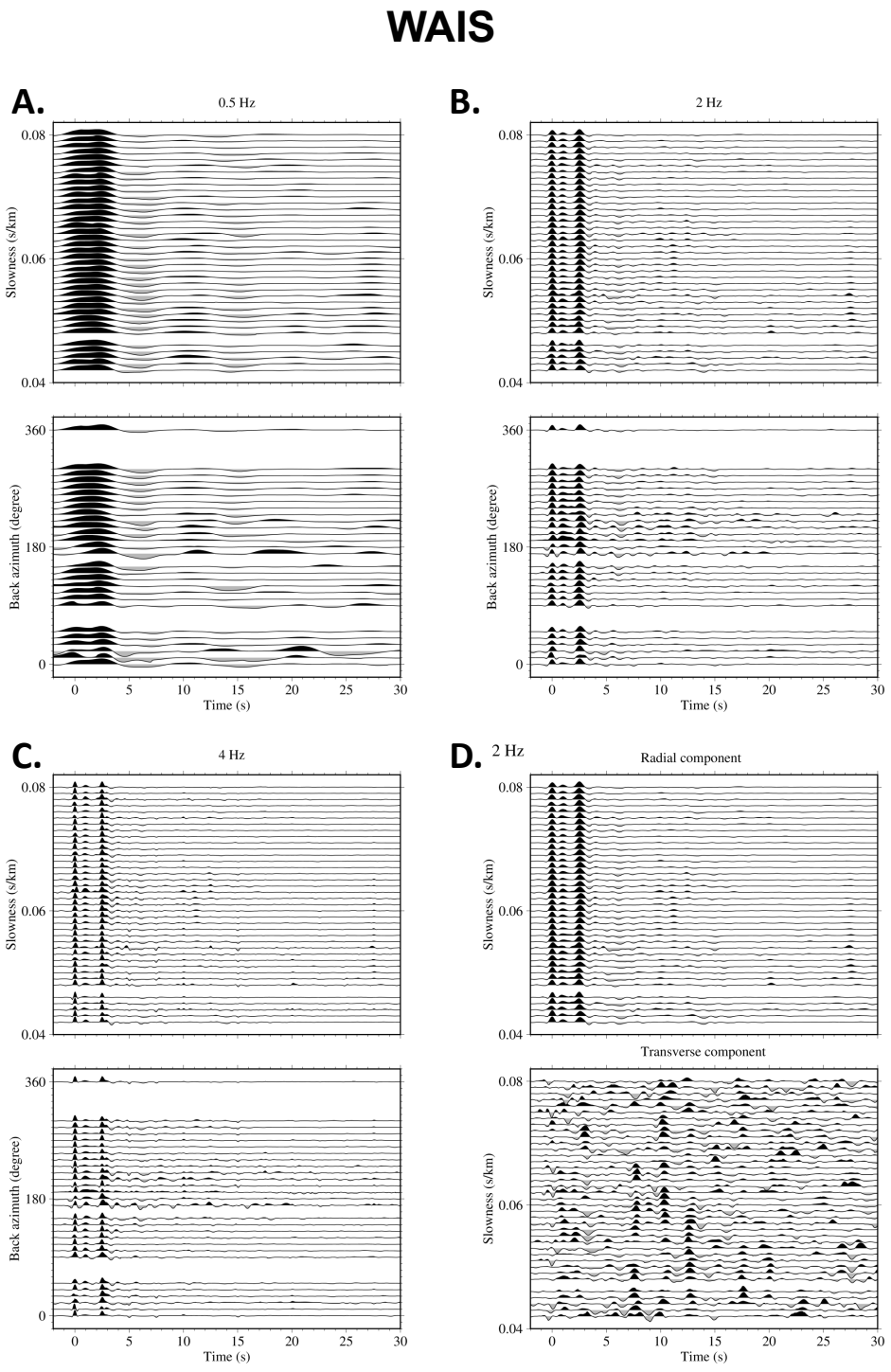

Figure A.35: Receiver functions computed at WAIS plotted by back azimuth and slowness. Receiver functions are binned by back azimuth every 10°and by slowness every 0.001 s/km. a) Receiver functions calculated with a maximum frequency of 0.5 Hz. b) Receiver functions calculated with a maximum frequency of 2 Hz. c) Receiver functions calculated with a maximum frequency of 4 Hz. d) 2 Hz maximum frequency radial and transverse receiver functions plotted by slowness.

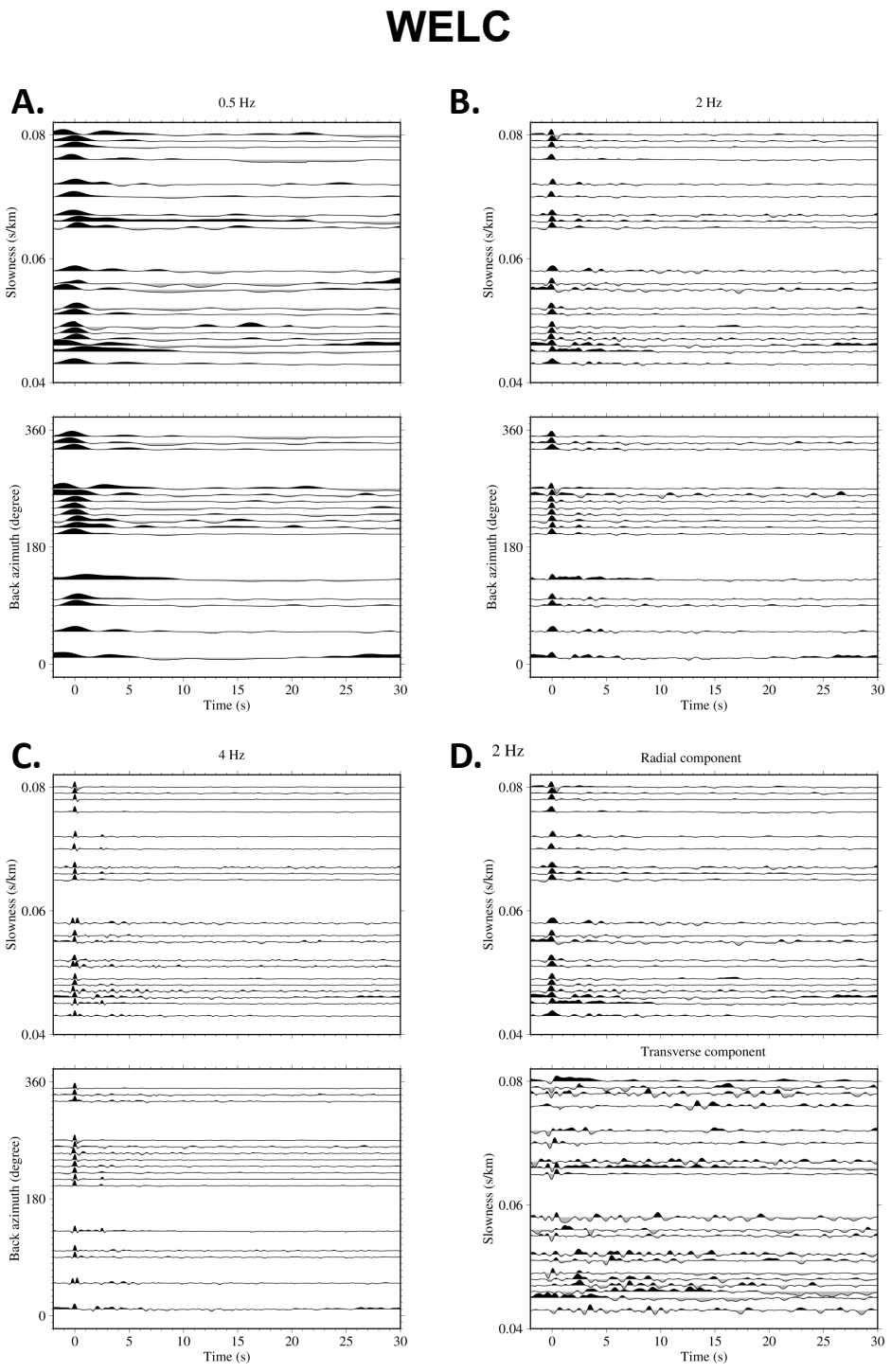

Figure A.36: Receiver functions computed at WELC plotted by back azimuth and slowness. Receiver functions are binned by back azimuth every 10°and by slowness every 0.001 s/km. a) Receiver functions calculated with a maximum frequency of 0.5 Hz. b) Receiver functions calculated with a maximum frequency of 2 Hz. c) Receiver functions calculated with a maximum frequency of 4 Hz. d) 2 Hz maximum frequency radial and transverse receiver functions plotted by slowness.

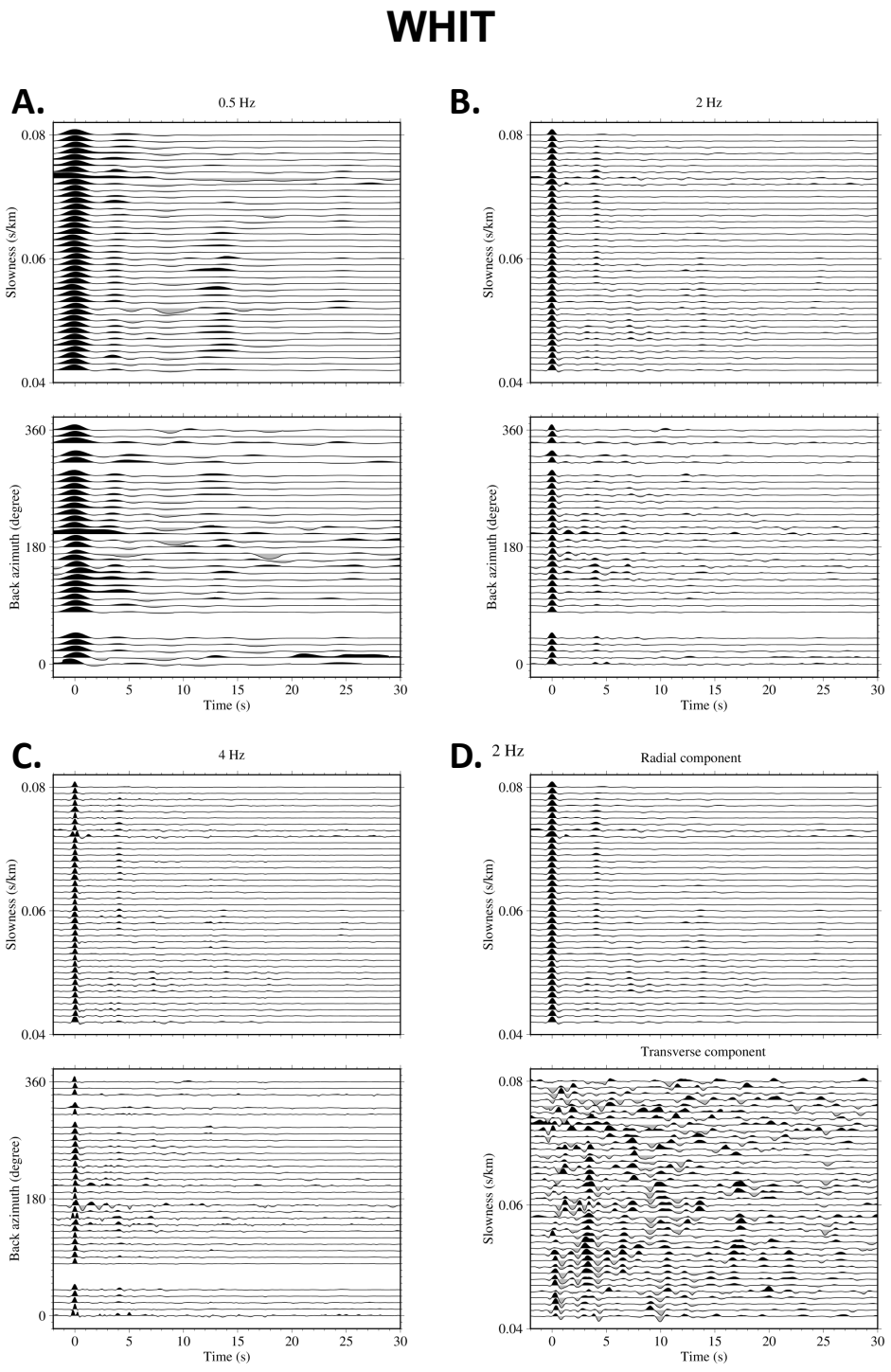

Figure A.37: Receiver functions computed at WHIT plotted by back azimuth and slowness. Receiver functions are binned by back azimuth every 10°and by slowness every 0.001 s/km. a) Receiver functions calculated with a maximum frequency of 0.5 Hz. b) Receiver functions calculated with a maximum frequency of 2 Hz. c) Receiver functions calculated with a maximum frequency of 4 Hz. d) 2 Hz maximum frequency radial and transverse receiver functions plotted by slowness.

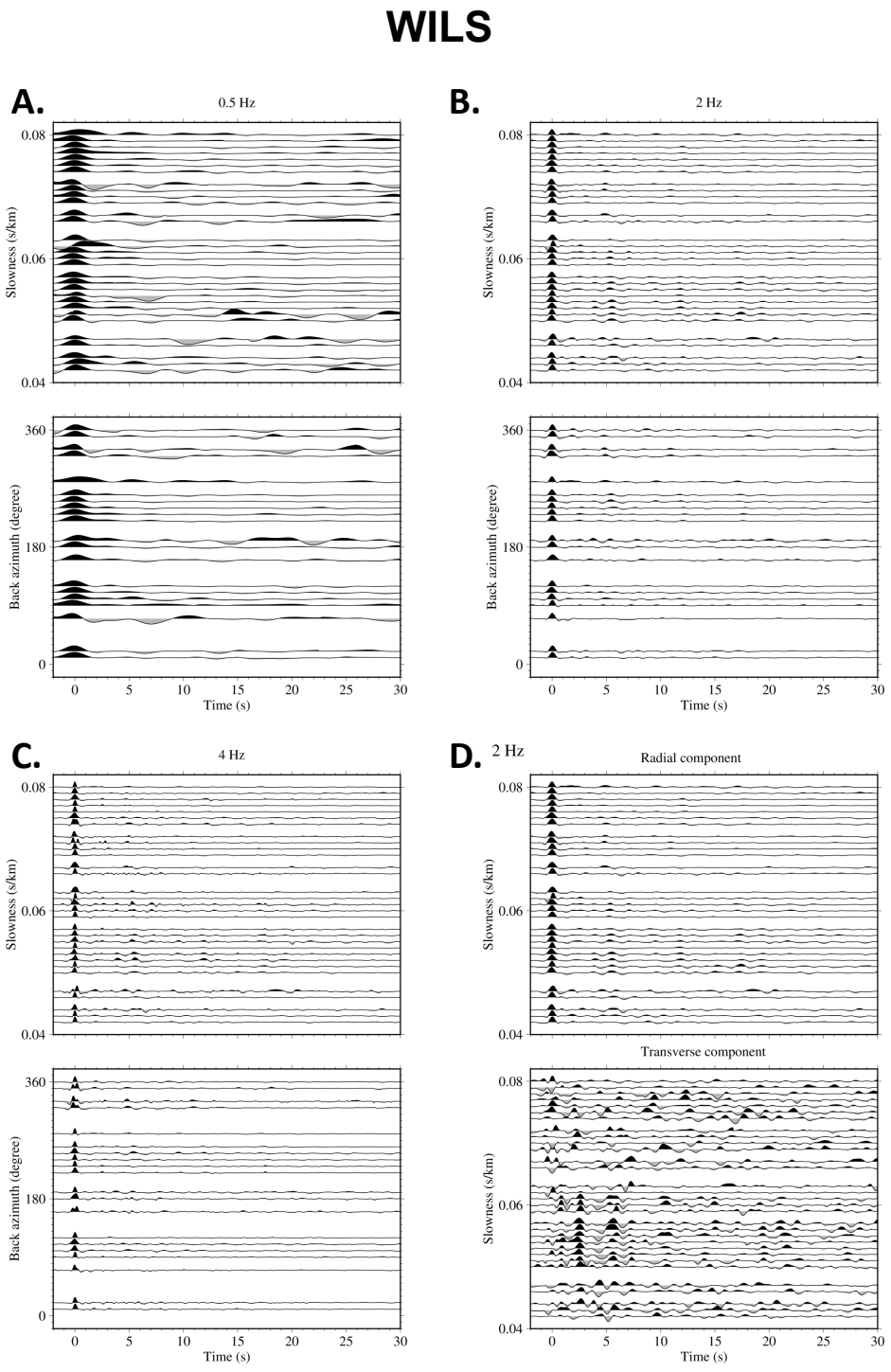

Figure A.38: Receiver functions computed at WILS plotted by back azimuth and slowness. Receiver functions are binned by back azimuth every 10°and by slowness every 0.001 s/km. a) Receiver functions calculated with a maximum frequency of 0.5 Hz. b) Receiver functions calculated with a maximum frequency of 2 Hz. c) Receiver functions calculated with a maximum frequency of 4 Hz. d) 2 Hz maximum frequency radial and transverse receiver functions plotted by slowness.

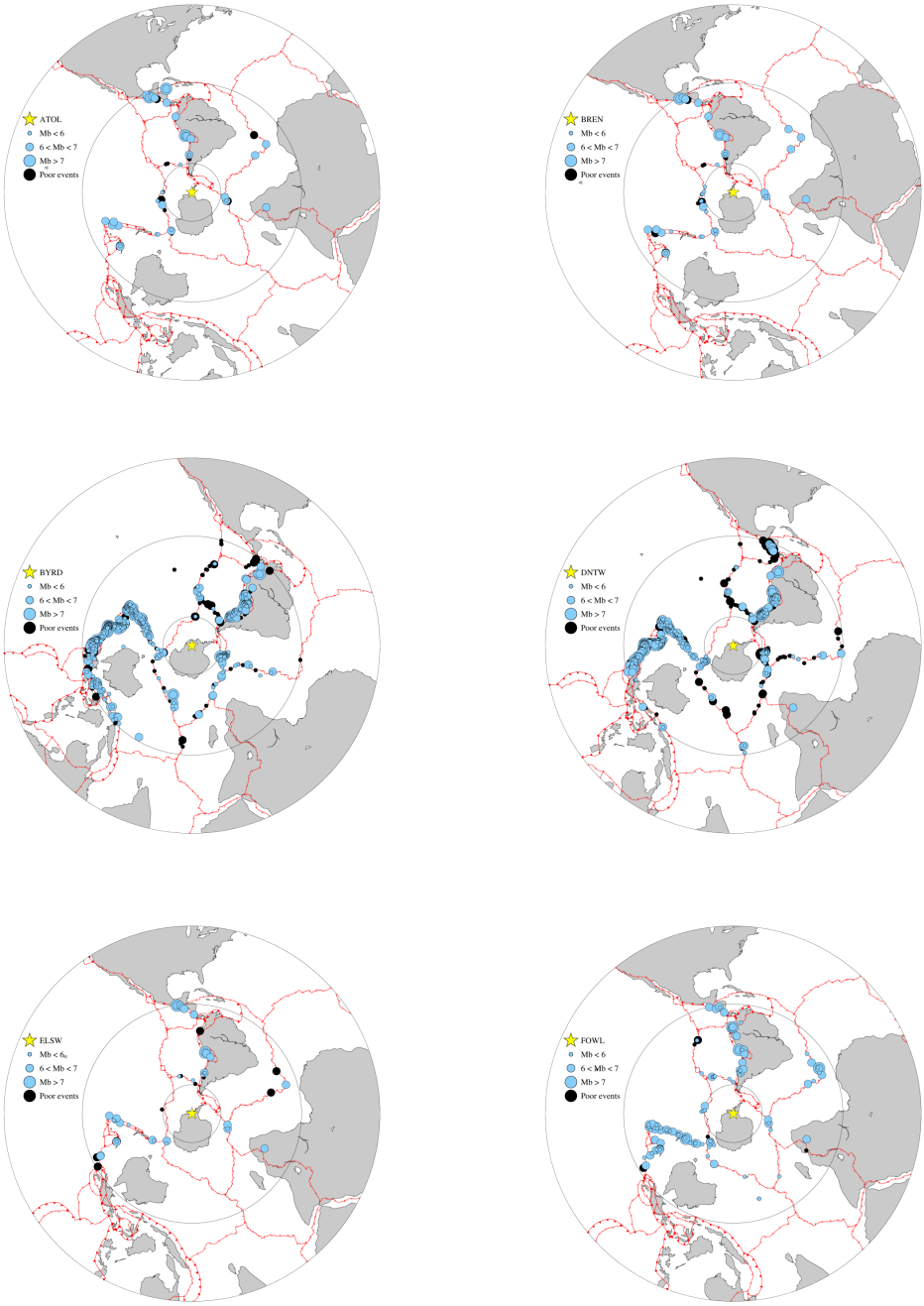

Figure A.39: Teleseismic event distribution for receiver function analysis at stations ATOL, BREN, BYRD, DNTW, ELSW and FOWL. The location of each station is shown by a yellow star. Events used are shown in light blue, whilst unused events are shown in black. Lines are added to shown distances of 30° and 90° from the station.

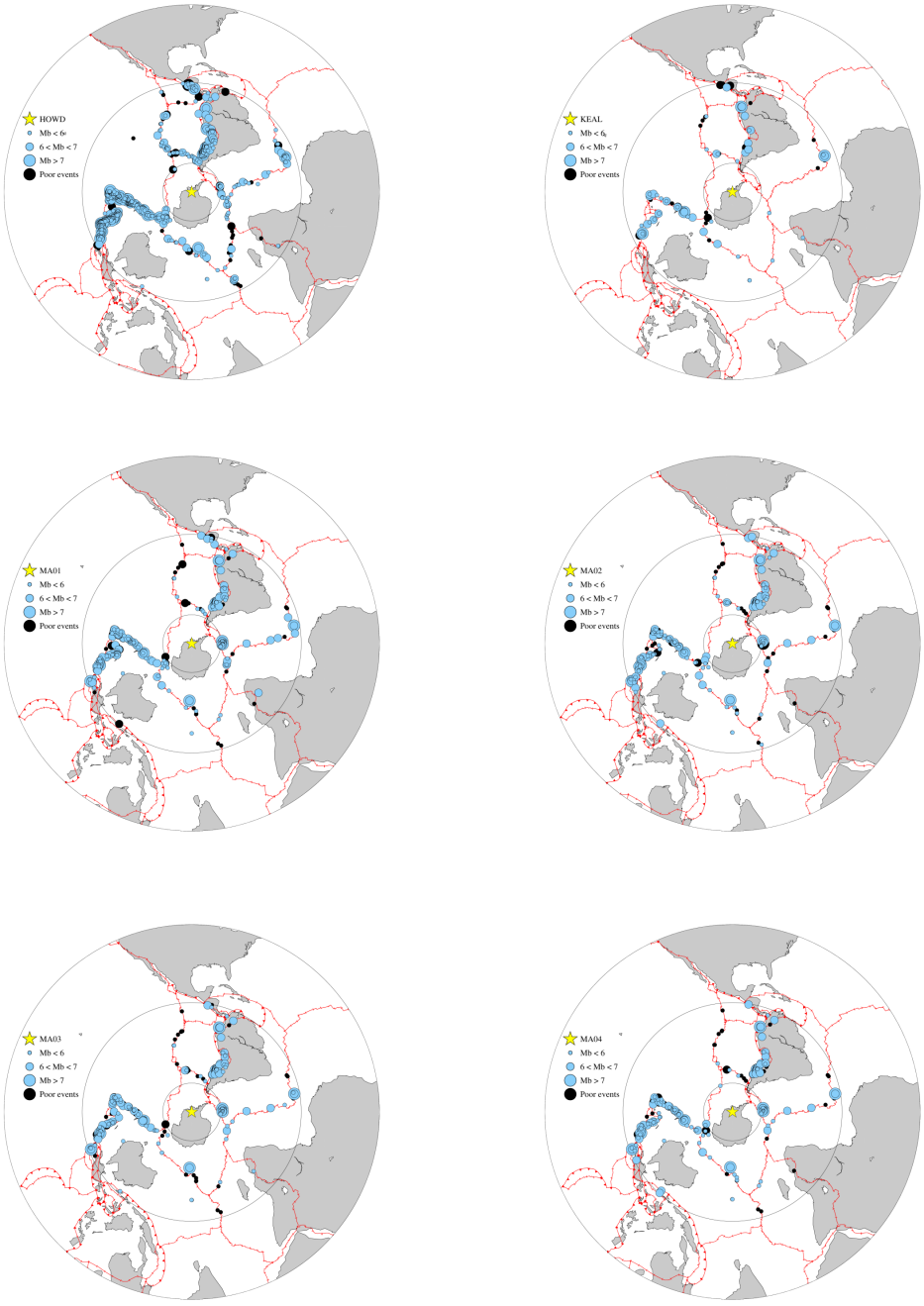

Figure A.40: Teleseismic event distribution for receiver function analysis at stations HOWD, KEAL, MA01, MA02, MA03 and MA04.

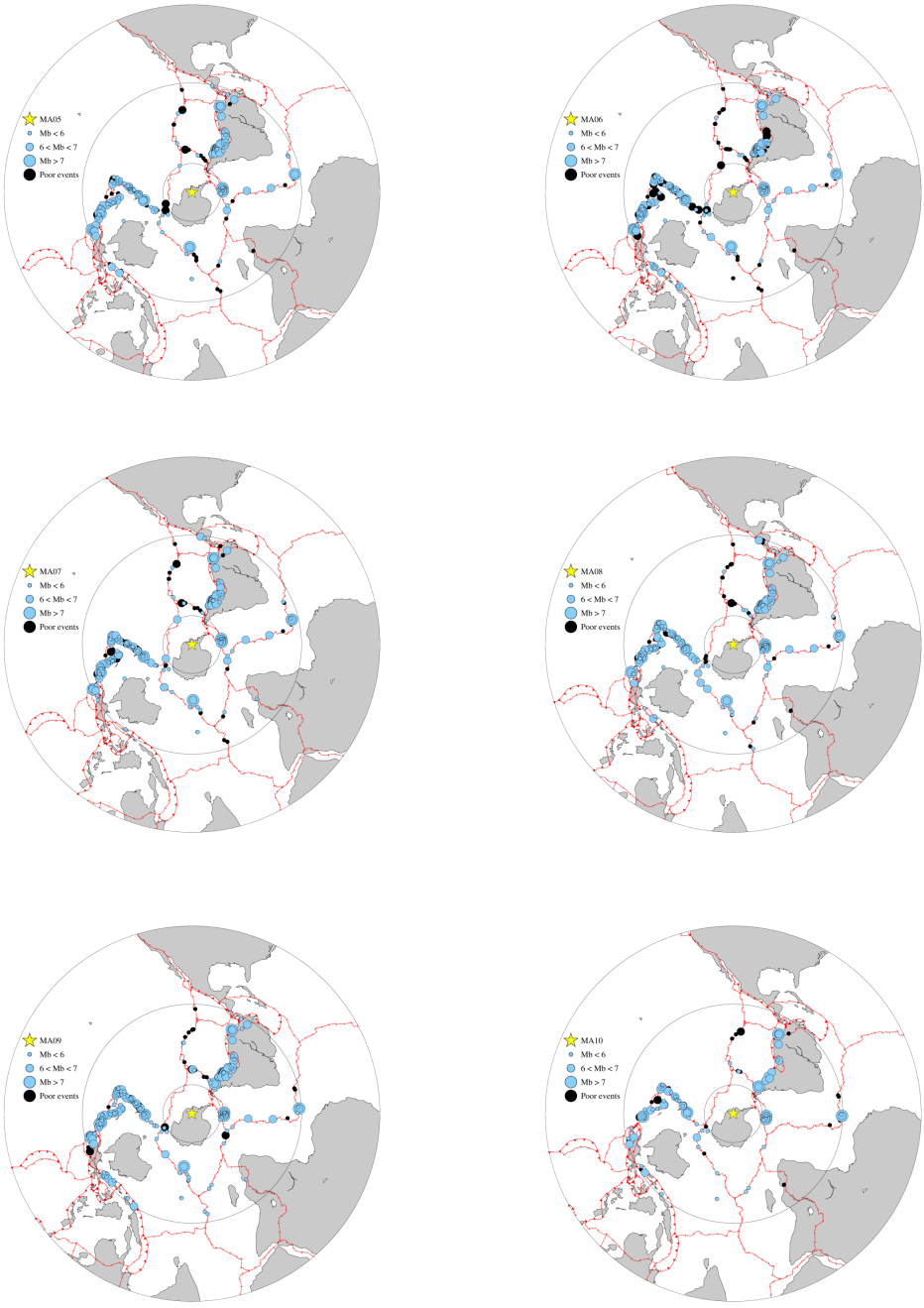

Figure A.41: Teleseismic event distribution for receiver function analysis at stations MA05, MA06, MA07, MA08, MA09 and MA10.

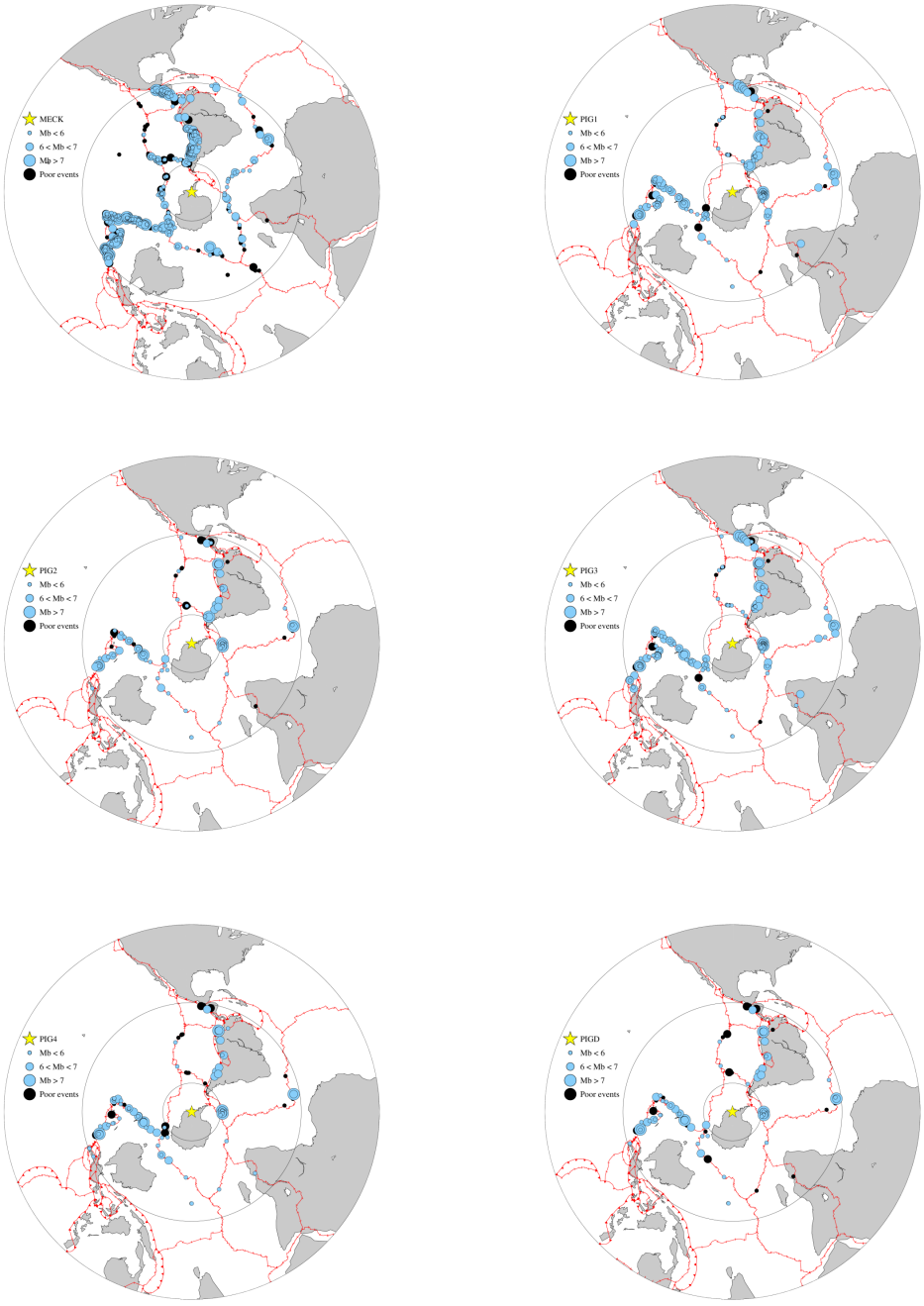

Figure A.42: Teleseismic event distribution for receiver function analysis at stations MECK, PIG1, PIG2, PIG3, PIG4 and PIGD.

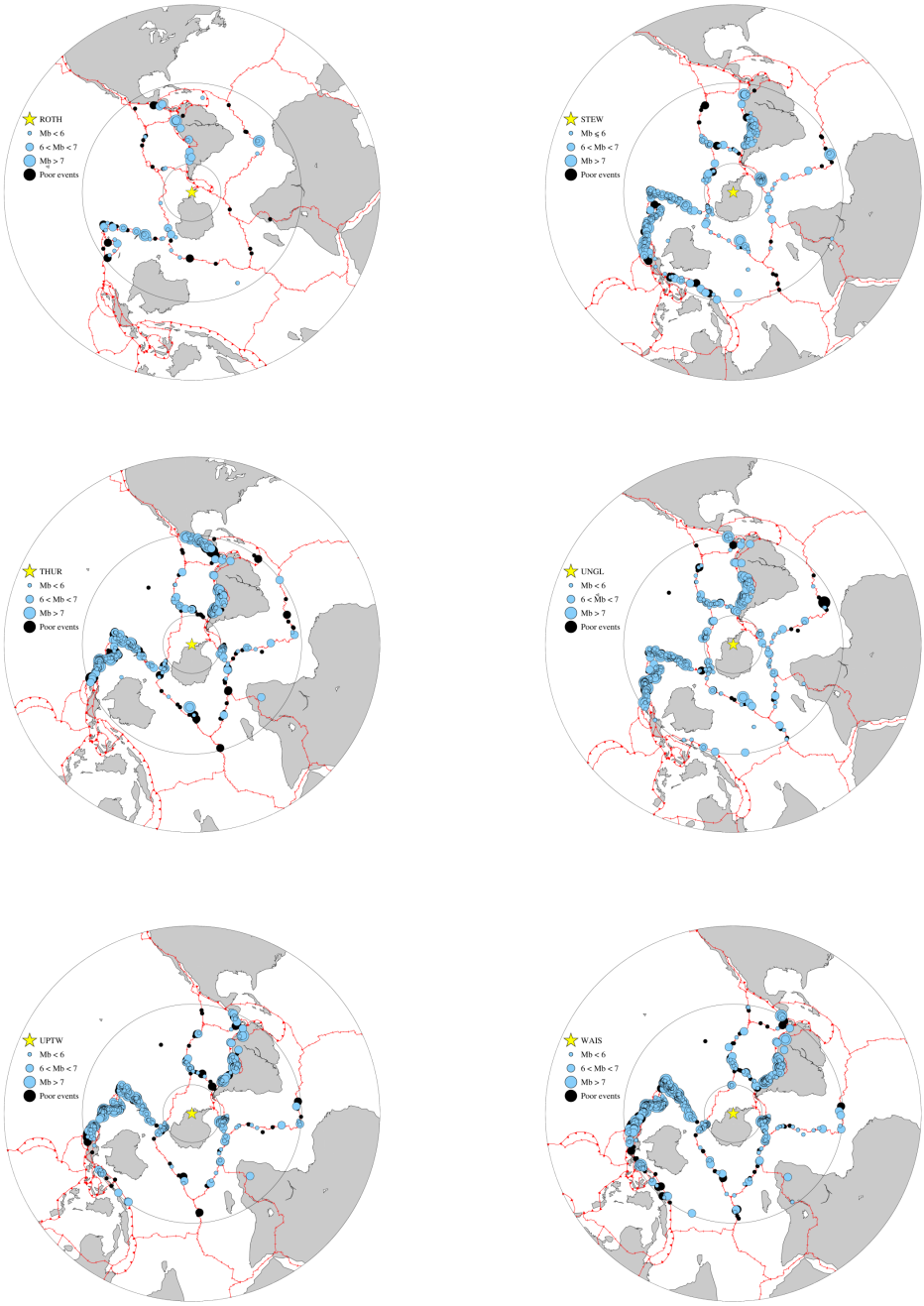

Figure A.43: Teleseismic event distribution for receiver function analysis at stations ROTH, STEW, THUR, UNGL, UPTW and WAIS.

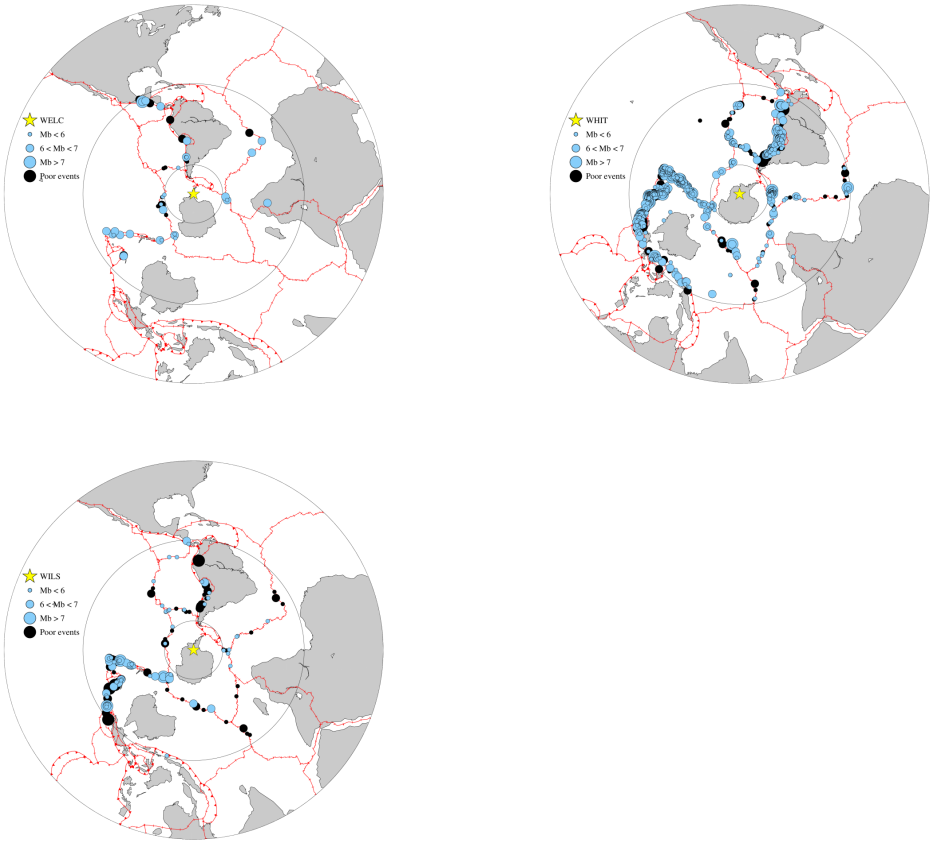

Figure A.44: Teleseismic event distribution for receiver function analysis at stations WELC, WHIT and WILS.

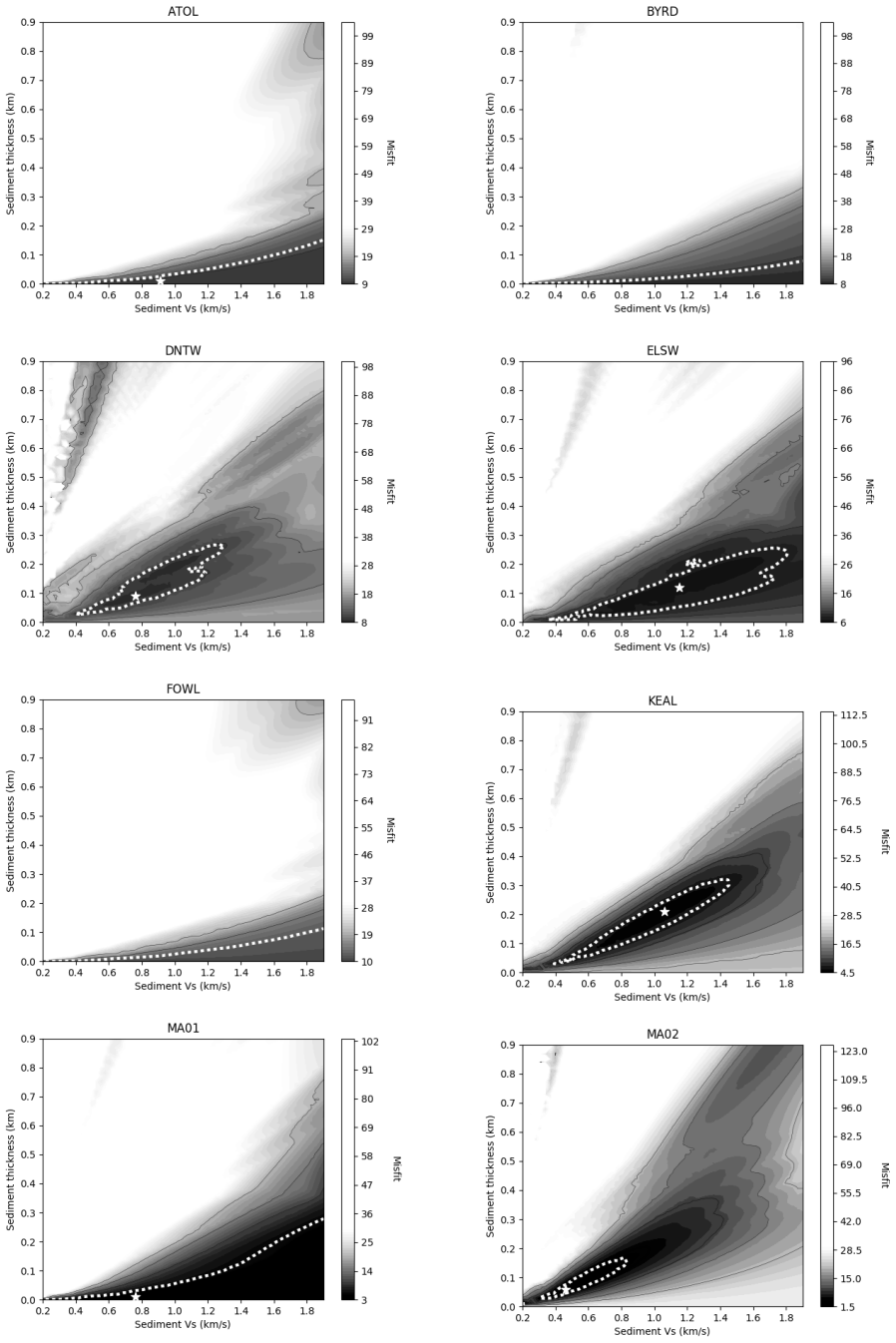

Figure A.45: Results from forward modelling for subglacial sediment at stations ATOL, BYRD, DNTW, ELSW, FOWL, KEAL, MA01 and MA02. The best fitting solution is denoted by a white star.

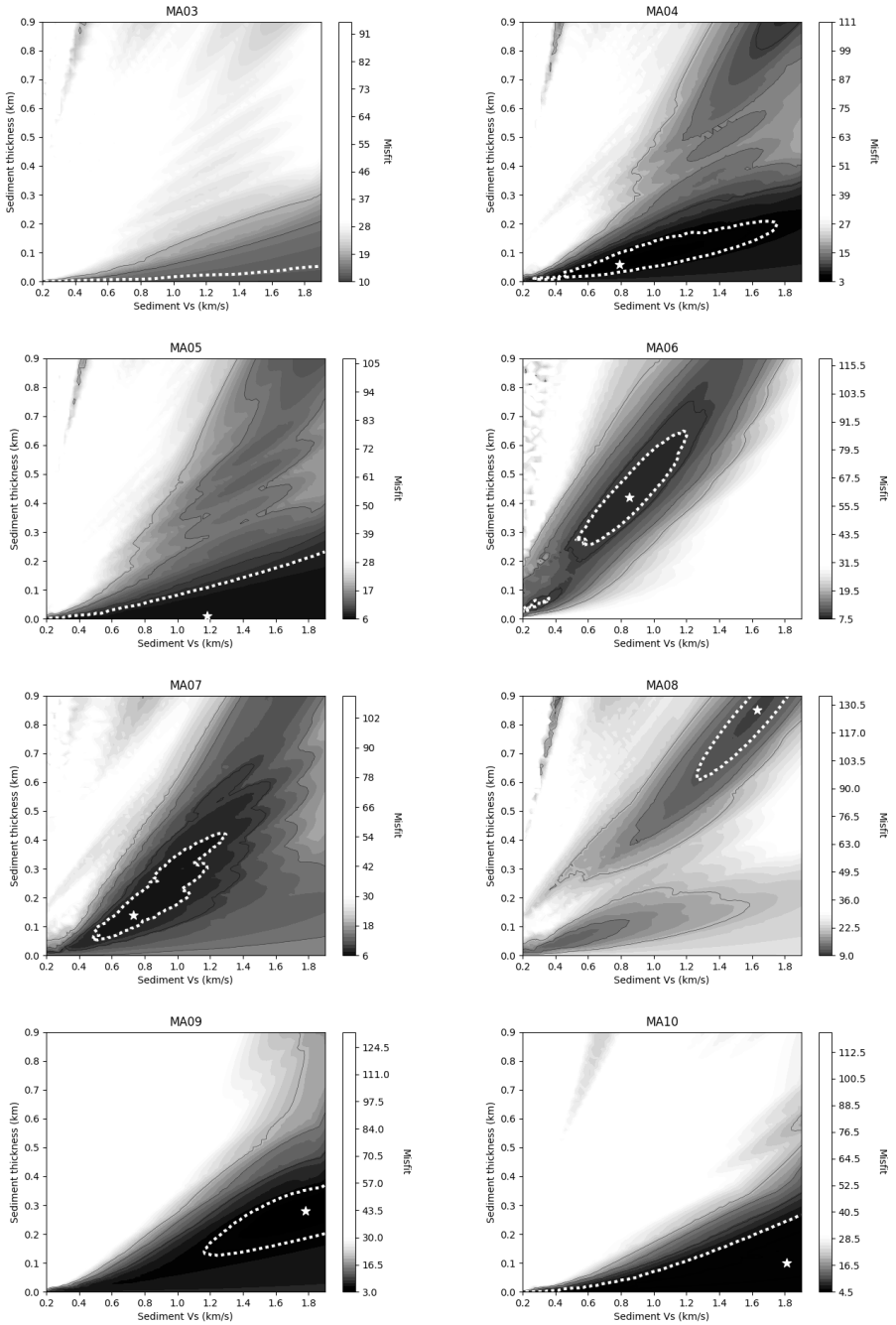

Figure A.46: Results from forward modelling for subglacial sediment at stations MA03, MA04, MA05, MA06, MA07, MA08, MA09 and MA10. The best fitting solution is denoted by a white star.

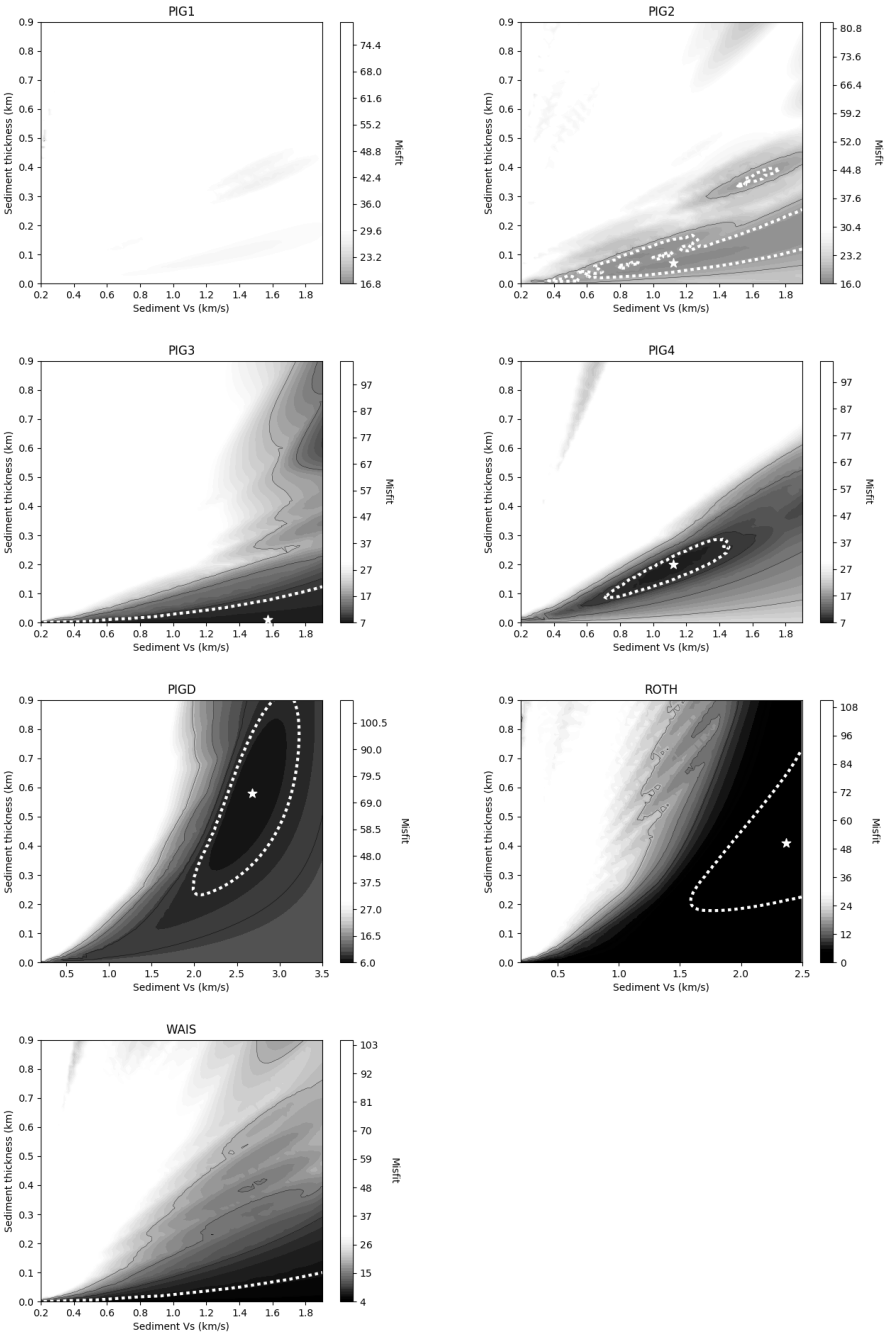

Figure A.47: Results from forward modelling for subglacial sediment at stations PIG1, PIG2, PIG3, PIG4, PIGD, ROTH, and WAIS. The best fitting solution is denoted by a white star.

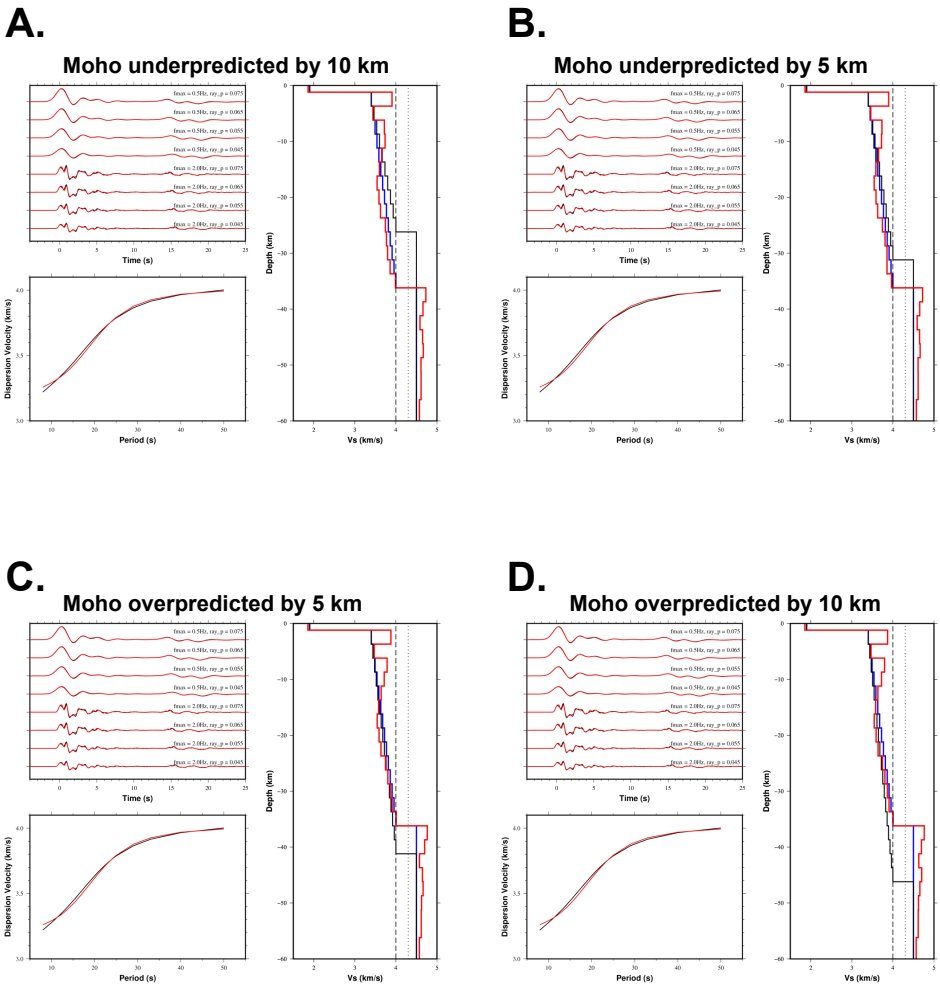

Figure A.48: Examples of synthetically testing the impact of incorrectly predicting the Moho depth in the joint inversion initial model. For each figure the top left panel shows receiver functions, bottom left panel shows dispersion curves and right hand panel shows the shear wave velocity-depth model. Black is the initial data/model, blue is the true model, and red the joint inversion output. In each case the joint inversion Moho converges on the true model Moho depth, irrespective of the Moho depth predicted in the initial model.

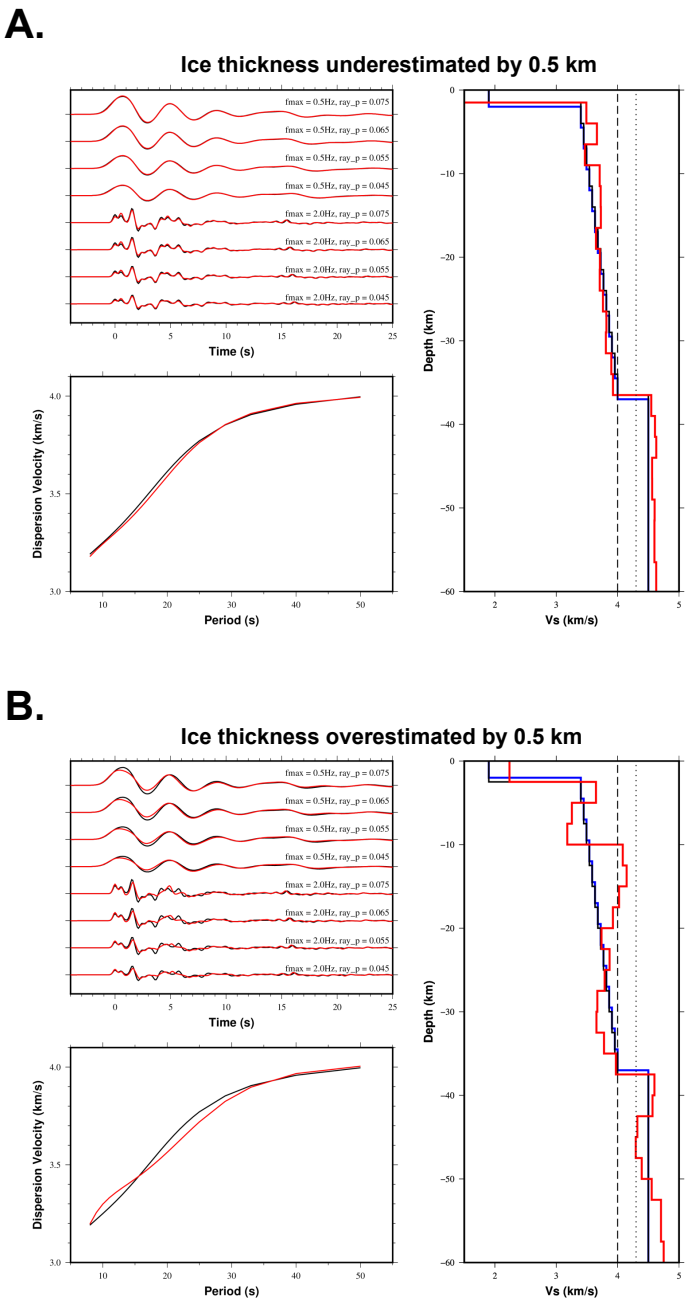

Figure A.49: Examples of synthetically testing the impact of incorrectly predicting the ice thickness in the joint inversion initial model by 0.5 km. For each figure the top left panel shows receiver functions, bottom left panel shows dispersion curves and right hand panel shows the shear wave velocity-depth model. Black is the initial data/model, blue is the true model, and red the joint inversion output.

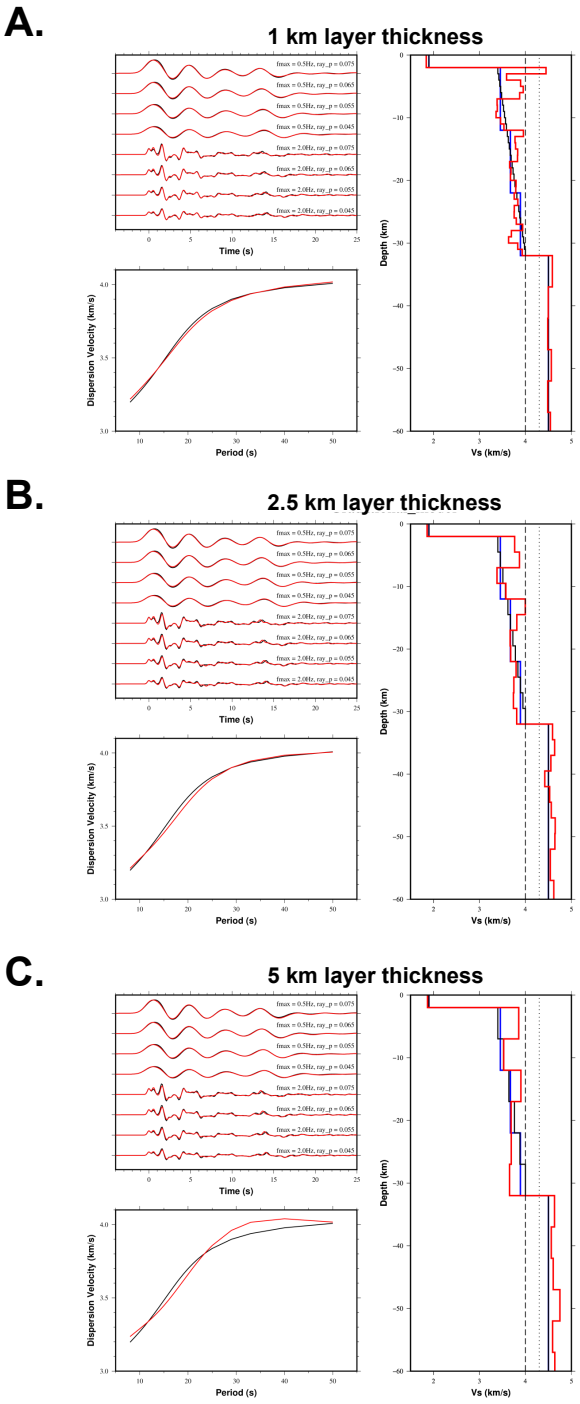

Figure A.50: Examples of synthetically testing the impact of using different layer thicknesses in the joint inversion. For each figure the top left panel shows receiver functions, bottom left panel shows dispersion curves and right hand panel shows the shear wave velocity-depth model. Black is the initial data/model, blue is the true model, and red the joint inversion output. The 1 km thick layers fits the data well, but with the risk of creating an unrealistic final model. The 5 km thick layers on the other hand has a poor fit to the dispersion data, but a more simplistic final model.

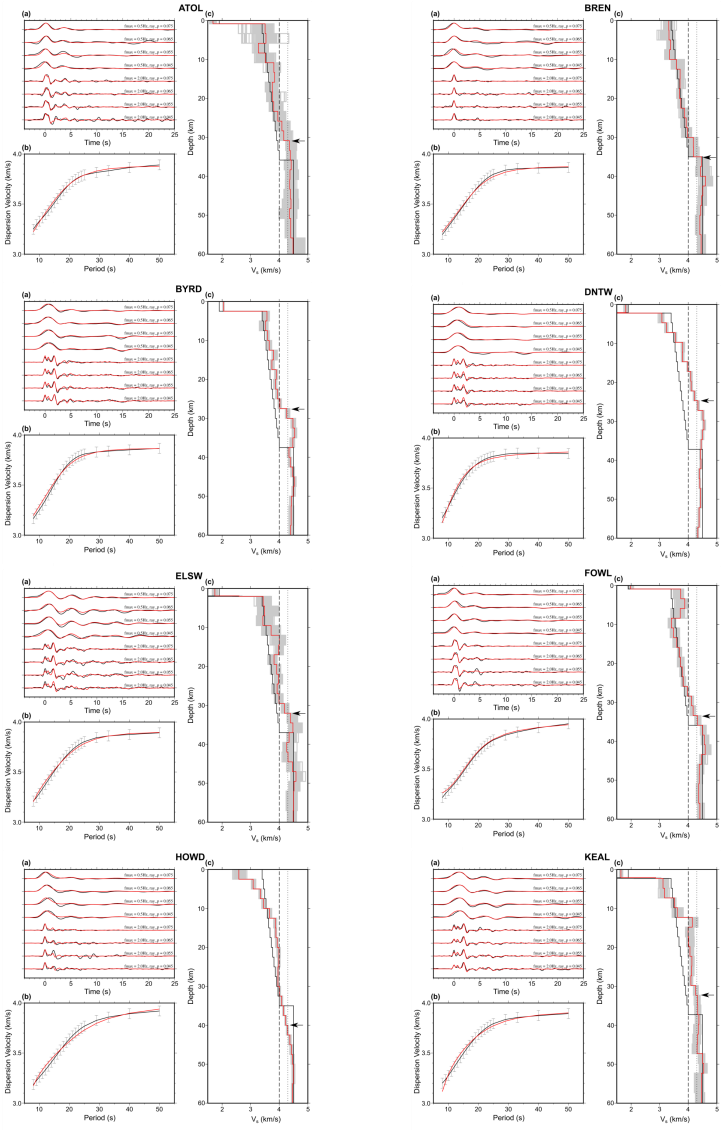

Figure A.51: Joint inversion results from stations ATOL, BREN, BYRD, DNTW, ELSW, FOWL, KEAL and HOWD. Top left panel: Receiver functions at two maximum frequencies (0.5 Hz and 2 Hz) stacked into narrow ray parameter bins (black) and the corresponding modelled receiver functions produced by the joint inversion (red). Bottom left panel: Rayleigh wave phase velocity dispersion curve is shown in black and the best fitting model in red. Right hand panel: Shear wave velocity-depth profile. The initial model is shown in black, best fitting final model in red and 500 bootstrap iterations in grey. Dashed and dotted lines are shown at 4.0 and 4.3 km/s respectively, to indicate mafic lower crust and the transition to upper mantle material. The interpreted Moho is shown with a black arrow.

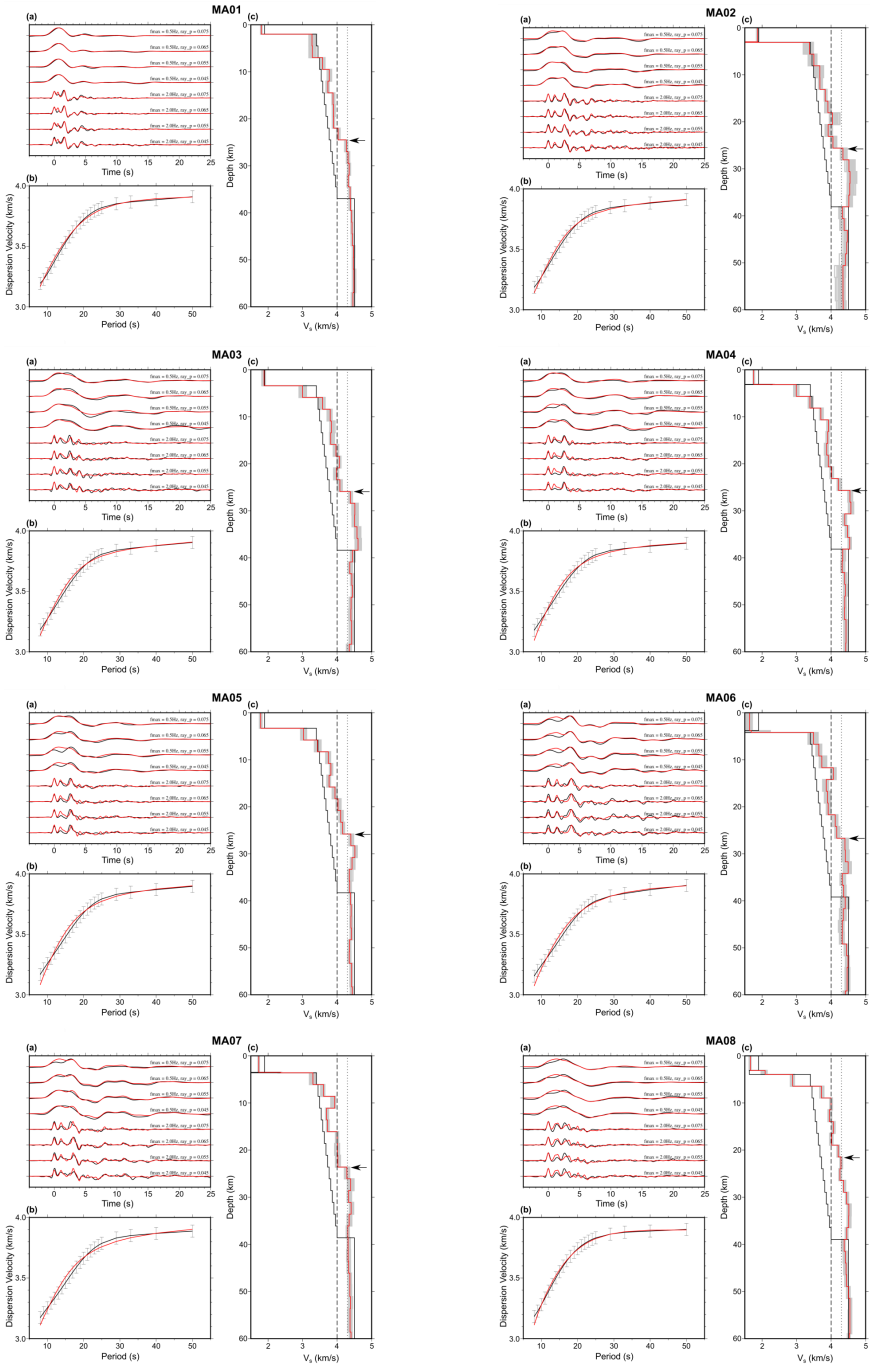

Figure A.52: Joint inversion results from stations MA01, MA02, MA03, MA04, MA05, MA06, MA07 and MA08.

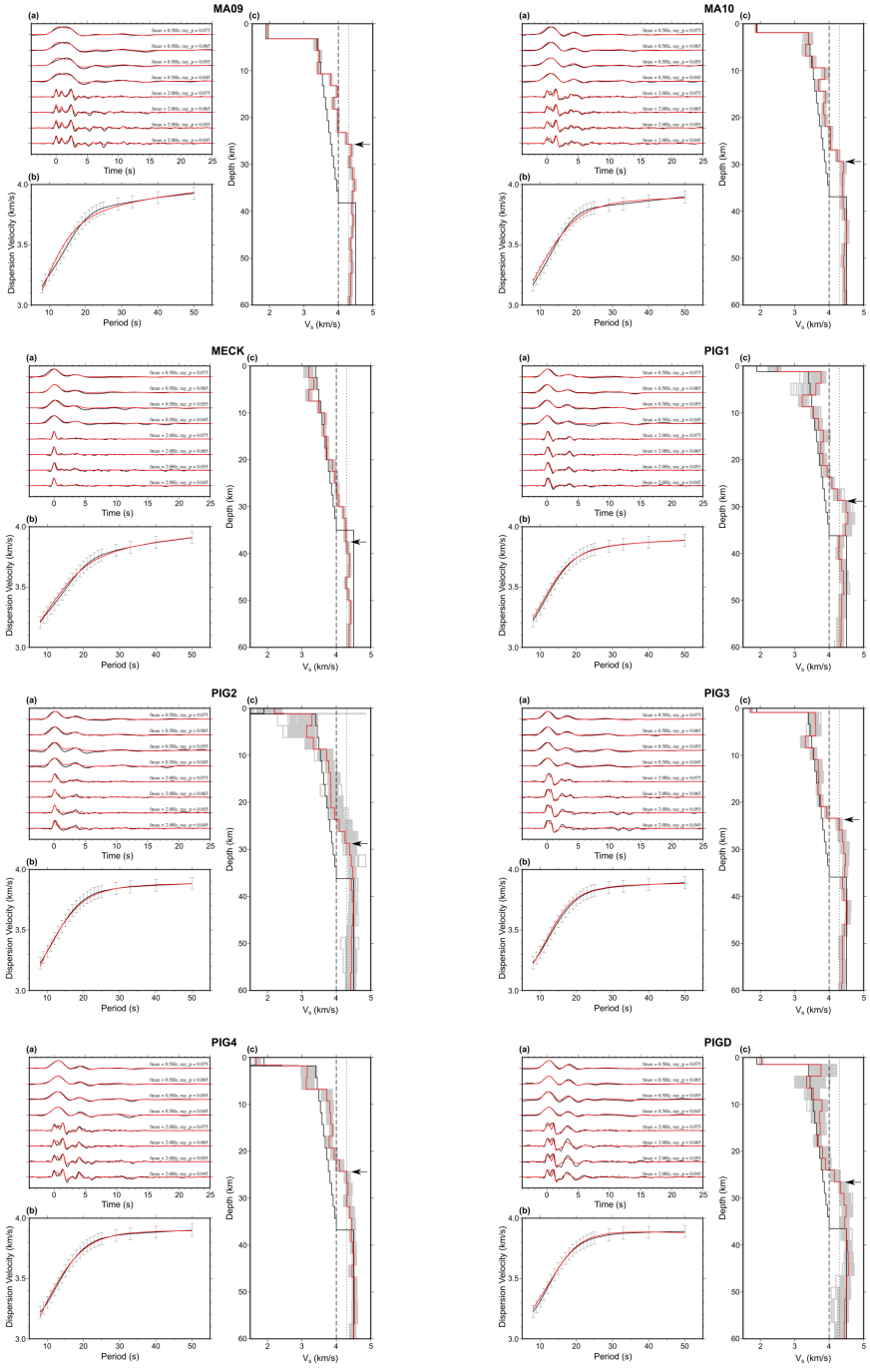

Figure A.53: Joint inversion results from stations MA09, MA10, MECK, PIG1, PIG2, PIG3, PIG4 and PIGD.

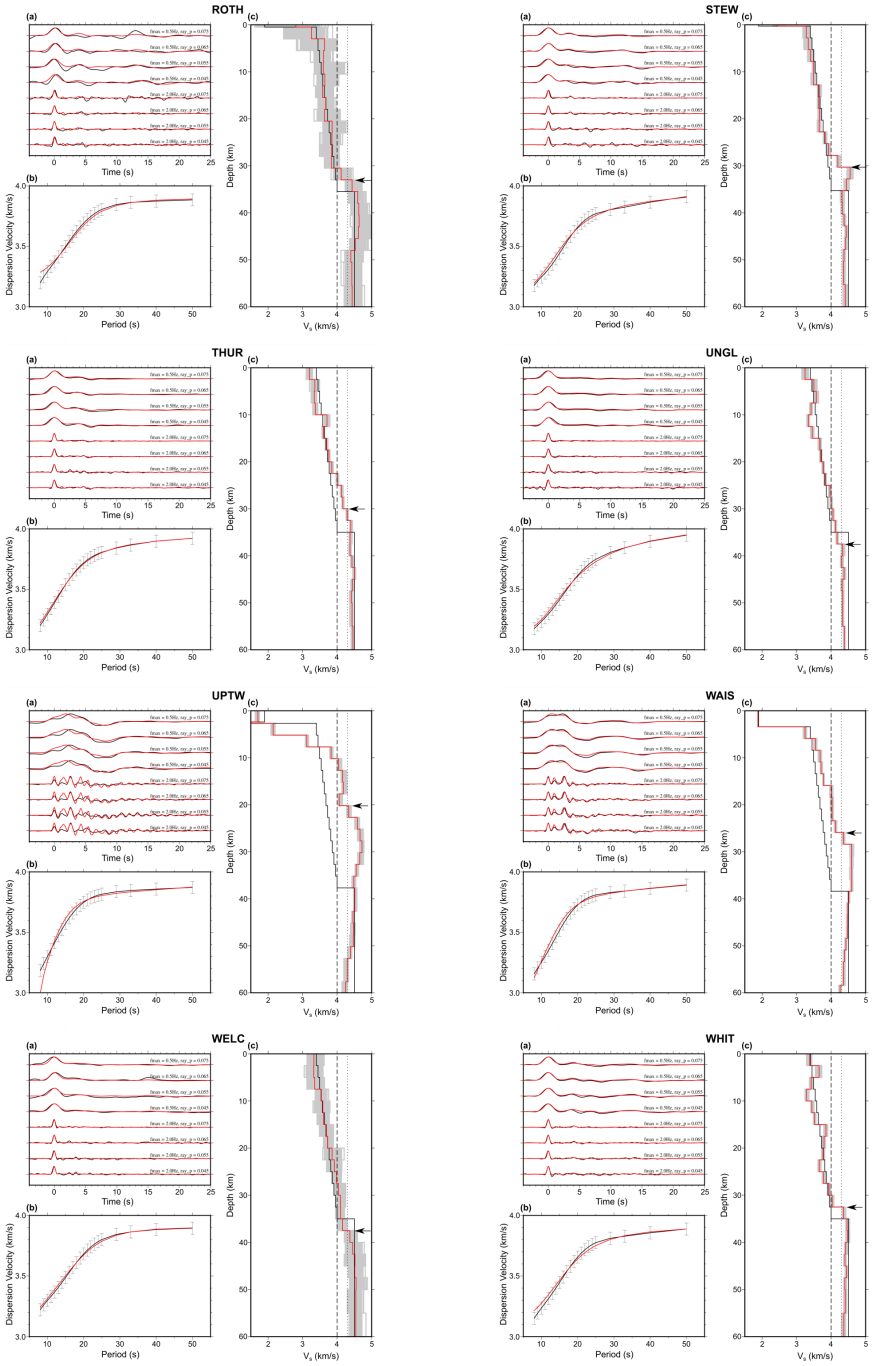

Figure A.54: Joint inversion results from stations ROTH, STEW, THUR, UNGL, UPTW, WAIS, WELC and WHIT.

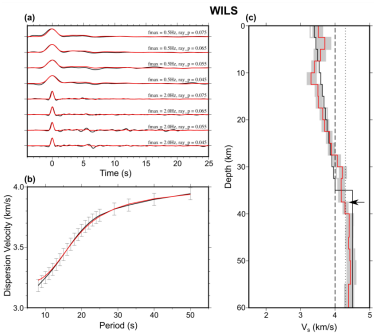

Figure A.55: Joint inversion results from station WILS.

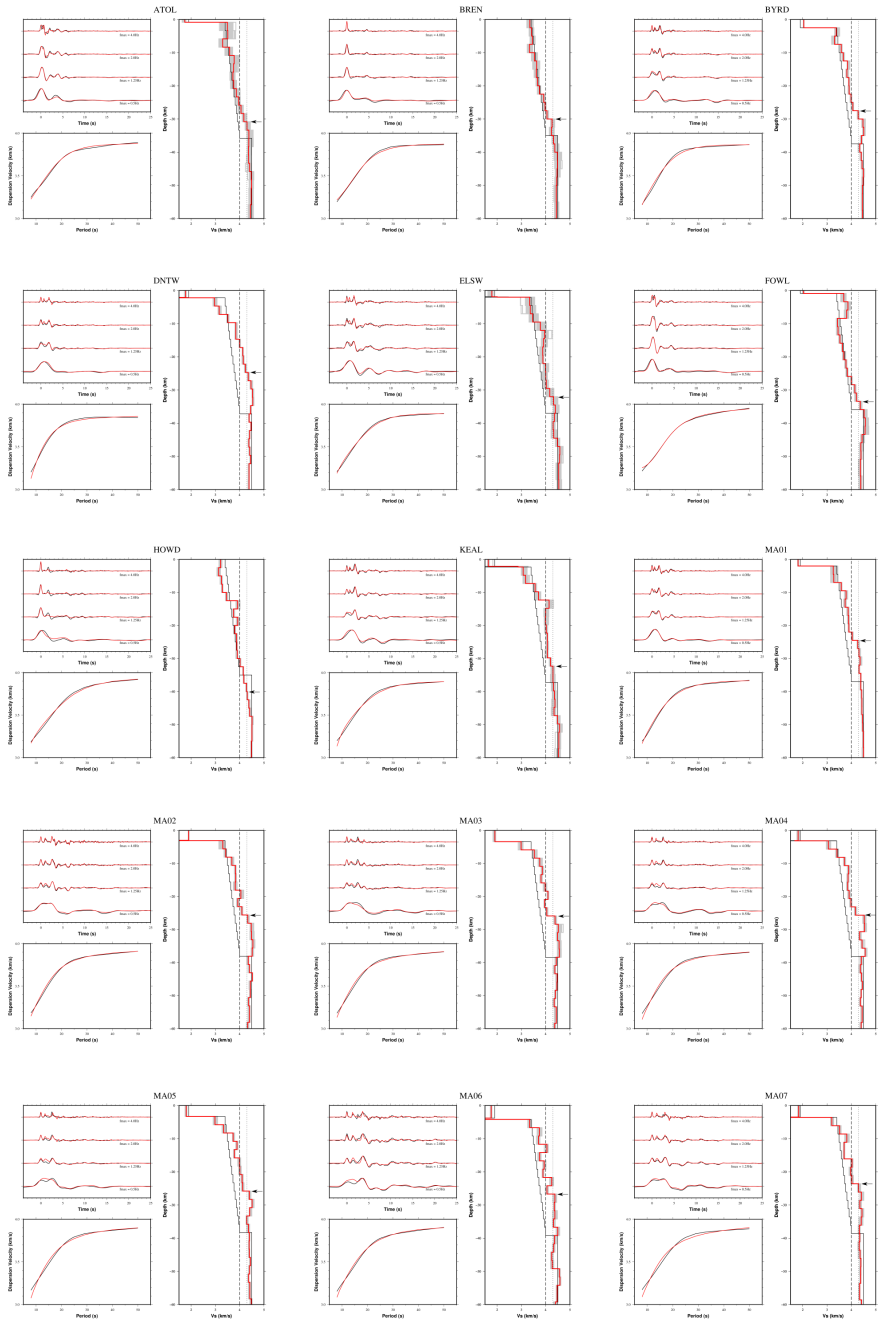

Figure A.56: Joint inversion results using moveout corrected and stacked receiver functions at four maximum frequencies (0.5 Hz, 1.25 Hz, 2 Hz and 4 Hz), rather than stacking into narrow ray parameter bins.

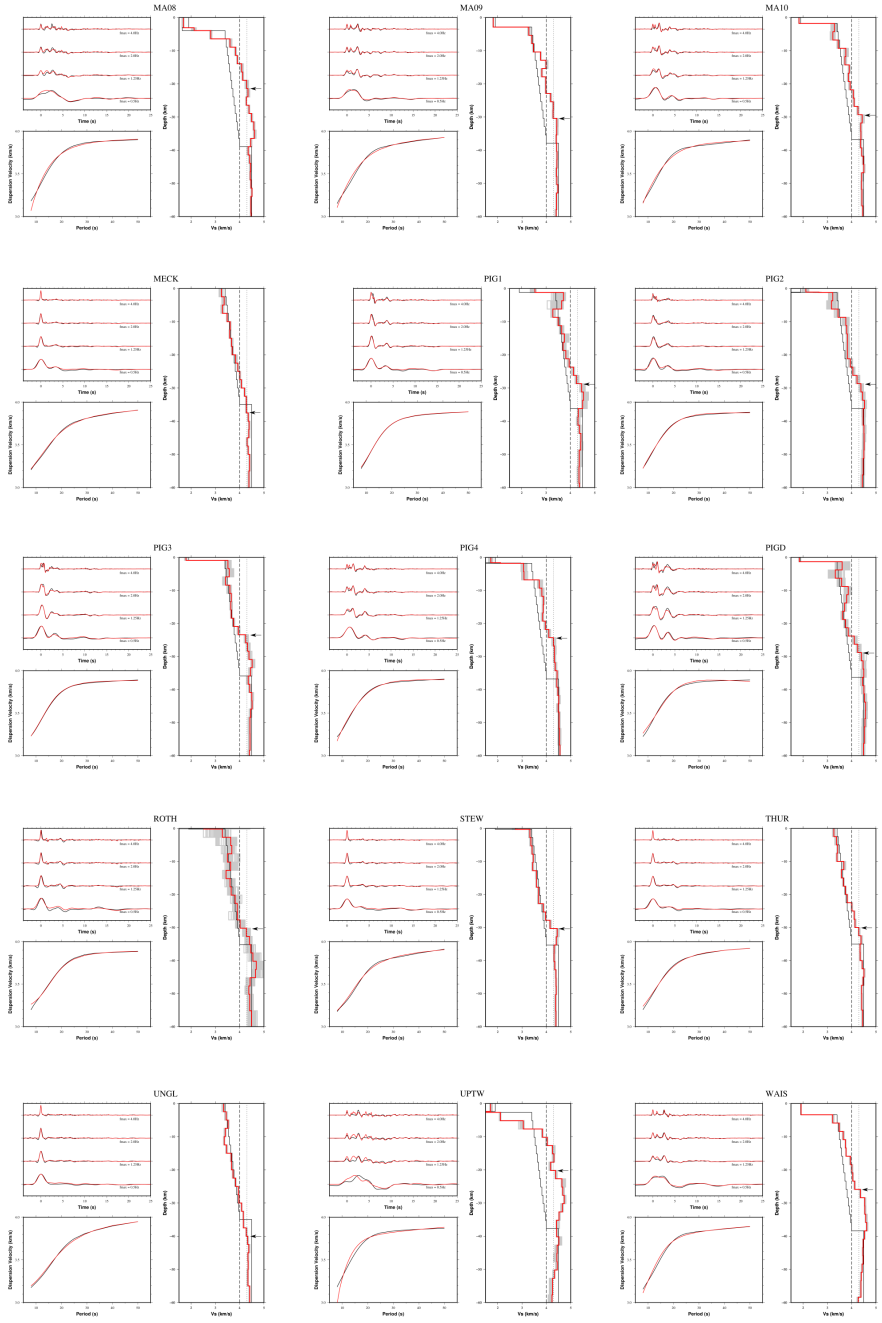

Figure A.57: Joint inversion results using moveout corrected and stacked receiver functions at four maximum frequencies (0.5 Hz, 1.25 Hz, 2 Hz and 4 Hz), rather than stacking into narrow ray parameter bins.

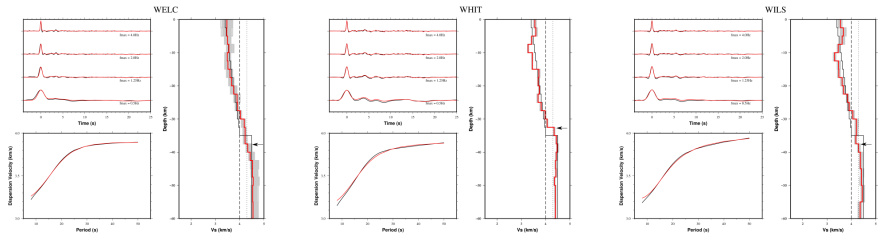

Figure A.58: Joint inversion results using moveout corrected and stacked receiver functions at four maximum frequencies (0.5 Hz, 1.25 Hz, 2 Hz and 4 Hz), rather than stacking into narrow ray parameter bins.

Appendix B

Appendix for Chapter 4

Table B.1: Event information for events located in Chapter 4 from January 2015- January 2018, as well as root mean square misfit between measured and predicted arrival times (RMS), horizonal error (ERH) and vertical error (ERZ) from Hypoinverse. Event classification abbreviations: Likely tectonic (T), possible ice-quake (P), likely ice-quake (I)

Predicted origin time	Lat	Lon	Depth (km)	ML	RMS (s)	ERH (km)	ERZ (km)	Classification
2015-05-29T20:01:53	-77.9505	-114.3157	7.0	1.4	4.0	15.0	31.6	T
2015-06-10T07:16:17	-75.2188	-100.5040	7.0	1.2	0.2	11.6	12.1	P
2015-07-30T19:43:51	-75.6208	-103.5320	0.9	1.7	1.3	52.7	28.3	P
2015-07-31T13:46:01	-75.3238	-102.9108	0.1	1.4	0.4	8.3	4.0	P
2016-01-29T11:16:28	-74.9225	-97.3538	44.2	1	0.1	13.4	4.3	T
2016-02-02T07:58:33	-75.3187	-94.9582	44.8	0.8	0.3	2.0	7.4	T
2016-02-02T21:04:08	-75.2698	-100.0705	0.0	0.5	0.4	2.2	1.7	P
2016-02-16T22:42:05	-74.0665	-95.1073	18.1	0.8	0.1	10.8	9.4	T
2016-02-22T00:10:19	-75.2975	-98.6745	7.4	0.8	0.2	0.5	2.0	I
2016-02-22T22:21:25	-75.5855	-96.0650	26.2	0.9	0.1	0.8	0.5	T
2016-02-23T04:33:33	-78.4590	-84.4425	0.0	0.5	3.3	6.2	6.8	P
2016-02-25T22:16:55	-75.1110	-100.5283	4.1	1.2	0.2	1.2	1.4	P
2016-02-26T13:54:31	-74.7590	-99.5493	8.4	0.9	0.1	0.6	0.6	T
2016-03-16T05:48:58	-74.8228	-99.1637	11.3	0.4	0.4	1.6	3.2	T
2016-03-19T19:37:49	-75.2458	-101.9237	17.0	0.6	0.2	2.1	1.7	T

Table B.1: Event information for events located in Chapter 4 from January 2015- January 2018, as well as root mean square misfit between measured and predicted arrival times (RMS), horizonal error (ERH) and vertical error (ERZ) from Hypoinverse. Event classification abbreviations: Likely tectonic (T), possible ice-quake (P), likely ice-quake (I)

Predicted origin time	Lat	Lon	Depth (km)	ML	RMS (s)	ERH (km)	ERZ (km)	Classification
2016-03-21T08:24:10	-77.0368	-85.2575	23.2	0.1	0.3	9.9	16.3	T
2016-03-30T07:56:42	-75.0698	-100.7303	4.7	0.3	0.2	0.6	0.4	P
2016-04-01T07:00:22	-75.3215	-99.9423	0.0	0.2	0.3	1.2	1.2	P
2016-04-02T21:44:42	-75.0660	-100.7680	5.4	0.5	0.1	0.5	0.7	P
2016-04-26T04:02:28	-75.2732	-99.2422	0.0	1.2	0.7	1.2	1.6	I
2016-04-27T19:31:06	-75.2922	-98.5400	15.0	0.9	0.4	1.3	4.3	I
2016-05-10T04:04:42	-77.5838	-82.5478	7.6	0.8	0.1	1.4	0.7	P
2016-05-10T19:53:11	-75.2958	-99.9547	0.0	1.1	0.3	0.6	0.8	I
2016-05-23T15:30:42	-77.2368	-81.5567	7.0	0	0.2	0.9	18.6	P
2016-06-04T20:37:35	-76.9967	-86.0682	3.6	0	0.1	11.5	12.0	P
2016-06-06T02:30:53	-75.3100	-98.5530	15.2	0.8	0.1	0.8	2.6	I
2016-06-08T10:00:26	-75.3260	-98.8725	2.4	1	0.2	0.6	4.5	I
2016-06-14T19:29:37	-75.1788	-98.9157	0.0	-0.2	0.2	0.6	0.6	P
2016-06-14T20:42:37	-75.8362	-106.1947	58.5	1	0.5	1.3	8.0	T
2016-06-20T15:44:10	-75.1408	-100.8637	2.4	0.4	0.2	0.8	0.8	P

Table B.1: Event information for events located in Chapter 4 from January 2015- January 2018, as well as root mean square misfit between measured and predicted arrival times (RMS), horizonal error (ERH) and vertical error (ERZ) from Hypoinverse. Event classification abbreviations: Likely tectonic (T), possible ice-quake (P), likely ice-quake (I)

Predicted origin time	Lat	Lon	Depth (km)	ML	RMS (s)	ERH (km)	ERZ (km)	Classification
2016-06-26T15:07:59	-75.7182	-96.8058	16.7	-0.2	0.1	0.6	0.3	T
2016-06-28T16:50:11	-75.1002	-100.6702	2.4	0.5	0.3	1.5	1.0	P
2016-07-03T00:56:15	-76.8952	-86.1192	3.5	-0.4	0.1	15.5	13.3	P
2016-07-07T02:19:16	-75.2325	-99.0543	0.9	1	0.3	0.7	1.4	I
2016-08-01T04:57:42	-75.1467	-101.3018	0.7	0.9	0.2	1.3	0.6	P
2016-08-02T08:08:10	-75.0957	-102.0887	29.4	0.7	0.2	1.8	13.6	T
2016-08-11T11:22:17	-75.1152	-100.1173	11.6	0.9	0.1	0.5	0.8	P
2016-08-11T11:28:07	-75.0655	-100.2678	26.2	0.4	0.2	1.1	21.9	P
2016-08-13T20:14:49	-75.7992	-96.6235	16.8	0	0.1	0.7	0.4	T
2016-08-17T02:03:20	-75.0233	-100.4048	26.9	-0.1	0.2	0.8	16.0	P
2016-08-19T18:07:17	-75.2907	-98.6043	11.2	1	0.1	0.4	0.9	I
2016-08-30T08:03:43	-75.2865	-99.1965	0.0	0.7	0.6	1.1	1.7	I
2016-08-30T15:06:20	-75.1585	-96.5648	11.8	0.3	0.1	1.0	1.0	T
2016-08-30T20:50:01	-75.2988	-100.1567	0.0	0.2	0.6	3.0	2.3	P
2016-09-02T05:27:16	-74.7297	-95.8603	6.7	0.9	0.1	1.6	16.7	T

Table B.1: Event information for events located in Chapter 4 from January 2015- January 2018, as well as root mean square misfit between measured and predicted arrival times (RMS), horizonal error (ERH) and vertical error (ERZ) from Hypoinverse. Event classification abbreviations: Likely tectonic (T), possible ice-quake (P), likely ice-quake (I)

Predicted origin time	Lat	Lon	Depth (km)	ML	RMS (s)	ERH (km)	ERZ (km)	Classification
2016-09-02T07:38:37	-75.2957	-98.6562	7.8	1.2	0.7	1.4	4.3	I
2016-09-02T10:05:20	-75.3340	-99.0607	8.6	1	0.1	0.4	1.2	I
2016-09-06T16:20:43	-76.9903	-86.0437	14.4	-0.2	0.0	12.0	11.8	P
2016-09-08T13:00:57	-75.5717	-95.0165	14.5	0.6	0.3	1.2	0.7	T
2016-09-12T00:15:01	-75.2908	-99.5795	0.0	0.9	0.9	1.3	2.0	P
2016-09-19T02:29:08	-73.9172	-98.5692	15.8	0.9	0.1	1.0	1.0	T
2016-09-20T16:20:07	-74.6793	-99.6907	8.2	1.4	0.1	0.4	0.5	T
2016-09-23T08:44:25	-77.6207	-85.6002	5.1	0.3	0.3	1.8	2.5	I
2016-09-30T18:11:34	-74.9912	-101.6382	8.3	1.2	0.2	1.8	2.5	I
2016-10-06T08:58:48	-77.4465	-81.7165	3.0	0.2	0.4	1.1	16.7	P
2016-10-13T04:05:53	-75.2278	-101.2440	7.6	0.6	0.2	0.9	0.9	P
2016-10-14T06:07:20	-74.9298	-101.0475	3.7	0.4	0.1	2.0	2.1	I
2016-10-17T05:49:11	-75.2313	-101.1965	7.2	0.8	0.1	1.5	1.5	P
2016-10-20T05:41:54	-75.2803	-99.2128	0.0	1	0.7	1.2	1.8	I
2016-11-09T00:44:21	-76.1548	-113.8278	7.0	1.7	5.5	14.0	31.6	P

Table B.1: Event information for events located in Chapter 4 from January 2015- January 2018, as well as root mean square misfit between measured and predicted arrival times (RMS), horizonal error (ERH) and vertical error (ERZ) from Hypoinverse. Event classification abbreviations: Likely tectonic (T), possible ice-quake (P), likely ice-quake (I)

Predicted origin time	Lat	Lon	Depth (km)	ML	RMS (s)	ERH (km)	ERZ (km)	Classification
2016-11-10T10:59:19	-75.3127	-100.9312	11.5	0.5	0.1	1.2	1.9	T
2016-11-11T12:08:28	-75.0673	-100.6358	12.3	0.7	0.6	5.7	6.4	P
2016-11-16T11:52:39	-78.2338	-121.3355	7.0	1.3	1.6	4.9	31.6	T
2016-11-20T04:41:09	-74.8075	-98.7387	0.5	0.8	0.1	1.3	0.8	P
2016-12-05T22:32:37	-75.2880	-98.5225	9.3	1.3	0.6	1.9	4.5	I
2016-12-21T19:13:32	-74.8640	-94.3745	9.0	0.5	0.1	0.7	0.5	T
2017-01-01T15:37:35	-74.7720	-99.5217	8.0	1.1	0.0	0.9	1.2	T
2017-01-02T22:06:55	-75.4235	-105.7717	35.0	1.3	0.6	3.6	8.7	T
2017-01-11T06:42:03	-74.2055	-101.8005	0.0	1.3	0.4	1.8	1.1	I
2017-02-07T15:30:06	-74.7867	-98.2400	14.6	0.8	0.0	2.7	3.3	T
2017-02-19T21:45:24	-75.3935	-106.1880	28.4	1.2	0.7	6.3	22.3	T
2017-03-11T05:28:04	-74.7330	-98.1160	8.9	1.1	0.2	3.1	4.6	T
2017-03-11T05:34:33	-74.7495	-97.8375	16.9	0.4	0.3	4.8	4.5	T
2017-03-13T16:08:18	-76.6702	-107.6705	10.0	2.4	0.1	10.5	10.6	T
2017-04-09T08:47:36	-76.9053	-106.9427	0.0	1.1	3.4	43.0	19.4	T

Table B.1: Event information for events located in Chapter 4 from January 2015- January 2018, as well as root mean square misfit between measured and predicted arrival times (RMS), horizonal error (ERH) and vertical error (ERZ) from Hypoinverse. Event classification abbreviations: Likely tectonic (T), possible ice-quake (P), likely ice-quake (I)

Predicted origin time	Lat	Lon	Depth (km)	ML	RMS (s)	ERH (km)	ERZ (km)	Classification
2017-04-20T10:33:21	-75.1538	-100.5068	17.6	0.7	0.0	2.4	3.8	P
2017-04-30T23:50:42	-75.2752	-97.9287	13.1	1	0.0	3.1	1.3	I
2017-06-08T18:18:02	-75.1005	-100.5242	18.1	0.7	0.0	0.8	2.0	P
2017-06-15T20:46:32	-72.0998	-103.8162	7.0	2.3	2.6	12.1	31.6	T
2017-06-27T00:13:09	-74.5525	-98.2183	7.9	1.1	0.0	5.0	11.5	T
2017-07-12T05:21:28	-75.1795	-102.0478	21.9	1.9	0.2	0.6	1.2	T
2017-07-13T03:11:43	-75.1910	-102.0430	19.9	1.4	0.1	0.5	1.0	T
2017-07-13T08:27:36	-75.1997	-102.1797	21.0	0.7	0.1	0.7	1.2	T
2017-08-26T18:12:24	-74.6502	-99.1665	26.5	0.8	0.1	1.5	12.1	T
2017-11-10T04:07:45	-75.0882	-100.0092	9.0	0.7	0.0	1.3	2.6	P
2017-12-03T01:52:40	-75.2090	-98.4508	6.7	0.1	0.0	1.1	1.0	P

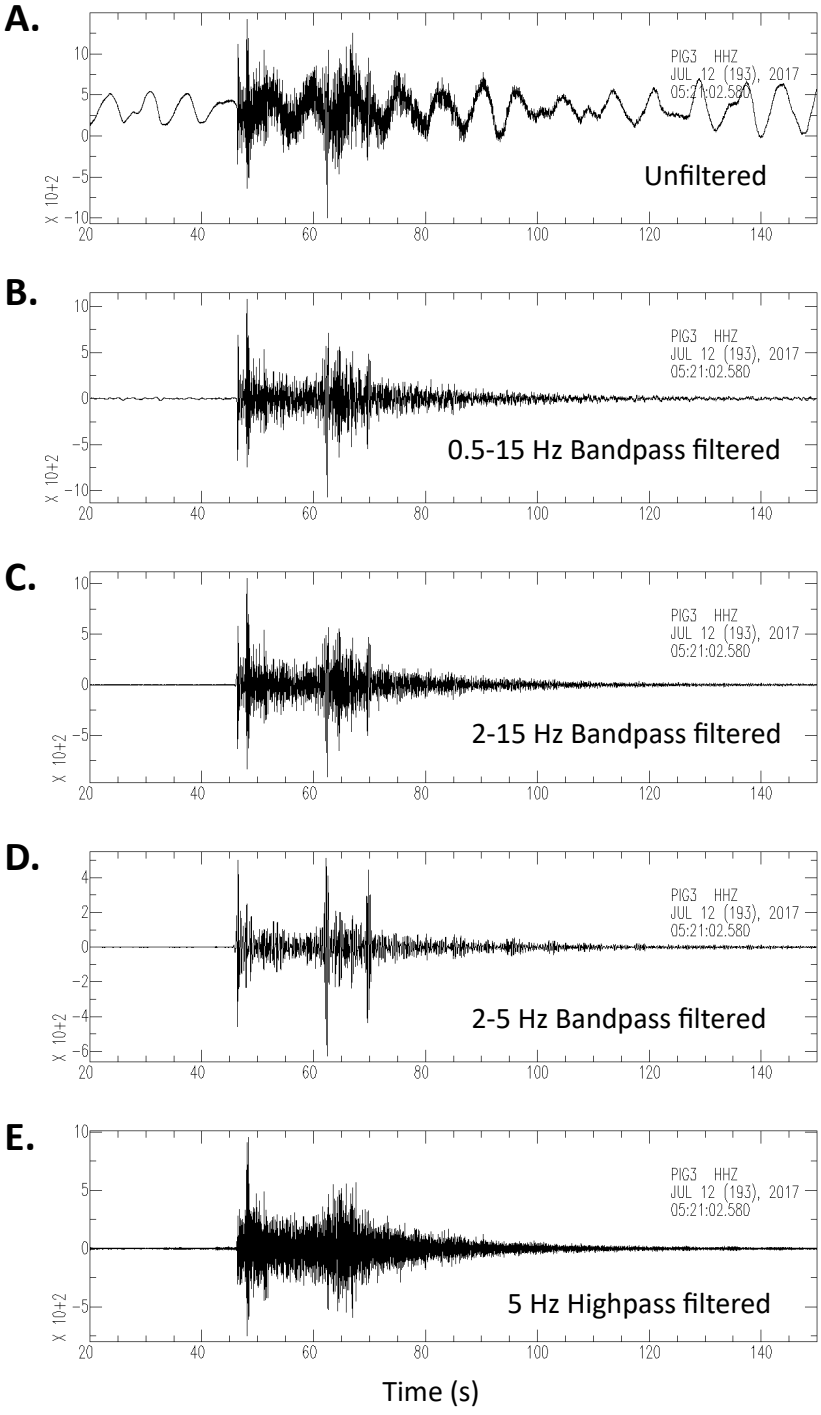

Figure B.1: Examples of filter testing for a local event recorded on the vertical component at PIG3. a) The unfiltered vertical component, b) 0.5-15 Hz bandpass filtered, c) 2-15 Hz bandpass filtered, d) 2-5 Hz bandpass filtered, e) 5 Hz highpass filtered.

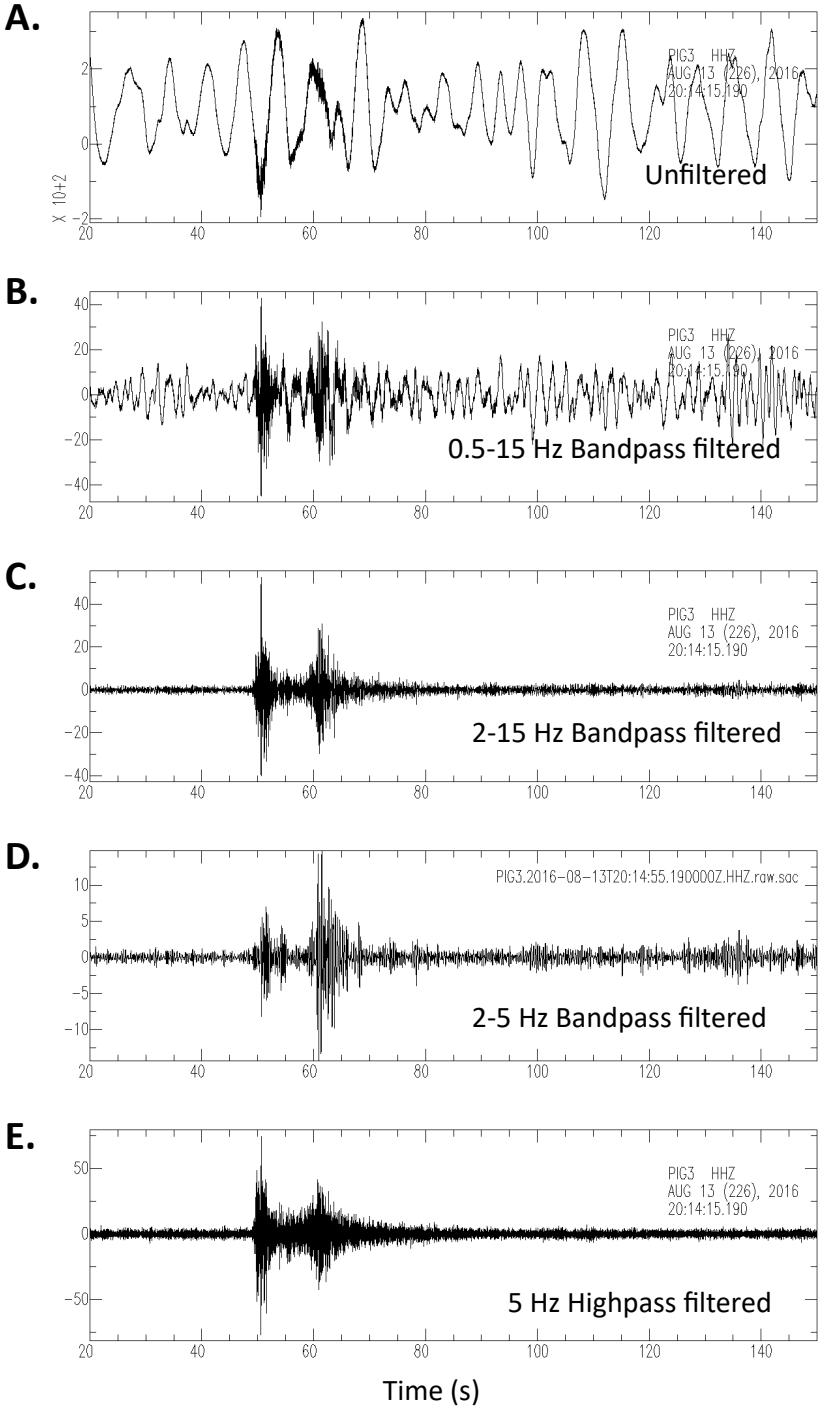

Figure B.2: Examples of filter testing for a weaker local event recorded on the vertical component at PIG3. a) The unfiltered vertical component, b) 0.5-15 Hz bandpass filtered, c) 2-15 Hz bandpass filtered, d) 2-5 Hz bandpass filtered, e) 5 Hz highpass filtered.

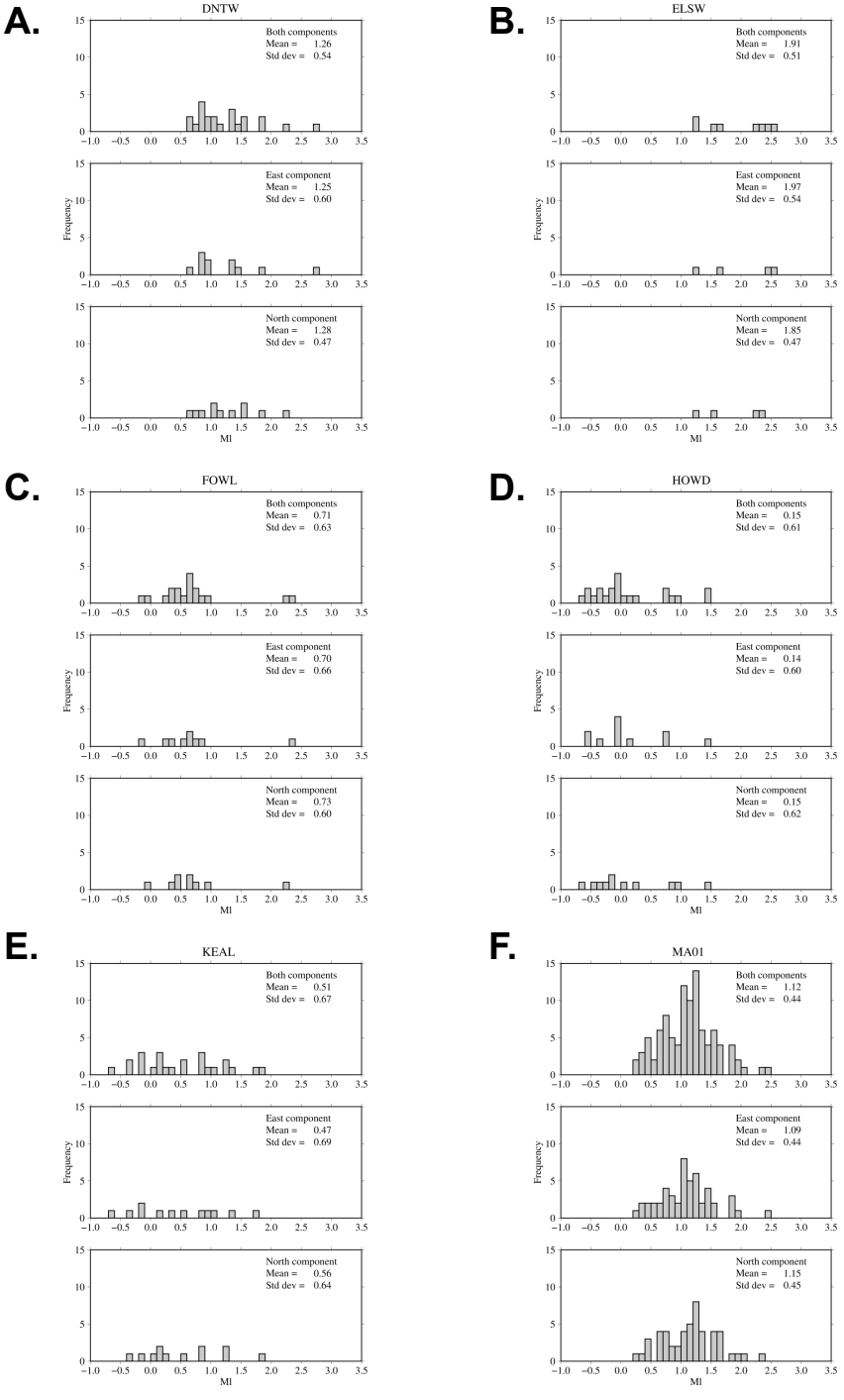

Figure B.3: Histograms of local magnitude calculated at each station for both components (top panel) East component (middle panel) and North component (bottom panel). Stations shown are DNTW (A.), ELSW (B.), FOWL (C.), HOWD (D.), KEAL (E.), MA01 (F.).

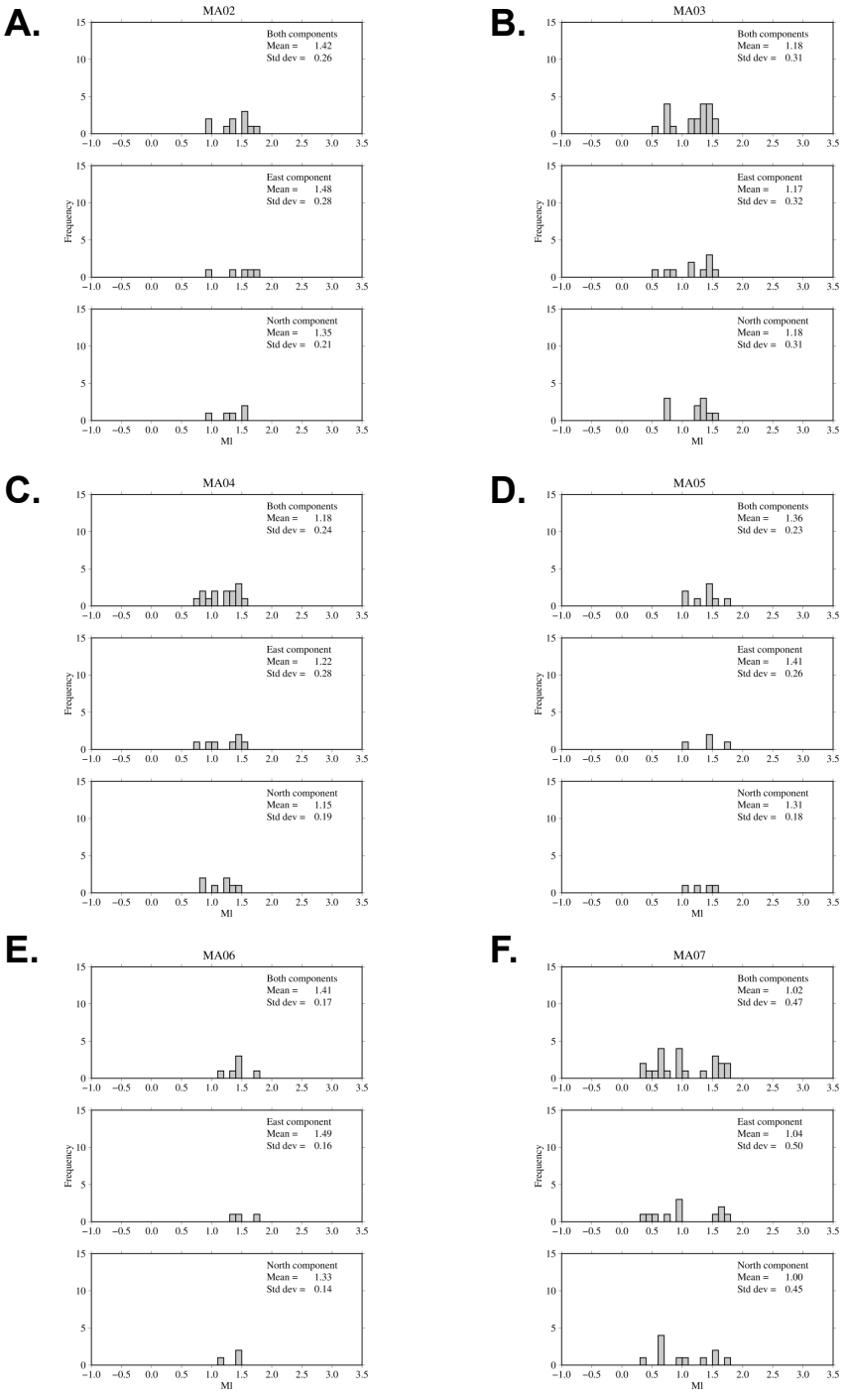

Figure B.4: Histograms of local magnitude calculated at each station for both components (top panel) East component (middle panel) and North component (bottom panel). Stations shown are MA02 (A.), MA03 (B.), MA04 (C.), MA05 (D.), MA06 (E.), MA07 (F.).

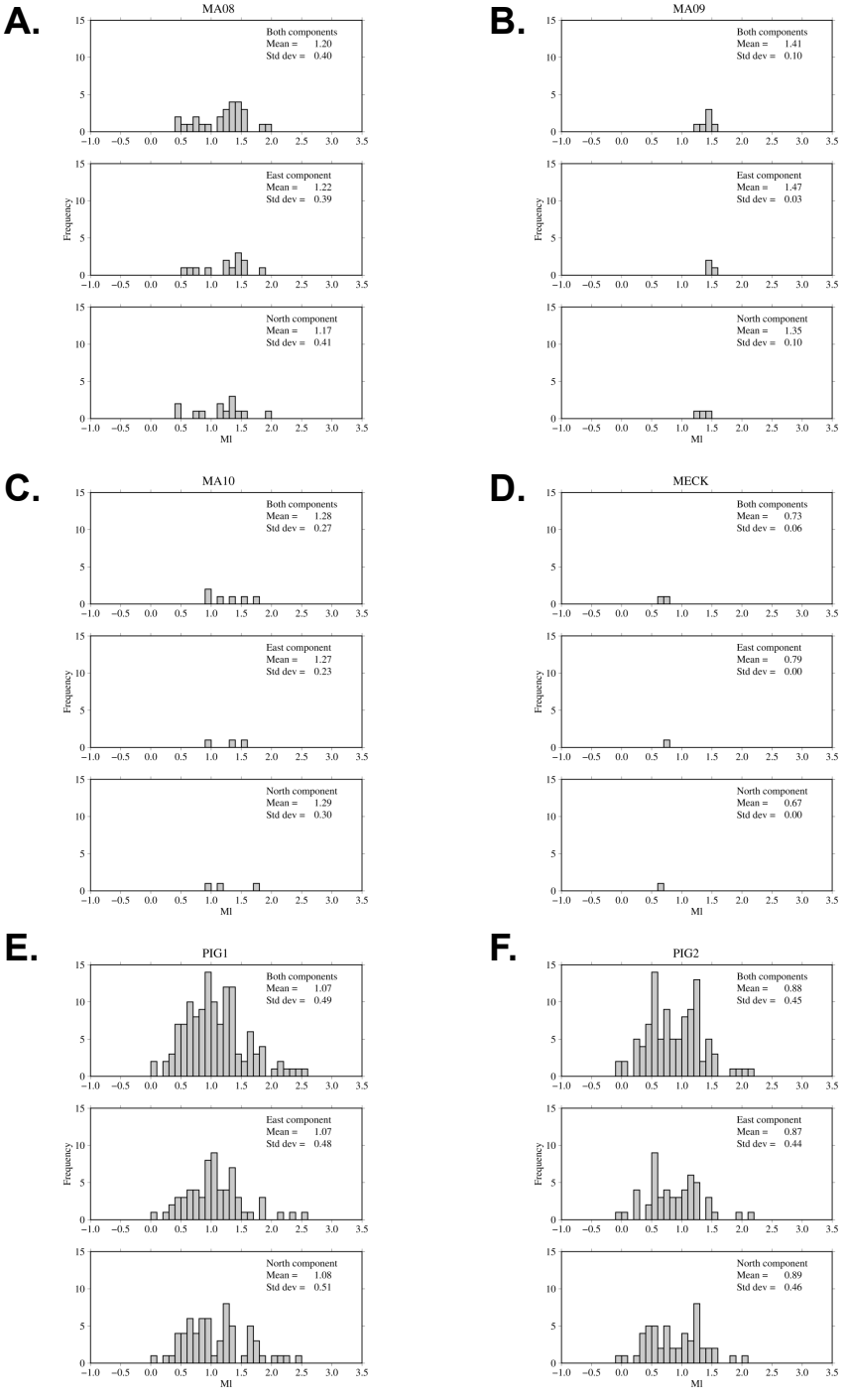

Figure B.5: Histograms of local magnitude calculated at each station for both components (top panel) East component (middle panel) and North component (bottom panel). Stations shown are MA08 (A.), MA09 (B.), MA10 (C.), MECK (D.), PIG1 (E.), PIG2 (F.).

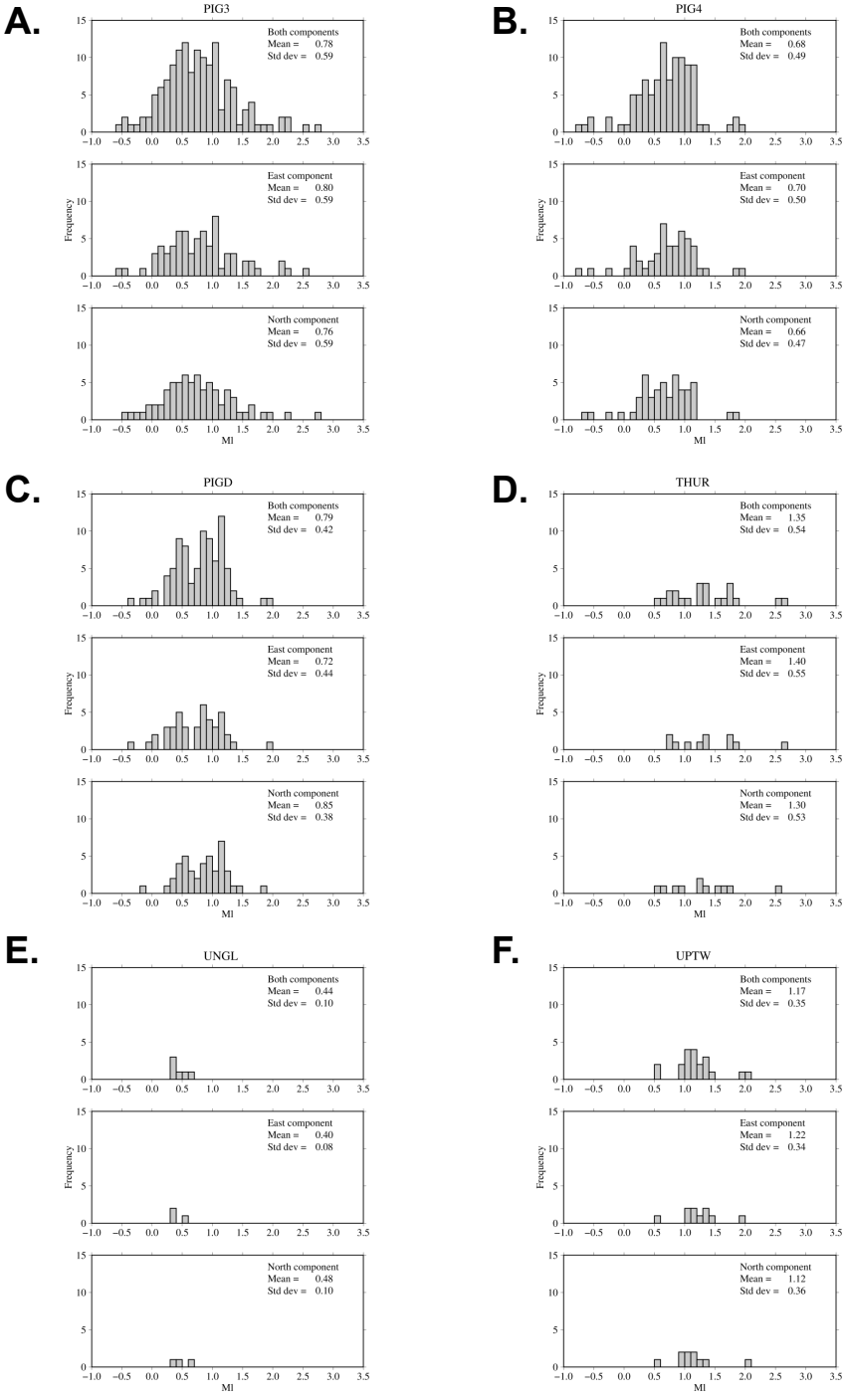

Figure B.6: Histograms of local magnitude calculated at each station for both components (top panel) East component (middle panel) and North component (bottom panel). Stations shown are PIG3 (A.), PIG4 (B.), PIGD (C.), THUR (D.), UNGL (E.), UPTW (F.).

Appendix C

Appendix for Chapter 5

Table C.1: Event information for events clustered around Pine Island Glacier's ice melánge from Chapter 5.

Predicted origin time	Lat	Lon	Depth (km)	M_L	RMS (s)	ERH (km)	ERZ (km)
2016-02-14T22:21:07	-74.7942	-100.7952	4.0	0.3	0.1	0.6	1.1
2016-03-04T15:08:31	-74.8948	-100.4940	0.0	0.7	0.2	1.3	0.7
2016-03-04T18:52:24	-74.8680	-100.5822	8.9	0.6	0.1	0.5	1.4
2016-03-05T07:47:23	-74.8620	-100.6813	7.1	0.9	0.1	1.1	0.7
2016-03-13T09:47:44	-74.8615	-100.6347	8.8	0.7	0.0	0.6	1.3
2016-03-13T11:31:19	-74.8680	-100.5913	4.5	0.8	0.0	0.6	0.8
2016-03-13T13:37:07	-74.8595	-100.6455	4.2	0.7	0.1	0.6	0.7
2016-03-13T22:34:21	-74.8675	-100.5925	5.8	0.5	0.1	0.7	1.1
2016-03-14T12:02:26	-74.8523	-100.7360	4.8	0.7	0.1	0.5	0.9
2016-03-14T16:51:01	-74.8668	-100.7392	4.8	0.5	0.1	0.9	1.3
2016-03-14T20:42:56	-74.8585	-100.7128	3.8	0.6	0.1	0.6	0.6
2016-03-15T06:34:31	-74.8632	-100.6170	7.7	0.6	0.1	0.6	1.2
2016-04-21T10:27:43	-74.8685	-100.6842	4.4	0.2	0.1	0.7	0.8
2016-04-28T05:33:57	-74.8750	-100.6145	0.0	0.5	0.2	1.1	0.7
2016-04-28T20:28:22	-74.8703	-100.6288	3.7	0.2	0.1	0.7	1.4
2016-04-29T12:09:07	-74.8733	-100.6000	10.2	0.2	0.1	0.5	0.8

Table C.1: Event information for events clustered around Pine Island Glacier's ice melánge from Chapter 5.

Predicted origin time	Lat	Lon	Depth (km)	M_L	RMS (s)	ERH (km)	ERZ (km)
2016-05-02T17:56:07	-74.8515	-100.7760	1.0	0.4	0.2	1.0	1.2
2016-05-14T21:19:17	-74.8545	-100.6922	4.7	0.5	0.1	0.8	1.4
2016-07-11T22:45:18	-74.8707	-100.6087	5.8	0.3	0.1	0.6	1.4
2016-07-12T07:09:30	-74.8400	-100.7977	5.0	0.4	0.1	0.7	1.5
2016-07-27T23:54:51	-74.8627	-100.5927	4.9	0.2	0.1	0.7	1.4
2016-07-28T07:03:52	-74.8293	-100.7860	5.0	0.4	0.0	0.7	1.4
2016-07-30T06:04:18	-74.8540	-100.7107	7.2	0.3	0.3	1.0	1.6
2016-08-28T20:13:32	-74.9628	-101.2828	6.1	0.4	0.1	3.5	4.4
2016-10-08T04:15:44	-74.8930	-101.0458	0.5	0.7	0.1	0.7	0.5
2016-10-15T13:32:01	-74.8605	-100.8577	0.0	0.4	0.3	0.8	0.7
2016-10-15T16:57:18	-74.8640	-100.8285	2.3	0.4	0.1	1.4	0.7
2016-10-16T02:23:19	-74.8598	-100.7648	7.3	0.3	0.1	1.2	2.5
2016-10-16T06:12:15	-74.8617	-100.8418	5.3	0.3	0.1	1.1	0.9
2016-10-16T12:35:17	-74.8570	-101.0553	4.3	0.5	0.1	1.6	1.8
2016-11-28T07:31:07	-74.8895	-100.6842	4.5	0.6	0.0	0.7	1.5
2016-12-06T00:08:30	-74.8613	-100.7698	2.3	0.6	0.1	0.6	0.5

Table C.1: Event information for events clustered around Pine Island Glacier's ice melánge from Chapter 5.

Predicted origin time	**Lat**	**Lon**	**Depth (km)**	$\mathbf{M}_L$	**RMS (s)**	**ERH (km)**	**ERZ (km)**
2016-12-06T21:56:01	-74.7847	-100.9443	8.9	0.9	0.1	1.1	1.3
2016-12-08T11:49:02	-74.9575	-101.5112	6.7	0.4	0.1	1.7	2.7

References

Accardo, N. J., D. a. Wiens, S. Hernandez, R. C. Aster, A. Nyblade, A. Huerta, S. Anandakrishnan, T. Wilson, D. S. Heeszel, and I. W. D. Dalziel (2014), Upper mantle seismic anisotropy beneath the west antarctic rift system and surrounding region from shear wave splitting analysis, *Geophysical Journal International*, *198*(1), 414–429.

Adalgeirsdóttir, G., A. M. Smith, T. Murray, M. King, K. Makinson, K. W. Nicholls, and A. Behar (2008), Tidal influence on rutford ice stream, west antarctica: observations of surface flow and basal processes from closely spaced gps and passive seismic stations, *Journal of Glaciology*, *54*(187), 715–724.

Adams, R., and A. Akoto (1986), Earthquakes in continental antarctica, *Journal of geodynamics*, *6*(1-4), 263–270.

Adams, R., A. Hughes, and B. Zhang (1985), A confirmed earthquake in continental antarctica, *Geophysical Journal International*, *81*(2), 489–492.

An, M., D. a. Wiens, Y. Zhao, M. Feng, A. a. Nyblade, M. Kanao, Y. Li, A. Maggi, and J.-J. Lévêque (2015), S-velocity model and inferred Moho topography beneath the Antarctic Plate from Rayleigh waves, *Journal of Geophysical Research: Solid Earth*, *120*(Figure 1), 2007–2010.

Anandakrishnan, S., and R. Alley (1997), Tidal forcing of basal seismicity of ice stream c, west antarctica, observed far inland, *Journal of Geophysical Research: Solid Earth*, *102*(B7), 15,183–15,196.

Anandakrishnan, S., and J. P. Winberry (2004), Antarctic subglacial sedimentary layer thickness from receiver function analysis, *Global And Planetary Change*, *42*, 167–176.

Anthony, R. E., R. C. Aster, D. Wiens, S. Anandakrishnan, A. Huerta, J. P. Winberry, T. Wilson, C. Rowe, A. Nyblade, S. Anandakrishnan, A. Huerta, J. P. Winberry, T. Wilson, and C. Rowe (2015), The Seismic Noise Environment of Antarctica, *Seismological Research Letters*, *86*(1), 89–100.

Arndt, J. E., R. D. Larter, P. Friedl, K. Gohl, K. Höppner, et al. (2018), Bathymetric controls on calving processes at pine island glacier, *The Cryosphere*, *12*(6), 2039–2050.

Bao, X., X. Sun, M. Xu, D. W. Eaton, X. Song, L. Wang, Z. Ding, N. Mi, H. Li, D. Yu, et al. (2015), Two crustal low-velocity channels beneath se tibet revealed by joint inversion of rayleigh wave dispersion and receiver functions, *Earth and Planetary Science Letters*, *415*, 16–24.

Baranov, a., and a. Morelli (2013), The Moho depth map of the Antarctica region, *Tectonophysics*, *609*, 299–313.

Baranov, A., R. Tenzer, and A. Morelli (2021), Updated antarctic crustal model, *Gondwana Research*, *89*, 1–18.

Barletta, V. R., M. Bevis, B. E. Smith, T. Wilson, A. Brown, A. Bordoni, M. Willis, S. A. Khan, M. Rovira-Navarro, I. Dalziel, et al. (2018), Observed rapid bedrock uplift in amundsen sea embayment promotes ice-sheet stability, *Science*, *360*(6395), 1335–1339.

Begeman, C. B., S. M. Tulaczyk, and A. T. Fisher (2017), Spatially variable geothermal heat flux in west antarctica: evidence and implications, *Geophysical Research Letters*, *44*(19), 9823–9832.

Behrendt, J. C. (1999), Crustal and lithospheric structure of the west Antarctic Rift System from geophysical investigations - A review, *Global and Planetary Change*, *23*(1-4), 25–44.

Behrendt, J. C., and A. Cooper (1991), Evidence of rapid cenozoic uplift of the shoulder escarpment of the cenozoic west antarctic rift system and a speculation on possible climate forcing, *Geology*, *19*(4), 315–319.

Behrendt, J. C., W. E. LeMasurier, a. K. Cooper, F. Tessensohn, a. Tréhu, and D. Damaske (1991), Geophysical studies of the West Antarctic Rift System, *Tectonics*, *10*(6), 1257.

Bell, R., D. Blankenship, C. Finn, D. Morse, T. Scambos, J. Brozena, and S. Hodge (1998), Influence of subglacial geology on the onset of a west antarctic ice stream from aerogeophysical observations, *Nature*, *394*(6688), 58–62.

Benn, D. I., and J. A. Åström (2018), Calving glaciers and ice shelves, *Advances in Physics: X*, *3*(1), 1513,819.

Beyreuther, M., R. Barsch, L. Krischer, T. Megies, Y. Behr, and J. Wassermann (2010), Obspy: A python toolbox for seismology, *Seismological Research Letters*, *81*(3), 530–533.

Bialas, R. W., W. R. Buck, M. Studinger, and P. G. Fitzgerald (2007), Plateau collapse model for the transantarctic mountains-West Antarctic rift system: Insights from numerical experiments, *Geology*, *35*(8), 687–690.

Bindschadler, R. A., P. L. Vornberger, M. A. King, and L. Padman (2003), Tidally driven stick–slip motion in the mouth of whillans ice stream, antarctica, *Annals of Glaciology*, *36*, 263–272.

Bingham, R. G., F. Ferraccioli, E. C. King, R. D. Larter, H. D. Pritchard, A. M. Smith, and D. G. Vaughan (2012), Inland thinning of west antarctic ice sheet steered along subglacial rifts, *Nature*, *487*(7408), 468.

Bird, P. (1991), Lateral extrusion of lower crust from under high topography in the isostatic limit, *Journal of Geophysical Research: Solid Earth*, *96*(B6), 10,275–10,286.

Blankenship, D., D. Morse, C. Finn, R. Bell, M. Peters, S. Kempf, S. Hodge, M. Studinger, J. C. Behrendt, and J. Brozena (2001), Geologic controls on the initi-

ation of rapid basal motion for west antarctic ice streams: A geophysical perspective including new airborne radar sounding and laser altimetry results, *The West Antarctic ice sheet: behavior and environment*, *77*, 105–121.

Blankenship, D. D., R. E. Bell, S. M. Hodge, J. M. Brozena, J. C. Behrendt, and C. A. Finn (1993), Active volcanism beneath the west antarctic ice sheet and implications for ice-sheet stability, *Nature*, *361*(6412), 526–529.

Block, A. E., R. E. Bell, and M. Studinger (2009), Antarctic crustal thickness from satellite gravity: Implications for the Transantarctic and Gamburtsev Subglacial Mountains, *Earth and Planetary Science Letters*, *288*(1-2), 194–203.

Boger, S. D. (2011), Antarctica—before and after gondwana, *Gondwana Research*, *19*(2), 335–371.

Brisbourne, A. M., A. M. Smith, D. G. Vaughan, E. C. King, D. Davies, R. Bingham, E. Smith, I. Nias, and S. H. Rosier (2017), Bed conditions of pine island glacier, west antarctica, *Journal of Geophysical Research: Earth Surface*, *122*(1), 419–433.

Brocher, T. M. (2005), Empirical relations between elastic wavespeeds and density in the earth's crust, *Bulletin of the Seismological Society of America*, *95*(6), 2081–2092.

Burton-Johnson, A., J. Halpin, J. M. Whittaker, F. S. Graham, and S. J. Watson (2017), A new heat flux model for the antarctic peninsula incorporating spatially variable upper crustal radiogenic heat production, *Geophysical Research Letters*, *44*(11), 5436–5446.

Cande, S., J. Stock, R. Müller, and T. Ishihara (2000), Cenozoic motion between east and west Antarctica, *Nature*, *404*(6774), 145–50.

Chai, C., C. Ammon, S. Anandakrishnan, C. Ramirez, and A. Nyblade (2017), Estimating subglacial structure using p-wave receiver functions, *Geophysical Journal International*.

Chaput, J., R. C. Aster, A. Huerta, X. Sun, A. Lloyd, D. Wiens, A. Nyblade, S. Anan-

dakrishnan, J. P. Winberry, and T. Wilson (2014), The crustal thickness of West Antarctica, *J. Geophys. Res. Solid Earth*, *119*(August 2013), 378–395.

Cho, T. (2011), Removing Reverberation in Ice Sheets from Receiver Functions, *Seismological Research Letters*, *82*(2), 207–210.

Christensen, N. I. (1996), Poisson's ratio and crustal seismology, *Journal of Geophysical Research: Solid Earth*, *101*(B2), 3139–3156.

Christensen, N. I., and W. D. Mooney (1995), Seismic velocity structure and composition of the continental crust: A global view, *Journal of Geophysical Research: Solid Earth*, *100*(B6), 9761–9788.

Clark, M. K., J. W. Bush, and L. H. Royden (2005), Dynamic topography produced by lower crustal flow against rheological strength heterogeneities bordering the tibetan plateau, *Geophysical Journal International*, *162*(2), 575–590.

Cogley, J. G. (1984), Deglacial hypsometry of Antarctica, *Earth and Planetary Science Letters*, *67*, 284–296.

Colgan, W., H. Rajaram, W. Abdalati, C. McCutchan, R. Mottram, M. S. Moussavi, and S. Grigsby (2016), Glacier crevasses: Observations, models, and mass balance implications, *Reviews of Geophysics*, *54*(1), 119–161.

Corr, H. F., and D. G. Vaughan (2008), A recent volcanic eruption beneath the west antarctic ice sheet, *Nature Geoscience*, *1*(2), 122–125.

Dalziel, I. W. (1992), Antarctica; a tale of two supercontinents?, *Annual Review of Earth and Planetary Sciences*, *20*(1), 501–526.

Dalziel, I. W. D., and D. H. Elliot (1982), West Antarctica: Problem child of Gondwanaland, *Tectonics*, *1*(1), 3.

Damiani, T. M., T. A. Jordan, F. Ferraccioli, D. A. Young, and D. D. Blankenship (2014), Variable crustal thickness beneath thwaites glacier revealed from airborne gravimetry, possible implications for geothermal heat flux in west antarctica, *Earth and Planetary Science Letters*, *407*, 109–122.

Danesi, S., S. Bannister, and A. Morelli (2007), Repeating earthquakes from rupture of an asperity under an antarctic outlet glacier, *Earth and Planetary Science Letters*, *253*(1-2), 151–158.

de Vries, M. v. W., R. G. Bingham, and A. S. Hein (2017), A new volcanic province: an inventory of subglacial volcanoes in west antarctica, *Geological Society, London, Special Publications*, *461*, SP461–7.

de Vries, M. v. W., R. G. Bingham, and A. S. Hein (2018), A new volcanic province: an inventory of subglacial volcanoes in west antarctica, *Geological Society, London, Special Publications*, *461*(1), 231–248.

Diehl, T. M. (2008), *Gravity analyses for the crustal structure and subglacial geology of West Antarctica, particularly beneath Thwaites Glacier*, The University of Texas at Austin.

Divenere, V., D. V. Kent, and I. W. Dalziel (1996), Summary of palaeomagnetic results from west antarctica: implications for the tectonic evolution of the pacific margin of gondwana during the mesozoic, *Geological Society, London, Special Publications*, *108*(1), 31–43.

DiVenere, V. J., D. V. Kent, and I. Dalziel (1994), Mid-cretaceous paleomagnetic results from marie byrd land, west antarctica: A test of post-100 ma relative motion between east and west antarctica, *Journal of Geophysical Research: Solid Earth*, *99*(B8), 15,115–15,139.

Donnellan, A., and B. P. Luyendyk (2004), Gps evidence for a coherent antarctic plate and for postglacial rebound in marie byrd land, *Global and Planetary Change*, *42*(1), 305–311.

Dunham, C., J. O'Donnell, G. Stuart, A. Brisbourne, S. Rost, T. Jordan, A. Nyblade, D. Wiens, and R. Aster (2020), A joint inversion of receiver function and rayleigh wave phase velocity dispersion data to estimate crustal structure in west antarctica, *Geophysical Journal International*, *223*(3), 1644–1657.

Durrheim, R. J., and W. D. Mooney (1991), Archean and proterozoic crustal evolution: Evidence from crustal seismology, *Geology*, *19*(6), 606–609.

Dziadek, R., K. Gohl, N. Kaul, et al. (2019), Elevated geothermal surface heat flow in the amundsen sea embayment, west antarctica, *Earth and Planetary Science Letters*, *506*, 530–539.

Dziak, R. P., M. J. Fowler, H. Matsumoto, D. R. Bohnenstiehl, M. Park, K. Warren, and W. S. Lee (2013), Life and death sounds of iceberg a53a, *Oceanography*, *26*(2), 10–13.

Efron, B., and R. Tibshirani (1991), Statistical data analysis in the computer age, *Science*, *253*(5018), 390–395.

Ekström, G., M. Nettles, and G. A. Abers (2003), Glacial earthquakes, *Science*, *302*(5645), 622–624.

Emry, E. L., a. a. Nyblade, J. Julia, S. Anandakrishanan, R. C. Aster, D. a. Wiens, a. D. Huerta, and T. J. Wilson (2015), The mantle transition zone beneath West Antarctica: Seismic evidence for hydration and thermal upwellings, *Geochemistry, Geophysics, Geosystems*, *16*(1), 40–58.

Evison, F., C. Ingham, a. Orr, RH, and J. Le Fort (1960), Thickness of the earth's crust in antarctica and the surrounding oceans, *Geophysical Journal International*, *3*(3), 289–306.

Favier, L., G. Durand, S. L. Cornford, G. H. Gudmundsson, O. Gagliardini, F. Gillet-Chaulet, T. Zwinger, A. Payne, and A. M. Le Brocq (2014), Retreat of pine island glacier controlled by marine ice-sheet instability, *Nature Climate Change*, *4*(2), 117–121.

Ferraccioli, F., C. a. Finn, T. a. Jordan, R. E. Bell, L. M. Anderson, and D. Damaske (2011), East Antarctic rifting triggers uplift of the Gamburtsev Mountains, *Nature*, *479*(7373), 388–392.

Finn, C. A., R. D. Müller, and K. S. Panter (2005), A cenozoic diffuse alkaline magmatic province (damp) in the southwest pacific without rift or plume origin, *Geochemistry, Geophysics, Geosystems*, *6*(2).

Fisher, A. T., K. D. Mankoff, S. M. Tulaczyk, S. W. Tyler, N. Foley, et al. (2015), High geothermal heat flux measured below the west antarctic ice sheet, *Science Advances*, *1*(6), e1500,093.

Flowerdew, M., I. L. Millar, M. L. Curtis, A. Vaughan, M. Horstwood, M. J. Whitehouse, and C. M. Fanning (2007), Combined u-pb geochronology and hf isotope geochemistry of detrital zircons from early paleozoic sedimentary rocks, ellsworth-whitmore mountains block, antarctica, *Geological Society of America Bulletin*, *119*(3-4), 275–288.

Frankinet, B., T. Lecocq, and T. Camelbeeck (2020), Wind-induced seismic noise at the princess elisabeth antarctica station, *The Cryosphere Discussions*, pp. 1–16.

Fretwell, P., H. D. Pritchard, D. G. Vaughan, J. L. Bamber, N. E. Barrand, R. Bell, C. Bianchi, R. G. Bingham, D. D. Blankenship, G. Casassa, G. Catania, D. Callens, H. Conway, a. J. Cook, H. F. J. Corr, D. Damaske, V. Damm, F. Ferraccioli, R. Forsberg, S. Fujita, Y. Gim, P. Gogineni, J. a. Griggs, R. C. a. Hindmarsh, P. Holmlund, J. W. Holt, R. W. Jacobel, a. Jenkins, W. Jokat, T. Jordan, E. C. King, J. Kohler, W. Krabill, M. Riger-Kusk, K. a. Langley, G. Leitchenkov, C. Leuschen, B. P. Luyendyk, K. Matsuoka, J. Mouginot, F. O. Nitsche, Y. Nogi, O. a. Nost, S. V. Popov, E. Rignot, D. M. Rippin, a. Rivera, J. Roberts, N. Ross, M. J. Siegert, a. M. Smith, D. Steinhage, M. Studinger, B. Sun, B. K. Tinto, B. C. Welch, D. Wilson, D. a. Young, C. Xiangbin, and a. Zirizzotti (2013), Bedmap2: Improved ice bed, surface and thickness datasets for Antarctica, *Cryosphere*, *7*(1), 375–393.

Gohl, K. (2012), Basement control on past ice sheet dynamics in the amundsen sea embayment, west antarctica, *Palaeogeography, Palaeoclimatology, Palaeoecology*, *335*, 35–41.

Gohl, K., F. Nitsche, K. Vanneste, H. Miller, N. Fechner, L. Oszko, C. Hübscher,

E. Weigelt, and A. Lambrecht (1997), Tectonic and sedimentary architecture of the bellingshausen and amundsen sea basins, se pacific, by seismic profiling, in *In: Ricci, CA (Ed.), The Antarctic Region: Geological Evolution and Processes, p. 719-723, Terra Antartica Publication, Siena*, EPIC.

Gohl, K., D. Teterin, G. Eagles, G. Netzeband, J. Grobys, N. Parsiegla, P. Schlüter, V. T. Leinweber, R. D. Larter, G. Uenzelmann-Neben, et al. (2007), Geophysical survey reveals tectonic structures in the amundsen sea embayment, west antarctica, *US Geological Survey Open-File Report, 2007-1047 {http://pubs. usgs. gov/of/2007/1047/srp/srp047/}*.

Golynsky, A., F. Ferraccioli, J. Hong, D. Golynsky, R. von Frese, D. Young, D. Blankenship, J. Holt, S. Ivanov, A. Kiselev, et al. (2018), New magnetic anomaly map of the antarctic, *Geophysical Research Letters*, *45*(13), 6437–6449.

Granot, R., S. C. Cande, J. M. Stock, and D. Damaske (2013), Revised Eocene-Oligocene kinematics for the West Antarctic rift system, *Geophysical Research Letters*, *40*(October 2012), 1–6.

Grunow, M., D. V. Kent, and I. W. D. Dalziel (1991), New paleomagnetic data from Thurston Island: Implications for the tectonics of west Antarctica and Weddell Sea opening, *Journal of Geophysical Research*, *96*(B11), 17,935.

Gudmundsson, G. H. (2006), Fortnightly variations in the flow velocity of rutford ice stream, west antarctica, *Nature*, *444*(7122), 1063.

Hansen, S. E., A. M. Reusch, T. Parker, D. K. Bloomquist, P. Carpenter, J. H. Graw, and G. R. Brenn (2015), The transantarctic mountains northern network (tamnnet): Deployment and performance of a seismic array in antarctica, *Seismological Research Letters*, *86*(6), 1636–1644.

Heeszel, D. S., D. A. Wiens, S. Anandakrishnan, R. C. Aster, I. W. Dalziel, A. D. Huerta, A. A. Nyblade, T. J. Wilson, and J. P. Winberry (2016), Upper mantle structure of central and west antarctica from array analysis of rayleigh wave phase velocities, *Journal of Geophysical Research: Solid Earth*, *121*(3), 1758–1775.

Helffrich, G. (2006), Extended-time multitaper frequency domain cross-correlation receiver-function estimation, *Bulletin of the Seismological Society of America*, *96*(1), 344–347.

Hogg, A., A. Shepherd, and N. Gourmelen (2015), A first look at the performance of sentinel-1 over the west antarctic ice sheet, FRINGE.

Holbrook, W. S., W. D. Mooney, and N. I. Christensen (1992), The seismic velocity structure of the deep continental crust, *Continental lower crust*, *23*, 1–43.

Hu, J., J. Badal, H. Yang, G. Li, and H. Peng (2018), Comprehensive crustal structure and seismological evidence for lower crustal flow in the southeastern margin of tibet revealed by receiver functions, *Gondwana Research*, *55*, 42–59.

Hutton, L., and D. M. Boore (1987), The ml scale in southern california, *Bulletin of the Seismological Society of America*, *77*(6), 2074–2094.

Jacobs, J., S. Pisarevsky, R. J. Thomas, and T. Becker (2008), The kalahari craton during the assembly and dispersal of rodinia, *Precambrian Research*, *160*(1-2), 142–158.

Jeong, S., I. M. Howat, and J. N. Bassis (2016), Accelerated ice shelf rifting and retreat at pine island glacier, west antarctica, *Geophysical Research Letters*, *43*(22), 11–720.

Johnston, A. C. (1987), Suppression of earthquakes by large continental ice sheets, *Nature*, *330*(6147), 467–469.

Jordan, T., F. Ferraccioli, D. Vaughan, J. Holt, H. Corr, D. Blankenship, and T. Diehl (2010), Aerogravity evidence for major crustal thinning under the pine island glacier region (west antarctica), *Bulletin*, *122*(5-6), 714–726.

Jordan, T., F. Ferraccioli, and P. Leat (2017), New geophysical compilations link crustal block motion to jurassic extension and strike-slip faulting in the weddell sea rift system of west antarctica, *Gondwana Research*, *42*, 29–48.

Jordan, T. A., T. R. Riley, and C. S. Siddoway (2020), The geological history and evolution of west antarctica, *Nature Reviews Earth & Environment*, pp. 1–17.

Joughin, I., E. Rignot, C. E. Rosanova, B. K. Lucchitta, and J. Bohlander (2003), Timing of recent accelerations of pine island glacier, antarctica, *Geophysical Research Letters*, *30*(13).

Julia, J., C. Ammon, R. Herrmann, and A. M. Correig (2000), Joint inversion of receiver function and surface wave dispersion observations, *Geophysical Journal International*, *143*(1), 99–112.

Kaufmann, G., P. Wu, and E. R. Ivins (2005), Lateral viscosity variations beneath antarctica and their implications on regional rebound motions and seismotectonics, *Journal of Geodynamics*, *39*(2), 165–181.

Keiding, M., C. Kreemer, C. Lindholm, S. Gradmann, O. Olesen, and H. Kierulf (2015), A comparison of strain rates and seismicity for fennoscandia: depth dependency of deformation from glacial isostatic adjustment, *Geophysical Journal International*, *202*(2), 1021–1028.

Keir, D., G. Stuart, A. Jackson, and A. Ayele (2006a), Local earthquake magnitude scale and seismicity rate for the ethiopian rift, *Bulletin of the Seismological Society of America*, *96*(6), 2221–2230.

Keir, D., C. Ebinger, G. Stuart, E. Daly, and A. Ayele (2006b), Strain accommodation by magmatism and faulting as rifting proceeds to breakup: Seismicity of the northern ethiopian rift, *Journal of Geophysical Research: Solid Earth*, *111*(B5).

Kennett, B. (2005), Seismological tables: ak135, *Research School of Earth Sciences, Australian National University Canberra, Australia*, pp. 1–289.

Kennett, B., and E. Engdahl (1991), Traveltimes for global earthquake location and phase identification, *Geophysical Journal International*, *105*(2), 429–465.

Kennett, J. P. (1977), Cenozoic evolution of antarctic glaciation, the circum-antarctic ocean, and their impact on global paleoceanography, *Journal of geophysical research*, *82*(27), 3843–3860.

Kind, R., G. Kosarev, and N. Petersen (1995), Receiver functions at the stations of the german regional seismic network (grsn), *Geophysical Journal International*, *121*(1), 191–202.

King, E. C., J. Woodward, and A. M. Smith (2007), Seismic and radar observations of subglacial bed forms beneath the onset zone of rutford ice stream, antarctica, *Journal of Glaciology*, *53*(183), 665–672.

King, E. C., H. D. Pritchard, and A. M. Smith (2016), Subglacial landforms beneath rutford ice stream, antarctica: detailed bed topography from ice-penetrating radar, *Earth System Science Data*, *8*(1), 151–158.

Kissling, E., U. Kradolfer, and H. Maurer (1995), Program velest user's guide-short introduction, *Institute of Geophysics, ETH Zurich*.

Klein, F. W. (1989), User's guide to hypoinverse, a program for vax computers to solve for earthquake locations and magnitudes.

Köhler, A., C. Nuth, J. Schweitzer, C. Weidle, and S. J. Gibbons (2015), Regional passive seismic monitoring reveals dynamic glacier activity on spitsbergen, svalbard, *Polar Research*, *34*(1), 26,178.

Kohnen, H. (1974), the Temperature Dependence of Seismic Waves, *Journal of Glaciology*, *13*(67), 144–147.

Kovach, R. L., and F. Press (1961), Surface wave dispersion and crustal structure in antarctica and the surrounding oceans, *Annals of Geophysics*, *14*(2), 211–224.

Langston, C. a. (1979), Structure under Mount Rainier, Washington, inferred from teleseismic body waves, *Journal of Geophysical Research*, *84*(B9), 4749.

Langston, C. A., R. Brazier, A. A. Nyblade, and T. J. Owens (1998), Local magnitude scale and seismicity rate for tanzania, east africa, *Bulletin of the Seismological Society of America*, *88*(3), 712–721.

Larter, R. D., and P. F. Barker (1991), Effects of ridge crest-trench interaction on antarctic-phoenix spreading: forces on a young subducting plate, *Journal of Geophysical Research: Solid Earth*, *96*(B12), 19,583–19,607.

Lawver, L. A., L. M. Gahagan, and M. F. Coffin (1992), The development of paleoseaways around antarctica, *Antarctic research series*, *56*, 7–30.

Lebedev, S., J. Boonen, and J. Trampert (2009), Seismic structure of precambrian lithosphere: new constraints from broad-band surface-wave dispersion, *Lithos*, *109*(1-2), 96–111.

LeMasurier, W., and D. Rex (1989), Evolution of linear volcanic ranges in marie byrd land, west antarctica, *Journal of Geophysical Research: Solid Earth*, *94*(B6), 7223–7236.

Ligorría, J. P., and C. J. Ammon (1999), Iterative deconvolution and receiver-function estimation, *Bulletin of the Seismological Society of America*, *89*(5), 1395–1400.

Llubes, M., N. Florsch, B. Legresy, J. M. Lemoine, S. Loyer, D. Crossley, and F. Rémy (2003), Crustal thickness in Antarctica from CHAMP gravimetry, *Earth and Planetary Science Letters*, *212*(1-2), 103–117.

Lodge, A., and G. Helffrich (2006), Depleted swell root beneath the cape verde islands, *Geology*, *34*(6), 449–452.

Loose, B., A. C. Naveira Garabato, P. Schlosser, W. J. Jenkins, D. Vaughan, and K. J. Heywood (2018), Evidence of an active volcanic heat source beneath the pine island glacier, *Nature Communications*.

Lough, A. C., D. a. Wiens, C. Grace Barcheck, S. Anandakrishnan, R. C. Aster, D. D. Blankenship, A. D. Huerta, A. Nyblade, D. a. Young, and T. J. Wilson (2013), Seismic detection of an active subglacial magmatic complex in Marie Byrd Land, Antarctica, *Nature Geoscience*, *6*(December), 1031–1035.

Lough, A. C., C. G. Barcheck, D. A. Wiens, A. Nyblade, and S. Anandakrishnan (2015),

A previously unreported type of seismic source in the firn layer of the east antarctic ice sheet, *Journal of Geophysical Research: Earth Surface*, *120*(11), 2237–2252.

Lough, A. C., D. A. Wiens, and A. Nyblade (2018), Reactivation of ancient antarctic rift zones by intraplate seismicity, *Nature Geoscience*, *11*(7), 515.

Lucas, E., N. Accardo, A. Nyblade, R. Aster, A. Lloyd, D. Wiens, J. O'Donnell, G. Stuart, I. Dalziel, T. Wilson, A. Huerta, and J. Winberry (2020), Upper mantle seismic anisotropy of antarctica from shear wave splitting (in prep), *TBC*, *N/A*(N/A), N/A.

Luyendyk, B. P. (1995), Hypothesis for Cretaceous rifting of east Gondwana caused by subducted slab capture, *Geology*, *23*(4), 373–376.

MacAyeal, D., E. Okal, R. Aster, and J. Bassis (2008), Seismic and hydroacoustic tremor generated by colliding icebergs, *Journal of Geophysical Research: Earth Surface*, *113*(F3).

MacAyeal, D. R., R. A. Bindschadler, and T. A. Scambos (1995), Basal friction of ice stream e, west antarctica, *Journal of Glaciology*, *41*(138), 247–262.

Martos, Y. M., M. Catalán, T. A. Jordan, A. Golynsky, D. Golynsky, G. Eagles, and D. G. Vaughan (2017), Heat flux distribution of antarctica unveiled, *Geophysical Research Letters*, *44*(22), 11–417.

Maslanyj, M., and B. Storey (1990), Regional aeromagnetic anomalies in ellsworth land: crustal structure and mesozoic microplate boundaries within west antarctica, *Tectonics*, *9*(6), 1515–1532.

Maule, C. F., M. E. Purucker, N. Olsen, and K. Mosegaard (2005), Heat flux anomalies in antarctica revealed by satellite magnetic data, *Science*, *309*(5733), 464–467.

Medley, B., I. R. Joughin, B. Smith, S. B. Das, E. J. Steig, H. Conway, S. Gogineni, C. S. Lewis, A. S. Criscitiello, J. R. McConnell, et al. (2014), Constraining the recent mass balance of pine island and thwaites glaciers, west antarctica, with airborne observations of snow accumulation.

Millar, I., and R. Pankhurst (1987), Rb-sr geochronology of the region between the antarctic peninsula and the transantarctic mountains: Haag nunataks and mesozoic granitoids, *Gondwana six: structure, tectonics, and geophysics*, *40*, 151–160.

Muto, A., L. E. Peters, K. Gohl, I. Sasgen, R. B. Alley, S. Anandakrishnan, and K. L. Riverman (2016), Subglacial bathymetry and sediment distribution beneath pine island glacier ice shelf modeled using aerogravity and in situ geophysical data: New results, *Earth and Planetary Science Letters*, *433*, 63–75.

Muto, A., S. Anandakrishnan, R. B. Alley, H. J. Horgan, B. R. Parizek, S. Koellner, K. Christianson, and N. Holschuh (2019), Relating bed character and subglacial morphology using seismic data from thwaites glacier, west antarctica, *Earth and Planetary Science Letters*, *507*, 199–206.

Nield, G. A., P. L. Whitehouse, W. van der Wal, B. Blank, J. P. O'Donnell, and G. W. Stuart (2018), The impact of lateral variations in lithospheric thickness on glacial isostatic adjustment in west antarctica, *Geophysical Journal International*, *214*(2), 811–824.

O'Donnell, J., K. Selway, A. A. Nyblade, R. Brazier, D. Wiens, S. Anandakrishnan, R. Aster, A. Huerta, T. Wilson, and J. Winberry (2017), The uppermost mantle seismic velocity and viscosity structure of central west antarctica, *Earth and Planetary Science Letters*, *472*, 38–49.

O'Donnell, J., A. Brisbourne, G. Stuart, C. Dunham, Y. Yang, G. Nield, P. Whitehouse, A. Nyblade, D. Wiens, S. Anadakrishnan, et al. (2019a), Mapping crustal shear wave velocity structure and radial anisotropy beneath west antarctica using seismic ambient noise, *Geochemistry, Geophysics, Geosystems*.

O'Donnell, J., G. Stuart, A. Brisbourne, K. Selway, Y. Yang, G. Nield, P. Whitehouse, A. Nyblade, D. Wiens, R. Aster, et al. (2019b), The uppermost mantle seismic velocity structure of west antarctica from rayleigh wave tomography: Insights into tectonic structure and geothermal heat flow, *Earth and Planetary Science Letters*, *522*, 219–233.

O'Donnell, J. P., and a. a. Nyblade (2014), Antarctica's hypsometry and crustal thickness: Implications for the origin of anomalous topography in East Antarctica, *Earth and Planetary Science Letters*, *388*, 143–155.

Owens, T. J., G. Zandt, and S. R. Taylor (1984), Seismic evidence for an ancient rift beneath the cumberland plateau, tennessee: A detailed analysis of broadband teleseismic p waveforms, *Journal of Geophysical Research: Solid Earth*, *89*(B9), 7783–7795.

Pankhurst, R., P. Leat, P. Sruoga, C. Rapela, M. Márquez, B. Storey, and T. Riley (1998a), The chon aike province of patagonia and related rocks in west antarctica: A silicic large igneous province, *Journal of volcanology and geothermal research*, *81*(1-2), 113–136.

Pankhurst, R., S. Weaver, J. Bradshaw, B. Storey, and T. Ireland (1998b), Geochronology and geochemistry of pre-jurassic superterranes in marie byrd land, antarctica, *Journal of Geophysical Research: Solid Earth*, *103*(B2), 2529–2547.

Pankhurst, R. J., C. W. Rapela, C. Fanning, and M. Márquez (2006), Gondwanide continental collision and the origin of patagonia, *Earth-Science Reviews*, *76*(3-4), 235–257.

Park, J., and V. Levin (2000), Receiver functions from multiple-taper spectral correlation estimates, *Bulletin of the Seismological Society of America*, *90*(6), 1507–1520.

Park, J., N. Gourmelen, A. Shepherd, S. Kim, D. G. Vaughan, and D. Wingham (2013), Sustained retreat of the pine island glacier, *Geophysical Research Letters*, *40*(10), 2137–2142.

Parker, T., B. Beaudoin, J. Gridley, and K. Anderson (2011), Next generation polar seismic instrumentation challenges, in *AGU Fall Meeting Abstracts*, vol. 1, p. 04.

Piana Agostinetti, N., and A. Malinverno (2018), Assessing uncertainties in high-resolution, multifrequency receiver-function inversion: A comparison with borehole data, *Geophysics*, *83*(3), KS11–KS22.

Podolskiy, E. A., and F. Walter (2016), Cryoseismology, *Reviews of geophysics*, *54*(4), 708–758.

Pourpoint, M., D. Wiens, W. Shen, R. C. Aster, A. Nyblade, and T. J. Wilson (2019), Constraints on shallow subglacial structure beneath thwaites glacier from joint inversion of receiver function and surface wave data, *AGUFM*, *2019*, NS11B–0632.

Ramirez, C., A. Nyblade, S. Hansen, D. Wiens, S. Anandakrishnan, R. Aster, A. Huerta, P. Shore, and T. Wilson (2016), Crustal and upper-mantle structure beneath ice-covered regions in antarctica from s-wave receiver functions and implications for heat flow, *Geophysical Journal International*, *204*(3), 1636–1648.

Ramirez, C., A. Nyblade, E. Emry, J. Julià, X. Sun, S. Anandakrishnan, D. Wiens, R. Aster, A. Huerta, P. Winberry, et al. (2017), Crustal structure of the transantarctic mountains, ellsworth mountains and marie byrd land, antarctica: constraints on shear wave velocities, poisson's ratios and moho depths, *Geophysical Journal International*, *211*(3), 1328–1340.

Randall, D. E., and C. Mac Niocaill (2004), Cambrian palaeomagnetic data confirm a natal embayment location for the ellsworth—whitmore mountains, antarctica, in gondwana reconstructions, *Geophysical Journal International*, *157*(1), 105–116.

Reading, A. M. (2002), Antarctic seismicity and neotectonics, *Royal Society of New Zealand Bulletin*, *35*, 479–484.

Reading, A. M. (2007), The seismicity of the antarctic plate, *SPECIAL PAPERS-GEOLOGICAL SOCIETY OF AMERICA*, *425*, 285.

Richter, C. F. (1935), An instrumental earthquake magnitude scale, *Bulletin of the seismological society of America*, *25*(1), 1–32.

Richter, C. F. (1958), *Elementary Seismology*, W. H. Freeman and Co., San Francisco.

Rignot, E., J. L. Bamber, M. R. Van Den Broeke, C. Davis, Y. Li, W. J. Van De Berg, and E. Van Meijgaard (2008), Recent antarctic ice mass loss from radar interferometry and regional climate modelling, *Nature Geoscience*, *1*(2), 106–110.

Rignot, E., J. Mouginot, and B. Scheuchl (2011), Ice flow of the antarctic ice sheet, *Science*, *333*(6048), 1427–1430.

Riley, T., M. Flowerdew, and M. Whitehouse (2012), U–pb ion-microprobe zircon geochronology from the basement inliers of eastern graham land, antarctic peninsula, *Journal of the Geological Society*, *169*(4), 381–393.

Riley, T. R., M. J. Flowerdew, R. J. Pankhurst, M. L. Curtis, I. L. Millar, C. M. Fanning, and M. J. Whitehouse (2017), Early jurassic magmatism on the antarctic peninsula and potential correlation with the subcordilleran plutonic belt of patagonia, *Journal of the Geological Society*, *174*(2), 365–376.

Ritzwoller, M. H., N. M. Shapiro, A. L. Levshin, and G. M. Leahy (2001), Crustal and upper mantle structure beneath Antarctica and surrounding oceans, *Journal Of Geophysical Research-Solid Earth*, *106*(12), 30,645–30,670.

Robertson Maurice, S. D., D. A. Wiens, P. J. Shore, E. Vera, and L. M. Dorman (2003), Seismicity and tectonics of the south shetland islands and bransfield strait from a regional broadband seismograph deployment, *Journal of Geophysical Research: Solid Earth*, *108*(B10).

Robinson, E. S., and J. F. Splettstoesser (1986), Structure of the transantarctic mountains determined from geophysical surveys, *Geology of the Central Transantarctic Mountains*, *36*, 119–162.

Rocchi, S., W. E. LeMasurier, and G. Di Vincenzo (2006), Oligocene to holocene erosion and glacial history in marie byrd land, west antarctica, inferred from exhumation of the dorrel rock intrusive complex and from volcano morphologies, *Geological Society of America Bulletin*, *118*(7-8), 991–1005.

Rowley, P., T. Laudon, K. La Prade, and W. LeMasurier (1986), Volcanoes of the antarctic plate and southern oceans.

Rudnick, R. L., and D. M. Fountain (1995), Nature and composition of the continental crust: a lower crustal perspective, *Reviews of geophysics*, *33*(3), 267–309.

Schimmel, M., and H. Paulssen (1997), Noise reduction and detection of weak, coherent signals through phase-weighted stacks, *Geophysical Journal International*, *130*(2), 497–505.

Schopf, J. M. (1969), Cllsworth mountains: Position in west antarctica ue to sea-floor spreading, *Science*, *164*(3875), 63–66.

Schroeder, D. M., D. D. Blankenship, D. A. Young, and E. Quartini (2014), Evidence for elevated and spatially variable geothermal flux beneath the west antarctic ice sheet, *Proceedings of the National Academy of Sciences*, *111*(25), 9070–9072.

Seroussi, H., E. R. Ivins, D. A. Wiens, and J. Bondzio (2017), Influence of a west antarctic mantle plume on ice sheet basal conditions, *Journal of Geophysical Research: Solid Earth*, *122*(9), 7127–7155.

Shapiro, N. M., and M. H. Ritzwoller (2004), Inferring surface heat flux distributions guided by a global seismic model: Particular application to Antarctica, *Earth and Planetary Science Letters*, *223*(1-2), 213–224.

Shen, W., D. A. Wiens, S. Anandakrishnan, R. C. Aster, P. Gerstoft, P. D. Bromirski, S. E. Hansen, I. W. Dalziel, D. S. Heeszel, A. D. Huerta, et al. (2018), The crust and upper mantle structure of central and west antarctica from bayesian inversion of rayleigh wave and receiver functions, *Journal of Geophysical Research: Solid Earth*.

Siddoway, C. S., and C. M. Fanning (2009), Paleozoic tectonism on the east gondwana margin: Evidence from shrimp u–pb zircon geochronology of a migmatite–granite complex in west antarctica, *Tectonophysics*, *477*(3-4), 262–277.

Siddoway, C. S., S. L. Baldwin, P. G. Fitzgerald, C. M. Fanning, and B. P. Luyendyk (2004), Ross sea mylonites and the timing of intracontinental extension within the West Antarctic rift system, *Geology*, *32*, 57–60.

Smith, A. M., and T. Murray (2009), Bedform topography and basal conditions beneath a fast-flowing west antarctic ice stream, *Quaternary Science Reviews*, *28*(7-8), 584–596.

Snoke, J. A. (2003), Focmec: Focal mechanism determinations, *International Handbook of Earthquake and Engineering Seismology*, *85*, 1629–1630.

Spiegel, C., J. Lindow, P. J. Kamp, O. Meisel, S. Mukasa, F. Lisker, G. Kuhn, and K. Gohl (2016), Tectonomorphic evolution of marie byrd land–implications for cenozoic rifting activity and onset of west antarctic glaciation, *Global and Planetary Change*, *145*, 98–115.

Steffen, R. (2013), The influence of glacial isostatic adjustment on intraplate seismicity in northeastern canada.

Stein, S., and M. Wysession (2009), *An introduction to seismology, earthquakes, and earth structure*, John Wiley & Sons.

Stern, T. a., and U. S. ten Brink (1989), Flexural uplift of the Transantarctic Mountains, *Journal of Geophysical Research: Solid Earth*, *94*(B8), 10,315–10,330.

Storey, B., and I. Dalziel (1987), Outline of the structural and tectonic history of the ellsworth mountains-thiel mountains ridge, west antarctica, *Gondwana six: structure, tectonics, and geophysics*, *40*, 117–128.

Storey, B. C., A. P. Vaughan, and I. L. Millar (1996), Geodynamic evolution of the antarctic peninsula during mesozoic times and its bearing on weddell sea history, *Geological Society, London, Special Publications*, *108*(1), 87–103.

Sykes, L. R. (1978), Intraplate seismicity, reactivation of preexisting zones of weakness, alkaline magmatism, and other tectonism postdating continental fragmentation, *Reviews of Geophysics*, *16*(4), 621–688.

Thelen, W. A., K. Allstadt, S. De Angelis, S. D. Malone, S. C. Moran, and J. Vidale (2013), Shallow repeating seismic events under an alpine glacier at mount rainier, washington, usa, *Journal of Glaciology*, *59*(214), 345–356.

Thurber, C. H., X. Zeng, A. M. Thomas, and P. Audet (2014), Phase-weighted stacking applied to low-frequency earthquakes, *Bulletin of the Seismological Society of America*, *104*(5), 2567–2572.

Thybo, H., and I. M. Artemieva (2013), Moho and magmatic underplating in continental lithosphere, *Tectonophysics*, *609*, 605–619.

Thybo, H., and C. A. Nielsen (2009), Magma-compensated crustal thinning in continental rift zones, *Nature*, *457*(7231), 873.

Trnkoczy, A. (2009), Understanding and parameter setting of sta/lta trigger algorithm, in *New Manual of Seismological Observatory Practice (NMSOP)*, pp. 1–20, Deutsches GeoForschungsZentrum GFZ.

Vaughan, D. G., A. M. Smith, P. C. Nath, and E. Le Meur (2003), Acoustic impedance and basal shear stress beneath four antarctic ice streams, *Annals of Glaciology*, *36*, 225–232.

Vaughan, D. G., H. F. Corr, R. A. Bindschadler, P. Dutrieux, G. H. Gudmundsson, A. Jenkins, T. Newman, P. Vornberger, and D. J. Wingham (2012), Subglacial melt channels and fracture in the floating part of pine island glacier, antarctica, *Journal of Geophysical Research: Earth Surface*, *117*(F3).

von Frese, R. R. B., L. Tan, J. Woo Kim, and C. R. Bentley (1999), Antarctic crustal modeling from the spectral correlation of free-air gravity anomalies with the terrain, *J. Geophys. Res.*, *104*(B11), 25,275–25,296.

Wannamaker, P., G. Hill, J. Stodt, V. Maris, Y. Ogawa, K. Selway, G. Boren, E. Bertrand, D. Uhlmann, B. Ayling, et al. (2017), Uplift of the central transantarctic mountains, *Nature communications*, *8*(1), 1588.

Wiens, D. A., S. Anandakrishnan, J. P. Winberry, and M. A. King (2008), Simultaneous teleseismic and geodetic observations of the stick–slip motion of an antarctic ice stream, *Nature*, *453*(7196), 770–774.

Wilson, D. S., and B. P. Luyendyk (2006), Bedrock platforms within the ross embayment, west antarctica: Hypotheses for ice sheet history, wave erosion, cenozoic extension, and thermal subsidence, *Geochemistry, Geophysics, Geosystems*, *7*(12).

Wilson, T., R. Aster, M. Bevis, I. Dalziel, A. Nyblade, C. Raymond, R. Smalley, and D. Wiens (2006), Ipy: Polenet-antarctica: Investigating links between geodynamics and ice sheets.

Winberry, J. P. (2003), Seismicity and neotectonics of West Antarctica, *Geophysical Research Letters*, *30*(18), 1931.

Winberry, J. P., and S. Anandakrishnan (2004), Crustal structure of the West Antarctic rift system and Marie Byrd Land hotspot, *Geology*, *32*(11), 977–980.

Winberry, J. P., S. Anandakrishnan, R. B. Alley, R. A. Bindschadler, and M. A. King (2009), Basal mechanics of ice streams: Insights from the stick-slip motion of whillans ice stream, west antarctica, *Journal of Geophysical Research: Earth Surface*, *114*(F1).

Winberry, J. P., A. D. Huerta, S. Anandakrishnan, R. C. Aster, A. A. Nyblade, and D. A. Wiens (2020), Glacial earthquakes and precursory seismicity associated with thwaites glacier calving, *Geophysical Research Letters*, *47*(3), e2019GL086,178.

Wingham, D., D. Wallis, and A. Shepherd (2009), Spatial and temporal evolution of pine island glacier thinning, 1995–2006, *Geophysical Research Letters*, *36*(17).

Wörner, G. (1999), Lithospheric dynamics and mantle sources of alkaline magmatism of the Cenozoic West Antarctic Rift System, *Global and Planetary Change*, *23*, 61–77.

Yakymchuk, C., C. R. Brown, M. Brown, C. S. Siddoway, C. M. Fanning, and F. J. Korhonen (2015), Paleozoic evolution of western marie byrd land, antarctica, *Bulletin*, *127*(9-10), 1464–1484.

Yilmaz, Ö. (2001), *Seismic data analysis: Processing, inversion, and interpretation of seismic data*, Society of exploration geophysicists.

Zandt, G., S. C. Myers, and T. C. Wallace (1995), Crust and mantle structure across the basin and range-colorado plateau boundary at 37 n latitude and implications for cenozoic extensional mechanism, *Journal of Geophysical Research: Solid Earth*, *100*(B6), 10,529–10,548.

Zhu, L., and H. Kanamori (2000), Moho depth variation in southern california from teleseismic receiver functions, *Journal of Geophysical Research: Solid Earth*, *105*(B2), 2969–2980.

Zoet, L. K., S. Anandakrishnan, R. B. Alley, A. A. Nyblade, and D. A. Wiens (2012), Motion of an antarctic glacier by repeated tidally modulated earthquakes, *Nature Geoscience*, *5*(9), 623–626.